Modeling Macroscopic Shape Distortions during Sintering of Multi-layers

Tadesse Molla, Tesfaye; Frandsen, Henrik Lund; Pryds, Nini; Bjørk, Rasmus

Publication date:
2014

Document Version
Publisher's PDF, also known as Version of record

Modeling Macroscopic Shape Distortions during Sintering of Multi-layers

PhD Thesis

By: Tesfaye Tadesse Molla

Supervisors: **Henrik Lund Frandsen (Senior Scientist)**
Nini Pryds (Professor)
Rasmus Bjørk (Senior Scientist)

Department of Energy Conversion and Storage
Technical University of Denmark

June 2014

.

Department of Energy Conversion and Storage
Technical University of Denmark

Table of Contents

Foreword and Acknowledgment

This work has been carried out at the Department of Energy Conversion and Storage, Technical University of Denmark (DTU), during the period 2011-2014. The study has been supervised by Henrik Lund Frandsen (Senior scientist), and co-supervised by Nini Pryds (Professor) and Rasmus Bjørk (Senior scientist). This project is part of a larger project called "Optimized Processing of Multi-material Architectures for functional Ceramics or OPTIMAC". The project was funded by the Danish Agency for Science, Technology and Innovation (FTP) (Contract No. 09 - 072888), which is part of the Danish Council for Independent Research (DFF). OPTIMAC consists of three work packages (WPs) and this study is one of the sub projects i.e. SP-5 under WP-2, which focuses on mechanical modeling of sintering. The present study was carried out in close collaboration with SP-3 (Micro-scale modeling of sintering process), SP-9 (Sintering behaviors of complex structures) and SP-7 (Experimental extrusion of tubular multi-layer materials for oxygen membranes).

My foremost and heartfelt gratitude and appreciation goes to all my supervisors (Henrik Lund Frandsen, Nini Pryds and Rasmus Bjørk) who were right beside me throughout the course of this study providing every kind of assistance I needed. Their friendly approach, critical and insightful reviews and regular oversight to my work helped me enjoy, stay focused and push through the project. It has been a great experience working with them.

My sincere acknowledgment also goes to Professor Eugene Olevsky (from San Diego State University, USA) who not only inspired me to the field of sintering mechanics but also helped me throughout the different stages of my study. It was a privilege for me to work with him and share his abundant experience, which resulted in a number of valuable publications. Among the other international collaborations, I would also like to thank Professor Friedrich Raether (from the Fraunhofer Institut Silicatforschung ISC, Germany) and Dr. Veena Tikare (from Sandia National Laboratories, USA) for their comments and feedbacks during our casual meetings.

The vital collaborations with other researchers and students in the Department of Energy Conversion and Storage (DTU-ECS) including Dr. Vincenzo Esposito (senior scientist), Dr. De Wei Ni (researcher), Regina Bulatova (PhD student) and Dhavanesan K Ramachandran (PhD student) were important for the completion of this work. Hence, I extend my gratitude for their inputs especially in the experimental part of the work.

I am also indebted to Dr. Andreas Kaiser (senior scientist), Dr. Christian Bahl (senior scientist), Dr. Kawai Kwok (researcher), Dr. Francesca Teocoli (PostDoc), Dr. Benoit Charlas (PostDoc), Dr. Dino Boccaccini (researcher) and Kjeld Bøhm Andersen (development engineer) for their various supports and feedbacks. My appreciation also goes to all the stuff members in the department of DTU-ECS especially to the head of my section (Professor Peter Vang Hendriksen) and the very helpful secretaries (Heidi Adler Pedersen and Anita Voss).

My deepest appreciation and gratitude goes also to my beloved wife and parents together with my relatives and friends for their unconditional love, support and encouragement throughout my professional carrier. Last but by no means the least, praise and thanks unto the lord for the wisdom, perseverance and all the blessings that he has bestowed upon me throughout my life.

Tesfaye T. Molla

June 2014, Denmark

Summary

Ceramic multi-layered composites are being used as components in various technologies ranging from electronics to energy conversion devices. Thus, different architectures of multi-layers involving ceramic materials are often required to be produced by powder processing, followed by sintering (firing). However, unintended features like shape instabilities of samples, cracks or delamination of layers may arise during sintering of multi-layer composites. Among these defects, macroscopic shape distortions in the samples can cause problems in the assembly or performance of the final component, which could result in product rejection.

It is generally recognized that macroscopic shape distortion is linked to the sintering kinetics mismatch between the layer materials making the multi-layer during the co-firing process. However, there is still a need for better understanding of the deformational mechanisms with the application of flexible modeling techniques taking into account the various factors during co-firing. In addition, realistic microstructures in time/temperature need to be considered while defining the deformational behaviors of the sintering body in order to improve the predictive capabilities of the existing constitutive models.

In this context, a simulation method or framework has been developed, which involves the use of sintering experiments, analytical and numerical methods. In addition to the intrinsic material parameters (shrinkage and viscous behaviors), the effect of extrinsic factors such as gravity, friction and geometry of the sample on the evolution of shape of multi-layers have been investigated. Furthermore, a new type of modeling procedure with a potential to introduce the realistic microstructure of a porous body, while defining the intrinsic material parameters, has been developed.

The linear version of the Skorohod Olevsky Viscous Sintering (SOVS) model has been used in the developed simulation models. A combination of free shrinkage rate measurements from optical dilatometry and analytical models has been used to determine the necessary input parameters for simulation of sintering of multi-layer components. Validation of the input parameters has been made indirectly by comparing model predictions for camber evolution during sintering of a bi-layer with measurements thereof. Moreover, a 'master sintering curve'-type model of bi-layer sintering

has been derived. This model excels in requiring a single optical dilatometry run to collect all the necessary input parameters for modeling of the sintering of the bi-layers.

The determined input parameters have also been used in a finite element model, which is developed based on the continuum theory of sintering, to model the camber development during co-firing. The effect of extrinsic factors (e.g. gravity, thickness ratio and friction) on the shape evolution of bi-layers during co-firing has been studied using the developed model and experiments. Furthermore, a new analytical model describing stresses during sintering of tubular bi-layer structures has been developed by using the direct correspondence between elasticity and linear viscous problems. The finite element model developed in this study and sintering experiments of tubular bi-layer sample have been used to verify and validate the developed analytical model for tubular bi-layered structures.

A multi-scale model of shape distortions during co-firing has also been developed by coupling a meso-scale model of sintering based on kinetic Monte Carlo (kMC) methods and a macro-scale continuum model. In this case, computational homogenization theories were used to extract the viscous parameters from a representative volume element (RVE) of the porous body. The RVE was based on the microstructure obtained from the kMC model.

Results from the developed analytical as well as numerical models agree well with experimental measurements of densification and camber evolutions during co-firing of bi-layers. Optimizations of the co-firing process by controlling the initial geometry of the sample and structural characteristics are also suggested. Furthermore, the multi-scale model has also shown the expected behavior of shape distortions for different bi-layers systems involving layers with the same and different sinterabilities.

Based on the experimental and simulation results, the following conclusions are reached: during sintering of planar multi-layers, understanding of the effect of gravity on the camber evolution can be used in optimizing the co-sintering process so as to help achieve defect free multi-layer components. The initial thickness ratio between the layers making the multi-layer has also significant effect on the extent of camber evolution depending on the material systems. During sintering of tubular bi-layer structures, tangential (hoop) stresses are very large compared to radial stresses. The maximum value of hoop stress, which can generate processing defects such as cracks and coating peel-offs, occurs at the beginning of the sintering cycle.

Unlike most of the models defining material properties based on porosity and grain size only, the multi-scale model proposed in this study has no limitation as to the number of internal parameters to define shrinkage kinetics as well as viscous properties. This feature of the model makes it to be a promising approach for extending the continuum theory of sintering.

Key words: Sintering; Constrained sintering; Multi-layer ceramic composites; Modeling; Multi-scale modeling

Resumé

Keramisk multi-lags kompositter er i betragtning i udviklingen af komponenter, der kan bruges i forskellige teknologier, lige fra elektronik til energi-generatorer. Forskellige arkitekturer af systemer med flere af disse keramiske lag produceres ved hjælp af en sintringsprocess. Defekter såsom formændringer, revner og delaminering af lag kan opstå i behandlingen af disse multilagskomponenter. Forarbejdningsdefekter kan resultere i problemer både ved montering eller omkring ydeevnen af den endelige komponent, hvilket i sidste ende kan medføre at produktet kasseres. Blandt disse defekter undersøges den makroskopisk forminstabilitet under sintring af flerlagstrukturer i dette studie.

Det er almindeligt anerkendt, at formdefekter, altså ændring i den geometriske form af sintrede emner, er knyttet til et misforhold i sintringskinetik imellem de forskellige materialer i et givent multilagsystem, under sintringsprocessen (co-sintring). Der er stadig et behov for en bedre forståelse af deformationsmekanismerne ved anvendelse af fleksible modelberegninger under hensyntagen til de forskellige faktorer i løbet af co-sintring. Desuden er de eksisterende numeriske modeller begrænsede og skal forbedres yderligere at forbedre deres evne til at forudsige sintringsprocessen.

I denne sammenhæng er en simuleringsmetode blevet udviklet, som indebærer en kombination af eksperimenter, analytiske og numeriske metoder. Ud over de intrinsiske materialeparametre (sammentrækningskinetik og viskositet), er indvirkningen af ydre faktorer såsom tyngdekraft, friktion og prøvegeometri på udviklingen af en multilagprøves form blevet undersøgt. Endvidere er en ny type modelleringsprocedure blevet udviklet. Denne har potentiale til at inkludere mikrostruktureren af et porøst legeme i sintringsmodellen og hermed inkludere materialeparameters som i øjeblikket ikke betragtes i de eksisterende modeller.

Den lineære version af Skorohod Olevsky Viskøs Sintrings model (SOVS) er blevet anvendt til de udviklede sintringsmodeller. En kombination af målinger af sammentrækningsratens med optisk dilatometri og analytiske modeller er anvendt til at bestemme de nødvendige inputparametre til simulering af sintring af multilagskomponenter. Validering af disse input parametre er blevet gjort indirekte ved at sammenligne modelforudsigelser af bi-lagssystemers krumningsudvikling under sintring med eksperimentielle målinger heraf. Derudover er en 'master sintring kurve' type model

blevet udledt til beskrivelse af bilags sintring. Denne model udmærker sig ved at blot kræve et enkelt dilatometri eksperiment for at fastlægge alle de nødvendige input til simulering af sintring af bi-laget.

De fundne inputparametre er også blevet anvendt i en finite element model baseret på kontinuumsteorien for sintring til at modellere udviklingen i krumning under sintring af en multilagskomponent. Effekten af ydre faktorer (eksempelvis tyngdekraft, forholdet af tykkelse mellem de individuelle keramiske lag, samt friktion) på den tidslige udvikling af en bi-lags prøveform under co-sintring er blevet undersøgt ved hjælp af den udviklede model samt eksperimenter. Desuden er det elastiske lineære viskoelastiske korrespondensprincip blevet anvendt til at udvikle en analytisk model, der beskriver spændinger under sintring af rørformede dobbeltlagskomponenter. En finite element model udviklet i dette PhD studie samt tilhørende eksperimenter med rørformede bi-lagskomponenter er blevet brugt til at verificere og validere den udviklede analytiske model.

En multi-skala model af formændringer under co-sintring er også blevet udviklet ved at koble en meso-skala sintringsmodel baseret på kinetisk Monte Carlo (kMC) metoder og en makro-skala kontinuum model. Forskellige numeriske homogeniseringsteorier er blevet anvendt til at bestemme de viskøse parametre fra et repræsentativt volumen element (RVE) af det porøse legeme. RVE'et er baseret på simularede mikrostruktur i kMC modellen.

Resultaterne fra de udviklede analytiske såvel som numeriske modeller stemmer godt overens med eksperimentelle målinger af den tidslige densifikations- og krumningsudvikling under co-sintring. Optimering af co-sintringen ved at kontrollere prøvens oprindelige geometri og strukturelle karakteristika er også foreslået. Tilsvarende har multi-skala modellen også fremvist de forventede formændringer i forskellige bi-lagssystemer bestående af lag med enten den samme og forskellig sintringsevne.

Baseret på både de eksperimentelle-og simuleringsresultater er følgende konklusioner draget: under sintring af plane multi-lag kan forståelsen af effekten af tyngdekraften på krumningsudviklingen bruges til optimering af co-sintringsproces, således at defekt-fri multilagskomponenter kan fremstilles. Forholdet mellem tykkelsen af de individuelle lag i en prøve kan også betydeligt påvirke udviklingen af krumnings af en prøve. Under sintring af rørformede bi-lagsstrukturer er tangentielle spændinger er meget større i forhold til radiale spændinger. Den

maksimale værdi af de tangentielle spændinger, som kan generere procesdefekter såsom revner og delaminering, opstår ved begyndelsen af sintringen.

I modsætning til de fleste eksisterende modeller, der definerer materialeegenskaber baseret kun på porøsitet og kornstørrelse, så har den foreslåede multi-skala model ingen begrænsning i antallet af interne parametre til at definere densifikationskinetik samt viskøse egenskaber. Dette gør denne tilgang til en lovende mulighed for at udvide kontinuumsteorien for sintring.

Nøgleord: Sintring; Fastholdt sintring; Flerlags keramiske kompositter; Modellering; Multi-skala modellering

List of Publications

Publications (peer-reviewed)

1. T.T. Molla, H.L. Frandsen, R. Bjørk, D.W. Ni, E. Olevsky and N. Pryds, "Modeling kinetics of distortions in porous bi-layered structures," *J Eur Ceram Soc*, **33**, 1297-1305 (2013) [§]

2. E. Olevsky, T.T. Molla, H.L. Frandsen, R. Bjørk, V. Esposito, D.W. Ni, A. Ilyna and N. Pryds, "Sintering of multi-layered porous structures: Part I-Constitutive models," *J Am Ceram Soc*, **96** [8] 2657–2665 (2013) [§]

3. D.W. Ni, E. Olevsky, V. Esposito, T.T. Molla, S.P. Foghmoes, R. Bjørk, H.L. Frandsen, E. Alexandrova and N. Pryds, "Sintering of multi-layered porous structures: Part II-Experiments and model applications," *J Am Ceram Soc*, **96** [8] 2666–2673 (2013) [§]

4. T.T. Molla, D.W. Ni, R. Bulatova, R. Bjørk, C. Bahl, N. Pryds and H.L. Frandsen, "Finite element modeling of camber evolutions during sintering of bi-layer structures," *J Am Ceram Soc*, *in press* (2014) [§]

5. T.T. Molla, D.K. Ramachandran, D.W. Ni, V. Esposito, F. Teocoli, E. Olevsky, R. Bjørk, N. Pryds, A. Kaiser and H. L. Frandsen, "Constrained sintering of bi-layered tubular structures," *J Am Ceram Soc*, *under review* (2014) [§]

6. T.T. Molla, R. Bjørk, E. Olevsky, N. Pryds and H.L. Frandsen, "Multi-scale modeling of shape distortions during sintering of bi-layers," *J Comp Mat Sci*, **88** 28–36 (2014) [§]

7. H.L. Frandsen, E. Olevsky, T.T. Molla, V. Esposito, R. Bjørk and N. Pryds, "Modeling sintering of multi-layers under the influence of gravity," *J Am Ceram Soc*, **96** [1] 80–89 (2013)

8. D.W. Ni, V. Esposito, C. G. Schmidt, T.T. Molla, K. B. Andersen, A. Kaiser, S. Ramousse and N. Pryds, "Camber evolution and stress development of porous ceramic bi-layers during co-firing," *J Am Ceram Soc*, **96** [3] 972–978 (2013)

[§] Publications appended to the thesis report

Conference Publications and Presentations

1. T.T. Molla, H.L. Frandsen, V. Esposito, R. Bjørk, S.P. Foghmoes, E. Olevsky and N. Pryds, “Analysis of key factors controlling sintering of dense and porous CGO bi-layers,” Material Science and Technology (MS&T-2011), Columbus, Ohio (USA), 2011

2. F. Teocoli, D.W. Ni, T.T. Molla, K. Brodersen, S. Ramousse, H.L. Frandsen and V. Esposito, “Shape distortion and thermo-mechanical properties of SOFC components from green tape to sintering body,” Nordic Conference on Ceramic and Glass Technology, Roskilde (Denmark), 2012

3. T.T. Molla, H.L. Frandsen, V. Esposito, R. Bjørk, D. W. Ni, E. Olevsky and N. Pryds, “Improved modeling approaches for constrained sintering of bi-Layered porous structures,” Powder Metallurgy world congress and exhibition (PM-2012), Yokohma (Japan), 2012

4. T.T. Molla, R. Bjørk, E. Olevsky, N. Pryds and H.L. Frandsen, “Multi-scale modeling of shape distortions during sintering of bi-layers,” International Conference and exposition on Advanced Ceramics and Composits (ICACC-2014), Daytona beach, Florida (USA), 2014

List of Figures

1. Introduction

This section includes the introduction to the thesis starting with discussions about functionally graded ceramic multi-layered materials. A general introduction to sintering, which is one of the processing techniques in the manufacturing of multi-layered ceramics, is presented in Sections 1.2. Problems during sintering of multi-layered structures and the need for better and flexible simulation methods are discussed in Section 1.3. Furthermore, the objectives of the thesis, methodologies used throughout the study and organization of the thesis report are summarized in Sections 1.4, 1.5 and 1.6, respectively.

1.1. Functionally graded ceramic multi-layers

Since the first introduction of functionally graded materials (FGMs) in 1984 as a means of preparing thermal barrier materials, about 200 possibilities of utilizing the concept have been proposed.[1] Functionally graded materials are characterized by changing properties across the volume of the component due to spatial variation of composition, morphology, or microstructure of the material.[1, 2] The unique feature of FGMs is the ability to tailor a material for specific application. The design of FGMs can have a continuous or discrete variation of phases with the intention of taking advantage of the desirable features of each of the constituent phases.[3] Multi-layers made from layers with different phases can be categorized as discretely graded functional materials.

It is also the case that the performance of a ceramic component can be increased markedly if it is possible to vary the relevant properties (e.g. electrical, electrochemical, or magnetic) in a controlled manner along the extent of the component. Ceramic composites, in which layers of different composition and/or microstructure are combined in a certain architecture to achieve varying functionality across the component, are called functionally graded ceramic multi-layers. Functionally graded ceramic multi-layers find use in many different applications requiring materials with spatial variation of properties. These include, e.g. solid oxide fuel and/or electrolysis cells (SOFCs or SOECs), thermal barrier coatings (TBCs), piezoactuators, capacitors, gas membranes, and

filters.[4–14] Advances in ceramic forming have enabled low cost shaping techniques such as tape casting and extrusion to be used in some of the most challenging technologies. These advances allow the design of complex components adapted to desired specific properties and applications.

Different types of multi-layer architectures are being considered in the development of various technologies. Examples of these include planar, adjacently graded and tubular architectures for solid oxide fuel cell, magnetic refrigeration and gas membrane technologies, respectively.[9, 15, 16] Figure 1 shows schematics of the different types of multi-layer architectures. After shaping the multi-layer composite with the required architecture, it is often the case to fire the materials with the intention of increasing the density, mechanical strength, ionic conductivity, etc of the structure. Hence, simultaneous firing of the materials in the multi-layer (co-firing or co-sintering) is usually one of the important steps in the manufacturing of functionally graded composites.

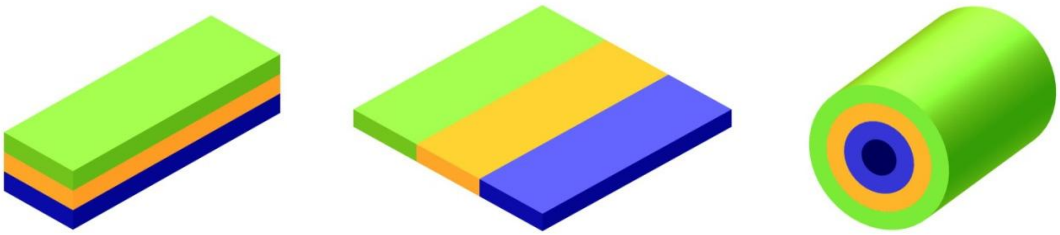

Figure 1: Schematics of different types of multi-layer architectures [OPTIMAC project[17]]

1.2. Sintering of ceramics

This section, which is an overview to sintering in general, is based on classical sintering textbook and handbook of advanced ceramics after Rahaman[18] and Somiya et *al*.[19]

Fabrication processes of ceramic materials often involve a heat treatment step in which a powder compact, formed into the required shape (often referred to as green body), is converted into a dense solid. This process is known as sintering (firing). There are four types of sintering depending on the composition of material being fired and on the extent to which second phases are involved during the heat treatment:

I. Solid state sintering: the green body involves pure polycrystalline materials and is heated to a temperature that is typically between 50 – 90 % of the melting point with no liquid present in the powder compact. Atomic diffusion in the solid state produces joining of particles and hence densification and coarsening.

II. Liquid state sintering: the green body involves a small amount of liquid typically less than a few volume percent of the original solid mixture at the sintering temperature. The liquid phase is insufficient to fill the pore space but provides a high diffusivity path for the transport of matter into the pores improving densification.

III. Vitrification: whenever the green body contains a relatively larger volume of liquid (more than 25 % of the original solid volume), which fills up the pore space, densification is driven by crystallization or vitrification. This type of sintering is common in clay based ceramics, such as porcelains.

IV. Viscous sintering: sintering process in amorphous bodies, like consolidated glass particles, occur by viscous flow of materials, which involves deformation of particles at the sintering temperature.

1.2.1. Driving force for sintering

Sintering is accompanied by lowering of free energy of the system, which can be achieved by 1) reduction in the curvature of the particle surface (i.e. lowers the surface free energy), 2) externally applied pressure or 3) chemical reaction.

In the absence of externally applied pressure and chemical reaction, the inherent tendency of materials to lower their free energy (by reducing the curvature of particle surfaces) drives sintering at elevated temperatures. To clarify this concept, let us consider a simple example involving a mole of powder consisting of spherical particles with a radius, a. The total number of particles can be given by:

$$N = \frac{3M}{4\pi a^3 \bar{\rho}} = \frac{3V_m}{4\pi a^3} \tag{1}$$

Here, $\bar{\rho}$, is the density of the particles, which are assumed to contain no internal porosity, M, is the molecular weight, and V_m is the molar volume. The surface area of the system of particles can be given by:

$$S_A = 4\pi a^2 N = 3V_m / a \quad (2)$$

If γ_s is the specific surface energy per unit area of the particles, then the total surface energy associated with the system of particles is:

$$E_s = 3\gamma_s V_m / a \quad (3)$$

E_s represents the decrease in surface energy of the system of particles, if a fully dense body were to be formed from the mole of particles, and provides motivation for sintering. Of course in the case of polycrystalline materials, a decrease in free energy associated with surfaces of particles increases the energy associated with grain boundaries due to formation of grains. This effect drives coarsening of particles (grain growth), through which the overall free energy of the system continues to lower. Therefore, the process of sintering brings two major changes to the sintering body: 1) volumetric densification of the porous compact or elimination of pores and 2) coarsening of powder particles or grain growth. Both changes help reduce the total free energy of the porous body and occur simultaneously during sintering. Application of external compressive pressure on the sintering body assists the internal driving force for sintering.

1.2.2. Mechanisms of sintering

Sintering of polycrystalline materials occurs by transport of matter along definite paths (lattice, grain boundary, and surface) that define the mechanisms of sintering. As schematized in Figure 2, there are six typical mechanisms of matter transport during sintering of polycrystalline materials. All mechanisms lead to bonding and neck growth between particles. They can also be generally classified as densifying and nondensifying mechanisms.

a. Nondensifying mechanisms include surface diffusion, volume (lattice) diffusion from the particle surfaces to the neck, and vapor transport (mechanisms 1, 2, and 3), which lead to neck coarsening without densification.

b. Densifying mechanisms include grain boundary diffusion and lattice diffusion from the grain boundary to the pore (mechanisms 4, 5 and 6), which permits neck growth, densification and plastic flow by dislocation motion.

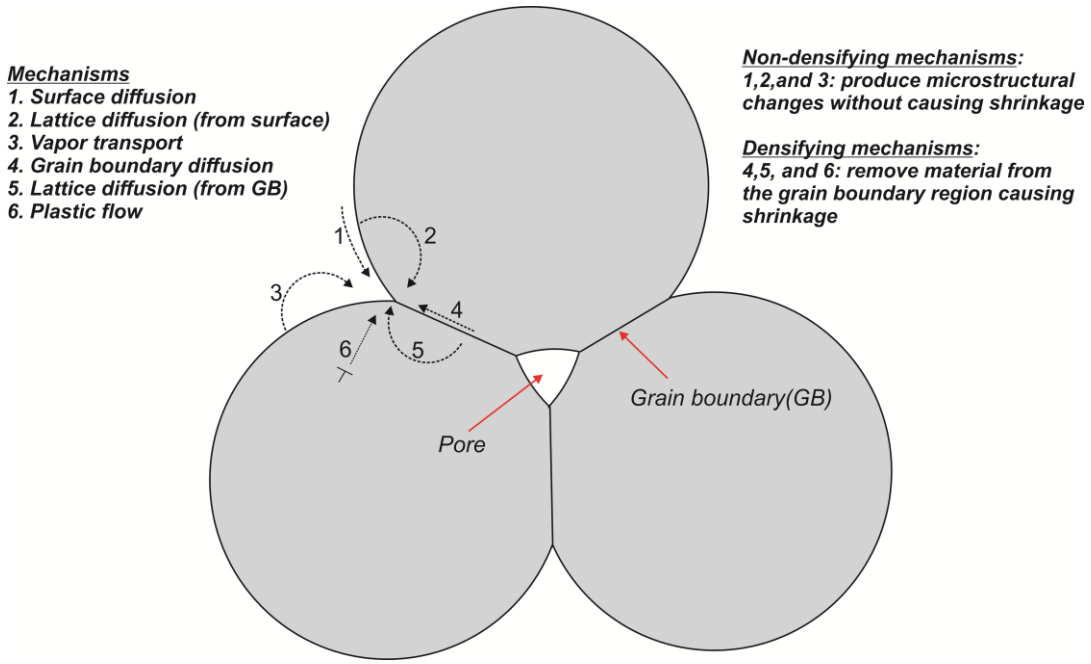

Figure 2: Schematic represenation of sintering mechanisms in polycrystalline materials [after Rahaman[18]]

1.2.3. Stages of sintering

For the sake of theoretical analysis, sintering processes are usually subdivided into three sequential stages referred to as: the initial, intermediate, and final stages. Figure 3 shows the schematic representation of the three stages of sintering with the help of three particles.

1. The initial stage: is dominated by rapid inter-particle neck growth by diffusion, vapor transport, plastic flow, or viscous flow, see Figure 3. Large initial differences in surface curvature characterize this stage, and densification accompanies neck growth for the densifying mechanisms.

2. The intermediate stage: this stage begins when pores have reached their equilibrium shapes as governed by the surface and interfacial tensions. Densification is assumed to result from pores simply shrinking to reduce their cross section. The intermediate stage normally covers the major part of the sintering process, and it comes to an end when the density of the porous body reaches close to 90 % of the fully dense body.

3. The final stage: the final stage begins when the pores pinch off and become isolated at the grain corners. This stage is mainly characterized by slower densification and rapid grain growth or coarsening.

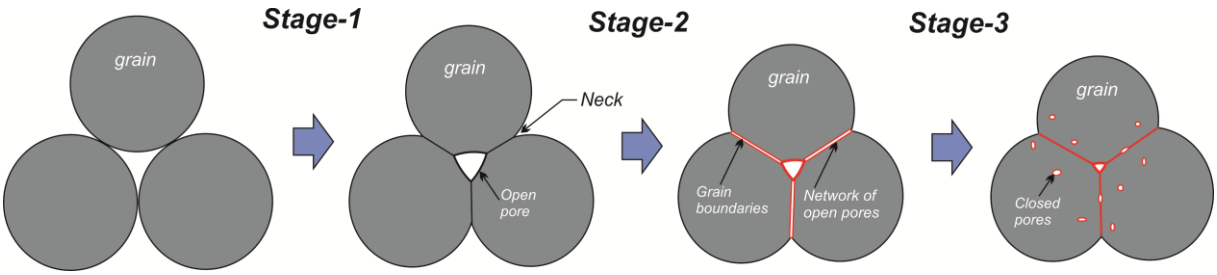

Figure 3: Schematic representation of the three stages of sintering [after Tanaka et *al*.[20]]

1.2.4. Characterization of sintering

Different measurements can be used to characterize densification and microstructural evolutions of a porous compact during sintering. Perhaps, the most widely used characterizations include measurements of the density (or shrinkage) and grain size. Some of the techniques used to measure density and/or linear shrinkage are described in Section 2. Sintering of a powder compact is often represented by the evolution of the relative density, ρ, or linear shrinkage, ε, as a function of time, t, and/or temperature, T. The relative density is defined by the bulk density of the porous compact divided by the theoretical density of the solid material. For isotropic densification with no significant mass change, the linear shrinkage of a sintering body can be defined by:

$$\varepsilon = \frac{\Delta L}{L_0} \tag{4}$$

where L_o is the initial length, L is the length at a given time or temperature and $\Delta L = L - L_o$. True strain measures can also be used if the sintering body involves large deformations. The relationship between the evolving relative density and shrinkage for a porous body with a green density of, ρ_o, is given by:

$$\rho = \frac{\rho_o}{(1 + \Delta L / L_o)^3} \tag{5}$$

The fraction of voids or porosity, θ, can be determined as: $\theta = 1 - \rho$. It is often necessary to determine the volumetric shrinkage rate or densification rate, $\dot{e}$, in terms of the time derivative of the relative density as:

$$\dot{e} = \frac{\dot{\rho}}{\rho} \quad \text{where} \quad \dot{\rho} = \frac{d\rho}{dt} \tag{6}$$

1.3. Sintering of multi-layer structures

The co-firing or co-sintering process is often challenging mainly due to the different densification rate between the constituent layers in the multi-layer systems. For instance, during sintering of bi-layers consisting of tapes with different sintering behavior, transient stresses are generated that hinder or speed up the densification in each layer. Such kind of stress could create processing defects like cracks or delamination at the interface between the layers. If the bi-layer structure is strong enough to remain enact, it relaxes the transient stresses generated inside the structure by warping or developing camber.

The buildup of stress and camber during co-firing of a bi-layer having layers with different densification rates is illustrated schematically in Figure 4. The relative difference in the shrinkage kinetics, $\dot{\varepsilon}^f$, between Layer-1 and 2 generates internal forces, N, and bending moments, M, across the thickness of the structure. These in turn causes a viscous deformation involving distortion of the sample with a camber, u. In this study, macroscopic shape distortion during co-firing refers to the camber or warpage evolution of the planar multi-layer structure.

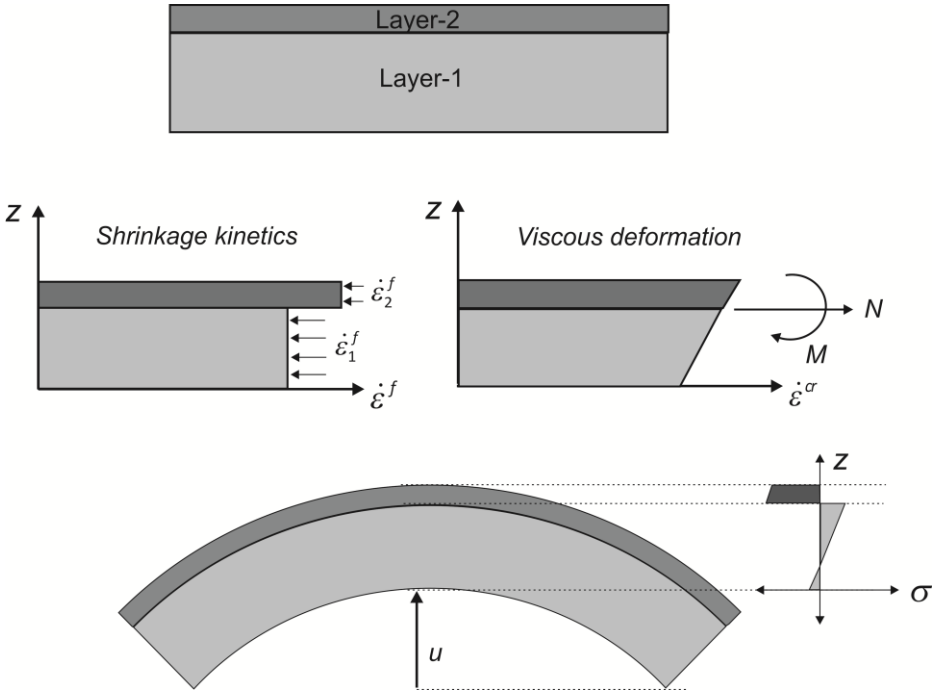

Figure 4: Schematics showing the free shrinkage, $\dot{\varepsilon}^f$, and constraint related, $\dot{\varepsilon}^{cr}$, strain rates with shape distortion, u, and stress, σ, distributions across the thickness of the bi-layer structure.

Developing a methodology to control and optimize the internal stresses during co-firing is crucial in the process of producing defect free multi-layers systems. In this regard, the development of modeling or simulation methods for co-firing of multi-layer structures will be important for critical understanding of the densification and deformation mechanisms. While developing a methodology to predict macrostructural shape distortions and stresses during co-firing, it is important to critically understand:

a. The deformational behaviors of sintering bodies (shrinkage rate and viscous mechanical behaviors) and

b. The extrinsic factors affecting the evolution of shape during sintering of multi-layer samples

The shrinkage and viscous behaviors of the porous bodies can be considered as the intrinsic material properties during sintering. For a given heating schedule, these parameters can be tailored mainly during the preparation of the green bodies. During co-firing, the differential shrinkage rate and relative viscosity between the layers making the multi-layer play a key role in controlling the extent of stress generation and hence shape distortions.

Measurement of the shrinkage as well as viscous behaviors during free sintering and high temperature creep experiments respectively are often used to collect the necessary input parameters for simulation of stress or camber during sintering of multi-layers. Nowadays, measurement of free shrinkage can be performed reliably with advanced in-situ measuring techniques such as non-contact optical dilatometers. On the other hand, the use of experimentally measured effective viscosities for modeling stresses in multi-layers is based on the assumption of similar microstructural evolution during co-firing and creep experiments. However, this might not be true as the porous body in the multi-layer structure is exposed to a different state of stress unlike creep experiments, which are mostly performed under uniaxial loads. I.e. the state of stress could affect the microstructural evolution and hence the effective viscosity of the sintering body at a given temperature and time. To avoid such assumptions, the viscosity of the fully dense body of the layers making the multi-layer can be first determined using a combination of models and experiments. Then the effective viscosity for modeling the multi-layer sample can be estimated from the fully dense body viscosity and a function for the microstructural evolution (e.g. density) during the co-firing process.

Extrinsic factors are those related to processing parameters like heating rate or other factors during processing such as geometry of the sample, gravity, friction or boundary conditions. These factors

can be features from the design of the multi-layer component, like the geometry, or they can be controlled during the co-firing process. Extrinsic factors also affect the camber evolutions of the multi-layers and hence they are also required to be understood in the processing of multi-layer composites.

Furthermore, the simulation method to predict stresses or shape instabilities needs to be flexible and robust enough to model sintering of multi-layers of any geometry under different conditions. This can be achieved by using numerical techniques such as the finite element methods (FEM). Some of the advantages of developing a flexible method to predict stresses/shape distortions during sintering of multi-layers are, for example:

a. It is possible to investigate the effect of the extrinsic factors such as geometry, gravity, friction, etc on the overall shape distortion in multi-layers
b. It is possible to model stress developments during constrained sintering of multi-layers with complex geometries such as tubular multi-layer systems.

1.4. Objectives of the thesis

The purpose of this study is to develop a simulation method that can predict the densification, macrostructural shape distortions and stresses during sintering of multi-layer composite structures. The simulation method is developed with the aim of making it flexible to model sintering of multi-layers of any geometry under different conditions. It is also intended to validate the simulation results with the help of sintering experiments involving planar and tubular multi-layers.

In addition to development of a simulation method, this study aims to investigate the effect of extrinsic factors such as gravity, friction and geometrical parameters of planar multi-layers on the evolution of shape distortion during co-firing process.

The type of sintering process, which is driven by chemical reaction, is out of the scope of the present study. Furthermore, the possible anisotropies of the sintering parameters and of the pore-grain structure are not considered in the development of the simulation models.

1.5. Methodology

To achieve the above goals, experiments, analytical models and numerical techniques based on finite element methods (FEM) are used with the following main tasks in chronological order:

I. Using a combination of analytical models and a single dilatometry run, an alternative way to creep experiment is proposed to obtain material parameters defining the viscosity of fully dense bodies, which can be used to find the effective viscosities during co-sintering.

II. The effective viscosities, which are updated based on the densification of each layer during co-sintering, are validated indirectly by comparing model predictions for camber evolution of a bi-layer (using the estimated effective viscosities) with experimental measurements.

III. Development of a numerical model using finite element method followed by verifications and validations against analytical models and experiments.

IV. Investigations of the effect of extrinsic factors (gravity, geometrical parameters and friction) on the evolution of shape distortion during co-firing

In this work, a combination of free sintering experiments and analytical models are first used to estimate the viscosity of fully dense bodies for each layer making the bi-layer. Then the effective viscosity of each layer in a bi-layer model is estimated from the viscosity of fully dense body and a function accounting the effect of microstructural evolution during co-sintering. To validate the effective viscosities, prediction of an analytical model for camber development is compared with experimental measurements during sintering of a bi-layer sample. Such an approach can also reduce the need for separate sets of creep experiments to measure viscosity. After validation, the shrinkage and viscous parameters become inputs for a simulation tool that is developed using finite element method to predict shape distortions during sintering of multi-layers in different conditions.

This study also presents a new methodology allowing the direct application of sintering models for the description of co-sintering of bi-layered structures. The methodology is based on normalized form of equations providing 'master sintering curve'-type solutions which are capable of describing the generic shrinkage and distortion kinetics for various material systems. Such an approach renders the possibility of the direct assessment of the co-firing process outcomes and of the impact of process controlling parameters. The application of the derived 'master sintering curve'-type

solutions to model the kinetics of shrinkage and distortion in an experiment involving sintering a bi-layer made from tapes of porous and dense cerium gadolinium oxide is also presented.

In addition to planar multi-layer systems, this work presents a new analytical model to describe stresses and densifications during constrained sintering of tubular multi-layers. Verification and validation of the analytical model is also made using the finite element model and sintering experiment of tubular bi-layer samples.

Finally, this study suggests an entirely different approach to extract the important input parameters for modeling stresses and camber development during sintering of multi-layer systems. The approach is based on multi-scale modeling techniques, where the continuum theory of sintering is combined with meso-scale model of solid state sintering based on kinetic Monte Carlo (kMC) methods. The kMC methods are shown to be robust in predicting the densification, grain growth as well as microstructural evolutions of a given powder compact during sintering.[21, 22] By using the shrinkage rate and the microstructure predicted by a kMC model, a new approach for modeling stresses/camber evolutions during sintering of multi-layers is presented.

Figure 5 shows a schematic diagram depicting the different stages in the development of a method for predicting stresses and/or shape distortions during sintering of multi-layers. There are four main stages starting with collection of input parameters to validation and study of the effect of extrinsic factors on shape evolutions. The four stages have been made in two separate categories as shown to the left and right of the schematic diagram. The approach in the left side of the diagram describes the procedure used to develop analytical and finite element models whereas, that on the right side of the diagram shows the use of multi-scale modeling approaches.

As to the computational tools used in this study, all the analytical and multi-scale models are developed and implemented using Matlab scripts. The numerical models are developed using commercial finite element software, COMSOL and ABAQUS^{TM}, with the help of external user subroutines programmed using FORTRAN.

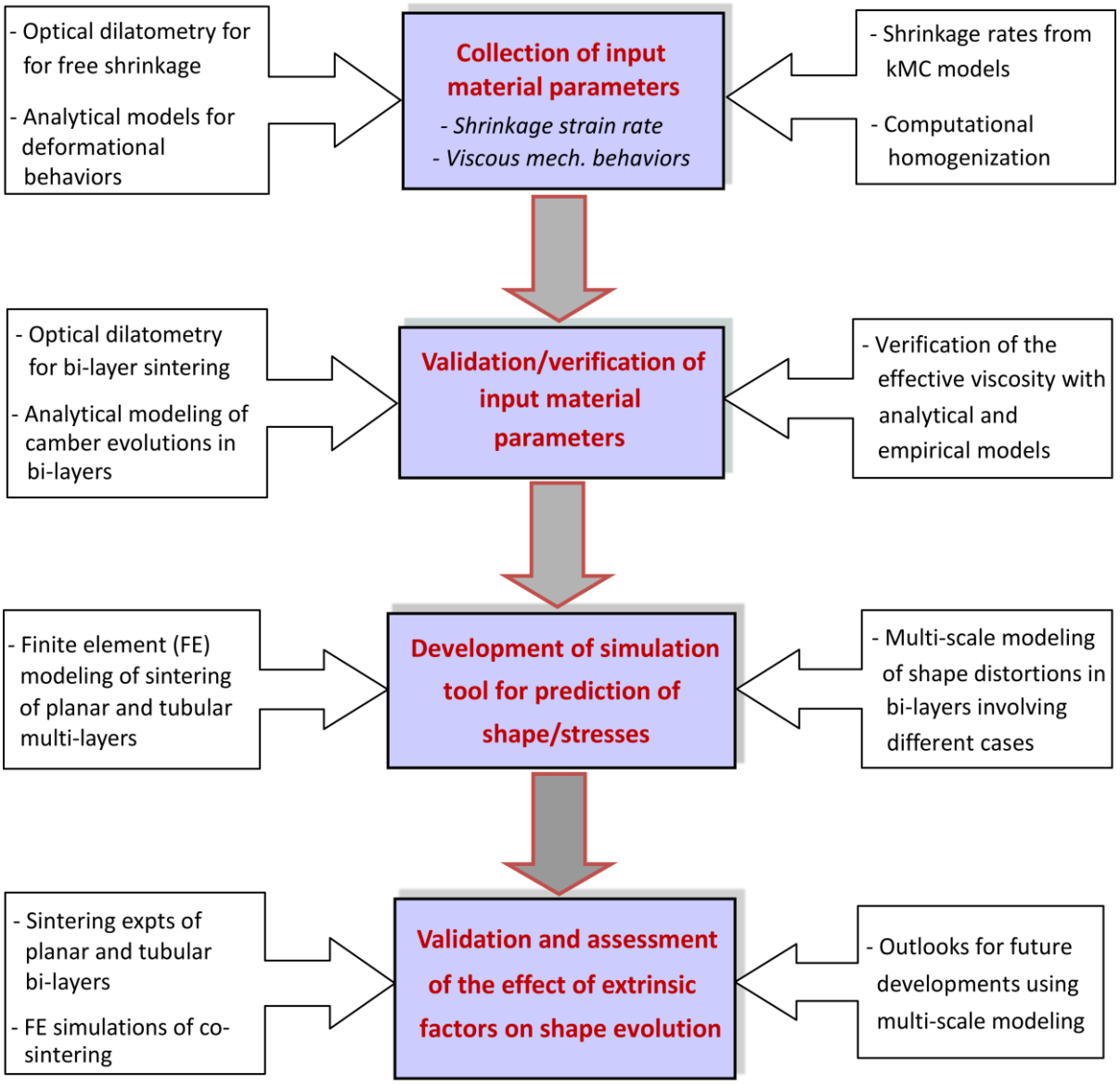

Figure 5: Schematic diagram showing summary of the different stages in the development of simulation method for shape instabilities during sintering of multi-layers.

1.6. Organization of the thesis

The thesis report is organized in the form of reviews focusing on previous studies of constitutive models for sintering bodies followed by highlighting the contributions made in the present study. Details of the procedures used while developing the models in the present study are found in the papers published through the course of this project. The papers appended to the thesis report,

which include the first six publications, are found in the Appendix. Therefore, the report is presented in the following sequence:

- The second chapter provides a review of various constitutive models for deformational behaviors (shrinkage kinetics and viscous mechanical properties) of porous bodies during sintering. In addition, review of the common experimental techniques for measuring the deformational behaviors of sintering bodies is presented. In this chapter, remarks on the various models are also included from the point of view of choosing the appropriate models for the development of a simulation tool for sintering of multi-layers.

- The third chapter presents the continuum description or theory of sintering together with various material models. A brief discussion of two models that can be implemented in the finite element code to model sintering of realistic bodies is also presented.

- In the fourth chapter, review of previous works on modeling densification and shape distortions during sintering of bi-layers is presented in comparison with what has been done in this study. Analytical as well as numerical models developed for co-firing of planar as well as tubular bi-layer structures are discussed in this section.

- The fifth chapter highlights the progress that has been made in using multi-scale modeling procedures for sintering in general and co-sintering in particular. In this chapter, an entirely new approach for modeling shape distortions during sintering of multi-layers by combining a meso-scale model based on kinetic Monte Carlo (kMC) method and the continuum theory is presented.

- Summaries of the papers published in the course of this study and appended to this thesis are presented in Chapter six.

- Finally Chapter seven provides a summary of the overall study together with outlooks for future studies.

2. Deformational Behaviors of Sintering Bodies

This section reviews the theoretical descriptions as well as experimental techniques used to measure the deformational behaviors of porous bodies during sintering (namely: shrinkage kinetics and viscous mechanical behavior). Theoretical approaches and models developed through time are discussed in brief. Finally remarks on the models from the point of view of modeling sintering of multi-layers are presented.

2.1. Kinetics of shrinkage

The free shrinkage kinetics is one of the important characteristics of a powder compact while studying sintering of multi-layers. This is because the development of stress during sintering of multi-layers is directly proportional to the difference in the shrinkage rates between the layers. The shrinkage kinetics of a free standing layer can be considered as the intrinsic material behavior during sintering. Generally the shrinkage kinetics in a porous body depends on:

1. Temperature
2. Material and microstructural features
3. External load

As described earlier, deformation in a sintering body occurs either by diffusion of matter as in the case of polycrystalline materials or through viscous flow as in the case of amorphous materials. Both types of matter transport are thermally activated. Furthermore, matter transport during sintering is a time dependent phenomenon and hence shrinkage kinetics is dependent on the temperature-time profile during the sintering process.

Free shrinkage, as an inherent characteristic of materials for reduction in free energy (from the surface of pores and grain boundaries), depends on the surface energy per unit area of the specific material. In addition, it depends on a number of internal parameters of the sintering body such as shape and amount of porosity, particle size distribution, etc. Other internal parameters like dihedral

angle and the pore-grain orientation, in the case of polycrystalline materials, also affects the shrinkage behavior of a porous structure.

Application of load on the sintering body affects the pore-grain structure of the powder compact, which in turn hinders or speeds up the shrinkage rate. This is because of the additional viscous or creep strain rate due to the load. The shrinkage kinetics with the application of external load is often called sinter forging, where the total shrinkage rate is the sum of the inherent free shrinkage and creep rate due to the load. Section 2.2 presents a review to the viscous deformation (viscous mechanical behaviors) of porous bodies during sintering. Directional application of loads produces anisotropic densification in the sintering body, which may affect final shape of the sample.

2.1.1. Constitutive models

Several models have been suggested by different people to describe the free shrinkage kinetics during sintering of a porous body. In the early 1950s, Herring described the shrinkage rate in terms of change in length scale, e.g. particle size, in a given powder compact.[23] This model had enhanced the early understanding of the effect of particle size on the sintering rates. However, it requires comparison of systems with geometrically similar microstructural changes, which are often difficult to obtain in real powder systems.

Later on, with the help of simplified or ideal geometries to represent the different stages during sintering of a powder compact, various analytical models have been developed.[24–27] These analytical models commonly assume spherical particles in the initial powder compact having the same size, as suggested by Coble.[26] The analysis is usually made on an isolated unit of powder system using appropriate boundary conditions and the rest of the powder compact is considered as a continuum structure consisting of the same microscopic properties. Most of the analytical models are developed to describe the shrinkage kinetics in the three stages of sintering commonly known as initial, intermediate and final stages.[18] Table 1 show summary of the different analytical models for the free shrinkage kinetics of powder compacts during the three stages of sintering.

Table 1: Summary of analytical models defining densification kinetics

Sintering stage	Densification kinetics	Constants				Ref
		Mechanism	H	m	n	
Initial $[\rho < 0.65]$	$\frac{\dot{\rho}}{\rho} = -3\left(\frac{H}{2^m G^n}\right)^{2/m} \frac{t^{2/m}}{dt}$	Surface diffusion	$\frac{56 D_s \delta_s \gamma_{sv} \Omega}{kT}$	7	4	[25]
		Lattice diffusion	$\frac{20 D_l \gamma_{sv} \Omega}{kT}$	4	3	[26]
		Grain Boundary diffusion	$\frac{96 D_{gb} \delta_{gb} \gamma_{sv} \Omega}{kt}$	6	4	[26]
		Viscous flow	$\frac{3\gamma_{sv}}{2\eta}$	2	1	[28]
Intermediate ρ: $[0.65 - 0.90]$	$\frac{\dot{\rho}}{\rho} = \frac{10 D_l \gamma_{sv} \Omega}{\rho G^3 kT}$	Lattice diffusion	-	-	-	[27]
	$\frac{\dot{\rho}}{\rho} = \frac{4}{3}\left[\frac{D_{gb} \delta_{gb} \gamma_{sv} \Omega}{\rho (1-\rho)^{1/2} G^4 kT}\right]$	Grain Boundary diffusion	-	-	-	[27]
	$\frac{\dot{\rho}}{\rho} = -\frac{9\gamma_{sv}}{8 G \eta_0}\left(\frac{1-\rho}{\rho}\right)$	Viscous flow	-	-	-	[29]
Final $[\rho > 0.90]$	$\frac{\dot{\rho}}{\rho} = \frac{112\pi D_l \gamma_{sv} \Omega}{kT}$	Lattice diffusion	-	-	-	[27]
	$\frac{\dot{\rho}}{\rho} = \frac{4\pi D_{gb} C_0 \gamma_{sv} \Omega^2}{kTr}$	Grain Boundary diffusion	-	-	-	[27]

Nomenclatures of variables

ρ = relative density and $\dot{\rho} = d\rho/dt$; D_x = diffusion coefficients of the respective mechanisms (x = *l, s, gb* for lattice, surface and grain boundary respectively); δ_s and δ_{gb} = thickness of surface and grain boundary diffusion; γ_{sv} = specific surface energy; Ω = atomic volume; k = Boltzmann constant; G = Grain size; η = the effective shear viscosity; η_0 = viscosity of the dense body; C_0 = initial vacancy concentration; r = cylindrical pore radius; T = temperature and t = time.

One of the major limitations of analytical models is the microstructural simplifications made in the models, which makes the models inadequate quantitative representations for the sintering behavior of a powder compact. Furthermore, most of the analytical models do not allow consideration of the entire sintering process from the beginning to the end. In an effort to develop a unified model for the entire sintering cycle, Hansen et *al*.[30] suggested a combined stage model using Herring's concept of length scales, see Eq (7) with the same meanings of symbols as in Table 1. Here, Γ, represents a dimensionless parameter relating microstructural parameter, e.g. G, with various geometrical features in the microstructure that can be defined in length scale. In spite of

their limitations, analytical models can provide good qualitative insights for understanding of the different sintering mechanisms and dependence of shrinkage on key process parameters.

$$\frac{\dot{\rho}}{\rho} = \frac{\gamma_{sv}\Omega}{kT}\left[\frac{\delta_{gb}D_{gb}\Gamma_{gb}}{G^4} + \frac{D_l\Gamma_l}{G^3}\right] \tag{7}$$

Numerical simulations can provide better platforms to analyze sintering of powder compacts compared to the analytical models. In such cases, equations of matter transport are solved numerically. This allows for handling complex geometries. Depending on the level of interest, numerical models can be developed for studying sintering at atomic, particle as well as continuum levels as summarized by Pan.[31] Examples could be of molecular dynamics simulations[32] and finite element analysis at particle and continuum levels.[33–35] In the numerical simulation of shrinkage kinetics, constitutive equations are used to relate the deformation rate with the stresses applied on the porous body. Reviews of such constitutive equations are given by Cocks[36] and Olevsky.[29]

Recently numerical techniques based on the kinetic Monte Carlo (kMC)[21] and discrete element methods (DEM) [37] are gaining momentum as a tool to describe the microstructural evolutions and densification of powder compacts during sintering. The model based on kMC method is able to simulate the underlying physics of many materials based on the statistical-mechanical nature of the model.[21, 22, 38, 39] They are shown to be robust in capturing the important features in the sintering process such as curvature driven grain growth, pore migration, vacancy formation and annihilations.[22] In addition to describing the microstructural evolutions of powder compacts, kMC based numerical techniques are also capable of predicting the densification kinetics in terms of shrinkage strains.[40] The limitations of such models are that, they work based on some idealized parameters, which makes it difficult to study changes in process parameters like temperature. Furthermore, they also lack application in the early stages of sintering. In this regard, DEMs are based on physical parameters and they can also describe the early stage sintering (which is dominated by grain boundary and surface diffusion) better.[37, 41, 42] However, DEMs lack accuracy while describing the shrinkage kinetics in the later stage of the sintering cycle.

The other approach uses phenomenological models, where empirical equations are developed fitting sintering data usually in the form of density versus time. This kind of approach could be useful in numerical models though they do not provide explicit understanding to the sintering process. Coble explained the theoretical descriptions to his semi-logarithmic equations, which was used to fit relative density data as a function of sintering time.[27] The limitation of such approach are

that more than one equation can provide a good fit to any of the sintering data and predicting shrinkage for new materials and/or new processing technique require new experiments.

A practical approach involving construction of so-called sintering maps has also been developed by Ashby and Swinkels.[43, 44] The initial maps were constructed to show the dominant sintering mechanism and the rate of neck growth for the given temperature and particle size.[43] Alternatively, Su and Johnson used the combined stage sintering model to map the densification with respect to a master variable (i.e. defined using the thermal history of the sintering body).[45] This technique is usually referred to as the master sintering curve (MSC). In the construction of such curves, the parameters in the combined rate equations are separated, with those related to the microstructure and temperature terms, which are then related to each other using experimental data of densification. The basic assumption in the MSC is that the geometric parameters of the microstructure are independent of the thermal history of the sintering. Once the MSC is constructed for a particular powder system, it can be used to predict the sintering behavior of compacts with a different sintering profile. Generalized formulations for MSC are also proposed based on several constitutive equations including both densification and grain growth.[46] The major drawback of the MSC approach is, its application requires powder systems processed in the same manner having the same green density. In addition, the microstructural evolution is assumed to be a function of density only with constant activation energy throughout the densification.

The other mapping technique based on information contained in the macroscopic data similar to the MSC is the Kinetic field (KF) theory suggested by Palmour [47] and used extensively by Raether et *al*.[48, 49] The shrinkage rate is predicted by time iterations within the field limits knowing temperature and temperature change (set by the user) and a starting density. The KF diagrams can be used to identify specific mechanisms during the densification process without the use of adjustable parameters. In addition, rotation of the so-called iso-strain lines in the KF diagram provides information about coarsening and the associated activation energies. A 3D extension of the KF diagram was also suggested with the integration of external stresses, which has been named the master sintering diagram (MSD).[50]

2.1.2. Remarks on models for shrinkage kinetics

Usually free shrinkage kinetics of layers making the multi-layer are measured by dilatometer and are used in continuum models together with the creep properties to describe stresses and camber developments during co-firing. However, it is sometimes necessary to use models to describe the

free shrinkage kinetics while working with the continuum models. The appropriate model to describe the shrinkage kinetics while analyzing problems of sintering of multi-layers depends on different factors. Examples of such factors include the input data available (e.g. diffusion coefficients) and/or information desired from the analysis. For instance, for analysis focusing on the mechanism of defect formations during sintering of multi-layers, numerical models that can describe the microstructural evolutions would be ideal. Numerical models are also highly effective in multi-scale modeling approaches.

Among the other approaches, for example, the use of MSC is confined to powder compacts made from the same powder and by the same green body processing. In addition, it would not be direct forward to model stresses as it is difficult to include the effect of stress into the MSC. Some of the limitations of the MSC can be circumvented by the use of the kinetic field (KF) or the master sintering diagram (MSD) as described by Raether et *al*.[48] However, building the KF or the three dimensional MSD incorporating stress fields requires detailed experimental works. Most of the time, analytical models are developed for a specific mechanism of matter transport and are applicable in a specific stage of sintering. However, analytical or empirical equations are still suitable models to use during the analysis of stress and macroscopic shape distortions of multi-layers. Among these, the viscous sintering description of shrinkage kinetics is not only simple for implementation (requiring less number of adjustable parameters) but also it is used extensively in the literature. Though originally developed for materials that sinter by viscous flow, these models can also describe sintering of crystalline bodies with good approximation. Section 3 and 4 presents further discussions on the use of viscous models for problems of multi-layer sintering including review of previous studies.

2.1.3. Measurement techniques

Accurate measurement of shrinkage kinetics during the sintering cycle is critical to determine adjustable parameters in the proposed models and to validate them. In this section, an overview is presented to the most common techniques used while studying stress and shape distortion during sintering of multi-layer systems. In addition to measuring the material behaviors, an overview of techniques for characterization of sintering of multi-layer systems are also presented.

I. Linear shrinkage

Push rod dilatometry is usually used for measuring the linear shrinkage of samples during sintering. In this technique, the shrinkage of the sample is transferred via a rigid rod, which is in contact with

the sample surface, to a displacement transducer outside the furnace.[51] To achieve accurate measurement during the entire sintering process using classical contact dilatometers, the interaction between the measuring system and the sample has to be minimized. In push rod dilatometry, movement of the sample can be caused by a reaction between the push rod and sample material. Also, the pressure on the sample during push rod dilatometry may cause a deformation of the sample by high temperature creep. Therefore, non-contact methods for the determination of sintering shrinkage are preferred.

While studying the effect of mismatch in sintering kinetics of layers on bi-layer camber evolutions, Lu et al showed the use of non-contact optical scanning techniques for in-situ linear shrinkage measurement of sintering samples.[5] This technique exploits the contrast between the reflective surface of the setter and the rough surface of the sample to measure the dimensional changes. Other non-contact dimensional measurements at high temperatures include, for example laser dilatometry that use interferometric methods, which can resolve length changes in nano meter range.[52]

A non-contact optical method that relies on a simple and robust CCD (Charged Coupled Devices) camera applicable up to 2000 ^{o}C was first suggested by Raether et *al*.[53] Such system exploits the image contrast created due to illumination of light in the furnace chamber. It is often called TOM (thermo-mechanical measuring device) and can be used for heating rates up to 10 K/min with a resolution of less than 1 µm.[53] Figure 6 shows the schematics of such system, which can provide continuous measurement of the linear shrinkage or densification rate. Since the introduction of this technique, there have been a number of works reported by using TOM for measuring the shrinkage behavior of different materials.[54–56]

Measurement of shrinkage kinetics during co-firing is often challenging. Garino and Bowen showed the use of laser reflectance apparatus to measure the shrinkage across the thickness of constrained films on rigid substrate.[57] Direct observation of the fractured surfaces of samples using images from SEM (Scanning Electron Microscope) before and after sintering can be used to analyze the linear shrinkage. In such cases the sintering operation should be interrupted at different temperatures where the dimensional measurement is required to be taken. The procedure is experimentally cumbersome and it does not allow continuous measurement of shrinkages. But it is sometimes used to analyze linear shrinkage of the constituent layers in multi-layered samples.[4]

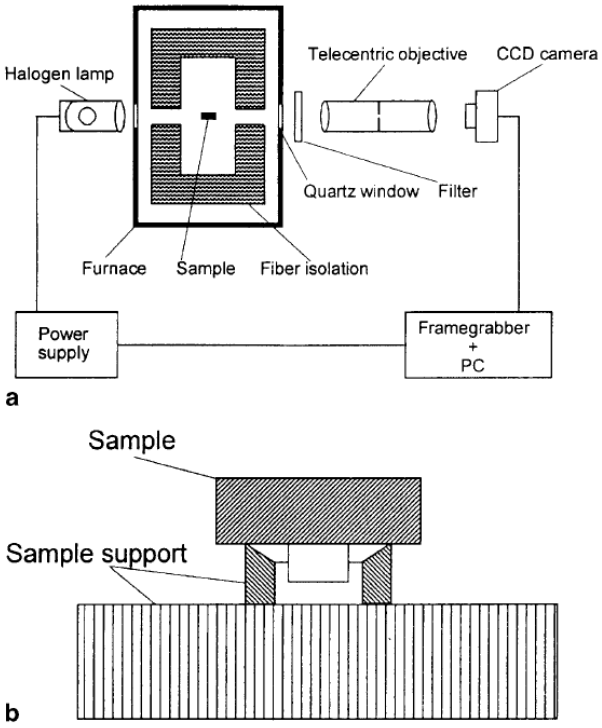

Figure 6: (a) Set-up of the optical dilatometer and (b) cross section through sample and sample support [Raether et *al*.[53]]

II. Porosity and microstructural characterizations

In-situ measurements of linear shrinkage during sintering can be used to estimate the density of the porous body as a function of time if the shrinkage is assumed to be isotropic and there is no significant mass change, see Eq (5). The corresponding fraction of voids or relative porosity can be determined as: $\theta = 1 - \rho$. Other techniques that can be used to measure density of a sintering body having interconnected pores include the Archimedes method [58] and mercury porosimetry.[59]

Characterization of microstructure during co-firing is important to study grain growth, pore size distributions, possible anisotropies in the pore-grain structure etc. In the case of constrained sintering, investigations of anisotropies induced into the pore-grain structure due to the stress from the constraint are important to refine the available models based on parameters such as pore shape and orientation factors. In this regard, 2D sections of the sintering body are often used to analyze the different internal features of the microstructure using SEM.[55, 60, 61] Recently 3D in-situ characterization tool such as X-ray computed micro-tomography (XCMT) has been used successfully to monitor the microstructural evolutions during sintering of multi-layers.[62] This technique uses X-ray radiographies of a rotating specimen from which a 3D representation of the local details is

computed using special computer software.[63] Other advanced techniques such as focused ion beam (FIB) tomography could also be used for detailed and in-situ characterization of microstructure during sintering.[64]

2.2. Viscous mechanical behaviors

The viscous mechanical properties of a sintering body can be defined as the inherent resistance to creep or densification in response to external or internal stress. Depending on the stress state, they can be described either by shear and bulk viscosities or uni-axial viscosity and viscous Poisson's ratio. The three main factors affecting the effective viscosity of a sintering body are:

1. The temperature
2. The fraction of void (porosity) in the sintering body
3. The grain size

The effective viscosity is often a strong function of temperature in the early stage of sintering whereas the grain size becomes crucial in the final stages of sintering. In addition, microstructural features like the grain size distribution, powder packing, the amount, shape and orientations of porosities, etc during the sintering cycle can also affect the effective viscosity. Various models have been reported to theoretically describe the evolution of the effective viscosity of a porous body during sintering. Below is the summery of some of the models developed through time.

2.2.1. Constitutive models

In the early works by Bordia and Raj [65] and Hsueh et *al*.[66], the porous body during sintering had been characterized by viscoelastic materials. Hence, the mechanical properties of the sintering bodies were modeled using combinations of elastic springs and viscous dashpots. For example, Bodia and Raj proposed a model based on viscoelastic Kelvin-Voigt element to predict the densification response of a porous body. On the other hand, the shear relaxation of the porous body had been modeled by a viscoelastic Maxwell element, which consists of a series combination of elastic spring and viscous dashpot.[65] While it is reasonable to assume that the sintering compact is viscoelastic, the elastic strain is very small during sintering compared to the densification strains. Later on, hence, Bordia and Scherer argued that a simple linear viscous formulation is sufficient to

model the mechanical response of the porous compact.[67] Table 2 summarizes some of the models developed through time for the shear and bulk viscosity of the porous body during sintering.

Table 2: Summary of various models defining the viscous behavior of porous compacts during sintering

S.No	Models for viscous mechanical behavior		Ref
	Effective shear viscosity, G_p	Effective bulk viscosity, K_p	
1	Viscoelastic analogy Maxwell element for shear viscosity	Viscoelastic analogy Kelvin Voigt element for Bulk viscosity	65
2	$G_p = \eta_R \frac{\rho^p}{(1-\rho)^\lambda}$ Two adjustable parameters p and λ depending on the density and grain size	$K_p = \eta_R \frac{\rho\tau(1-\rho_0)^\gamma}{(1-\rho)^{1+\gamma}}$ τ = coupled measure of grain size and grain growth kinetics and a constant γ	68
3	$G_p = \frac{3\eta_o\rho}{6-4\rho+(3\rho-2\rho^2)^{1/2}}$	$K_p = \frac{2\eta_o\rho}{3-2\rho+(3\rho-2\rho^2)^{1/2}}$	69
4	$G_p = \eta_o\rho^a$ One adjustable parameter, *a*	$K_p = \frac{4\eta_o\rho^b}{3(1-\rho)}$ One adjustable parameter, *b*	70
5	$G_p = AC_{1(\rho)}T\exp(\frac{E_a}{RT})$ Adjustable function of density, C_1 and a constant, *A*.	$K_p = AC_{2(\rho)}T\exp(\frac{E_a}{RT})$ Adjustable function of density, C_2 and a constant, *A*.	71
6	$G_p = \frac{1}{A}\rho G^3\exp(-2a_o(1-\rho))$ Grain growth is considered with two adjustable parameters *A and* a_o	$K_p = \frac{1}{A}\rho G^3\exp(-a_o(1-\rho))$ Grain growth is considered with two adjustable parameters *A and* a_o	72
7	$G_p = \frac{1}{3B}\rho G^3$ Grain growth is considered with one adjustable parameter, *B*	$K_p = \frac{G^3}{B\rho}[\ln(1-\rho)+0.5\rho(\rho+2)]$ Grain growth is considered with one adjustable parameter, *B*	73
Nomenclature of variables η_R =reference viscosity at a given density; η_0 =viscosity of fully dense body; ρ = relative density; E_a =apparent activation energy; *R* = Universal gas constants and *T*=Temperature			

In most of the models suggested, the effect of the evolving density as well as grain size on the viscosity of the porous compact is often handled by adjustable parameters/functions. For example, the model by Hsueh et *al*. has two adjustable functions: ρ^p gives the dependence of G_p on density for constant grain size whereas $(1-\rho)^{-\lambda}$ accounts for the grain growth accompanied by densification.[68] Such functions, which account for the changing density or grain sizes during sintering, can be formulated empirically or by using micro-mechanical models. For example, Scherer

et *al*.[69] derived a function, which accounts for the evolving density based on microstructural models whereas Rahaman et *al*.[72] relied on an empirical model. Though it does not have explicit function to consider the instantaneous grain size during sintering, the model suggested by Skorohod has been used extensively for the continuum modeling.[70]

In addition to the amount of fraction of voids or porosity, the shape and orientations of porosities during the sintering cycle can also affect the effective viscosity of the sintering body. Boccacini tried to quantify and incorporate shape and orientation factors into his model for the effective viscosity, which is derived based on the analogy between flow and transport properties.[74]

$$\eta_p = \eta_0 \rho^n \quad \text{where } n = \frac{1-\cos^2\alpha}{1-F} + \frac{\cos^2\alpha}{2F} \tag{8}$$

The shape factor, *F*, is taken as a function of ratio of the two axis of spheroid, which is assumed to represent pore shapes with the orientation, α, being the angle between the flow direction and the rotational axis of the spheroids.

2.2.2. Remarks on viscosity models

Despite the number of studies, the existing models for the effective viscosity of a sintering body show certain drawbacks. Mohanram et *al*. reported comparison of the various models with experimental measurements depicting discrepancies between the models as well as between the models and measurements.[75] Developing a unified model, which can explicitly consider all the internal variables of the evolving microstructure of a porous body, is a daunting challenge. However, those models suggested by Scherer et *al*.[69], Skorohod[70] and Reiterer et *al*.[71] have been used frequently with the continuum models and also require less number of adjustable parameters. In this study, the model suggested by Reiterer et *al*., is used, where the viscosity of the fully dense body, η_0 , is given by:

$$\eta_0 = ATexp\left(\frac{Q_s}{RT}\right) \tag{9}$$

Here A and Q_s are the Arrhenius pre-exponential factor and the apparent activation energy for range of density in consideration respectively. The influence of porosity on the effective shear and bulk viscosity of the sintering body can be accounted by normalized shear, φ, and bulk, ψ , factors.

To improve the prediction of this model, the phenomenological grain growth could also be included with more experimental works as explained by Arguello et *al*.[76]

2.2.3. Measurement techniques

Accurate measurement of the mechanical response of the porous bodies during sintering is important as it is one of the parameter while studying sintering of multi-layers. There are different techniques employed by various authors to measure the effective viscosity of samples during sintering. Some of these include cyclic loading dilatometry, sinter forging, bending creep tests, vertical sintering, and constrained sintering.

Almost all the measurement techniques use a dilatometer allowing the application loading upon the specimen. Early studies of sintering including viscosity measurements were reported by Rahaman et *al*.[72, 77], Chu et *al*.[78] and Bordia et *al*.[65, 79]. In most of the techniques, the basic idea is to measure the viscous strain rate of the porous body at sintering temperatures by applying known values uni-axial loading or stress. For example, Rahaman et *al*. used loadings in the range of 8 - 80 kPa on porous samples of ZnO and CdO and compared the viscous strain rate with the free shrinkage rate.[77] Based on such comparisons, results for uni-axial viscosities as a function of relative density can be calculated. From their measurement, Rahaman et *al*. were also able to conclude and show that the creep strain rate varies linearly with the applied stress for the materials considered.[77, 80]

Perhaps the most comprehensive experimental work was reported by Cai et *al*. to determine the mechanical response of porous samples from room to sintering temperatures.[81] In this work, they used cyclic loading dilatometry in which an intermittent load on the sintering samples was applied using different heating and loading schedules. The technique is advantageous as one experiment is sufficient to determine the elastic as well as viscous properties of the sintering body at different temperatures. Interestingly, Cai et *al*. clearly showed the transition of porous Alumina from elastic at low temperatures to viscous behaviors at high temperatures. Such technique can be implemented using thermo mechanical analyzer (TMA) with a vertical loading rod. The range of the applied stress used by Cai et *al*. was 0.25 - 1 MPa wherein a creep rate under load is clearly shown to vary linearly with the applied stress. Such technique has also been used by other authors on different sets of materials.[55, 82]

The use of uni-axial load on the sintering specimen and measurement of the radial and axial strain rate components separately is called sinter-forging technique. By applying a uni-axial load, the

shrinkage rate difference along the loaded and unloaded directions together with the free shrinkage rate can be used to determine the viscous mechanical properties of the specimen.[83] In this technique, the main challenge is to have accurate and concurrent measurements of the radial and axial strain rates. Furthermore, the applied load could induce directional anisotropies in the microstructure of the sample. With the goal of improving measurement inaccuracies that may occur due to anisotropies in the pore-grain structure due to uni-axial loading, Zuo et *al*. suggested a technique called discontinuous hot forging.[84] This is an improved sinter forging technique, where the sample is first allowed to sinter freely to a prescribed density, and then the load is applied followed by instantaneous measurements of radial and axial shrinkage strains. The drawback in this approach may be, the instantaneous short measurements could only capture primary creep.

Lee et *al*. suggested another technique based on creep in a bending beam test to measure the uni-axial viscosity of a sintering body.[85] They used the closed form solution of an elastic beam deflection under gravity and/or under the influence of external loads based on the analogy between the linear elastic–linear viscous problems. Tapes (beams) of porous samples can be allowed to deform between two sample supports during sintering while changes in the deflection rate, thickness and length together with density are monitored. Such technique could put the tapes in a stress state somehow similar to tapes in multi-layer systems and hence causing a similar microstructural evolution during the sintering cycle.

Cologna et *al*. followed another approach by performing a vertical sintering of the porous samples under the influence of gravity.[86] The difference in shrinkage rate between a sample sintered hanging vertically and free shrinkage rate is used together with gravitational load on the vertically oriented sample to estimate the uni-axial viscosity. In this technique, it might be difficult to achieve the stress levels occurring, e.g. in bending bi-layers, as the gravity has less influence in tension than in the bending of the co-sintering multi-layers.

Mohanram at *al*. showed how the viscous Poisson's ratio of a porous body at sintering temperature can be determined using a simple technique of pressure-less constrained sintering.[87] By sintering the porous sample between two non-sintering bodies, one can achieve the entire densification to occur in only one direction. The difference between the shrinkage rates in unconstrained direction and free sintering body could be used to determine the viscous Poisson's ratio using the formulations in the continuum theory of sintering. The technique is simple and does not involve any external loading.

3. Continuum Description of Sintering

In this section, the continuum description of a sintering body is discussed together with material models that can be used to describe stresses and macroscopic shape distortions during co-firing. Furthermore, continuum mechanics based constitutive models that can be implemented as a subroutine to a finite element program to describe densification and deformations in realistic (macroscopic) sintering bodies are also discussed.

3.1. Introduction

The continuum theory of sintering assumes the sintering body as a two-phase material consisting of skeleton and voids (pores), where the voids are distributed isotropically throughout the structure.[29] Figure 7 shows the schematic representation of the continuum description of sintering body. According to mechanics of porous structures, porous bodies, unlike fully dense bodies, can cause the structure to yield even under hydrostatic stress.[88]

Hence the continuum theory assumes that sintering occurs due to the response of the structure to the inherent hydrostatic potential, which is often called sintering stress. Whenever there are additional applications of load on the porous structure, the response of the body to the applied load can be treated either by viscoelastic or viscous models. Thus the total deformation in the porous structure includes deformations from the internal sintering stress and that of from the applied loads.[29]

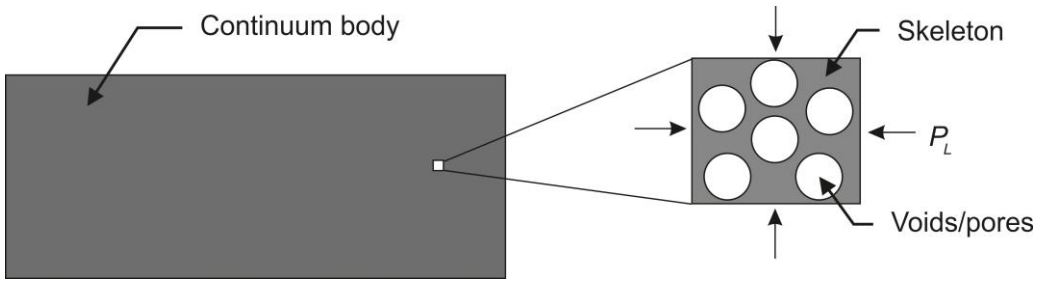

Figure 7: Schematic representation of the continuum sintering body

3.1.1. Viscoelastic models

According to Bordia and Raj, if the viscoelastic properties do not vary with time, the viscoelastic solution of sintering problems can be made using viscoelastic/elastic (VE) analogy.[65] This is based on the fact that the Laplace transform of viscoelastic constitutive equations is equivalent to the elastic constitutive equations. For instance, the constitutive equation for a porous material modeled by viscoelastic Maxwell element with an inherent shrinkage rate, $\dot{\varepsilon}^f$, can be expressed as:

$$\dot{\varepsilon}_{ij} = \dot{\varepsilon}_{ij}^{el} + \dot{\varepsilon}_{ij}^{cr} + \dot{\varepsilon}^f \delta_{ij}$$
$$\dot{\varepsilon}_{ij} = \frac{1}{E}[(1+\nu)\dot{\sigma}_{ij} - \nu\dot{\sigma}_{kk}\delta_{ij}] + \frac{1}{\eta}[(1+\nu_p)\sigma_{ij} - \nu_p\sigma_{kk}\delta_{ij}] + \dot{\varepsilon}^f\delta_{ij} \quad (10)$$

where the total strain rate, $\dot{\varepsilon}_{ij}$, is the sum of the elastic, $\dot{\varepsilon}_{ij}^{el}$, creep, $\dot{\varepsilon}_{ij}^{cr}$ and the free shrinkage strain rates. δ_{ij} is the Kroneckers symbol ($\delta_{ij}=1$ if $i=j$ and $\delta_{ij}=0$ if $i\neq j$). Note that, $\dot{\sigma}_{ij}$, is the rate of change of stress, σ_{ij}; E is Young's modulus; η is uniaxial viscosity; ν and ν_p are the elastic and viscous Poison's ratios respectively and $i, j = x, y, z$ with Einstein's summation convention.

Later on, Bordia and Scherer[67] invalidated the previous model of porous bodies based on viscoelastic analogy because of:

1. The elasticity as well as viscosity of a sintering body is a function time which does not allow the use of linear viscoelastic analogy and
2. The observed strains during densification are so much larger compared to elastic strains resulting the entire deformation from viscous flow or creep.

Instead, they formulated a less cumbersome model based on linear viscous formulations to describe the stresses during sintering by viscous flow.[67]

3.1.2. Linear viscous models

During sintering of a porous body, where there is a deformation dominated by viscous flow/creep, the total strain rate can simply be given by the sum of the free shrinkage rate and the creep rate:

$$\dot{\varepsilon}_{ij} = \dot{\varepsilon}_{ij}^{cr} + \dot{\varepsilon}^f\delta_{ij} \quad (11)$$

The linear viscous material is analogous to elastic material where the elastic parameters such as strain, ε_{ij}, Young's modulus, E , and Poisson's ratio, ν ,are replaced by the corresponding creep

strain rate, $\dot{\varepsilon}_{ij}^{cr}$, uni-axial viscosity, η, and viscous Poisson's ratio, ν_p. For example, the viscous or creep strain rate can be given by Eq (12). There also exists a direct correspondence between linear elastic and linear viscous models enabling the use of analogies of elastic solutions (by replacing viscous mechanical properties) for linear viscous materials during sintering. Detailed discussions of the correspondence principle for functionally graded materials can be found in Refs [89, 90].

$$\dot{\varepsilon}_{ij}^{cr} = \frac{1}{\eta}[(1+\nu_p)\sigma_{ij} - \nu_p \sigma_{kk}\delta_{ij}] \tag{12}$$

3.2. Phenomenological models of sintering

For simulation of sintering in a realistic 3D body, a continuum mechanics based constitutive sintering models are important. In this context, the Skorohod-Olevsky Viscous Sintering (SOVS)[29] and the Riedel-Svoboda solid state sintering (RS)[91] models find use in analytical as well as finite element simulation of sintering for realistic components.

3.2.1. The Skorohod-Olevsky Viscous Sintering model (SOVS)

A general description of viscous sintering based on the continuum framework is presented by the Skorohod viscous sintering model commonly known as SOVS.[29] According to SOVS, the constitutive equation for linear as well as non linear viscous materials with a total strain rate tensor, $\dot{\varepsilon}_{ij}$, is given by:

$$\sigma_{ij} = \frac{\sigma(W)}{W}\left[\varphi\dot{\varepsilon}_{ij} + \left(\psi - \frac{1}{3}\varphi\right)\dot{e}\delta_{ij}\right] + P_L\delta_{ij} \tag{13}$$

where W is the equivalent strain rate and $\sigma(W)$ is the equivalent stress; φ and ψ are the normalized shear and bulk viscosities; $\dot{e}$ is the volumetric strain rate of the porous body or the first invariant of the strain rate tensor and P_L is the inherent sintering stress of the material. In the SOVS framework, porosity, θ, is defined as the volume fraction of voids in the porous body. The equivalent strain rate, W, is a function of the invariants of the strain rate tensor as:

$$W = \frac{1}{\sqrt{1-\theta}}\sqrt{\varphi\dot{\gamma}^2 + \psi\dot{e}^2} \tag{14}$$

where $\dot{\gamma}$ is the second invariant of the strain rate tensor, which represents the rate of change of shape in the porous body and is given by:

$$\dot{\gamma} = \left[\left(\dot{\varepsilon}_{ij} - \frac{1}{3}\dot{e}\delta_{ij} \right) \left(\dot{\varepsilon}_{ij} - \frac{1}{3}\dot{e}\delta_{ij} \right) \right]^{1/2} \tag{15}$$

Note that $\sigma(W)$ determines the constitutive behavior of the porous material and if it is given by a linear relationship, for example, $\sigma(W) = 2\eta_0 W$, Eq (16) expresses the linear constitutive model as:

$$\sigma_{ij} = 2\eta_0 \left[\varphi \dot{\varepsilon}_{ij} + \left(\psi - \frac{1}{3}\varphi \right) \dot{e}\delta_{ij} \right] + P_L \delta_{ij} \tag{16}$$

The sintering stress, P_L, is the intrinsic material property which develops due to the tendency of the porous body for minimization of surface energy. According to SOVS, the effective sintering stress is given by a product of local sintering stress, $P_{L0} = -3\alpha/G$, and the normalized sintering stress, $\overline{P}_L$.

$$P_L = P_{L0}\overline{P}_L = \frac{3\alpha}{G}\overline{P}_L \tag{17}$$

The parameters, $\overline{P}_L, \varphi$ and ψ are functions of porosity and they have to be determined based on the pore-grain structure evolving during the densification process.[29] Summary of various functions proposed by different authors for P_L, φ and ψ is found in Ref [29]. Eq (16) can be reformulated in a way showing the components of viscous/creep strain rate, $\dot{\varepsilon}_{ij}^{cr}$, and free strain rate, $\dot{\varepsilon}^f$, by the first and second terms in Eq (18) respectively. Here, σ'_{ij} *and* σ_m, are the deviatoric and mean stress components in the porous body respectively.

$$\dot{\varepsilon}_{ij} = \left[\frac{\sigma'_{ij}}{2\eta_0\varphi} + \frac{\sigma_m}{6\eta_0\psi} \right] - \left[\frac{P_L}{6\eta_0\psi} \right] \delta_{ij} \tag{18}$$

Hence, for pressure-less sintering (free sintering), the shrinkage rate can be found from Eq (18) as:

$$\dot{\varepsilon}^f = -\frac{P_L}{6\eta_0\psi} \tag{19}$$

Often the SOVS model is implemented together with a continuity equation derived from the principle of conservation of mass. It relates the volumetric shrinkage rate, $\dot{e} = \varepsilon^f \delta_{kk}$, with the evolution of porosity, θ, in the porous body as:

$$\dot{e} = \frac{\dot{\theta}}{1-\theta} \tag{20}$$

3.2.2. The Riedel-Svoboda solid state sintering model (RS)

A description of solid state sintering based on microstructure of a sintering body that can be used in macro-scale modeling of sintering is developed by Reidel and Svoboda.[91–93] The RS model considers the diffusive transport of matter and grain coarsening. It also distinguishes between open and closed porosity. The constitutive equation relating the total macroscopic strain rate, $\dot{\varepsilon}_{ij}$, to the stress tensors can be expressed as:

$$\dot{\varepsilon}_{ij} = \frac{\sigma'_{ij}}{2G} + \frac{\sigma_m - P_L + \Delta P}{6K}\delta_{ij} \tag{21}$$

where G and K are the shear and bulk viscosities and ΔP is a gas pressure that can develop in closed pores. The shear and bulk viscosities, G and K, contain a term for source controlled diffusion, which modifies the linear viscosities, G_{lin} and K_{lin}, as [94]:

$$K = K_{lin}\left(1 + \frac{\alpha_{RS}}{\bar{\sigma}R^2}\right); \quad G = G_{lin}\left(1 + \frac{\alpha_{RS}}{\bar{\sigma}R^2}\right) \tag{22}$$

where α_{RS} is an adjustable parameter, R is the mean grain radius, and $\bar{\sigma}$ is the effective stress, which can be calculated considering the von Mises stress, σ_e, as: $\bar{\sigma} = \frac{1}{2}\left|\sigma_m - P_L + \Delta P\right| + \frac{1}{2}\sigma_e$ [94]. Details on the contributions of the different diffusion mechanisms to viscosity and the microstructural assumptions in the RS model can be found in Refs[91, 94].

Compared to the SOVS model, the RS model is very sophisticated and requires large number of parameters and adjustable functions, which makes it flexible for describing solid state sintering. However, the SOVS model, being a lean continuum mechanical approach, can predict almost with the same level of accuracy as the RS model. This has been demonstrated by Reiterer and Ewsuk[95] after comparing both models with each other and with data from experimental measurements. The SOVS model, though developed to describe viscous sintering, is also shown describing sintering of polycrystalline Alumina powder compact.[95] In the present study, the SOVS model has been chosen to develop analytical as well as finite element models.

4. Shape Distortions and Stresses during Co-firing

This section reviews previous studies on modeling shape distortions during sintering of multi-layers together with the contributions made in the present study. Summary of the improvements made through time in the analytical as well as numerical models to describe sintering of multi-layers is also presented.

4.1. Analytical modeling

Modeling stresses and shape distortions during sintering of multi-layers is based on the fact that the structure remains under mechanical equilibrium if there are no applications of external forces. This requires the integrals of forces, N, and bending moments, M, across the thickness axis, z, of the multi-layer to be zero, see Eq (23). Figure 8 shows schematics of a bi-layer structure with distortion, u, measured from the horizontal axis. The deformations in each layer can be formulated by viscoelastic, see Eq (10) or simply by viscous material models as shown in Eq (11).

$$N = \int \sigma_x(z)dz = 0 \text{ and}$$
$$M = \int \sigma_x(z)zdz = 0 \tag{23}$$

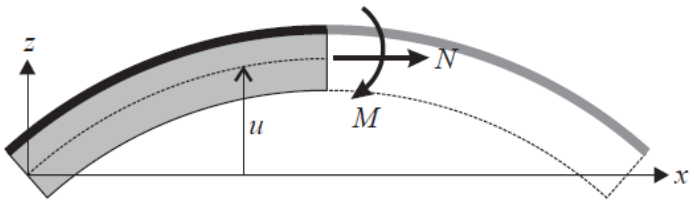

Figure 8: Schematic representation of a bi-layered structure with distortion, u, measured from the horizontal axis [PAPER-VII]

During eighties, problems of multi-layer sintering were analyzed by formulating the response of the sintering body for applied loads (viscous deformations) by viscoelastic models.[60, 65] While using viscoelastic models, solving for the time dependent stress, for example, in the case of sintering of porous bi-layered structures is challenging. This is because of the variation of the viscoelastic

parameters, E and η, with time, which contradicts the basic assumption in the viscoelastic/elastic analogy. In such cases, an approximation has to be made in order to find the stress solution. Bordia and Raj discussed a procedure to find the time dependent stress solution and expressed the viscoelastic stress in terms of short and long term solutions.[60, 65] The other approach is the use of a reduced time such that the stress relaxation function is normalized and has the same form at any temperature as explained by Cai et *al*.[96]

By using viscoelastic material, for example, the solution for the time dependent stress during sintering of planar bi-layer with layers 1 and 2 can be derived using simplified force balance and geometric constraints considering the in-plane stresses and strain rates as shown by Eq (24). Here *h* represents the respective thickness of the layers. The analysis based on viscoelastic models requires not only knowledge of linear shrinkage and viscosity but also requires knowledge of parameters such as the instantaneous shear and bulk moduli as they are dependent on temperature and time.

$$\begin{aligned} \sigma_1 h_1 + \sigma_2 h_2 &= 0 \\ \dot{\varepsilon}_1 &= \dot{\varepsilon}_2 \end{aligned} \tag{24}$$

After measuring the elastic and viscous properties of the constituent layers, by cyclic loading dilatometry, Cai et *al*. reported an extensive analysis of the stress and shrinkage kinetics during sintering of Alumina/Zirconia laminates.[96] However, their analysis is based on the assumption of similar densification in each layer during free sintering and co-firing, which may be true if the compatibility stress during co-firing is not large enough to change the microstructural evolution. Furthermore, thickness evolutions of the layers are not updated during the simulation of co-firing.

An early work using the linear viscous material model to analyze stresses during sintering of porous glass (silicate gel) on a rigid substrate is reported by Scherer and Garino.[97] By using a unit cell representation of the microstructure, they were able to derive the shrinkage kinetics, which is then used to estimate the stresses in the constrained sintering. One of the major observations in this study was the small effect of pore orientation on the densification kinetics during constrained sintering. Scherer and Garino were able to show this using tubular unit cells, which could develop extreme anisotropy in constrained sintering.[97]

Later on Garino and Bowen[57] applied the linear viscous formulation for constrained sintering to validate the shrinkage kinetics model developed by Scherer and Garino[97]. Their methodology includes predicting shrinkage kinetics in constrained sintering after extracting model parameters by

fitting their free shrinkage expression and the respective experimental data. Parameters extracted from viscous sintering experiments fit predictions made by their model well. However, parameters from densifications by solid state sintering deviate from the predicted behavior. This would show that their expression for free shrinkage by solid state diffusion was not as good as the one for viscous sintering. Since the early nineties, the use of linear viscous formulations for analysis of stress and densification during sintering of multi-layers has been verified and validated by a number of authors.[5, 7, 55, 81, 98–101]

Analytical models for sintering of multi-layers are often developed assuming uniform distribution of strain rates across the thickness of each layer.[5, 7, 100–102] This assumption makes the implementation of the linear viscous model simple as no spatial discretization across the thickness is needed to compute stresses and camber evolutions. However, the rigorous linear distribution of strains across the thickness can also be used as suggested by Kanters et *al*.[6], see Eq (25). In such case, the viscous analogy of classical laminate theory can be used to determine the strain rate at the neutral axis, $\dot{\varepsilon}_0$, and curvature rate, $\dot{k}$, based on force and moment equilibrium. Here, $\dot{\varepsilon}^{cr}(z)$, represents the distributions of viscous strain rates across the thickness, *z*, of each layer.

$$\dot{\varepsilon}^{cr}(z) = \dot{\varepsilon}_0 - z\dot{k} \tag{25}$$

Using the linear strain rate distributions, Kanters et *al*. analyzed densification and warpage during co-firing of bi-layers produced from nanocrystalline Zirconia.[6] Furthermore, they tried to refine their model incorporating coarsening and microstructural evolutions together with anisotropies in shrinkage kinetics. During the co-firing, the compatibility stresses in the bi-layer are found to scale inversely with the grain size. They were also successful in predicting the camber evolutions of bi-layers with different thickness ratios and heating schedules.[6]

In most of the studies, separate experiments for the shrinkage and effective viscosity of the porous layers in the bi-layer are conducted to be able to use the continuum model for prediction of camber evolutions during co-firing. Alternatively, parameters defining the viscosity of the fully dense body, for e.g. A and Q_s see Eq (9), can be determined by fitting the model for free shrinkage rate given in Eq (19) with measurements from optical dilatometry. In this study, the later procedure is used to determine the viscosity of fully dense layers making the bi-layer.[103] The effective viscosity of each layer during co-firing is then estimated from the viscosity of fully dense body and a function

considering the effect of microstructural changes during co-firing. For details of the methodology and microstructural assumptions, please refer to Appendix A (PAPER-I).

Validation of the effective viscosity of each layer is then made by comparing model predictions for camber evolution during sintering of a bi-layer based on the individual layers and experimental measurements. The advantage of this procedure is 1) a single dilatometry run can be conducted to measure the free shrinkage of each layer as well as camber evolution in the bi-layer and 2) the effective viscosity of each layer in the bi-layer can be updated based on the stress state and microstructural evolution in the bi-layer or during co-firing.

As described in PAPER-I, the analytical model to predict camber evolutions during sintering of the bi-layer is developed by using the continuum theory (SOVS) taking gravity into considerations.[103] Figure 9 shows comparison of camber prediction from the analytical model and measurements after implementing the procedures explained above. The observed agreement between the model and measurements can be considered as a validation for the estimated effective viscosity of each layer. Furthermore, the model is shown to capture the significant effect of gravity on the camber evolution in the later stage of the sintering unlike the model by Cai et *al*.[81]

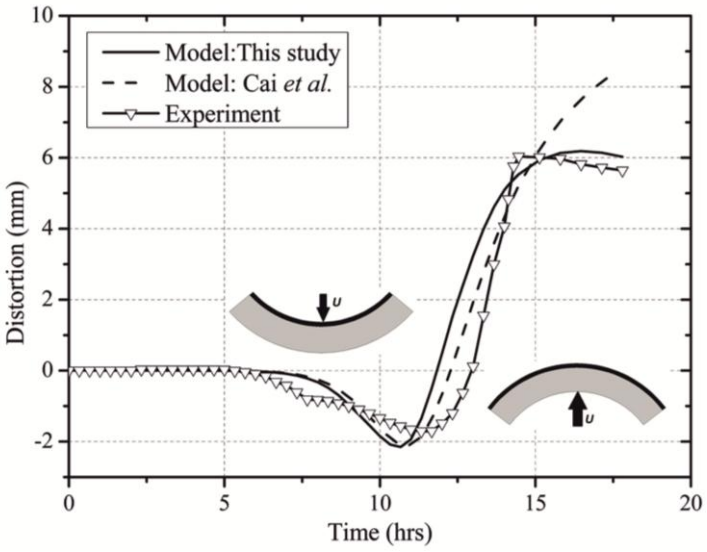

Figure 9: Comparison of the model and measurements of distortion (u) during the entire sintering [PAPER-I]

Note that the distortion, u, is the maximum deflection at the center of the bi-layer sample, which is calculated by integrating the rate of curvature, $\dot{k}$, along the horizontal, x, axis, see Figure 8, as:

$$u(l/2) = \int_0^{l/2} \int_0^{l/2} \dot{k} dx = \frac{1}{8} \dot{k} l^2 \tag{26}$$

This study (in PAPER-II) has also presented a new 'master sintering curve'-type solution derived for problems of sintering of bi-layers.[104] The proposed solution employs the conversion between real and specific time of sintering, τ_s, which is defined as:

$$\tau_s = 3 \int_0^t \frac{\alpha}{\eta_0 G} dt \tag{27}$$

where α, η_0 *and G* are the surface energy per unit area, viscosity of fully dense body and grain size respectively. By using the expressions proposed by Olevsky et *al*.[29] for sintering stress i.e., $P_L = \frac{2\alpha}{3G}(1-\theta)^2$, and normalized bulk viscosity, $\psi = \frac{2}{3\theta}(1-\theta)^3$, together with Eqs (19) and (20), the equation for porosity, θ, evolution during free sintering can be found as:

$$\frac{\dot{\theta}}{\theta} = -\frac{9\alpha}{8\eta_0 G} \tag{28}$$

Considering Eq (27), the solution for porosity evolution can be given by Eq (29). Hence, the specific time of sintering can be calculated from the porosity evolution during free sintering of one of the layers in the bi-layer.

$$\theta = \theta_0 \exp\left(-\frac{3}{8}\tau_s\right) \quad or \quad \tau_s = -\frac{8}{3}\ln\left(\frac{\theta}{\theta_0}\right) \tag{29}$$

In addition, the methodology utilizes material-specific parameters such as the relative intensity of sintering, λ, between the layers making the bi-layer and the ratio of fully dense body viscosities, $\xi = \eta_{02}/\eta_{01}$. The relative intensity of sintering is a function of local sintering stress and dense body viscosity of each layer, $\lambda = \frac{P_{L02}}{\eta_{02}} \Big/ \frac{P_{L01}}{\eta_{01}}$, and it can be estimated from the densification data of each layer during free sintering. A novel methodology is also proposed to find the ratio of fully dense body viscosities using a symmetric tri-layered sample in the same dilatometry experiment employed to measure the free shrinkage of each layer. This approach also enables the determination of all input parameters necessary for modeling sintering of bi-layers using optical dilatometry applied to each individual layer and to a symmetric tri-layered porous structure based on the two-layer materials utilized in the bi-layer system.[104]

Based on the material specific and dimensionless parameters defined to facilitate solution of bi-layer sintering, Eq (30) for example, shows the solution of normalized curvature rate:

$$\frac{d\bar{\kappa}}{d\tau_s} = \frac{\frac{1}{6}\left[\frac{\lambda\bar{P}_{L2}}{\psi_2} - \frac{\bar{P}_{L1}}{\psi_1}\right](1+\chi)}{2\frac{\varphi_1\bar{h}_1^3 + \xi\chi^3\varphi_2\bar{h}_2^3}{\bar{h}_1+\chi\bar{h}_2}\left[\frac{1}{\varphi_1\bar{h}_1} + \frac{1}{\xi\chi\varphi_2\bar{h}_2}\right] + \frac{\bar{h}_1+\chi\bar{h}_2}{2}} \tag{30}$$

where the normalized thickness, $\bar{h}_i = h_i/h_{0i}$ *for* $i = 1$ *or* 2, with the instantaneous thickness, h, and initial thickness, h_0 of each layer in the bi-layer. The factor, χ, is the ratio initial thickness of the layers making the bi-layer, i.e $\chi = h_{02}/h_{01}$ and all the other symbols are as defined in Section 3.4.

Uniform as well as the more accurate assumption of linear distributions of strains across the thickness of the layers are considered while deriving the solutions. For detailed derivation of the solution and application of the methodology, please refer to Appendix B and C (PAPER-II and III). Validation of the derived solutions using sintering of bi-layer made from tapes of porous and dense cerium gadolinium oxide (CGO_P and CGO_D) is also made, wherein the model results are found to agree well with experimental measurements, see Figure 10.[105]

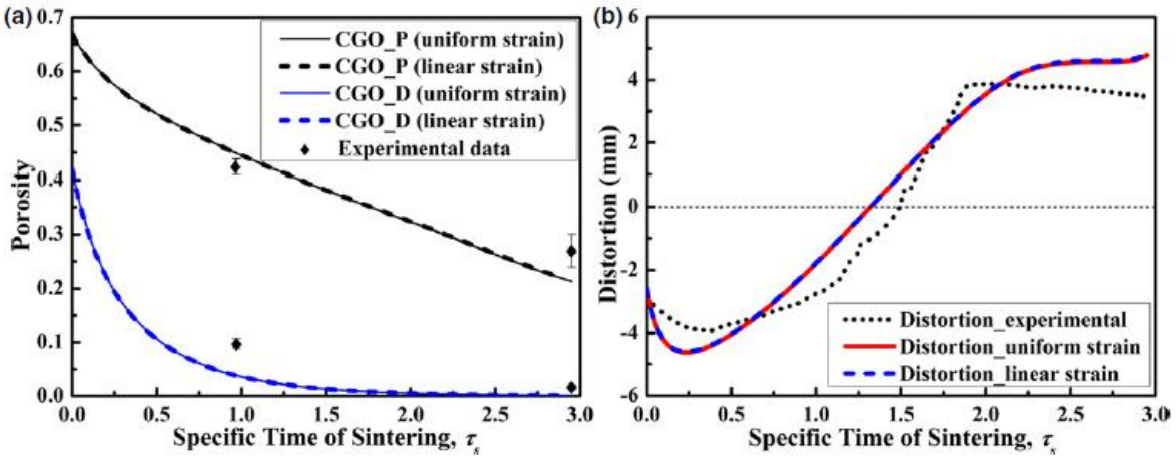

Figure 10: Comparison of the model results for (a) densification and (b) shape distortions together with measurements during the entire sintering [PAPER-III]

4.2. Numerical modeling

Previous studies of stress developments during sintering using finite element (FE) models mainly focus on powder compaction processes.[88, 106–109] In most of the studies, mechanism based constitutive models, e.g. those developed based on a single dominant diffusion mechanism, often limit the predictive capabilities of the finite element simulations. With the aim of addressing the limitations in the constitutive models, Kiani et *al*. showed an alternative approach using empirical models in their finite element code. Their approach is based on the use of experimental data, for e.g. shrinkage as a function of time, instead of constitutive models to predict deformations during sintering.[109]

Finite element implementation procedures using the linear viscous model to simulate densifications and shape distortions during sintering of layered structures is also discussed by Olevsky et *al*.[110] The procedure requires writing a finite element program, e.g. using Matlab or other programming software, to solve problems of bi-layer sintering. Manual programming of boundary conditions including geometry of the samples makes the approach tedious to simulate complex 3D geometries with different boundary conditions. Similarly Arguello et *al.* discussed the use of self developed non-linear 3D finite element (FE) code to simulate sintering using the linear viscous material model.[76] In addition to FE implementation of the linear viscous model, verification (with analytical model) and validation (with sintering experiment) were discussed in detail. Arguello et *al.* also suggested modifications to parameters defining the effective viscosity in the SOVS considering the phenomenological grain growth.[76] The proposed modifications require further experimental works such as measuring the instantaneous grain growth so as to improve the simulation results.

In this study (PAPER-IV), we have developed a finite element model in the commercial software, ABAQUS™, based on the continuum theory of sintering in order to predict the curvature evolution during sintering of multi-layered structures. This was made possible by implementing the linear-viscous form of the continuum theory of sintering (SOVS) in ABAQUS™ with the help of a user subroutine. Figure 11 shows the comparison of evolution of the bi-layer shape during sintering experiment and finite element simulation depicting stress in XX direction.

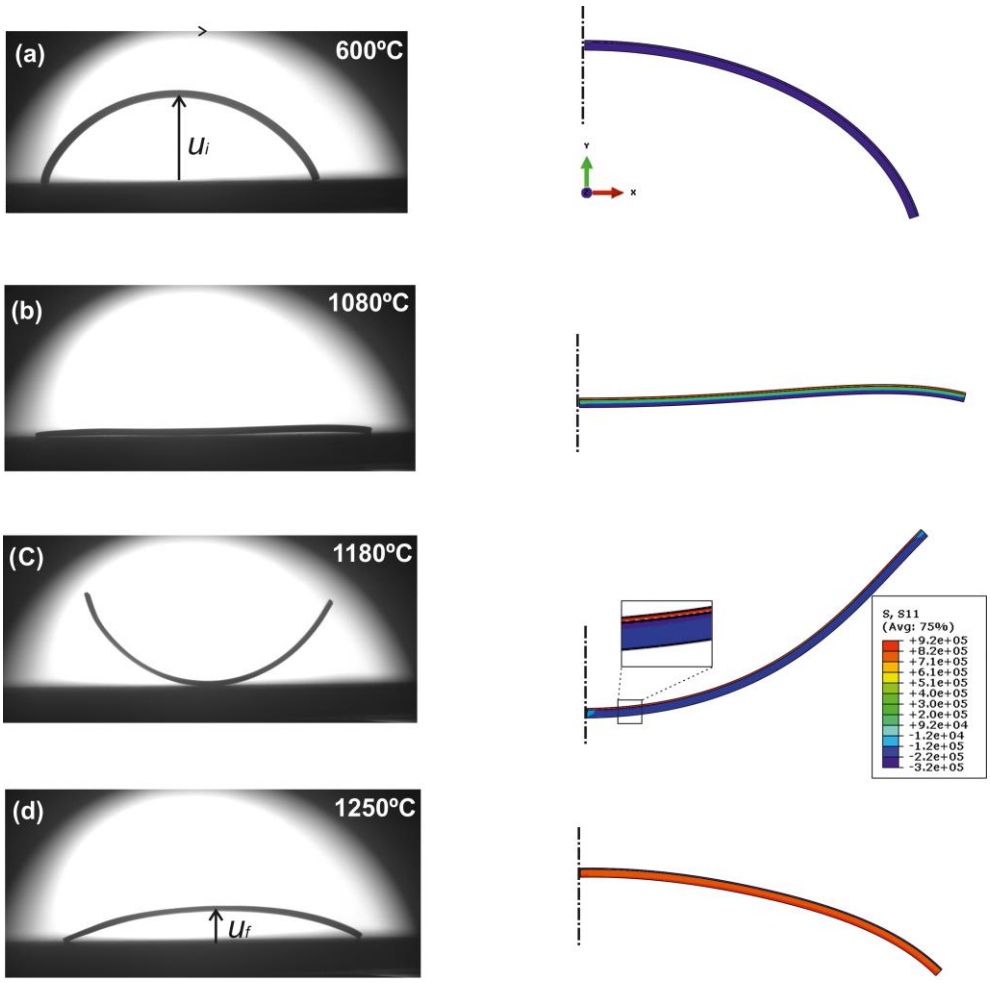

Figure 11: Comparison of the shape evolution during sintering of bi-layer experiment (left) and finite element model (right) [PAPER-IV]

4.3. Extrinsic factors affecting shape distortion

In addition to the inherent properties of the sintering body (shrinkage kinetics and viscous behaviors), the extent of shape distortions during co-firing is also affected by extrinsic factors. These factors include geometry of the sample, gravity and friction as well as processing parameters like heating rates and temperature distribution. Therefore, it is equally important to establish the necessary understanding of the relative effects of the above factors in the process of developing defect free multi-layer systems using co-firing.

Chiang et *al*. showed the effect of heating rate on camber evolution during sintering of asymmetric bi-layers consisting layers with different initial density.[100] At a given temperature, lower camber

with higher rate of change is observed for bi-layer sintered with higher heating rate. Generally higher temperatures are required to attain the maximum curvature for bi-layers sintered with high heating rates.[100] Kanters et *al*. also noticed a minor dependence of camber evolution of bi-layer samples on the heating rate during co-firing.[6] However, difference in camber evolutions from experiments with different heating rates may also occur due to errors in the measurement of temperature if high heating rates are used.[6, 11]

The possible effect of gravity on the development of camber during co-firing of multi-layers is discussed in Refs [10, 11, 111]. Mucke et *al*. argued about the effect of gravity on the distortion of samples after experimental investigation on sintering bi-layers in horizontal and vertical orientations.[10] The impact of own weight of the sample or gravity on camber evolution is also observed during the experimental studies of bi-layered samples reported by Atkinson et *al*.[111]

In this study, Frandsen et *al*. introduced the bending moment due to own weight of the sample into the continuum model to simulate camber during sintering of bi-layer.[112] Interesting comparisons have been reported showing the significance of the effect of gravity during sintering of bi-layer structures.[112] Figure 12 shows comparison of curvatures during sintering of bi-layers from various models together with experimental measurements.[113] The deviation of FE results from the model by Frandsen et *al*., which considers gravity, could be due to simplifications in the analytical implementations of the effect of gravity.

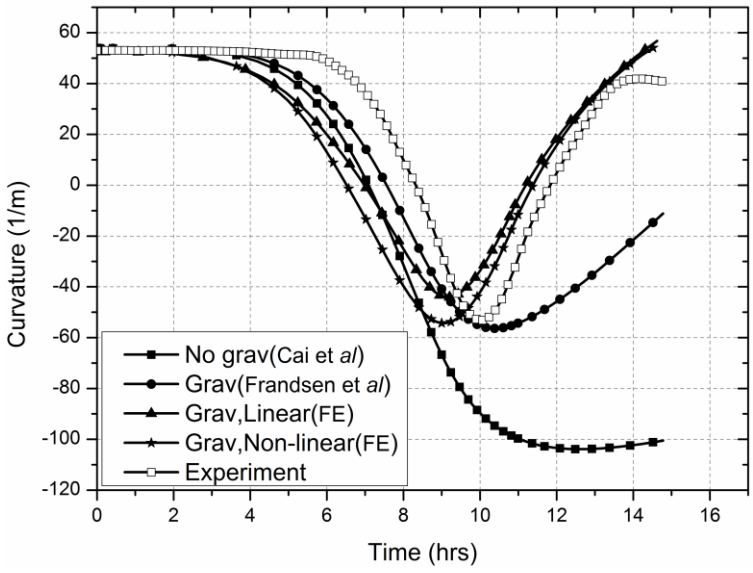

Figure 12: Comparison of experiment and different model simulations for camber evolutions in time showing the effect of gravity during sintering of bi-layers [PAPER-IV]

In addition, the initial thickness ratio between the layers making the bi-layer is one of the geometrical parameter that has significant effect on the evolution of curvature during co-firing. Kanters et *al*. showed the difference between the curvature evolutions of bi-layers made from undoped Zirconia and 3-mole%-yttria-stabilized zirconia tapes with different thickness ratio.[6] Similarly Lee et *al*. investigated the effect of the ratio of thickness evolution on the camber evolution.[114] They showed an increase in the distortion with the reduction of thickness ratio.[114]

In this study, systematic investigation of the effect of the initial thickness ratio on the overall curvature of a bi-layer sample has been studied using experiments and the most advanced model (which includes effect of gravity). The bi-layer in this study consists of layers with different initial porosities and different sinterabilities.[113] Figure 13 shows the variation of curvature with respect to the thickness ratio of a bi-layer after sintering for 8 hrs.[113] Extreme variation of curvature is shown for bi-layers with an initial thickness ratio less than 2.

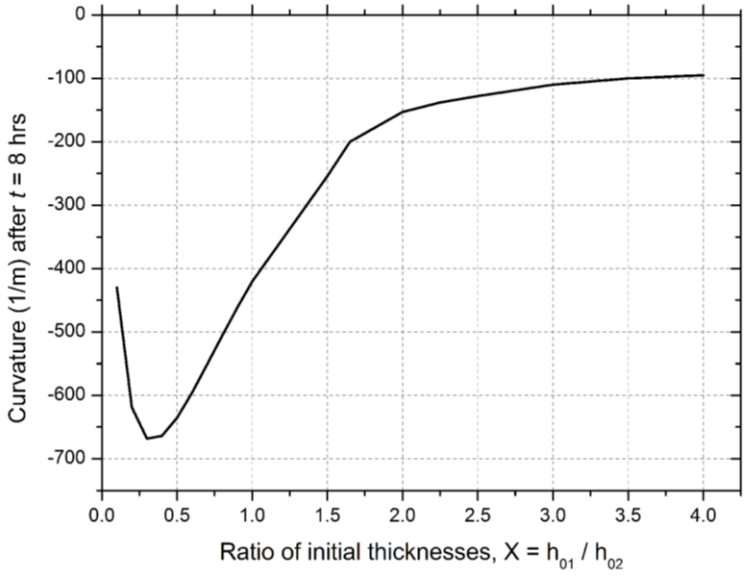

Figure 13: Variation of final curvatures after sintering for 8 hrs as a function of initial thickness ratio [PAPER-IV]

Furthermore, the friction between the edges of the bi-layer and the sample support surface inside the sintering furnace could also alter the camber evolution. As soon as the camber grows, if the edges of the planar multi-layer are in contact with the surface of the sample support, there would be a force opposing the movement of sample. Such forces could reduce the overall development of curvature in the bi-layer.

In this study, the effect of friction during sintering of bi-layers (made from cerium gadolinium oxide, CGO and lanthanum strontium manganite, LSM) is studied experimentally after co-sintering of two similar samples in different orientations, see Figure 14.[113] The bi-layer in Orientation-1 is observed to have larger curvature at the end of the sintering cycle compared to the other sample placed in reverse orientation.

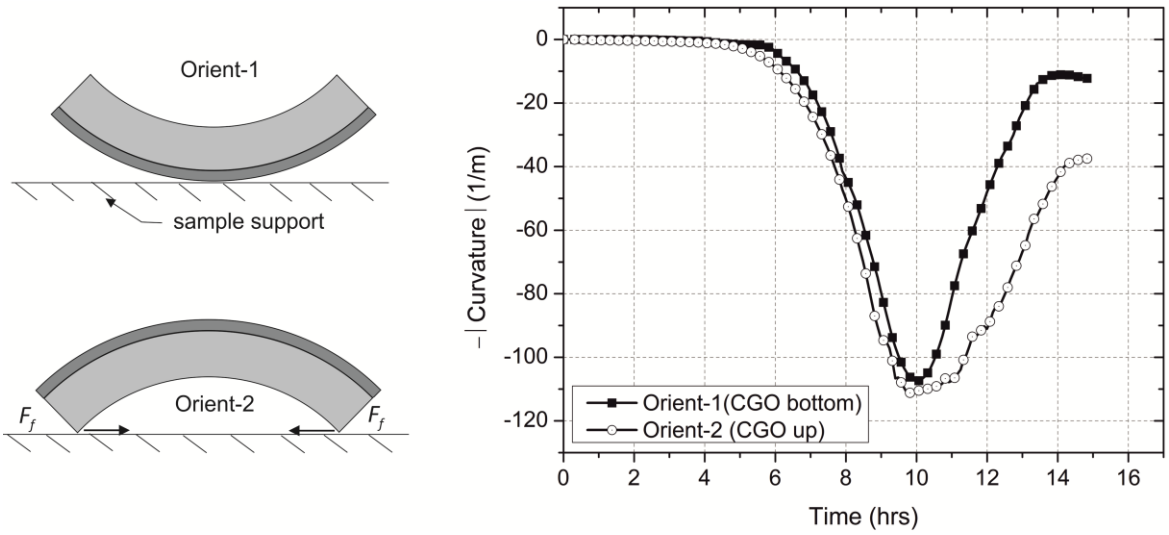

Figure 14: Two similar bi-layer samples in different orientations (left) and curvature evolution showing the effect of friction [PAPER-IV] (right)

4.4. Stresses during sintering of tubular bi-layers

As discussed in Section 1, functionally graded multi-layer composites are being developed in various architectures, see Figure 1. Among these, tubular multi-layer structures are used for membrane and solid oxide fuel cell technologies.[16, 115–117] Processing defect such as delamination and coating peel-offs can occur due to the transient stresses during sintering of tubular multi-layer structures. In contrary to reports on planar multi-layer structures, there was no prior study to analytically describe the densification and stress evolutions during sintering of tubular multi-layer systems.

In this study, a new analytical model has been developed to describe densification and stress developments during sintering of tubular bi-layered samples.[118] The developed analytical model has been verified using the finite element model developed in Ref[113]. Furthermore, the analytical model is validated using densification results from sintering of bi-layered tubular supported ceramic

oxygen membrane based on porous MgO (support) and $Ce_{0.9}Gd_{0.1}O_{1.95-d}$ (membrane) layers. Figure 15 shows the schematic representation the tubular bi-layer system.

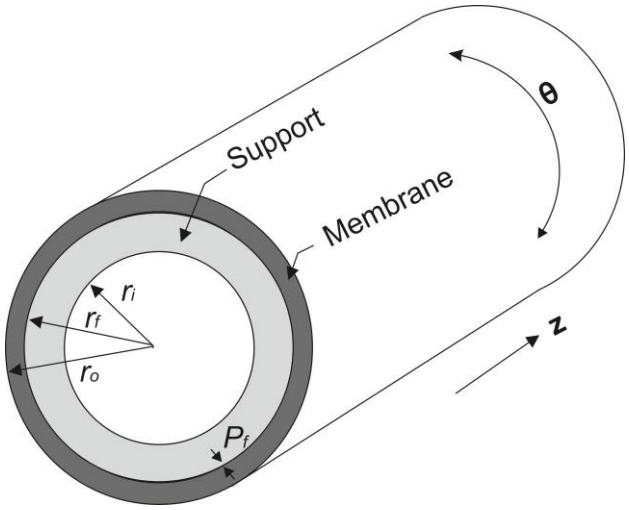

Figure 15: Schematic cross section of porous bi-layered tubular structure [PAPER-V]

Model results for the evolution of hoop (tangential) stresses in the support as well as membrane during the sintering cycle are shown in Figure 16. The hoop stress, which is the main factor for processing defects like coating (membrane) peel-offs, is found to be maximum at the beginning of the sintering cycle.

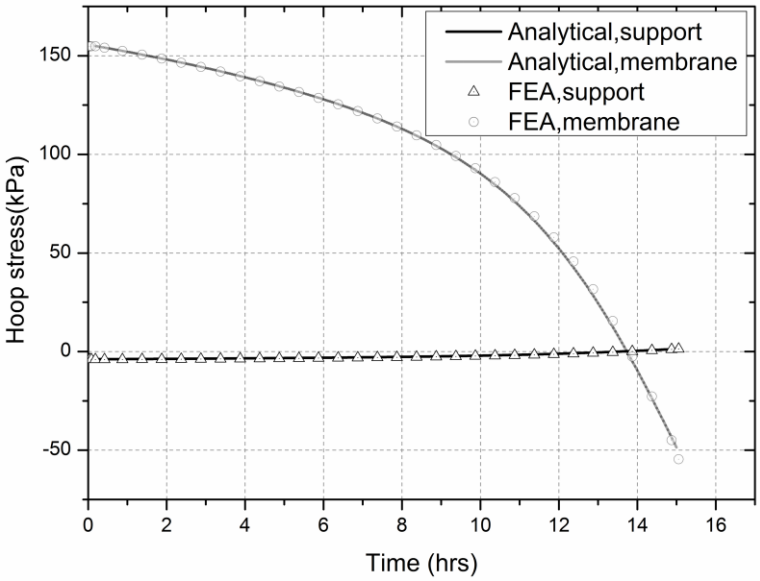

Figure 16: The evolution of hoop stress in the support and membrane during the sintering cycle [PAPER -V]

In addition, the developed model was able to predict the significant retardation of densification in the CGO membrane during co-firing. This has been observed by comparing model predictions for shrinkage in the constrained CGO membrane with experiment as well as free shrinkage of the CGO tape, see Figure 17.[118] Model results for the evolution of geometrical parameters of the tubular sample (radii and thickness of each layer) are also found to agree well with experimental measurements.[118] The densification and stress analysis during constrained sintering of tubular bi-layer structures would help to optimize stresses, for example, as a function of thickness of the support or membrane.

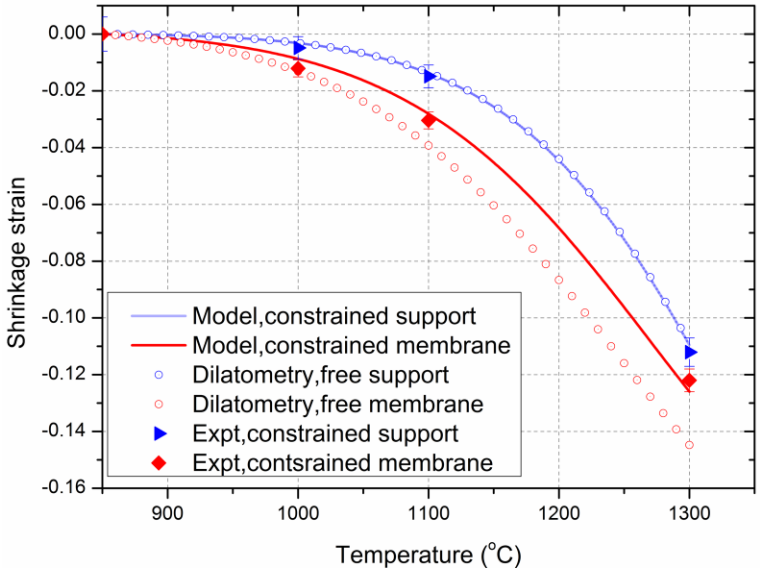

Figure 17: Comparison of linear shrinkage in free and constrained sintering together with experimental measurements for constrained sintering [PAPER-V]

4.5. Improvements in multi-layer sintering models

There have been studies depicting the limitations of the linear viscous model while describing densification, stresses and/or shape distortions during sintering of multi-layers. For instance, Kim et *al*. showed a wide discrepancy between their experimental results and predictions by the linear viscous model for densifications in constrained sintering.[13] Anisotropy in the pore grain structure especially of heterogeneous microstructure is explained to be the main reason for discrepancy between the model and experiments.[13]

Similarly Ollagnier et *al*. made studies of camber development during sintering of asymmetric porous laminates with an emphasis on microstructure of the shrinking layer.[11] They showed that both models by Cai et *al*. and Kanters et *al*. deviate significantly from their experimental measurements for camber evolution. Here also anisotropy in the microstructure is one of the reasons explained to be the possible cause for the observed discrepancies in addition to gravity. In the same study, a significant discrepancy between model and experiments were also shown for camber evolution during sintering of viscous layer on rigid substrate. According to Ollagnier et *al*., such phenomenon could occur because of loss of stiffness in the rigid substrate due to formation of micro-cracks and interfacial slip during co-firing.[11]

These and other limitations become motivations to include further enrichments to the linear viscous model so as to enable it describe various effects during sintering of multi-layers. With regards to microstructural anisotropy, Bordia et *al*. quantified the effect during constrained sintering and proposed a framework for the modeling of anisotropic sintering of films constrained by rigid substrate.[119] The framework proposed by Bordia and Bowen requires determination of anisotropic viscosities and Poisson's ratio's together with the free strain rates in the principal directions of the sintering body.[119] In an effort to consider the effect of different pore sizes on the constitutive parameters, Lu et *al*. also tried to incorporate bi-modal pore distribution factors into the linear viscous models while analyzing camber developments during co-firing of bi-layers.[102] Similarly Darcovich et *al*. used the continuum model with a field variable, which accounts for the effect of particle size distributions on the material properties of the sintering body, in their FE analysis of deformations during sintering of heterogeneous samples.[120] In the present study, the effect of gravity was included in the analytical implementation of the continuum model and it was found that gravity actually affects camber evolution during co-firing of planar bi-layers.[103, 112] This is also found to be consistent with the arguments made by Mucke et *al*.[10] and Ollagnier et *al*.[11]

Furthermore, a two dimensional implementation of the linear viscous material model for sintering of thin films on rigid substrates with interfacial shear traction is reported by Jagota and Hu.[121] The possible interfacial slip is considered by a shear traction, which varies with the average in-plane velocity and enters the theory through the body forces. Jagota and Hu were able to investigate the limiting cases of very low and high friction on the rate of deformation and stresses during sintering of thin films.[121] Such kinds of analysis will be useful to enrich the continuum model of sintering as it provides the methodology to account for stress relaxations because of interfacial slips.

Through time, various improvements to the continuum model have been made in order to successfully describe the densification and/or shape distortions during sintering of multi-layers. Table 3 summarizes various implementations of the linear viscous models for simulating sintering of multi-layers based on their unique features.

Table-3: Comparison of bi-layer models based on their unique features

S.N	**Author**	**Microstructural refinements in the models**	**Strain distributions across the thickness** (*for analytical models*)	**Effect of gravity**	**Ref**
1	Cai et *al*.	-	Uniform	x	[81, 96]
2	Lu et *al*.	Bi-modal pore distributions	Uniform	x	[102]
3	Kanters et *al*.	Anisotropies in shrinkage kinetics, Coarsening	Linear	x	[6]
4	Li et *al*.	Anisotropic constitutive law	-	-	[122]
5	Olevksy et *al*.	Damage development	-	-	[123]
6	Jagota and Hu	Interfacial slip between layers	-	x	[121]
7	Darcovich et *al*.	Particle size distributions	-	x	[120]
8	Frandsen et *al*.	-	Linear	✓	[112]
9	Molla et *al*. (This study)	Grain growth	Linear	✓	[103]

5. Multi-scale Modeling of Sintering

In this section, the use of multi-scale modeling approaches to describe sintering in general and sintering of multi-layers in particular are briefly reviewed. With this regard, the contribution made in this study is also discussed.

5.1. Introduction

Macroscopic deformations during sintering process are highly sensitive to changes in the microstructure of the sintering body. Theoretically, the microstructure of a porous body at a given time is a function of a number of internal variables in addition to porosity and grain size. The ability of existing continuum sintering models is highly limited due to the challenge of defining constitutive parameters that can explicitly consider every internal variable in the microstructure. These challenges have provided a platform for integrating the different modeling techniques, for instance at the atomistic, particle and continuum levels. Integration of these models in a multi-scale manner will be the natural extension to the continuum models so as to improve their predictive capabilities of densification as well as stresses during sintering.

Recently the need for multi-scale approaches for modeling sintering in general and multi-layer sintering in particular is growing. Pan and Huang reported an overview to the sintering models at different length scales and stressed the need for coupling the existing models from the atomic scale to the continuum level.[124] Similarly a review of multi-scale modeling is reported by Olevsky et *al*. wherein the possibility of extracting some of the constitutive parameters for the continuum models from a meso-scale model is discussed.[125] In their study, constitutive parameters for the continuum model such as sintering stress and normalized bulk viscosity of a porous compact during sintering were determined using the meso-scale model based on kinetic Monte Carlo method.[125] However, the procedures for coupling of the meso- and macro-scale models has not been shown.

5.2. Multi-scale modeling of sintering of multi-layers

Maximenko et *al*. suggested a multi-scale approach for modeling sintering of macroscopically inhomogeneous materials by specifying material properties through the definition of microscopic unit cells.[126] They were able to show the application of the so-called Direct Multi-scale Modeling (DMM) for solid state as well as viscous sintering of inhomogeneous porous bodies. While this study is useful to study the relative effects of shape and orientation of pores on the overall shape or camber evolution during sintering of inhomogeneous structures, it does not consider coarsening or grain growth during sintering.

On the other hand, Aizawa et *al*. presented a coupled micro-macro scale models to describe hot deformation and sintering behaviors of materials.[127] Using computational homogenization on unit cell models of idealized geometries as well as SEM images of microstructures, they were able to extract the elastic constitutive parameters of the continuum body to model hot pressing processes.[127] However, Aizawa et *al*. did not show how the sintering constitutive parameters could be extracted from the unit cells and be used in the macro-scale models.

With regards to modeling stresses in multi-layer systems, Kuzmov at *al*. presented an approach for modeling viscous sintering based on parallel monitoring of micro- and macro-scale models.[128] Interestingly, they were able to show microstructural anisotropies during constrained sintering of bi-layers using unit cells based on spherical pores. A numerical study on the effect of pore shape distributions on the overall shape of porous bi-layer samples after co-firing has also been shown.[128]

Matrin and Bordia used models developed using discrete element methods (DEMs) to show the effect of rigid substrate on sintering of constrained films with regards to microstructural anisotropy.[129] Similarly Rasp et *al*. presented particle based simulations using DEMs to analyze shape distortion and delamination during constrained sintering of thick films.[130]

In the present study, a new multi-scale modeling procedure for predicting shape distortions during sintering of bi-layer porous structures has been suggested.[131] The approach couples meso- and macro-scale models enabling direct exchange of the constitutive parameters between the two at each time step.[131] The meso-scale model is developed based on kMC method whereas the continuum theory implemented by using finite element methods is used for the macro-scale model. The shrinkage rate of the porous compact is calculated from the densification of the microstructure predicted by the kMC model. Simultaneously, the microstructure is used to homogenize the

effective viscosity of the porous compact. Figure 18 shows the schematics of information flow in the multi-scale model suggested in this study. Here, D_{ijkl}, represents the homogenized effective viscosity tensor.

Computational homogenization is used to extract the effective viscosity of the porous compact assuming the microstructure at each time step as the representative volume element (RVE) of the continuum body. Figure 19 shows the schematic representation of the boundary value problems (BVPs) set up using the RVE at each time step during the computational homogenization.

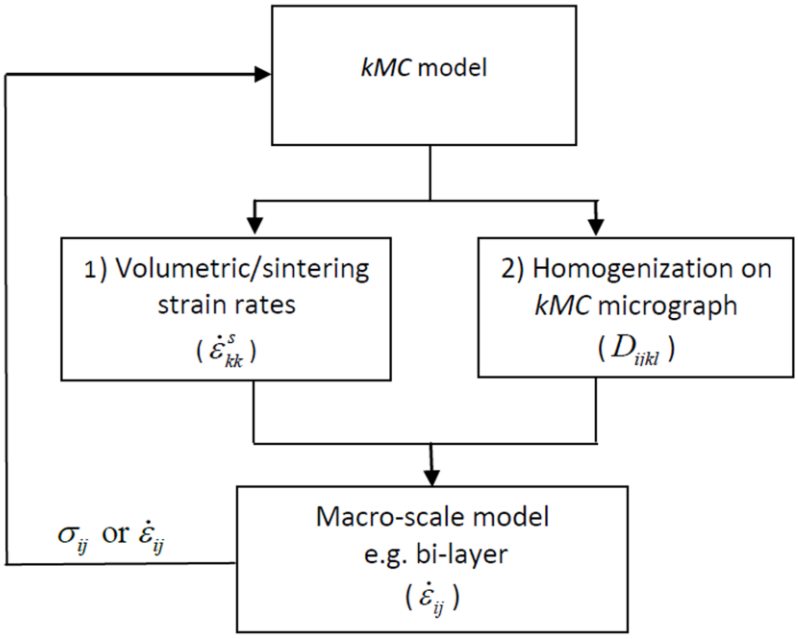

Figure 18: Schematics of organization of the multi-scale model [PAPER-VI]

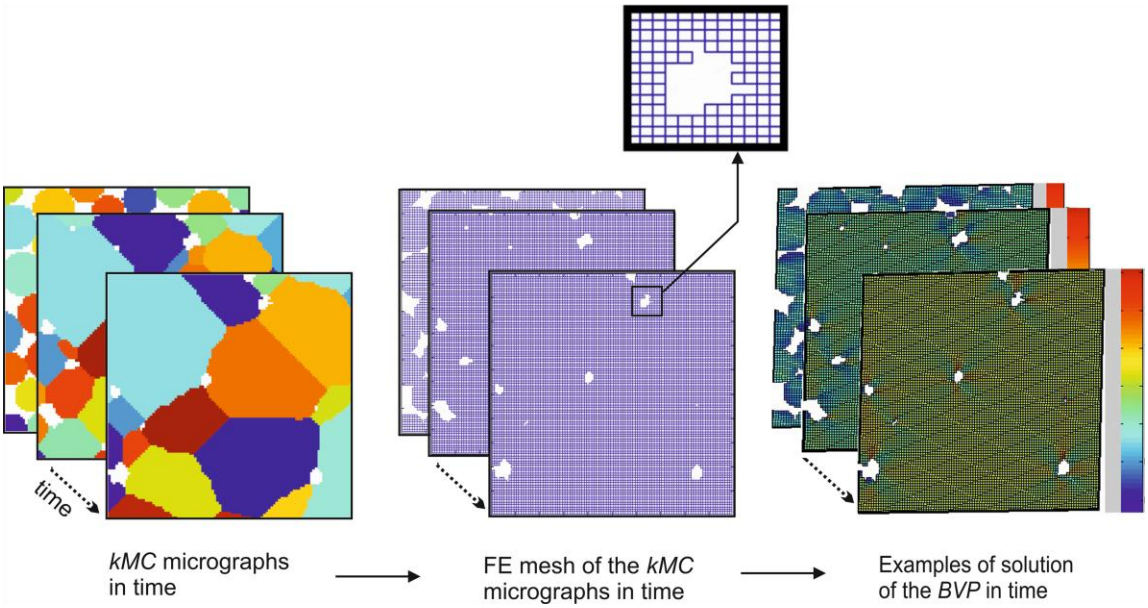

Figure 19: Schematics of the procedure used to model the effective viscosity of the porous body using boundary value problems (BVP) [PAPER-VI]

To illustrate the methodology, application of the model has been discussed using different types of bi-layers systems (e.g. Bilayer A and B consisting layers with the same and different sinterabilities and initial porosities). Interestingly the expected behaviors of camber evolution in time for both types of bi-layers were observed, see Figure 20.

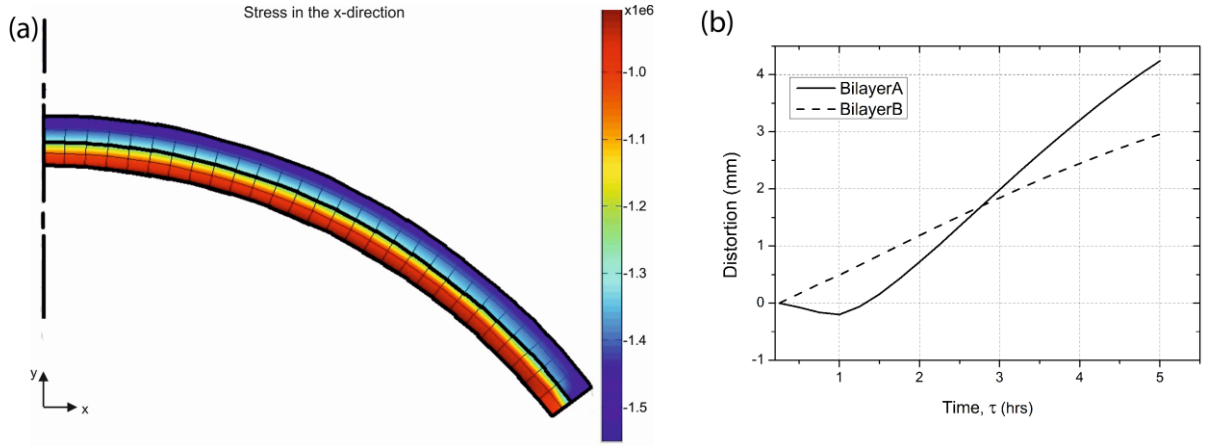

Figure 20: Distortion in the bi-layer system: a) contour plot of stress b) distortions in bi-layer types A and B [PAPER-VI]

6. Summary of Appended Papers

In this chapter a short summary of the papers appended in the thesis report are provided.

6.1. Paper-I

T.T. Molla, H.L. Frandsen, R. Bjørk, D.W. Ni, E. Olevsky and N. Pryds, "Modeling kinetics of distortions in porous bi-layered structures," *J Eur Ceram Soc*, **33** 1297-1305 (2013)

Shape distortions during constrained sintering experiment of bi-layer porous and dense cerium gadolinium oxide (CGO) structures have been modeled. Technologies like solid oxide fuel cells require co-firing thin layers with different green densities, which often exhibit differential shrinkage because of different sintering rates of the materials resulting in undesired distortions of the component. An analytical model based on the continuum theory of sintering has been developed to describe the kinetics of densification and distortion in the sintering processes. A new approach is used to extract the material parameters controlling shape distortion through optimizing the model to experimental data of free shrinkage strains. The significant influence of weight of the sample (gravity) on the kinetics of distortion is taken in to consideration. The modeling predictions indicate good agreement with the results of sintering of a bi-layered CGO system in terms of evolutions of bow, porosities and also layer thickness.

6.2. Paper-II

E. Olevsky, T.T. Molla, H.L. Frandsen, R. Bjørk, V. Esposito, D.W. Ni, A. Ilyna and N Pryds, "Sintering of multi-layered porous structures: Part I-Constitutive models," *J Am Ceram Soc*, **96** [8] 2657–2665 (2013)

Theoretical analyses of shrinkage and distortion kinetics during sintering of bi-layered porous structures are carried out. The developed modeling framework is based on the continuum theory of sintering; it enables the direct assessment of the co-firing process outcomes and of the impact of process controlling parameters. The derived 'master sintering curve'-type solutions are capable of describing and optimizing the generic sintering shrinkage and distortion kinetics for various material systems. The approach utilizes the material-specific parameters, which define the relative kinetics of layer shrinkages such as the relative intensity of sintering, and employs the conversion between real and specific times of sintering. A novel methodology is also developed for the determination of the ratio of the shear viscosities of the layer's fully-dense materials. This new technique enables the determination of all input parameters necessary for modeling sintering of bi-layers using experimental techniques like optical dilatometry of the individual layers and a symmetric tri-layered porous structure based on the two layer materials utilized in the bi-layered system. Examples of sintering different porous bi-layered systems are presented to justify the capability of the model in predicting and optimizing sintering kinetics.

6.3. Paper-III

D.W. Ni, E. Olevsky, V. Esposito, T.T. Molla, S. P. Foghmoes, R. Bjørk, H.L. Frandsen, E. Alexandrova and N Pryds, "Sintering of multi-layered porous structures: Part II-Experiments and model applications," *J Am Ceram Soc*, **96** [8] 2666–2673 (2013)

Experimental analyses of shrinkage and distortion kinetics during sintering of bi-layered porous and dense gadolinium-doped ceria $Ce_{0.9}Gd_{0.1}O_{1.95-d}$ structures are carried out, and compared with the theoretical models developed in Part I of this work. A novel approach is developed for the determination of the shear viscosities ratio of the layer fully dense materials. This original technique enables the derivation of all the input parameters for the bi-layer sintering modeling from one set of optical dilatometry measurements, including the conversion between real and specific times of sintering, the layers' relative sintering intensity, and the shear viscosities ratio of the layer fully dense materials. These optical dilatometry measurements are conducted simultaneously for each individual layer and for a symmetric tri-layered porous structure based on the two layers utilized in the bi-layered system. The obtained modeling predictions indicate

satisfactory agreement with the results of sintering of a bi-layered cerium–gadolinium oxide system in terms of distortion and shrinkage kinetics.

6.4. Paper-IV

T.T. Molla, D.W. Ni, R. Bulatova, R. Bjørk, C. Bahl, N. Pryds and H.L. Frandsen, "Finite element modeling of camber evolutions during sintering of bi-layer structures," *J Am Ceram Soc*, in press (2014)

The need for understanding the mechanisms and optimization of shape distortions during sintering of bi-layers is necessary while producing structures with functionally graded architectures. A finite element model based on the continuum theory of sintering was developed to understand the camber developments during sintering of bi-layers composed of $La_{0.85}Sr_{0.15}MnO_3$ and $Ce_{0.9}Gd_{0.1}O_{1.95}$ tapes. Free shrinkage kinetics of both tapes were used to estimate the parameters necessary for the finite element models. Systematic investigations of the factors affecting the kinetics of distortions such as gravity and friction as well as the initial geometric parameters of the bi-layers were made using optical dilatometry experiments and the model. The developed models were able to capture the observed behaviors of the bi-layers' distortions during sintering. Finally, we present the importance of understanding and hence making use of the effect of gravity and friction to minimize the shape distortions during sintering of bi-layers.

6.5. Paper-V

T.T. Molla, D. K. Ramachandran, D.W. Ni, V. Esposito, F. Teocoli, E. Olevsky, R. Bjørk, N. Pryds, A. Kaiser and H.L. Frandsen, "Constrained sintering of bi-layered tubular structures," *J Am Ceram Soc*, under review (2014)

Constrained sintering of tubular bi-layered structures is being used in the development of various technologies. Due to mismatch in the densification rate between the layers in the tubular geometry, stresses develop and sometimes create various processing defects. An analytical model

is developed to describe the densification and stress developments during constrained sintering of tubular bi-layered samples. The direct correspondence between linear elastic and linear viscous theories is used as a basis for the model development. The developed analytical model is first verified by finite element simulation for the constrained sintering of tubular bi-layer system. Furthermore, the analytical model is validated using densification results from sintering of bi-layered tubular supported ceramic oxygen membrane based on porous MgO and $Ce_{0.9}Gd_{0.1}O_{1.95-d}$ layers. Model input parameters, such as the shrinkage kinetics and viscous parameters are obtained experimentally using optical dilatometry and thermo-mechanical analysis. Results from the analytical model are found to agree well with finite element simulations as well as measurements from sintering experiment.

6.6. Paper-VI

T.T. Molla, R. Bjørk, E. Olevsky, N. Pryds and H.L. Frandsen, "Multi-scale modeling of shape distortions during sintering of bi-layers," *J Comp Mat Sci*, **88** 28–36 (2014)

Models for deformational behaviors of porous bodies during sintering often rely on limited number of internal variables as they are formulated based on simplified or ideal microstructures. Considering realistic microstructures can improve the predictive capabilities of the already established theories like the continuum theory of sintering. A new multi-scale numerical approach for modeling of shape distortions during sintering of macroscopically inhomogeneous structures combined with a microstructure model is developed. The microstructures of the porous body are described by unit cells based on kinetic Monte Carlo (kMC) model of sintering. During the sintering process the shrinkage rate is calculated from the kMC model. With the help of computational homogenization, the effective viscosity of the powder compact is also estimated from a boundary value problem defined on the microstructures of unit cells simulated by the kMC model. Examples of simulation of sintering of bi-layers based on different material systems are presented to illustrate the multi-scale model. The approach can be considered as an extension to the continuum theory of sintering combined with the meso-scale kinetic Monte Carlo model.

7. Summary and Outlooks

This section summarizes the works performed in the present study with respect to analytical, numerical and multi-scale modeling. In addition, outlooks for further studies are suggested.

7.1. Summary

7.1.1. Analytical model

Experimentally observed behaviors of shrinkage and camber development during sintering of bi-layer samples of porous and dense cerium gadolinium oxide (CGO) layers were studied. With the help of the new method proposed, data collected from a single optical dilatometry experiment conducted simultaneously for individual layers and an asymmetric bi-layer porous sample was sufficient to model the kinetics of densification and shape distortion. The viscous parameters, i.e. the pre-exponential factor and the apparent activation energies in the Arrhenius-type viscosity function were first determined as those providing the least deviation between the free shrinkage strains recorded in the experiment and those obtained by the model.

By using the determined viscous parameters, the effective viscosities of each layer are updated based on the densification in the bi-layer model developed to describe shape distortion during sintering of an asymmetric bi-layer sample. A good agreement between model predictions and experimental measurements of distortions was found, which is also considered as a validation for the estimated material parameters. This is also supported by subsequent comparisons with literature values.

The model is able to capture all the important phenomenon of shape changes observed during the experiment. These include the significant effect of gravity on the evolution of shape of the bi-layer sample at the later stages of the sintering.

In addition, a new model framework enabling engineering level solutions for problems of sintering of bi-and tri-layered porous systems has been developed. The applications and capabilities of the modeling framework are explained by considering different types of bi-layer systems as well as

comparing model results with experimental measurements. The elaborated solutions allow not only the predictions but also optimizations of the sintering outcomes by controlling the system's initial geometry and structural characteristics together with adjustment of the sintering regime.

Furthermore, a new closed form analytical model based on the analogy between linear elastic and linear viscous theories has been developed to describe densification and stress development during sintering of tubular bi-layered samples. Stresses during constrained sintering of tubular bi-layered structures develop not only due to mismatch in the shrinkage rate of the layers but also because of the radial gradients in the internal shrinkage rate of each layer.

The developed analytical model was first verified by finite element simulation for the constrained sintering of tubular bi-layer systems. Furthermore, it was validated using densification results from sintering of bi-layered tubular supported ceramic oxygen membranes based on porous MgO and $Ce_{0.9}Gd_{0.1}O_{1.95-d}$ layers. Results from the analytical model agree well with finite element simulations as well as measurements from the experiment.

In general, the radial stresses in the bi-layered tubular structures are very small throughout the sintering cycle as compared to the tangential (hoop) stresses. Processing defects like axial cracks and coating peel-offs mainly occur due to the hoop stress, which is maximum at the beginning of the sintering cycle. Hence, the model provided in this study could be used to minimize the transient stress generations during constrained sintering of tubular bi-layered structures.

7.1.2. Numerical model

Finite element models based on the continuum theory of sintering were developed to describe the distortions during sintering experiments of bi-layers composed of $La_{0.85}Sr_{0.15}MnO_3$ (LSM) and $Ce_{0.9}Gd_{0.1}O_{1.95}$ (CGO) tapes. Free shrinkage kinetics of both tapes were used to estimate the input parameters necessary for the finite element models.

Systematic studies on the effect of extrinsic factors such as gravity and friction together with the initial geometries on the kinetics of distortions of bi-layers during sintering were presented. The finite element model simulations were able to capture the observed behaviors of distortions during different sets of experiments involving different bi-layers. Some discrepancies are still observed, and it was speculated that these were due to stress relaxation near the interfaces of the bi-layers due to micro-crack growth. In addition, the possible causes for the observed discrepancies between the model and experiments have been discussed. Some of these are:

1. Explicit consideration of grain growth while defining the effective viscosity of the porous compact during sintering
2. The linear viscous model, originally developed for bodies that sinter by viscous flow, has limitations when it is used for bodies that sinter by solid state diffusion
3. Activation energy of crystalline bodies could vary as a function of density during sintering, as observed by Raether et *al*.[49], which may have contributed to the observed discrepancy as constant activation energy throughout the sintering are considered in this study.

Generally, understanding the effect of factors such as gravity and friction during sintering of multi-layered porous structures could be helpful to reduce the shape distortion problems usually observed during co-firing.

7.1.3. Multi-scale model

A new multi-scale modeling procedure using unit cells simulated by the kinetic Monte Carlo (kMC) method is developed to be able to model shape distortion during sintering of bi-layer systems. The kMC model is able to predict the shrinkage rate as well as the microstructure of the powder compact, which is then used to calculate the effective viscosities through homogenization. The approach presented here has no limitation on the number of internal parameters considered for modeling the densification as well as viscous behaviors of powder compacts.

Comparison of the normalized shear viscosities calculated using the approach developed in this study is found to be in good agreement with other theories from the literature, see Appendix F (Paper-VI). Using the new procedures, it was possible to model curvature evolution of bi-layers that consist of layers of the same, as well as different materials. The expected behavior of the distortion of the bi-layer is observed. The developed multi-scale algorithm can be considered as an extension to the continuum theory of sintering in which the kinetic Monte Carlo model is included.

7.2. Outlooks for future works

Shape distortions during co-firing of multi-layer samples occur not only during the sintering cycle, but also throughout the heating and cooling stages. For instance, significant distortions of bi-layer samples were observed during de-binding cycle of the heat treatment. In addition, accumulation of residual stress also occurs during the cooling cycle, which enhances the need for including the de-

binding and cooling cycles in the already developed models. Therefore, it is necessary to develop a unified model to describe stresses and shape distortions during the entire heating including the effect of differential de-binding between the layers and residual stresses during the cooling cycle.

In addition, enrichment of the developed model could be made so as to capture various three dimensional as well as other effects during co-firing process. Some of these could be:

- Edge curl during sintering of solid oxide fuel cells (SOFCs)
- Collapse of horizontally sintered tubes because of gravity
- Friction between the sample and sample support
- Model variation of curvature inside a production furnace due to gradient in temperature

Furthermore, modeling of other processing defects, for example crack growth in one of the layers and delamination between the layers during sintering of multi-layers could be performed.

In order to explicitly address the drawbacks of existing models while defining the deformational behaviors of sintering bodies, the natural way forward is to extend the existing models with the help of multi-scale modeling approaches. An initial work has been reported in this study, which is found to be a motivation for further developments. A fully coupled meso-macro scale 3D model would be promising to successfully describe the experimental observations during sintering in general and co-sintering in particular. In addition to the kMC methods for modeling microstructural evolution of the porous body, 3D-models based on DEMs can also be considered together with computational homogenization. This approach could be useful for modeling slip between layers and crack opening during sintering.

Bibliography

[1] L.L. Shaw, "Thermal residual stresses in plates and coatings composed of multi-layered and functionally graded materials," *Compos Part B Eng*, **29** [3] 199–210 (1998).

[2] R. Mahamood, E. Akinlabi, M. Shukla, and S. Pityana, "Functionally graded material: an overview," *Proc world Congr Eng*, **III** 2–6 (2012).

[3] A. Markworth, K. Ramesh, and W. Parks, "Review: Modelling studies applied to functionally graded materials," *J Mater Sci*, **30** 2183–2193 (1995).

[4] D.J. Green, O. Guillon, and I. Roedel, "Constrained sintering: A delicate balance of scales," *J Eur Ceram Soc*, **28** [3] 1451–1466 (2008).

[5] G.Q. Lu, R.C. Sutterlin, and T.K. Gupta, "Effect of mismatched sintering kinetics on camber in a low-temperature co-fired ceramic package," *J Am Ceram Soc*, **76** [8] 1907–1914 (1993).

[6] J. Kanters, U. Eisele, and J. Rodel, "Cosintering simulation and experimentation: Case study of nanocrystalline Zirconia," *J Am Ceram Soc*, **84** [12] 2757–2763 (2001).

[7] J. Chang, O. Guillon, J. Roedel, and S.-J.L. Kang, "Characterization of warpage behaviour of Gd-doped ceria/NiO-yttria stabilized zirconia bi-layer samples for solid oxide fuel cell application," *J Power Sources*, **185** [2] 759–764 (2008).

[8] G.R. Brown, R.A. Levine, A. Shaikh, and E.A. Olevsky, "Three-dimensional solar cell finite-element sintering simulation," *J Am Ceram Soc*, **92** [7] 1450–1455 (2009).

[9] M. Cologna, V.M. Sglavo, and M. Bertoldi, "Sintering and deformation of solid oxide fuel cells produced by sequential tape casting," *Int J Appl Ceram Technol*, **7** [6] 803–813 (2010).

[10] R. Muecke, N.H. Menzler, H.P. Buchkremer, and D. Stoever, "Cofiring of thin Zirconia films during SOFC manufacturing," *J Am Ceram Soc*, **92** [1] S95–S102 (2009).

[11] J.B. Ollagnier, O. Guillon, and J. Roedel, "Constrained sintering of a glass ceramic composite: I. Asymmetric laminate," *J Am Ceram Soc*, **93** [1] 74–81 (2010).

[12] J.B. Ollagnier, D.J. Green, O. Guillon, and J. Roedel, "Constrained sintering of a glass ceramic composite: II. Symmetric laminate," *J Am Ceram Soc*, **92** [12] 2900–2906 (2009).

[13] J.S. Kim, R.A. Rudkin, X. Wang, and A. Atkinson, "Constrained sintering kinetics of 3YSZ films," *J Eur Ceram Soc*, **31** [13] 2231–2239 (2011).

[14] J. Phair, N. Lönnroth, M. Lundberg, and A. Kaiser, "Characteristics of cerium-gadolinium oxide (CGO) suspensions as a function of dispersant and powder properties," *Colloids Surfaces A: Physicochem Eng Aspects,* **341** [1-3] 103–109 (2009).

[15] L.T. Kuhn, N. Pryds, C.R.H. Bahl, and A. Smith, “Magnetic refrigeration at room temperature – from magnetocaloric materials to a prototype,” *J Phys Conf Ser*, **303** [1] 012082 (2011).

[16] Z. Liu, G. Zhang, X. Dong, W. Jiang, W. Jin, and N. Xu, “Fabrication of asymmetric tubular mixed-conducting dense membranes by a combined spin-spraying and co-sintering process,” *J Memb Sci*, **415-416** 313–319 (2012).

[17] N. Pryds, Optimized processing of multi-material architectures for functional ceramics, *OPTIMAC project (Contract No. 09-072888),* Roskilde, 2011.

[18] M.N. Rahaman, Sintering of Ceramics. *Taylor and Francis Group*, 6000 Broken sound parkway NW, Suite 300, Boca Raton, FL 33487-2742, 2008.

[19] S. Somiya, F. Aldinger, R.M. Spriggs, K. Uchino, K. Koumoto, M. Kaneno, Handbook of Advanced Ceramics: Materials, Applications, Processing and Properties*, Volume 2*. 2003.

[20] H. Tanaka, A. Yamamoto, J. Shimoyama, H. Ogino, and K. Kishio, “Strongly connected ex situ MgB 2 polycrystalline bulks fabricated by solid-state self-sintering,” *Supercond Sci Technol*, **25** [11] 115022 (2012).

[21] V. Tikare, M.A. Miodownik, and E.A. Holm, “Three-dimensional simulation of grain growth in the presence of mobile pores,” *J Am Ceram Soc*, **84** [6] 1379–1385 (2001).

[22] V. Tikare, M. Braginsky, D. Bouvard, and A. Vagnon, “Numerical simulation of microstructural evolution during sintering at the mesoscale in a 3D powder compact,” *Comput Mater Sci*, **48** [2] 317–325 (2010).

[23] C. Herring, “Effect of change of scale on sintering phenomena,” *J Appl Phys*, **21** [4] 301–303 (1950).

[24] G.C. Kuczynski, “Self-diffusion in sintering of metallic particles,” *Trans Am Inst Min Metall Eng*, **185** [2] 169–178 (1949).

[25] W.D. Kingery and M. Berg, “Study of the initial stages of sintering solids by viscous flow, evaporation-condensation, and self-diffusion,” *J Appl Phys*, **26** [10] 1205–1212 (1955).

[26] R.L. Coble, “Initial sintering of Alumina and Hematite,” *J Am Ceram Soc*, **41** [2] 55–62 (1958).

[27] R.L. Coble, “Sintering crystalline solids .1. Intermediate and final stage diffusion models,” *J Appl Phys*, **32** [5] 787–& (1961).

[28] J. Frenkel, “Viscous flow of crystalline bodies,” *Zhurnal Eksp i Teor Fiz*, **16** [1] 29–38 (1946).

[29] E.A. Olevsky, “Theory of sintering: from discrete to continuum,” *Mater Sci Eng R-Reports*, **23** [2] 41–100 (1998).

[30] J.D. Hansen, R.P. Rusin, M.H. Teng, and D.L. Johnson, “Combined-stage sintering model,” *J Am Ceram Soc*, **75** [5] 1129–1135 (1992).

[31] J.Z. Pan, “Modelling sintering at different length scales,” *Int Mater Rev*, **48** [2] 69–85 (2003).

[32] V.N. Koparde and P.T. Cummings, “Molecular dynamics simulation of titanium dioxide nanoparticle sintering,” *J Phys Chem B*, **109** [51] 24280–24287 (2005).

[33] F.A. Nichols and W.W. Mullins, “Morphological changes of a surface of revolution due to capillary-induced surface diffusion,” *J Appl Phys*, **36** [6] 1826–& (1965).

[34] P. Bross and H.E. Exner, “Computer-simulation of sintering processes,” *Acta Metall*, **27** [6] 1013–1020 (1979).

[35] A.V. Vorst, “Numerical simulation of viscous sintering by a periodic lattice of a represenattive unit cell,” *J Am Ceram Soc*, **81** [8] 2147–2156 (1998).

[36] A.C. Cocks, “The structure of constitutive laws for the sintering of fine-grained materials,” *Acta Metall Mater*, **42** [7] 2191–2210 (1994).

[37] F. Parhami and R.M. McMeeking, “A network model for initial stage sintering,” *Mech Mater*, **27** [2] 111–124 (1998).

[38] R. Bjørk, V. Tikare, H.L. Frandsen, and N. Pryds, “The sintering behavior of close-packed spheres,” *Scr Mater*, **67** [1] 81–84 (2012).

[39] R. Bjørk, V. Tikare, H.L. Frandsen, and N. Pryds, “The effect of particle size distributions on the microstructural evolution during sintering,” *J Am Ceram Soc*, **96** [1] 103–110 (2013).

[40] R. Bjørk, H.L. Frandsen, V. Tikare, E. Olevsky, and N. Pryds, “Strain in the meso-scale kinetic Monte Carlo model for sintering,” *Comput Mater Sci*, **82** 293–297 (2014).

[41] C.L. Martin, L.C. Schneider, L. Olmos, and D. Bouvard, “Discrete element modeling of metallic powder sintering,” *Scr Mater*, **55** [5] 425–428 (2006).

[42] A. Wonisch, O. Guillon, T. Kraft, M. Moseler, H. Riedel, and J. Roedel, “Stress-induced anisotropy of sintering alumina: Discrete element modelling and experiments,” *Acta Mater*, **55** [15] 5187–5199 (2007).

[43] M.F. Ashby, “First report on sintering diagrams,” *Acta Metall*, **22** [3] 275–289 (1974).

[44] F.B. Swinkels and M.F. Ashby, “A 2nd report on sintering diagrams,” *Acta Metall*, **29** [2] 259–281 (1981).

[45] H.H. Su and D.L. Johnson, “Master sintering curve: A practical ppproach to sintering,” *J Am Ceram Soc*, **79** [12] 3211–3217 (1996).

[46] S.J. Park, P. Suri, E. Olevsky, and R.M. German, “Master sintering curve formulated from constitutive models,” *J Am Ceram Soc*, **92** [7] 1410–1413 (2009).

[47] III.H. Palmer, “Rate controlled sintering technology for PM and composites,” *Powder Met Rep*, **9** 572–579 (1988).

[48] F. Raether, P.S. Horn, and P. Schulze Horn, “Investigation of sintering mechanisms of Alumina using kinetic field and master sintering diagrams,” *J Eur Ceram Soc*, **29** [11] 2225–2234 (2009).

[49] F. Raether and M. Arefin, “Kinetic field approach to study liquid phase sintering of ZnO based ceramics,” *Ceram Int*, **36** [4] 1429–1437 (2010).

[50] D. Marc, A phenomenological approach to the prediction of material behaviors during co-sintering, *PhD Thesis*, Univ Würzbg, (2009).

[51] S. Winkler, P. Davies, and J. Janoschek, “High-temperature dilatometer with pyrometer measuring system and rate-controlled sintering capability,” *J Therm Anal*, **40** [3] 999–1008 (1993).

[52] A.R. Boccaccini and B. Hamann, “In situ High-temperature optical microscopy,” *J Mater Sci*, **34** [22] 5419–5436 (1999).

[53] F. Raether, R. Springer, and S. Beyer, “Optical dilatometry for the control of microstructure development during sintering,” *Mater Res Innov*, **4** [4] 245–250 (2001).

[54] F. Raether, A. Khmera, J. Baber, and a. Klimera, “In situ measurement and simulation of temperature and stress gradients during sintering of large ceramic components,” *Ceram Int*, **34** [2] 385–389 (2008).

[55] D. Ravi and D.J. Green, “Sintering stresses and distortion produced by density differences in bi-layer structures,” *J Eur Ceram Soc*, **26** [8] 17-25 (2006).

[56] A. Kaiser, A.S. Prasad, S.P. Foghmoes, S. Ramousse, N. Bonanos, and V. Esposito, “Sintering process optimization for multi-layer CGO membranes by in situ techniques,” *J Eur Ceram Soc*, **33** [3] 549–556 (2013).

[57] T.J. Garino and H.K. Bowen, “Kinetics of constrained-film sintering,” *J Am Ceram Soc*, **73** [2] 251–257 (1990).

[58] N. Ozkan and B.J. Briscoe, “Prediction of overall shape of sintered Alumina compacts,” *J Eur Ceram Soc*, **14** [2] 143–151 (1994).

[59] H.M. Rootare and R.G. Craig, “Characterization of compaction and sintering of hydroxyapatite powders by mercury porosimetry,” *Powder Technol*, **9** [4] 199–211 (1974).

[60] T.N. Cheng and R. Raj, “Flaw generation during constrained sintering of metal-ceramic and metal-glass multi-layer films,” *J Am Ceram Soc*, **72** [9] 1649–1655 (1989).

[61] R.Z. Zuo, E. Aulbach, R.K. Bordia, and J. Rodel, “Critical evaluation of hot forging experiments: Case study in Alumina,” *J Am Ceram Soc*, **86** [7] 1099–1105 (2003).

[62] R. Bjørk, V. Esposito, E. Lauridsen, P. Jorgensen, J. Kife, K. Andersen, S. Foghmoes, and N. Pryds, "In situ Characterization of Delamination and Crack Growth of a CGO-LSM Multi-layer Ceramic Sample Investigated by X-ray Tomographic Microscopy," *J Eur Ceram Soc*, in press (2014).

[63] D. Bernard, D. Gendron, J.M. Heintz, S. Bordere, J. Etourneau, and S. Bordere, "First direct 3D visualisation of microstructural evolutions during sintering through X-ray computed microtomoaraphy," *Acta Mater*, **53** [1] 121–128 (2005).

[64] P.S. Jørgensen, K. V Hansen, R. Larsen, and J.R. Bowen, "Geometrical characterization of interconnected phase networks in three dimensions.," *J Microsc*, **244** [1] 45–58 (2011).

[65] R.K. Bordia and R. Raj, "Sintering behavior of ceramic films constrained by a rigid substrate," *J Am Ceram Soc*, **68** [6] 287–292 (1985).

[66] C.H. Hsueh, A.G. Evans, R.M. Cannon, and R.J. Brook, "Viscoelastic stresses and sintering damage in heterogeneous powder compacts," *Acta Metall*, **34** [5] 927–936 (1986).

[67] R.K. Bordia and G.W. Scherer, "On constrained sintering .1. Constitutive model for a sintering body," *Acta Metall*, **36** [9] 2393–2397 (1988).

[68] C.H. Hsueh, "Mathematical-model of viscosity measurements for viscoelastic solids," *J Am Ceram Soc*, **69** [3] C48–C49 (1986).

[69] G.W. Scherer, "Sintering inhomogeneous glasses - Application to optical-waveguides," *J Non Cryst Solids*, **34** [2] 239–256 (1979).

[70] V.V. Skorohod, Rheological basis of the theory of sintering. *Naukova Dumka*, Kiev, 1972.

[71] M.W. Reiterer, K.G. Ewsuk, and J.G. Arguello, "An Arrhenius-type viscosity function to model sintering using the skorohod-olevsky viscous sintering model within a finite-element code," *J Am Ceram Soc*, **89** [6] 1930–1935 (2006).

[72] M.N. Rahaman, L.C. DeJonghe, G.W. Scherer, and R.J. Brook, "Creep and densification during sintering of glass powder compacts," *J Am Ceram Soc*, **70** [10] 766–774 (1987).

[73] K.R. Venkatachari and R. Raj, "Shear deformation and densification of powder compacts," *J Am Ceram Soc*, **69** [6] 499–506 (1986).

[74] A.R. Boccaccini, "Viscosity of porous sintered glasses," *J Mater Sci*, **30** [22] 5663–5666 (1995).

[75] A. Mohanram, G.L. Messing, and D.J. Green, "Densification and sintering viscosity of low-temperature co-fired ceramics," *J Am Ceram Soc*, **88** [10] 2681–2689 (2005).

[76] J.G. Arguello, M.W. Reiterer, and K.G. Ewsuk, "Verification, performance, validation, and modifications to the SOVS continuum constitutive model in a nonlinear large-deformation finite element code," *J Am Ceram Soc*, **92** [7] 1442–1449 (2009).

[77] M.N. Rahaman, L.C. DeJonghe, and C.H. Hsueh, “Creep during sintering of porous compacts,” *J Am Ceram Soc*, **69** [1] 58–60 (1986).

[78] M.Y. Chu, L.C. DeJonghe, and M.N. Rahaman, “Effect of temperature on the densification-creep viscosity during sintering,” *Acta Metall*, **37** [5] 1415–1420 (1989).

[79] R.K. Bordia and R. Raj, “Analysis of sintering of a composite with a glass or ceramic matrix,” *J Am Ceram Soc*, **69** [3] C55–C57 (1986).

[80] M.N. Rahaman, L.C. DeJonghe, and R.J. Brook, “Effect of shear-stress on sintering,” *J Am Ceram Soc*, **69** [1] 53–58 (1986).

[81] P.Z. Cai, D.J. Green, and G.L. Messing, “Constrained densification of Alumina/Zirconia hybrid laminates .1. Experimental observations of processing defects,” *J Am Ceram Soc*, **80** [8] 1929–1939 (1997).

[82] O. Gillia, C. Josserond, and D. Bouvard, “Viscosity of WC-Co compacts during sintering,” *Acta Mater*, **49** [8] 1413–1420 (2001).

[83] G.W. Scherer, “Viscous sintering under a uniaxial load,” *J Am Ceram Soc*, **69** [9] C206–C207 (1986).

[84] R.Z. Zuo, E. Aulbach, and J. Rodel, “Experimental determination of sintering stresses and sintering viscosities,” *Acta Mater*, **51** [15] 4563–4574 (2003).

[85] S.H. Lee, G.L. Messing, and D.J. Green, “Bending creep test to measure the viscosity of porous materials during sintering,” *J Am Ceram Soc*, **86** [6] 877–882 (2003).

[86] M. Cologna and V.M. Sglavo, “Vertical sintering to measure the uniaxial viscosity of thin ceramic layers,” *Acta Mater*, **58** [17] 5558–5564 (2010).

[87] A. Mohanram, S.H. Lee, G.L. Messing, and D.J. Green, “A novel use of constrained sintering to determine the viscous Poisson’s ratio of densifying materials,” *Acta Mater*, **53** [8] 2413–2418 (2005).

[88] M.-S. Jeong, J.-H. Yoo, S.-H. Rhim, S.-K. Lee, and S.-I. Oh, “A unified model for compaction and sintering behavior of powder processing,” *Finite Elem Anal Des*, **53** 56–62 (2012).

[89] G.H. Paulino and Z.-H. Jin, “Correspondence principle in viscoelastic functionally graded materials,” *J Appl Mech*, **68** [1] 129 (2001).

[90] S. Mukherjee and G.H. Paulino, “The elastic-viscoelastic correspondence principle for functionally graded materials,” *J Appl Mech Asme*, **70** [3] 359–363 (2003).

[91] H. Reidel and B. Blug, Comperhensive model for solid state sintering and its application to silcon-carbide, 84th ed. *Kluwer Academic Publishers*, Dordrecht, 2001.

[92] J. Svoboda, H. Riedel, and H. Zipse, “Equilibrium pore surfaces, sintering stresses and constitutive equations for the intermediate and late stages of sintering—I. Computation of equilibrium surfaces,” *Acta Metall Mater*, **42** [2] 435–443 (1994).

[93] H. Riedel, H. Zipse, and J. Svoboda, “Equilibrium pore surfaces, sintering stresses and constitutive equations for the intermediate and late stages of sintering—II. Diffusional densification and creep,” *Acta Metall Mater*, **42** [2] 445–452 (1994).

[94] T. Kraft and H. Riedel, “Numerical simulation of solid state sintering: Model and application,” **24** [2] 361 (2004).

[95] M.W. Reiterer and K.G. Ewsuk, “An analysis of four different approaches to predict and control sintering,” *J Am Ceram Soc*, **92** [7] 1419–1427 (2009).

[96] P.Z. Cai, D.J. Green, and G.L. Messing, “Constrained densification of Alumina/Zirconia hybrid laminates .2. Viscoelastic stress computation,” *J Am Ceram Soc*, **80** [8] 1940–1948 (1997).

[97] G.W. Scherer and T. Garino, “Viscous sintering on a rigid substrate,” *J Am Ceram Soc*, **68** [4] 216–220 (1985).

[98] P.Z. Cai, G.L. Messing, and D.J. Green, “Determination of the mechanical response of sintering compacts by cyclic loading dilatometry,” *J Am Ceram Soc*, **80** [5] 1323 (1997).

[99] R.T. Hsu and J.H. Jean, “Key factors controlling camber behavior during the cofiring of bi-layer ceramic dielectric laminates,” *J Am Ceram Soc*, **88** [9] 2429–2434 (2005).

[100] M.-J. Chiang, J.-H. Jean, and S.-C. Lin, “Effects of green density difference on camber development during the cofiring of a bi-layer glass-based dielectric laminate,” *Mater Chem Phys*, **128** [3] 413–417 (2011).

[101] D.-W. Ni, V. Esposito, C.G. Schmidt, T.T. Molla, K. Andersen, A. Kaiser, S. Ramousse, and N. Pryds, “Camber evolution and stress development of porous ceramic bi-layers during co-firing,” *J Am Ceram Soc*, **96** [3] 972–978 (2013).

[102] J. Lu, H.H. Hng, X. Song, T. Zhang, and J. Ma, “Co-sintering of a bimodal pore distribution layered structure: Constitutive models and experiments,” *J Am Ceram Soc*, **94** [5] 1528–1535 (2011).

[103] T.T. Molla, H.L. Frandsen, R. Bjørk, D.W. Ni, E. Olevsky, and N. Pryds, “Modeling kinetics of distortion in porous bi-layered structures,” *J Eur Ceram Soc*, **33** [7] 1297–1305 (2013).

[104] E. Olevsky, T.T. Molla, H.L. Frandsen, R. Bjørk, V. Esposito, D.W. Ni, A. Ilyina, and N. Pryds, “Sintering of multi-layered porous structures: Part I-Constitutive models,” *J Am Ceram Soc*, **96** [8] 2657–2665 (2013).

[105] D.W. Ni, E. Olevsky, V. Esposito, T.T. Molla, S.P. Foghmoes, R. Bjørk, H.L. Frandsen, E. Alexandrova, and N. Pryds, “Sintering of multi-layered porous structures: Part II-Experiments and model applications,” *J Am Ceram Soc*, **96** [8] 2666–2673 (2013).

[106] H. Zipse, “Finite-element simulation of die pressing and sintering of a ceramic component,” *J Eur Ceram Soc*, **17** [14] 1707–1713 (1997).

[107] M. Gasik and B.S. Zhang, “A constitutive model and FE simulation for the sintering process of powder compacts,” *Comput Mater Sci*, **18** [1] 93–101 (2000).

[108] T. Kraft, H. Riedel, and O. Rosenfelder, “Compaction and sintering of a ceramic seal: Modeling and experimental response,” *Int J Powder Metall*, **39** [6] 27–34 (2003).

[109] S. Kiani, J. Pan, J.A. Yeomans, M. Barriere, and P. Blanchart, “Finite element analysis of sintering deformation using densification data instead of a constitutive law,” *J Eur Ceram Soc*, **27** [6] 2377–2383 (2007).

[110] E.A. Olevsky, V. Tikare, T.J. Garino, and M. V Braginsky, “Simulation of sintering of layered strcutures,” *Proc World Congr Powder Metall*, 2000.

[111] A. Atkinson, J.-S. Kim, R. Rudkin, S. Taub, and X. Wang, “Stress induced by constrained sintering of 3YSZ films measured by substrate creep,” *J Am Ceram Soc*, **94** [3] 717–724 (2011).

[112] H.L. Frandsen, E. Olevsky, T.T. Molla, V. Esposito, R. Bjørk, and N. Pryds, “Modeling sintering of multi-layers under influence of gravity,” *J Am Ceram Soc*, **96** [1] 80–89 (2013).

[113] T.T. Molla, D.W. Ni, R. Bulatova, R. Bjørk, C. Bahl, N. Pryds, and H.L. Frandsen, “Finite element modeling of camber evolution during sintering of bi-layer structures,” *J Am Ceram Soc*, in press (2014).

[114] S.H. Lee, G.L. Messing, and D.J. Green, “Warpage evolution of screen printed multi-layer ceramics during co-firing,” *Key Eng Mat*, **264** [268] 321–328 (2004).

[115] R. Bredesen, K. Jordal, and A. Bolland, “High-temperature membranes in power generation with CO_2 capture,” *Chem Eng Process*, **43** [9] 1129–1158 (2004).

[116] C. Zhang, Z. Xu, X. Chang, Z. Zhang, and W. Jin, “Preparation and characterization of mixed-conducting thin tubular membrane,” *J Memb Sci*, **299** [1-2] 261–267 (2007).

[117] M. Salehi, E.M. Pfaff, R.M. Junior, C.P. Bergmann, S. Diethelm, C. Neururer, T. Graule, B. Grobéty, and F.J. Clemens, “$Ba_{0.5}Sr_{0.5}Co_{0.8}Fe_{0.2}O_{3-\delta}$(BSCF) feedstock development and optimization for thermoplastic forming of thin planar and tubular oxygen separation membranes,” *J Memb Sci*, **443** 237–245 (2013).

[118] T.T. Molla, D.K. Ramachandran, V. Esposito, D.W. Ni, F. Teocoli, E. Olevsky, R. Bjørk, N. Pryds, A. Kaiser and H.L. Frandsen, “Constrained sintering of bi-layered tubular structures,” *J Am Ceram Soc*, under review (2014).

[119] R.K. Bordia, R.Z. Zuo, O. Guillon, S.M. Salamone, and J. Rodel, “Anisotropic constitutive laws for sintering bodies,” *Acta Mater*, **54** [1] 111–118 (2006).

[120] K. Darkovich, L. Béra, and K. Shinagawa, “Particle size distribution effects in an FEM model of sintering of porous ceramics,” *Mater Sci Eng A*, **341** [1-2] 247–255 (2003).

[121] A. Jagota and C.Y. Hui, “Mechanics of sintering thin films - I. formulation and analytical results,” *Mech Mater*, **9** [2] 107–119 (1990).

[122] F. Li, J. Pan, O. Guillon, and A. Cocks, “Predicting sintering deformation of ceramic film constrained by rigid substrate using anisotropic constitutive law,” *Acta Mater*, **58** [18] 5980–5988 (2010).

[123] E.A. Olevsky, A.L. Maximenko, J.H. Arterberry, and V. Tikare, “Dimension and damage control in sintering of multi-layer powder composites,” *Model Numer Simul Mater Behav Evol*, **731** 27–32 (2002).

[124] J. Pan and R. Huang, “Multi-scale modelling of sintering,” *High-Performance Ceram V, Pts 1 2*, **368-372** 1668–1672 (2008).

[125] E.A. Olevsky, V. Tikare, and T. Garino, “Multi-scale study of sintering: A review,” *J Am Ceram Soc*, **89** [6] 1914–1922 (2006).

[126] A. Maximenko, A. Kuzmov, E. Grigoryev, and E. Olevsky, “Direct multi-Scale modeling of sintering,” *J Am Ceram Soc*, **95** [8] 2383–2388 (2012).

[127] T. Aizawa, Y. Prawoto, and F. Tsumori, “Coupled, macro-micro modeling for hot deformation and sintering,” *J Comput Appl Math*, **149** [1] 307–324 (2002).

[128] A. Kuzmov, E. Olevsky, and A. Maximenko, “Multi-scale modeling of viscous sintering,” *Model Simul Mater Sci Eng*, **16** [3] 35002 (2008).

[129] C.L. Martin, H. Camacho-Montes, L. Olmos, D. Bouvard, and R.K. Bordiaz, “Evolution of defects during sintering: Discrete element simulations,” *J Am Ceram Soc*, **92** [7] 1435–1441 (2009).

[130] T. Rasp, C. Jamin, A. Wonisch, T. Kraft, and O. Guillon, “Shape distortion and delamination during constrained sintering of ceramic stripes: Discrete element simulations and experiments,” *J Am Ceram Soc*, **95** [2] 586–592 (2012).

[131] T.T. Molla, R. Bjørk, E. Olevsky, N. Pryds, and H.L. Frandsen, “Multi-scale modeling of shape distortions during sintering of bi-layers,” *Comput Mater Sci*, **88** 28–36 (2014).

Appendices

A. PAPER-I

T.T. Molla, H.L. Frandsen, R. Bjørk, D.W. Ni, E. Olevsky and N. Pryds, “Modeling kinetics of distortions in porous bi-layered structures,” *J Eur Ceram Soc*, **33** 1297-1305 (2013)

Available online at www.sciencedirect.com

SciVerse ScienceDirect

Journal of the European Ceramic Society 33 (2013) 1297–1305

www.elsevier.com/locate/jeurceramsoc

Modeling kinetics of distortion in porous bi-layered structures

Tesfaye Tadesse Molla [a,*], Henrik Lund Frandsen [a], Rasmus Bjørk [a], De Wei Ni [a], Eugene Olevsky [b], Nini Pryds [a]

[a] *Technical University of Denmark, Department of Energy Conversion and Storage, Risø Campus, Frederiksborgvej 399, P.O. Box 49, Building 779, 4000 Roskilde, Denmark*

[b] *San Diego State University, Mechanical Engineering Department, 5500 Campanile Dr., San Diego, CA 92182-1323, USA*

Received 22 September 2012; received in revised form 12 December 2012; accepted 25 December 2012
Available online 26 January 2013

Abstract

Shape distortions during constrained sintering experiment of bi-layer porous and dense cerium gadolinium oxide (CGO) structures have been modeled. Technologies like solid oxide fuel cells require co-firing thin layers with different green densities, which often exhibit differential shrinkage because of different sintering rates of the materials resulting in undesired distortions of the component. An analytical model based on the continuum theory of sintering has been developed to describe the kinetics of densification and distortion in the sintering processes. A new approach is used to extract the material parameters controlling shape distortion through optimizing the model to experimental data of free shrinkage strains. The significant influence of weight of the sample (gravity) on the kinetics of distortion is taken in to consideration. The modeling predictions indicate good agreement with the results of sintering of a bi-layered CGO system in terms of evolutions of bow, porosities and also layer thickness.

Keywords: Modeling; Sintering; Bi-layer; Distortion

1. Introduction

Discretely graded ceramic multi-layers are considered to be promising material structures due to their performances in the development of various energy efficient electromechanical systems.[1,2] These structures are often produced by laminating different porous layers and then sintering them together (co-firing). During co-firing of multi-layers, different densification rates can cause development of stresses leading to defects like cracks and macrostructural distortions.[3–11] Asymmetric arrangement of layers usually relaxes the mismatched stress evolutions by warping and hence creating instabilities in the shape of the component. For example in the case of planar solid oxide fuel cell (SOFC) technologies, the deformations in the shape of the components/cells reduce successful stack assembly, and thus it is not desired. Therefore there is a growing interest for understanding how the intrinsic material properties can affect the evolution of distortion in order to reduce the stress development and to allow components to be produced with the desired shape after co-firing. In this study, this is studied through a combination of sintering experiments and mechanical modeling.

The introduction of continuum mechanics with linear viscous material model for porous structures can be seen as an important development in addressing the problem of shape distortions during co-firing of ceramic layers.[12,13] Since then there have been a number of reported works that deal with distortions in bi-layer ceramic systems. One of these is the work by Lu et al.[14] in which the continuum model of sintering is used to describe the kinetics of densification and curvature evolution, taking the effect of particle coarsening and grain growth into consideration. Lu et al. also considered the impact of pore size on the densification behavior of each layer into account. From beam theory, the stress and strain distributions along the section of the layers are known to be linear, but in the model by Lu et al. a uniform strain distributions are assumed over each layer, which may affect the accuracy of the model.

Detailed work on experimental observation of processing defects and the corresponding viscoelastic stress computation for constrained densification of alumina/zirconia hybrid laminates has been published by Cai et al.[3–15] After measuring the viscous properties of the constituent layers using cyclic loading dilatometry, Cai et al. were able to model the bow evolution of

* Corresponding author. Tel.: +45 2074 5931; fax: +45 4677 5858.
E-mail address: ttmo@dtu.dk (T.T. Molla).

0955-2219/$ – see front matter
http://dx.doi.org/10.1016/j.jeurceramsoc.2012.12.019

bi-layers in good agreement with experimental results. Cai et al. however did not consider the evolution of thickness of each layer during densification, which is significant in the case of highly porous layers.[8,16]

The linear distribution of strains with the corresponding evolution of thicknesses in each layer has been considered in the model suggested by Kanters et al.[1] Kanters et al. reported a good agreement of the model prediction of curvature evolution for two types of bi-layer samples made from nanocrystalline yttria-stabilized zirconia with different thicknesses.

Kang et al.[4] used the models proposed by Cai et al. and Kanters et al. to study a bi-layered system of gadolinium-doped ceria and a cermet of nickel oxide in a backbone structure of yttria stabilized zirconia. In both cases, they found a good agreement of distortion evolutions with the measurements during the sintering. In a similar way, Ollagnier et al.[8] compared the models of Cai et al. and Kanters et al. on bi-layers of porous and dense low-temperature co-fired ceramics (LTCC) with different initial thickness ratios. Unlike Kang et al., they found a significant discrepancy between the model predictions and the measurements of camber for which anisotropy of sintering parameters, effects of gravity and heating rates were suggested as a cause. Ollagnier et al. also showed the influence of ratio of initial thicknesses of the bi-layered system on the amount of camber after the sintering. The importance of gravity is also suggested by Mücke et al.[2] after their experimental observations on SOFC samples prepared from 8YSZ. Mücke et al. compared curvature evolutions of two samples sintered in vertical and horizontal positions. They observed reduction in the camber development in the case of horizontally sintered sample in which the effect of gravity is significant.[2]

Modeling the mismatch stresses and curvature of bi-layered structures with the help of experimental characterization of the viscous properties of each layer using cyclic load dilatometry has also been reported by Chiang et al.[5] and Ravi and Green.[9]

Often experimental characterizations of the viscous behavior of each layer are used to model the curvature evolution during the sintering process. This requires another set of creep experiments to independently measure the viscous behaviors of individual layers.[3–10] In most of the works reported, techniques like cyclic loading[5,9] and sinter forging[4] are usually used. Cologna et al.[17] also proposed another technique, called vertical sintering, in which the sample is allowed to sinter vertically under the influence of its own gravity. A similar way of determining the viscosity of each layer by measuring the maximum deflection rate for beams of porous materials that are allowed to deform under their own weight or under applied loads was also suggested by Atkinson et al. and Lee et al.[18,19] Alternative to these experiments, the capabilities of proven modeling approaches, like the Skorohod Olevsky Viscous Sintering (SOVS) model,[12,13] could also be used together with one sintering experiment conducted simultaneously for individual layers and asymmetric bi-layer so as to study the kinetics of densification in the free layers and shape distortions in the bi-layer system.

The effect of differential shrinkage is explained very well to be the factor controlling distortion. But as the studies by Mücke et al. and Ollagnier et al. showed the weight of the sample (gravity) also affects the rate of distortion by being an additional factor generating creep in the porous layers. Thus with all the important contributions from the works cited, it is still necessary to modify the modeling approaches so as to improve the accuracy of the predictions while maintaining them simple. The work by Frandsen et al.[16] from which the basis for the modeling approach adopted in this study, is built on a viscous analogy of classical laminate theory, where the effect of weight of the sample (gravity) on the distortion is considered.

The objective of this study is to present an alternative way of obtaining material parameters that control shape distortion from a single dilatometry experiment so as to model kinetics of densification and distortion in the bi-layer system. Improved modeling approaches are used in such a way that the effect of weight of the sample on the distortion evolution is considered to be another stress generating factor in addition to the differential shrinkage. Also the thickness evolutions in each layer are considered through the effective densification of each layer in the thickness directions. The approach is applied to obtain the kinetics of shrinkage and bow development during the sintering of porous and dense cerium gadolinium oxide, $Ce_{0.9}Gd_{0.1}O_{1.95-d}$ (CGO) layers with the help of analytical methods implemented in Matlab.

2. Cosintering model

The analysis is made based on continuum theory of sintering, which describes the macrostructural behavior of a porous body during sintering. It relates the external load to the strain rate by nonlinear viscous constitutive relationship.[12,13] The continuum model for linear relationship between the equivalent stress and strain rates is given by:

$$\sigma_{ij} = 2\eta_0 \left[\varphi\dot{\varepsilon}_{ij} + \left(\psi - \frac{1}{3}\varphi\right)\dot{e}\delta_{ij}\right] + P_L\delta_{ij} \tag{1}$$

where η_0 is the shear viscosity of the fully dense materials, φ and ψ are the normalized shear and bulk viscosities, P_L is the effective driving potential for sintering or sintering stress, δ_{ij} the Kronecker delta and $\dot{\varepsilon}_{ij}$ and $\dot{e}$ are the total and bulk strain rates respectively related to the stress tensor σ_{ij}.[12,13] The normalized shear and bulk viscosities are considered to be functions of porosity or volume fractions of voids in the porous body, θ, see Eq. (2). The effective sintering stress is the product of normalized sintering stress and local sintering stress, which is a function of surface energy per unit area, α, and grain size, G, in the form shown by Eq. (3).

$$\varphi = (1-\theta)^2;\ \psi = \frac{2}{3}\frac{(1-\theta)^3}{\theta} \tag{2}$$

$$P_L = \frac{3\alpha}{2G}(1-\theta)^2 \tag{3}$$

The porosity evolution is related to the volumetric densification strain using the principle of mass conservation as[12]:

$$\dot{e} = \frac{\dot{\theta}}{1-\theta} \tag{4}$$

The axial shrinkage rate for freely sintering sample can be found from the general model in Eq. (1) using the effective sintering stress, P_L as:

$$\dot{\varepsilon}^f = -\frac{P_L}{6\eta_0\psi} \tag{5}$$

The relationship between the stress tensor, σ_{ij}, and the viscous (creep-related) strain rate tensor, $\dot{\varepsilon}'_{ij}$, can be deduced from Eq. (1) as[12]:

$$\sigma_{ij} = 2\eta_0\left[\varphi\dot{\varepsilon}'_{ij} + \left(\psi - \frac{1}{3}\varphi\right)\dot{e}'\delta_{ij}\right] \tag{6}$$

For a detailed description of the continuum theory of sintering, especially of its microstructural assumptions, please refer the work by Olevsky.[12] Note that possible anisotropies of the sintering parameters and of the pore-grain structure are not included in this analysis.

The shear viscosities of the fully dense bodies are assumed to vary with temperature, T, in each layer according to the Arrhenius type of viscosity function, see Eq. (7), as suggested by Reiterer et al.[20] to be suitable for the SOVS model.

$$\eta_0 = AT\exp\left(\frac{Q_s}{RT}\right) \tag{7}$$

Here A is the pre-exponential constant, Q_s the apparent activation energy for the range of density in consideration irrespective of the specific transport mechanism associated with the material and R is the universal gas constant.

The simultaneous grain growth during the sintering process can be considered using a function of time, t, limited by the activation energy for grain growth, Q_g, as shown in Eq. (8).[21,28] Here n is the grain growth exponent depending on the creep or diffusion mechanism (e.g. $n=2$ for Nabarro–Herring creep and $n=3$ for Coble creep) and k_o is the pre-exponential constant.[21]

$$G^n = G_0^n + k_0\exp\left(\frac{-Q_g}{RT}\right)t \tag{8}$$

2.1. Stresses in bi-layer system

Consider a bi-layer geometry consisting of thin dense layer over thick porous layer. The stresses developed in the bi-layer system that lead to bending of the sample are assumed to be because of two phenomena occurring simultaneously during co-firing. These are (1) creep due to stresses from differential shrinkage and (2) creep induced by the sample own weight (gravity).

As shown by the schematics of a sectioned bi-layer system in Fig. 1a, the relative difference in the rate of shrinkage between a porous thick layer and dense thin layer creates the densification mismatch, which leads to an internal in-plane force, N^f, and the bending moment, M^f. For the sample geometry the stress normal to the interface is very small compared to the in-plane stresses ($\sigma_z = 0$). So the relative difference in shrinkage generates a biaxial state of sintering stress ($\sigma = \sigma_x = \sigma_y$) and a bending moment that bends the sample towards the porous layer. Considering the above assumptions in Eq. (6), the viscous or creep strain rates, $\dot{\varepsilon}'$, can be described using the biaxial stress:

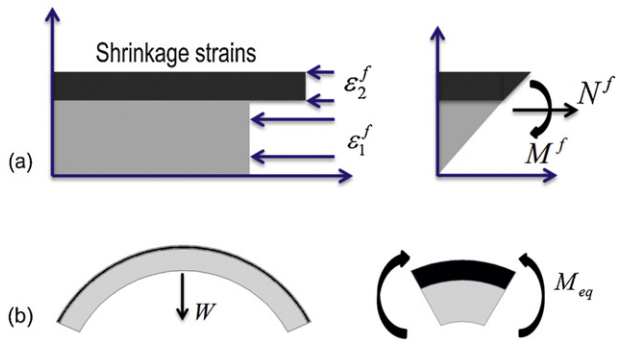

Fig. 1. Schematics showing stress in sintering of bi-layer structure (a) due to relative difference in shrinkage and (b) due to creep induced by sample own weight.

$$\dot{\varepsilon}' = \dot{\varepsilon}'_x = \dot{\varepsilon}'_y = \frac{3\psi + 2\varphi}{18\eta_0\varphi\psi}\sigma;\quad \dot{\varepsilon}'_z = -\frac{6\psi - 2\varphi}{18\eta_0\varphi\psi}\sigma \tag{9}$$

$$\sigma = E'_b\dot{\varepsilon}' \Rightarrow E'_b = \eta_0\frac{18\varphi\psi}{3\psi + 2\varphi} \tag{10}$$

This phenomenon can be considered as a creep process due to the internal sintering stress where the biaxial stress is linearly related to the viscosity of the porous body, E'_b, which is the product of viscosity of the fully dense material and a time dependent function of porosity, see Eq. (10).[16] Note that in this work, positive curvature is defined when the sample bows towards the porous layer.

Creep induced by the sample own weight, W, while it sinters is also another phenomena generating stresses in the bi-layer structure. Unlike creep due to the internal sintering stress, which deforms the structure towards the porous layer, creep due to the weight of the body will oppose the deformation (e.g. negative curvature) of a flat sintering tape. The reason for this is explained schematically in Fig. 1b. Since the width of the sample is small compared to its length, the structure can be considered as a beam with evenly distributed weight over its length. Therefore, the creep generates only a uniaxial state of stress ($\sigma = \sigma_x$) due to the equivalent bending moment, M_{eq}, which opposes the bending due to mismatch of the sample. Consideration of these assumptions into Eq. (6) gives the corresponding viscous or creep strain rates as:

$$\dot{\varepsilon}' = \dot{\varepsilon}'_x = \frac{6\psi + \varphi}{18\eta_0\varphi\psi}\sigma;\quad \dot{\varepsilon}'_y = \dot{\varepsilon}'_z = -\frac{3\psi - \varphi}{18\eta_0\varphi\psi}\sigma \tag{11}$$

$$\sigma = E'_u\dot{\varepsilon}' \Rightarrow E'_u = \eta_0\frac{18\varphi\psi}{6\psi + \varphi} \tag{12}$$

Here also the uniaxial stress is considered to be linearly proportional to other viscosity of the porous body, E'_u, which is again the product of viscosity of the fully dense material and another function of porosity, see Eq. (12).[16]

2.2. Kinetics of shrinkage and distortion in the bi-layer

In the present work, linear distribution of the constrained strain rate across the section of each layer is assumed. This will represent the reality better than the uniform strain rate. The viscous analogy of classical laminate theory has been used with the evolving curvature rate, $\dot{\kappa}$, and longitudinal strain rate, $\dot{\varepsilon}_0$, to describe the linear strain rate distribution, $\dot{\varepsilon}$, across the thickness. This is shown in Eq. (13) with z representing the vertical coordinate of a point in the layer.

$$\dot{\varepsilon} = \dot{\varepsilon}_0 + \dot{\kappa} z \tag{13}$$

The corresponding distribution of stress is also linear with the generalized material viscosity, E', which depends on the evolving viscosity of the porous body, see Eqs. (10) and (12), and the difference between the constrained, $\dot{\varepsilon}$, and free or unconstrained shrinkage rates, $\dot{\varepsilon}^f$.[16]

$$\sigma = E'\dot{\varepsilon}' = E'(\dot{\varepsilon} - \dot{\varepsilon}^f) = E'(\dot{\varepsilon}_0 + \dot{\kappa} z - \dot{\varepsilon}^f) \tag{14}$$

$$E' = \begin{cases} E'_b \text{ for biaxial stress} \\ E'_u \text{ for uniaxial stress} \end{cases} \tag{15}$$

The free shrinkage rates are calculated using Eq. (5) and the longitudinal strain rates, $\dot{\varepsilon}_0$, and the curvature rate, $\dot{\kappa}$, can be evaluated applying the equilibrium condition with the viscous analogy of classical laminate theory corresponding to the stresses and the bending moments in both layers as[16]:

$$\int_{\text{both layers}} \sigma dz = 0 \tag{16}$$

$$\int_{\text{both layers}} \sigma z dz = 0 \tag{17}$$

Therefore the constrained strain rate, $\dot{\varepsilon}$, can be obtained with the help of Eq. (13) for the coordinate point defined by z. The evolving porosity, θ, and the thickness, h, of each layer in the bi-layer are also updated through time considering the total stress states in each layer during the co-firing.

The lateral contraction ratios, ν', can be derived considering the viscous strains for each of the layers as shown in Eqs. (9) and (11). These parameters are related to porosity using the normalized shear and bulk viscosities for each stress conditions as shown by Eq. (18).

$$\nu' = -\frac{\dot{\varepsilon}'_z}{\dot{\varepsilon}'_x} = \begin{cases} \dfrac{6\psi - 2\varphi}{3\psi + 2\varphi} \text{ for biaxial stress} \\ \dfrac{3\psi - \varphi}{6\psi + \varphi} \text{ for uniaxial stress} \end{cases} \tag{18}$$

Thus in the SOVS model the lateral contraction ratios are independent of the material and only depend on the porosity of the body. This is an assumption built into the SOVS framework, and in general these parameters are difficult to measure as the lateral strain rate is small compared to other strain rate components, i.e. the longitudinal strain rate and sintering strain rates.

The above approaches can be used to solve two parallel problems simultaneously accounting for the biaxial stresses due to differential shrinkage and the uniaxial stresses induced by sample's own weight (gravity). The curvature evolution due to the weight of the sample could be approximated by assuming a constant equivalent bending moment, M_{eq}.[16] The total curvature rate is then calculated simulating the simultaneous effects in the same co-ordinate system. Further theoretical details and derivations of the model described above can be found in Frandsen et al.[16]

All the information for shrinkages and curvature development can be integrated through time according to the sintering profile used in the experiment if the viscosities of both layers at fully dense state, i.e. η_{01} *and* η_{02}, and the grain growth kinetics in each layer, G_1 *and* G_2, are known.

2.3. Obtaining the constitutive parameters

In this work, an alternative approach to experimentations has been employed to find the viscous material parameters required for modeling the shrinkage and curvature development observed during the entire sintering process. This is achieved through first modeling the free shrinkage behaviors of individual layers during the sintering process. The free densification strain rate, $\dot{\varepsilon}^f$, can be described explicitly by combining Eqs. (2), (3) and (5) with the fully dense body viscosity given by Eq. (7).

$$\dot{\varepsilon}^f = -\frac{3}{8}\frac{\alpha}{AGT}\exp\left(\frac{-Q_s}{RT}\right)\left(\frac{\theta}{1-\theta}\right) \tag{19}$$

The surface energy per unit area in each layer can be estimated which is often in order of 1 J/m^2 for most ceramic oxides.[1,28] Consider a co-firing process with a temperature profile that constitutes an iso-rate followed by isothermal stages. The grain sizes at the onset of the iso-rate sintering, i.e. G_{01} *and* G_{02}, and those at the onset of isothermal temperature, e.g. G'_1 and G'_2, could be used to estimate the grain growth pre-exponential factors, k_{01} and k_{02}, see Eq. (8), if the activation energies for grain growth are known. This would help to approximate the grain growth kinetics in the two layers during the entire sintering process as per the sintering temperature profile.

The model predictions for free shrinkage strain rate, $\dot{\varepsilon}^f$, in each layer can be optimized with the respective experimental data. This can be done by starting the model simulations with realistic guesses of the four unknown parameters of the two layers, i.e. A_1, A_2 and Q_{s1}, Q_{s2}. The unknown parameters can then be identified as those providing the minimum deviation as per Eq. (20) between the experimental data and model simulation.

$$\Delta = \left\{ \sum_{i=1}^{N} \left[\left(\frac{\varepsilon_1^{f,Sim} - \varepsilon_1^{f,Exp}}{mean(\varepsilon_1^{f,Exp})} \right)^2 + \left(\frac{\varepsilon_2^{f,Sim} - \varepsilon_2^{f,Exp}}{mean(\varepsilon_2^{f,Exp})} \right)^2 \right] \right\}^{1/2} \tag{20}$$

where ε^f is free shrinkage strain in the individual layers and the sum is taken over all N data points in time. A similar methodology has been used by Garino and Bowen[22] to estimate the constrained shrinkage of glass powders using free shrinkage measurement data and the viscous flow sintering model suggested by Scherer.[23] Therefore the approach adopted here could be used to approximate the temperature dependent

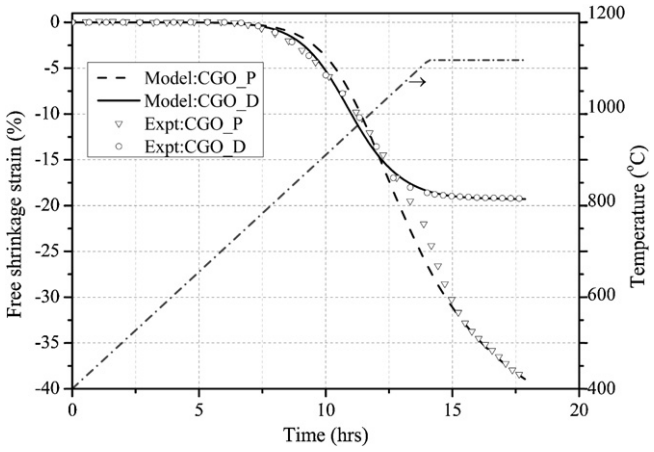

Fig. 2. Comparison of the model to the experimental data for free shrinkage strains.

viscous behaviors of fully dense bodies as per the Arrhenius type of viscosity function given in Eq. (7) without the need for other creep experiments.

3. Model verification and discussion

In this study, the experimental data reported by De et al.[24] on tapes made from CGO (Rhodia S.A., France) with a specific surface area of 6.6 m^2/g (d50 particle size 0.2 μm) are used for validating the presented modeling approach. De et al. fabricated samples that consisted of two layers of CGO tape-casted on top of each other. One of the layers contained a significant amount of pre-calcined powder and graphite powder (V-UF1 99.9, Graphit Kropfmühl, Germany) as a pore former and will be referred to as CGO_P. The other layer has a higher relative density and will be referred to as CGO_D. At the beginning of the sintering, the relative density and initial thickness of the porous layer was 23 vol.% and 380 μm, respectively. The corresponding dense layer was 56 vol.% dense and 27 μm thick initially. The dense and porous tapes of length 24.5 mm and width 5.1 mm were laminated. The samples were subsequently co-fired in a furnace with a temperature–time profile, which consists of iso-rate firing with 0.83 °C/min from 400 °C to 1100 °C followed by an isothermal sintering at 1100 °C for 4 h. Individual samples of each layer were also sintered in the same furnace in order to observe the free shrinkage of each layer. The evolutions of curvature in the bi-layer sample and shrinkage of the free samples were recorded in situ using a high temperature furnace equipped with an optical dilatometer (Fraunhofer-Institute Silicateforschung, Germany). SEM micrographs taken by De et al. are also used in this study.

From the sintering experiment considered in this study, the optimization procedure is applied on the two freely sintered samples to estimate the viscous behaviors of the layers based on the pre-exponential factors, i.e. A_1 and A_2, and the apparent activation energies, Q_{s1} and Q_{s2}. The free shrinkage strains as a function of time for CGO_P and CGO_D layers are shown in Fig. 2. The porous layer, CGO_P shows a faster and larger densification (close to 40%) than the dense layer, CGO_D, which shows less than 20% of shrinkage.

Table 1
Parameters defining the viscous behaviors of the layers.

	A (Pa s)	Q_s (kJ/mol)
CGO_P	0.71 ± 0.153	196 ± 4
CGO_D	0.03 ± 0.005	208 ± 3

Based on the optimization procedure applied on the free samples, Fig. 2 again shows comparison between results of the model and experimental data for free shrinkage strains. Shrinkage in the dense layer is also observed to bypass the shrinkage in the porous layer for a short time range in the sintering process. The model results are in good agreement with experimental free sintering strain data both for the CGO_P and CGO_D layers.

The parameters defining the viscous behaviors of each layer extracted from the optimization approach followed in this study are shown in Table 1. Theoretically, the porous as well as dense layers should have equal values of apparent activation energy, as they are same materials (CGO). But practically there might be differences due to the fact that both layers were prepared with different additions. The other reason for higher apparent activation energy in the case of CGO_D can be due to larger contribution of coarsening to microstructural changes at higher sintered densities.[21] The influence of grain growth on the viscosity of the fully dense body is not explicitly considered in this work instead both parameters, A and Q_s, are made free in the fitting for each layer. This is made to lump the influence of grain growth into the viscosity function, $\eta_0(T)$. The above assumption of the viscosity function is also consistent with the work reported by Reiterer et al. Note that no attempt has been made to link the Q_s in Table 1 to a specific material diffusion mechanism in CGO as suggested by Reiterer et al. Instead they are referred to be the apparent activation energy for the entire densification ranges observed in each layer.

The evolutions of uniaxial viscosities of the porous CGO_P and CGO_D as a function of temperature estimated after the respective viscous parameters were found are shown in Fig. 3. The porous layer is shown to have lower uniaxial viscosity

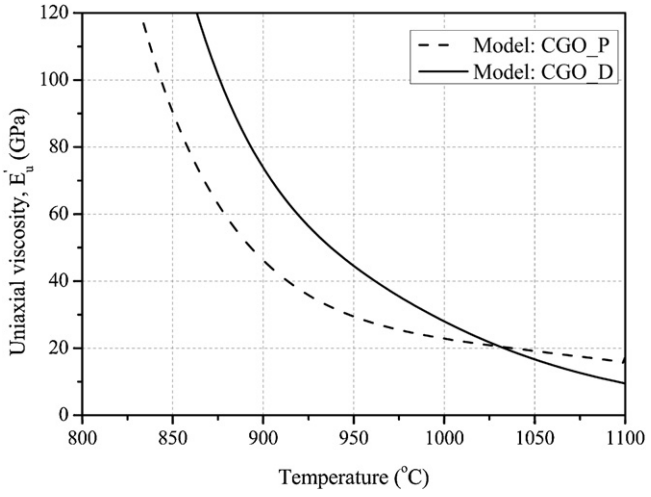

Fig. 3. Evolution of viscosity of the porous body of each layer, E'_u, during the iso-rate sintering.

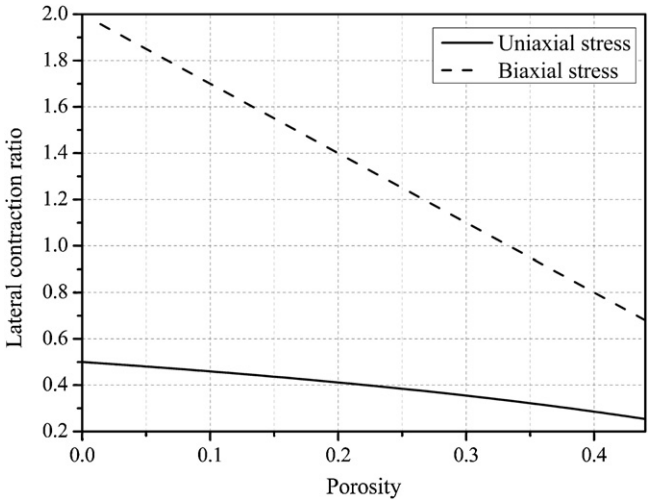

Fig. 4. Evolution of the lateral contraction ratios as a function of porosity.

compared to the dense one at low temperatures and evolves to be higher than the dense layer at higher temperatures. This is consistent with the high rate of densification observed in the porous layer towards higher temperatures. In addition, the trend in the evolution of the viscosities are also consistent with the results reported by Reiterer et al. for ZnO showing the influence of temperature at the beginning and the evolving density at higher temperatures. Note that although the two layers are prepared from the same material (CGO), it is believed that the different additives to the CGO_P affected the pore-grain interaction and hence the viscous behavior.

The contraction ratios are calculated using the porosity evolutions of each layer in the bilayer system and are shown in Fig. 4 for uniaxial as well as biaxial stress conditions. Note that the contraction ratio in the biaxial stress condition has nothing to do with Poisson's ratio as the later is defined for particular case in viscous problems i.e. for uniaxial relaxation experiments.[25] The CGO_P layer is very porous in the beginning of the sintering, and the lateral contraction ratios in Eq. (18) attain unrealistic low values. Therefore minimum value of 0.1 has been imposed. This has no significant influence on the results.

As mentioned earlier, creep experiments of single layered specimens could also have been used to obtain these material parameters. This approach would lead to greater certainty on the viscosity of the individual layer. It would however also require more extensive experimental work, as initial sintering of each layer must be done separately before performing the creep experiments. In a continuous development of new ceramic multi-layers the approach used here might be advantageous due to its simplicity.

While modeling the kinetics of shrinkage and distortion in the bi-layer system, the linear strain distributions across each layer are implemented through the viscous analogy of classical laminate theory which requires a perfect bonding between the bi-layers. This is confirmed by the SEM image observations of a section of the bi-layer at the end of isothermal sintering, see Fig. 5a. There were no sintering defects such as cracks or delamination in the interface of the CGO_P and CGO_D layers and this was found to be consistent with the studies by Jean et al.[26]

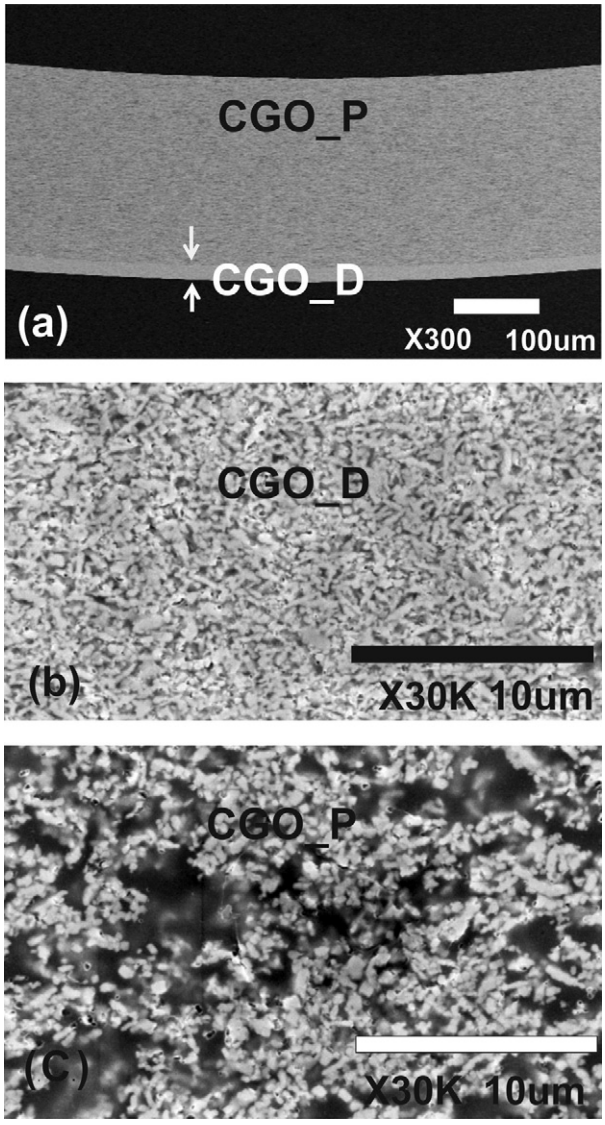

Fig. 5. Cross sectional SEM images of the microstructures: (a) CGO_D and CGO_P with no defects, (b) CGO_D at 875 °C after 2 h and (c) CGO_P at 875 °C after 2 h.

Cross sectional images of the dense and porous layers at 875 °C after 2 h of holding followed by quenching are also shown in Fig. 5b and c. The difference in the porosity can clearly be seen.

Using the estimated evolutions of viscosity and grain size throughout the entire (iso – rate and isothermal) sintering, densifications and the distortion development in the bi-layer system are modeled for the prescribed temperature profile used in the experiment. The initial porosities in the bi-layer at the onset of the sintering process are assumed to be comparable to the free samples as there were no prior sintering activities. Table 2 shows the different parameters used in the modeling of the entire sintering process.

The experimental measurements of shape distortion of the CGO_P/CGO_D bi-layer is shown in Fig. 6 in terms of bow, u, which is related to curvature, κ, through the length of the sample. It is observed that initially the bow bends towards the dense layer before turning to the porous layer. The effect of

Table 2
Material parameters used to model densification and distortion in the bi-layer system.

Parameter	CGO_P	CGO_D	Source
Surface energy per unit area (J/m^2)	1	1	Estimated
Activation energy for grain growth (kJ/mol)	413	430	[27]
Initial mean grain size, G_0 (μm)	0.3	0.25	[24]
Mean grain size at the holding temperature (μm)	1.0	1.25	Estimated
Initial mean porosity level (%)	77	44	[24]
Initial thickness (μm)	380	27	[24]
Grain growth pre-exponential factors (m^3/s)	1.0×10^{-7}	1.1×10^{-6}	Fitted

gravity is also observed to be significant during the last hours of sintering mainly in the isothermal regime where a decrease in the bow is clearly observed. This observation is also consistent with those seen by Ollagnier et al.[8]

The free sintering samples, especially the porous layer, are however shrinking throughout the experiment as seen in Fig. 2. Thus, if not for the gravity, the bow should increase throughout the experiment as well. The reason for the reduction of the bow in the final hours is that the sintering rate of the layers decreases, see Fig. 2, but the effect of gravity remains constant. Thus, at the same point the bow rate due to sintering decreases to be below the oppositely directed bow rate of gravity and hence the overall bow decreases.

The model prediction for the distortion evolution shows a good agreement with experimental observation as shown in Fig. 6. The model captured the development of the bow towards the dense layer due to the initial faster shrinkage observed in the CGO_D before it is reversed to the porous layer. The availability of pre-calcined powders in the porous layer can make the average initial grain size in the CGO_P larger than CGO_D

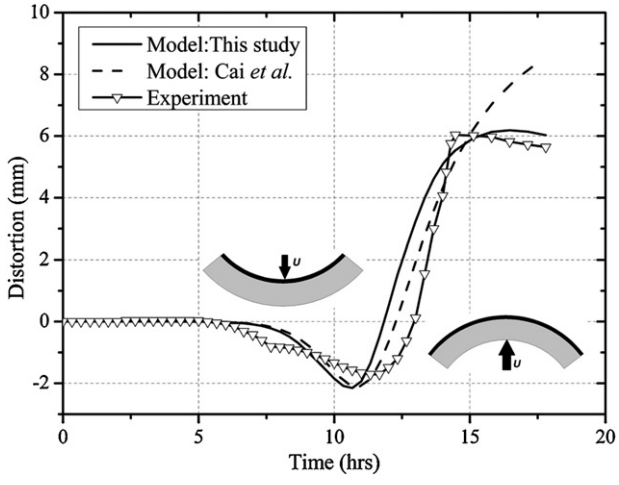

Fig. 6. Comparison of the model to the experimental data for distortion (u) during the entire sintering.

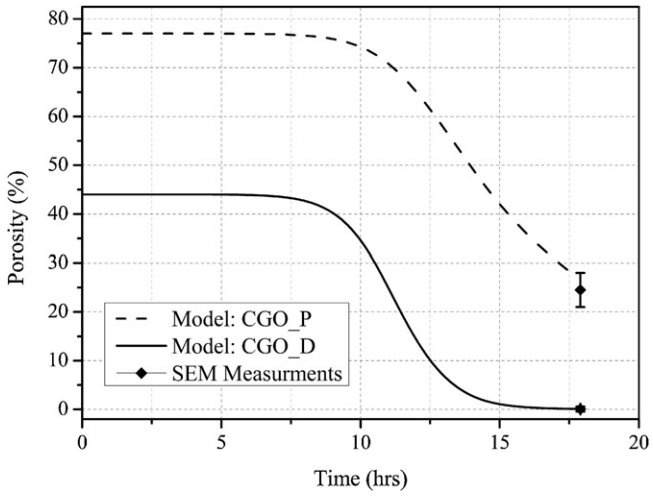

Fig. 7. Model predictions for porosity evolutions throughout the sintering process and experimental measurements at the end of the sintering.

slowing densification in the porous layer initially. This is followed by an initial curvature increase towards the dense layer. Shortly after, however, the high amount of porosity and slower grain growth in the porous layer allows faster densification in the CGO_P followed by curvature increase towards the porous layer.

The model is also able to indicate the decreasing trend of the evolution of bow in the final hours of the sintering due to gravity. For the sake of comparison, the modeling approach reported by Cai et al. is also implemented parallel to the approach followed in this study, see Fig. 6. It is clear to see the significance of considering weight of the sample or gravity especially in the last hours of the sintering experiment which is mainly in the isothermal regime. The influence of gravity in the iso-rate sintering is very small as the comparison reflects a similar evolution of bow due to higher sintering activities in both layers. The observed discrepancies between the model and experimental results in Fig. 6 are believed to be caused by friction between the sample support surface and of the sample edges while it deforms. Possible anisotropies of densifications from the tape casting might also be an explanation.

Apart from predicting the shape distortion, the model predictions of the final porosities are also in good agreement with the results measured from the SEM studies, see Fig. 7. As is expected, the porosity of the CGO_P layer shows a fast and large reduction compared with the reduction of the dense layer, CGO_D. Note that the model predicts only the average value as a function of time in each layer as the porosity variation across the thickness of the layer is beyond the scope of this study. The impact of constraint stress on the evolution of porosity in each layer has also been studied. Fig. 8 shows the ratio of porosity evolutions in the constrained and free samples as a function of time. The effect of constraint related stress on the CGO_P is shown to be minor and the porosity evolution in the CGO_P is almost unaffected. This is due to the magnitude of the constraint stress which is not large enough to affect the porosity evolution. These results are consistent with the observations reported by Frandsen et al.[16] However, there is a significant retardation of

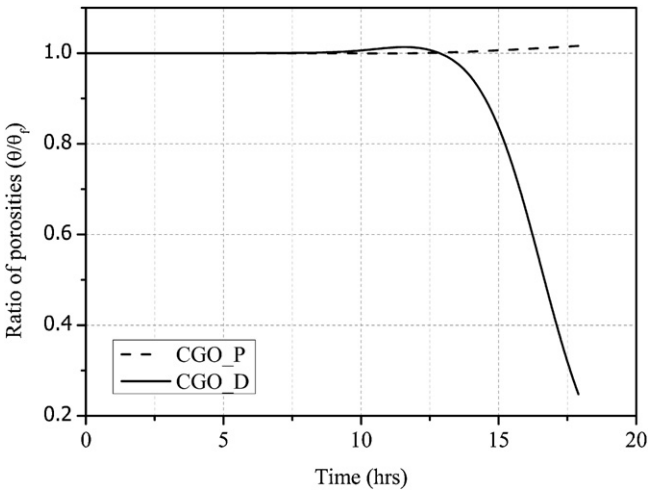

Fig. 8. Ratio of porosities in the constrained and free samples during the entire sintering cycle.

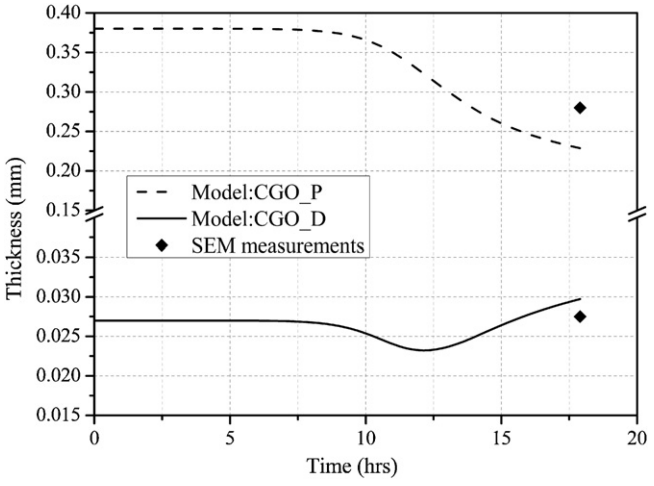

Fig. 9. Model predictions for thickness evolutions throughout the sintering process and experimental measurements at the end of the sintering.

porosity evolution in the thin CGO_D layer due to the constraint from the highly shrinking thick CGO_P layer as observed in the final hours of the sintering cycle.

The large reduction of thickness for CGO_P layer and almost no reduction in thickness for the CGO_D layer are also predicted by the model. The final thickness results predicted by the model agree with the experimental data as shown in Fig. 9. In the case of CGO_D a reduction of the thickness followed by thickening of the layer is predicted by the model in the final stage of the sintering. The thickening of the layer is found to be difficult to verify using the SEM images due to the small thickness changes (in order of 1 μm). However, this can be because of the compressive stress on the already dense CGO_D layer due to the bending moment induced by the weight of the sample in the final stage of the sintering.

4. Conclusions

Experimentally observed behaviors of shrinkage and bow development during sintering of bi-layer sample of porous and dense cerium gadolinium oxide (CGO) layers were studied. With the help of the new method proposed, data collected from one optical dilatometry experiment conducted simultaneously for individual layers and asymmetric bi-layer porous structure was sufficient to model kinetics of densification and shape distortion.

The viscous parameters, i.e. the pre-exponential factors and the apparent activation energies in the Arrhenius-type viscosity function were first determined as those providing the least deviation between the free shrinkage strains recorded in the experiment and those obtained by the model.

During the experiment, the bi-layer system is observed to have a reversal of the shape around half of the sintering time and reduction in the bow mainly in the isothermal sintering. The first one is believed to be because of an initial faster shrinkage in the dense layer due to the various additives. The reason for the later reduction in the camber growth was deducted to be due to weight of the sample or gravity, because the free sintering samples are observed to sinter throughout the experiment. However the influence of gravity is shown to be minimal in the iso-rate sintering stage as there are high amount of sintering activity in the porous thick layer.

The model is able to capture all the important phenomenon of shape changes observed during the experiment. The significant evolution of layer thickness in the porous thick layer could also justify the need to consider it in the modeling of curvature together with the corresponding linear distribution of strain across the thickness.

Acknowledgments

The authors would like to acknowledge the support of the Danish Council for Independent Research Technology and Production Sciences (FTP) which is part of The Danish Agency for Science, Technology and Innovation (FI) (Project # 09-072888) and the US National Aeronautics and Space Administration, Materials Science Program (NNX10AV38G).

References

1. Kanters J, Eisele U, Rodel J. Cosintering simulation and experimentation: case study of nanocrystalline zirconia. *J Am Ceram Soc* 2001;**84**:2757–63.
2. Muecke R, Menzler H, Buchkremer P, Stoever D. Cofiring of thin zirconia films during SOFC manufacturing. *J Am Ceram Soc* 2009;**92**:S95–102.
3. Cai Z, Green J, Messing L. Constrained densification of alumina/zirconia hybrid laminates. 1. Experimental observations of processing defects. *J Am Ceram Soc* 1997;**80**:1929–39.
4. Chang J, Guillon O, Roedel J, Kang SL. Characterization of warpage behaviour of Gd-doped ceria/NiO-yttria stabilized zirconia bi-layer samples for solid oxide fuel cell application. *J Power Sources* 2008;**185**:759–64.
5. Chiang M, Jean J, Lin S. Effects of green density difference on camber development during the cofiring of a bi-layer glass-based dielectric laminate. *Mater Chem Phys* 2011;**128**:413–7.
6. Green D, Guillon O, Roedel I. Constrained sintering: a delicate balance of scales. *J Eur Ceram Soc* 2008;**28**:1451–66.
7. Lu G, Sutterlin R, Gupta T. Effect of mismatched sintering kinetics on camber in a low-temperature cofired ceramic package. *J Am Ceram Soc* 1993;**76**:1907–14.
8. Ollagnier J, Guillon O, Roedel J. Constrained sintering of a glass ceramic composite: I. Asymmetric laminate. *J Am Ceram Soc* 2010;**93**:74–81.

9. Ravi D, Green D. Sintering stresses and distortion produced by density differences in bi-layer structures. *J Eur Ceram Soc* 2006;**26**:17–25.
10. Schoenberg E, Green J, Segall E, Messing L, Grader S, Halleck M. Stresses and distortion due to green density gradients during densification. *J Am Ceram Soc* 2006;**89**:3027–33.
11. Tzeng S, Jean J. Stress development during constrained sintering of alumina/glass/alumina sandwich structure. *J Am Ceram Soc* 2002;**85**:335–40.
12. Olevsky E. Theory of sintering: from discrete to continuum. *Mater Sci Eng R: Reports* 1998;**23**:41–100.
13. Olevsky E, Tikare V, Garino T. Multi-scale study of sintering: a review. *J Am Ceram Soc* 2006;**89**:1914–22.
14. Lu J, Hng H, Song X, Zhang T, Ma J. Cosintering of a bimodal pore distribution layered structure: constitutive models and experiments. *J Am Ceram Soc* 2011;**94**:1528–35.
15. Cai P, Green D, Messing G. Constrained densification of alumina/zirconia hybrid laminates. 2. Viscoelastic stress computation. *J Am Ceram Soc* 1997;**80**:1940–8.
16. Frandsen H, Olevsky E, Molla T, Esposito V, Bjørk R, Pryds N. Modeling sintering of multi-layers under the influence of gravity. *J Am Ceram Soc* 2013;**96**(1):80–9.
17. Cologna M, Sglavo V. Vertical sintering to measure the uniaxial viscosity of thin ceramic layers. *Acta Mater* 2010;**58**:5558–64.
18. Atkinson A, Kim J, Rudkin R, Taub S, Wang X. Stress induced by constrained sintering of 3YSZ films measured by substrate creep. *J Am Ceram Soc* 2011;**94**:717–24.
19. Lee S, Messing G, Green D. Bending creep test to measure the viscosity of porous materials during sintering. *J Am Ceram Soc* 2003;**86**:877–82.
20. Reiterer M, Ewsuk K, Arguello J. An Arrhenius-type viscosity function to model sintering using the skorohod–olevsky viscous sintering model within a finite-element code. *J Am Ceram Soc* 2006;**89**:1930–5.
21. Raether F, Horn P. Investigation of sintering mechanisms of alumina using kinetic field and master sintering diagrams. *J Eur Ceram Soc* 2009;**29**:2225–34.
22. Garino T, Bowen H. Kinetics of constrained-film sintering. *J Am Ceram Soc* 1990;**73**:251–7.
23. Scherer G, Brinker C, Roth E. Sol–gel–glass: viscous sintering. *J Non Cryst Solids* 1985;**72**:369–89.
24. De N., Olevsky E., Esposito V., Molla T., Bjørk R, Pryds N. Sintering of bi-layered porous structures: Part II experiments and model applications. J Am Ceram Soc; submitted for publication.
25. Tschoegl W, Knauss G, Emeri I. Poisson's ratio in linear viscoelasticity: a critical review. *Mech Time—Depend Mater* 2002;**6**:3–51.
26. Hsu R, Jean J. Key factors controlling camber behavior during the cofiring of bi-layer ceramic dielectric laminates. *J Am Ceram Soc* 2005;**88**:2429–34.
27. De Ni, Schmidt C, Teocoli F, Kaiser A, Andersen K, Ramousse S, Esposito V. Densification and grain growth during sintering of porous $Ce_{0.9}Gd_{0.1}O_{1.95}$ tape cast layers: a comprehensive study on heuristic methods, J Eur Ceram Soc, Submitted for publication.
28. Rahaman M. *Sintering of ceramics*. 1st ed. Boca Raton,Florida: CRC Press, Taylor & Francis Group; 2008.

B. PAPER-II

E. Olevsky, T.T. Molla, H.L. Frandsen, R. Bjørk, V. Esposito, D.W. Ni, A. Ilyna and N. Pryds, "Sintering of multi-layered porous structures: Part I-Constitutive models," *J Am Ceram Soc*, **96** [8] 2657–2665 (2013)

journal

J. Am. Ceram. Soc., 96 [8] 2657–2665 (2013)
DOI: 10.1111/jace.12375

Sintering of Multilayered Porous Structures: Part I-Constitutive Models

Eugene Olevsky,[§,¶,†] Tesfaye Tadesse Molla,[‡] Henrik Lund Frandsen,[‡] Rasmus Bjørk,[‡] Vincenzo Esposito,[‡] De Wei Ni,[‡] Aleksandra Ilyina,[¶] and Nini Pryds[‡]

[‡]Department of Energy Conversion and Storage, Technical University of Denmark, Frederiksborgvej 399, P.O. Box 49, DK-4000 Roskilde, Denmark

[§]Mechanical Engineering Department, San Diego State University, 5500 Campanile Dr., San Diego, California 92182-1323

[¶]Key Laboratory for Electromagnetic Field Assisted Processing of Novel Materials, Moscow Engineering Physics Institute, Moscow 115409, Russia

Theoretical analyses of shrinkage and distortion kinetics during sintering of bilayered porous structures are carried out. The developed modeling framework is based on the continuum theory of sintering; it enables the direct assessment of the cofiring process outcomes and of the impact of process controlling parameters. The derived "master sintering curve"-type solutions are capable of describing and optimizing the generic sintering shrinkage and distortion kinetics for various material systems. The approach utilizes the material-specific parameters, which define the relative kinetics of layer shrinkages such as the relative intensity of sintering, and employs the conversion between real and specific times of sintering. A novel methodology is also developed for the determination of the ratio of the shear viscosities of the layer's fully dense materials. This new technique enables the determination of all input parameters necessary for modeling sintering of bilayers using experimental techniques similar to optical dilatometry applied to each individual layer and to a symmetric trilayered porous structure based on the two-layer materials utilized in the bilayered system. Examples of sintering different porous bilayered systems are presented to justify the capability of the model in predicting and optimizing sintering kinetics.

I. Introduction

In accordance with the ISI Web of Science™, the total number of refereed publications related directly or indirectly to sintering of multilayered composite structures exceeded 1,500 in 2012. The interest toward this area is driven in particular by the growing demands of understanding of the cofiring process outcomes when sintering laminated ceramic tapes employed in fuel cell components[1–5] and in multilayered elements of electronic circuitry fabricated by LTCC technology (Low-Temperature Co-Fired Ceramics).[6–14]

Apparently, the first theoretical analysis of the stress development during sintering of laminated composites has been conducted by Cheng and Raj[15] in the end of 1980s. One of the first studies of the constrained shrinkage kinetics in cofired LTCC films has been carried out by Lu *et al.*[16] This work assumed that the in-plane strain rates are negligible compared with the strain rates of free sintering, which allowed a significant simplification of model equations. The analysis of sintering-enabled distortions of bilayered laminated component shapes as well as of stress distribution within the individual layers has been introduced in the end of 1990s by Cai *et al.*,[6–8] who pioneered the cyclic dilatometry approach for the determination of the constitutive properties (viscosity and sintering stress) of layer materials. The modeling framework developed by Cai *et al.*,[6–8] however, did not take into account the impact of the differential shrinkage on the sintering kinetics in the individual layers. Similar approach has been utilized by Jean and Chang.[17–19] In the course of 2000s, Olevsky *et al.*,[20–22] Rödel *et al.*,[2,9,23–25] and Molla *et al.*,[26] developed models of cosintering of bilayered structures which enabled coupled analysis of densification and of stress buildup in two-layer porous systems. These studies were based on the conceptual framework of the constrained linear-viscous sintering constitutive behavior described in the publications of Bordia and Scherer,[27] Olevsky and Skorohod,[28] and others. This modeling approach allows the direct application of the solutions obtained in the context of linear elastic behavior of laminated composites to the analysis of the cosintering process in multilayered structures.

The respective problems of the deformation of multilayered laminated composites have been considered by many authors starting from the fundamental work of Stoney[30] published in the beginning of 20th century. Stoney's famous equation describes residual stresses developed in a bilayer structure, i.e., of a thin film deposited on a substrate. It is suitable only for small deposit-to-substrate thickness ratios. More general relationships describing curvature and stresses of a distorted bilayered structure have been introduced by Timoshenko in 1925.[31] Timoshenko's approach assumes small aspect ratios of the bilayered objects, therefore, in case of composites with comparable length/width-to-thickness ratios, the respective equations have to be modified.[27] Timoshenko's equations have been utilized in a number of publications directly or in adjusted forms for the derivation of the bending curvature rate and stresses developed during sintering of bilayered composites.[1,2,7,10–12]

The solutions of the thermoelastic problems of the deformation of bi- and multilayered structures have been further developed toward various applications in the area of sensors and actuators.[27–29] Many of the publications in this field include useful relationships that can be employed for the analysis of linear-viscous sintering problems.

Schoenberg *et al.*[12] introduced a finite-element solution of the problem of sintering of bilayered powder specimens, and Olevsky *et al.*[13] developed a multiscale sintering modeling framework in which the evolution of the pore-grain structure was simulated at the mesoscale using a kinetic Monte Carlo model[32–34] and provided the values of the sintering constitutive parameters utilized in the finite-element solutions of the problems of bilayered porous structure sintering.

Most of the published to date works on the sintering of multilayered structures have been concentrated on the

R. Bordia—contributing editor

Manuscript No. 32472. Received December 14, 2012; approved April 10, 2013.
[†]Author to whom correspondence should be addressed. e-mail: eolevsky@mail.sdsu.edu

analysis of the overall structure distortion (curvature radius) and on the assessment of the stresses developed in cosintered composites. However, the current industrial practice (in particular, in the areas of fuel cell components, gas purification devices, etc.) demands the development of cofired multilayered structures with controlled levels of porosity in the individual layers. In this connection, the present work is focused on the explicit description of the shrinkage kinetics of the individual layers fully coupled with their distortions and stress evolution. Along with this, we describe a detailed methodology allowing the direct application of sintering models for the description of cofiring of bilayered structures. This methodology enables semianalytical engineering level solutions which do not require the usage of comprehensive finite-element codes.† Such approach renders the possibility of the direct assessment of the cofiring process outcomes and of the impact of process controlling parameters. Due to the normalized form of the derived equations, the developed modeling framework provides "master sintering curve" type of solutions which are capable of describing the generic shrinkage and distortion kinetics for various material systems. Part 2 of this work[35] presents the application of the method to model the kinetics of shrinkage and distortion in an experiment on sintering a bilayer cerium gadolinium oxide.

II. General Model Basis

The linear-viscous version of the continuum (in general, nonlinear) theory of sintering[28] is provided by the following constitutive relationship:

$$\sigma_{ij} = 2\eta_0\left[\varphi\dot{\varepsilon}_{ij} + \left(\psi - \frac{1}{3}\varphi\right)\dot{e}\delta_{ij}\right] + P_L\delta_{ij} \tag{1}$$

where σ_{ij} is a stress tensor's component, $\dot{\varepsilon}_{ij}$ is a strain rate tensor's component, η_0 is the shear viscosity of a fully dense material, φ and ψ are the normalized shear and bulk viscosities, δ_{ij} is the Kronecker symbol ($\delta_{ij} = 1$ if $i = j$ and $\delta_{ij} = 0$ if $i \neq j$), $\dot{e}$ is the first invariant of the strain rate tensor, i.e., sum of tensor diagonal components: $\dot{e} = \dot{\varepsilon}_{ii} = \dot{\varepsilon}_{11} + \dot{\varepsilon}_{22} + \dot{\varepsilon}_{33}$. Physically, $\dot{e}$ represents the volume change rate of a porous body. The porosity θ is defined as the volume fraction of voids in a porous body.

Effective sintering stress P_L is the product of the local sintering stress $P_{L0} = \frac{3\alpha}{G}$ (α is the surface tension, G is the average particle radius) and of the normalized effective sintering stress $\bar{P}_L = \frac{1}{2}(1-\theta)^2$:

$$P_L = P_{L0}\bar{P}_L = \frac{3\alpha}{G}\bar{P}_L = \frac{3\alpha}{2G}(1-\theta)^2 \tag{2}$$

The normalized shear and bulk viscosities ϕ and ψ are defined as:

$$\varphi = (1-\theta)^2; \psi = \frac{2}{3}\frac{(1-\theta)^3}{\theta} \tag{3}$$

Free sintering is characterized by the absence of externally applied stresses ($\sigma_{ij} = 0$, $\dot{e}_f = 3\dot{\varepsilon}_f$), hence Eq. (1) renders:

$$-P_L = 2\eta_0\psi\dot{e}_f = 6\eta_0\psi\dot{\varepsilon}_f \tag{4}$$

where $\dot{e}_f$ is the free sintering volume shrinkage rate and $\dot{\varepsilon}_f$ is the free sintering linear strain rate:

$$\dot{\varepsilon}_f = -\frac{P_L}{6\eta_0\psi} \tag{5}$$

Based on the conservation of mass, one can derive an important continuity equation, which interrelates the volume shrinkage and porosity rates $\dot{e}$ and $\dot{\theta}$:

$$\dot{e} = \frac{\dot{\theta}}{1-\theta} \tag{6}$$

Substituting (2), (3), and (4) in (6), one obtains:

$$\frac{\dot{\theta}}{\theta} = -\frac{9\alpha}{8\eta_0 G} \tag{7}$$

Integrating Eq. (7) provides the porosity kinetics during free sintering:

$$\theta = \theta_0 e^{-\frac{3}{8}\tau_s} \tag{8}$$

where θ_0 is the initial porosity and τ_s is the specific dimensionless time of sintering, defined as:

$$\tau_s = 3\int_0^t \frac{\alpha}{\eta_0 G}dt \tag{9}$$

where t is the physical time of sintering. Thus, the porosity kinetics for free sintering is characterized by an exponential porosity decrease with an asymptotic approaching a fully dense state, when porosity becomes negligible.

If isothermal sintering conditions and negligible grain growth are assumed, all the parameters in Eq. (9) become time invariant and the integral converts into a dimensionless product: $\tau_s = \frac{3\alpha}{\eta_0 G}t$. Using Eq. (8) the specific time of sintering can be determined based on the dilatometry data for a given porous material.

III. Sintering of Bilayered Porous Laminates: Model Framework

Let us consider a porous bilayered body distorted in the process of sintering due to the differential shrinkage of the layers (Fig. 1).

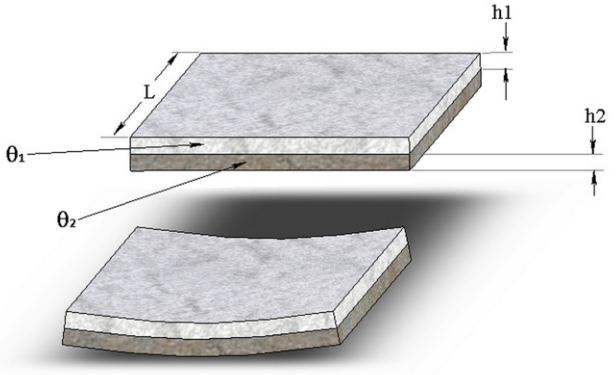

Fig. 1. Schematics of the bilayered porous composite.

†When utilizing a finite-element solution, it is a common practice to assess the obtained FE results by averaging the spatially distributed parameter values over a certain part of the considered system's volume (e.g., to calculate the average porosity of a given layer). This information, however, is directly available from the semi-analytical solution.

Each of the two layers' evolving porosity is assumed to be θ_1 and θ_2, respectively; the layers' evolving thicknesses are h_1 and h_2, respectively; initial thicknesses are h_{01} and h_{02}, respectively; the layers are assumed quadratic with length and width equal to l. Possible intrinsic anisotropy of the pore-grain structure is not included in the analysis.

For each layer, the portions of the axial strain rates imposed by the constraining stress caused by the other layer can be represented in the rectangular system of coordinates as:

$$\dot{\varepsilon}'_x = \dot{\varepsilon}_x - \dot{\varepsilon}_f;\ \dot{\varepsilon}'_y = \dot{\varepsilon}_y - \dot{\varepsilon}_f;\ \dot{\varepsilon}'_z = \dot{\varepsilon}_z - \dot{\varepsilon}_f \tag{10}$$

where "′" denotes the distortion (constraint-related) strain rate components, obtained after subtracting the free sintering rates $\dot{\varepsilon}_f$ from the total strain rate components. The constraint-related volume shrinkage rate is as follows:

$$\dot{e}' = \dot{\varepsilon}'_x + \dot{\varepsilon}'_y + \dot{\varepsilon}'_z \tag{11}$$

based on Eqs. (1), (4), (10), and (11), the normal stress components for each layer are as follows:

$$\begin{aligned}
\sigma_x &= 2\eta_0\left[\varphi\dot{\varepsilon}'_x + \left(\psi - \frac{1}{3}\varphi\right)\dot{e}'\right];\\
\sigma_y &= 2\eta_0\left[\varphi\dot{\varepsilon}'_y + \left(\psi - \frac{1}{3}\varphi\right)\dot{e}'\right];\\
\sigma_z &= 2\eta_0\left[\varphi\dot{\varepsilon}'_z + \left(\psi - \frac{1}{3}\varphi\right)\dot{e}'\right]
\end{aligned} \tag{12}$$

due to the absence of constraints in the direction perpendicular to the layers' interface (in z direction): $\sigma_z = 0$.

Based on Eqs. (10)–(12), one can obtain

$$\begin{aligned}
\dot{\varepsilon}'_x &= \frac{2\psi + \frac{\varphi}{3}}{6\eta_0\varphi\psi}\left[\sigma_x - \sigma_y\frac{\psi - \frac{\varphi}{3}}{2\psi + \frac{\varphi}{3}}\right];\\
\dot{\varepsilon}'_y &= \frac{2\psi + \frac{\varphi}{3}}{6\eta_0\varphi\psi}\left[\sigma_y - \sigma_x\frac{\psi - \frac{\varphi}{3}}{2\psi + \frac{\varphi}{3}}\right];\\
\dot{\varepsilon}'_z &= \frac{2\psi + \frac{\varphi}{3}}{6\eta_0\varphi\psi}\left[-(\sigma_x + \sigma_y)\frac{\psi - \frac{\varphi}{3}}{2\psi + \frac{\varphi}{3}}\right]
\end{aligned} \tag{13}$$

for an in-plane symmetrical bi-layered system (a bi-layered plate‡):

$$\sigma = \sigma_x = \sigma_y;\quad \dot{\varepsilon}' = \dot{\varepsilon}'_x = \dot{\varepsilon}'_y \tag{14}$$

Substituting Eq. (14) into Eq. (13), the normal stresses within each layer can be calculated:

$$\sigma_i = 6\dot{\varepsilon}'_i\eta_{0i}\varphi_i \text{ for } i = 1 \text{ to } 2 \tag{15}$$

where indices "1" and "2" refer to the first and the second layer, respectively.

(1) Kinetics of Shrinkage and Distortion Based on the Assumption of Linear Strain Rate Within Individual Layers

Assuming the linear distribution of the longitudinal strain rates in the direction perpendicular to the interface of the i-th layer, and taking into account the shrinkage of the layers' thicknesses:

$$\dot{\varepsilon}_i = \dot{\varepsilon}_0 + \dot{\kappa}z + \mathrm{sgn}(z)\kappa\frac{\dot{h}_i}{h_i}z \tag{16}$$

where κ is the curvature.

Then normal stresses within each layer, based on Eqs. (15) and (16):

$$\sigma_i = 6\eta_{0i}\varphi_i(\dot{\varepsilon}_0 + \dot{\kappa}z + \mathrm{sgn}(z)\kappa\frac{\dot{h}_i}{h_i}z - \dot{\varepsilon}_{fi}) \tag{17}$$

In the spirit of classical laminate theory, parameters $\dot{\varepsilon}_0$ and $\dot{\kappa}$ (rate of curvature change) can be determined based on the force (N) and moment of force (M) equilibrium:

$$\begin{cases}
N = \displaystyle\int_{z_0}^{z_1}\sigma dz + \ldots + \int_{z_{i-1}}^{z_i}\sigma dz \ldots + \int_{z_{n-1}}^{z_n}\sigma dz = \sum_{i=1}^{n}\int_{z_{i-1}}^{z_i}\sigma dz = \sum_{i=1}^{n}\int_{z_{i-1}}^{z_i}6\eta_{0i}\varphi_i(\dot{\varepsilon}_0 + \dot{\kappa}z + \mathrm{sgn}(z)\kappa\frac{\dot{h}_i}{h_i}z - \dot{\varepsilon}_{fi})dz\\
M = \displaystyle\int_{z_0}^{z_1}\sigma z dz + \ldots + \int_{z_{i-1}}^{z_i}\sigma z dz \ldots + \int_{z_{n-1}}^{z_n}\sigma z dz = \sum_{i=1}^{n}\int_{z_{i-1}}^{z_i}\sigma z dz = \sum_{i=1}^{n}\int_{z_{i-1}}^{z_i}6\eta_{0i}\varphi_i(\dot{\varepsilon}_0 + \dot{\kappa}z + \mathrm{sgn}(z)\kappa\frac{\dot{h}_i}{h_i}z - \dot{\varepsilon}_{fi})z dz
\end{cases} \tag{18}$$

or:

$$\begin{cases}
N = A\dot{\varepsilon}_0 + B\left(\dot{\kappa} + \kappa\displaystyle\sum_{i=1}^{n}(-1)^{1+n}\frac{\dot{h}_i}{h_i}\right) - N_f\\
M = B\dot{\varepsilon}_0 + D\left(\dot{\kappa} + \kappa\displaystyle\sum_{i=1}^{n}(-1)^{1+n}\frac{\dot{h}_i}{h_i}\right) - M_f
\end{cases} \tag{19}$$

where:

$$\begin{cases}
A = \displaystyle\sum_{i=1}^{n}6\eta_{0i}\varphi_i(z_i - z_{i-1});\ B = \sum_{i=1}^{n}6\eta_{0i}\varphi_i\frac{z_i^2 - z_{i-1}^2}{2};\ D = \sum_{i=1}^{n}6\eta_{0i}\varphi_i\frac{z_i^3 - z_{i-1}^3}{3}\\
N_f = \displaystyle\sum_{i=1}^{n}\int_{z_{i-1}}^{z_i}6\eta_{0i}\varphi_i\dot{\varepsilon}_{fi}dz;\ M_f = \sum_{i=1}^{n}\int_{z_{i-1}}^{z_i}6\eta_{0i}\varphi_i\dot{\varepsilon}_{fi}z dz
\end{cases} \tag{20}$$

Hence:

$$\begin{cases}
\dot{\varepsilon}_0 = \frac{D(N+N_f) - B(M_f+M)}{AD - B^2}\\
\dot{\kappa} = \frac{-B(N+N_f) + A(M_f+M)}{AD - B^2} - \kappa\displaystyle\sum_{i=1}^{n}(-1)^{1+n}\frac{\dot{h}_i}{h_i}
\end{cases} \tag{21}$$

To obtain simple expressions the coordinate system can be located so that parameter B is equal to zero. This condition means no coupling between the curvature change rate and the cross-sectional normal force, as well as no coupling between the strain rates at that axis and the bending moment. The coordinates of the layer external boundaries and the interface coordinate can then be written as:

‡For a bi-layered beam, Eq. (15) would have a form: $\sigma = \frac{18\eta_0\varphi\psi}{3\psi + 2\varphi}\dot{\varepsilon}'$

$$z = [z_0 - h_1, z_0, z_0 + h_2] \tag{22}$$

where z_0 is the distance between the bilayer interface and the desired coordinate system. Calculating B with the assumption in Eq. (22) provides,

$$B = 3\eta_{01}\varphi_1(z_0^2 - (z_0 - h_1)^2) + 3\eta_{02}\varphi_2((z_0 + h_2)^2 - z_0^2) \tag{23}$$

which, if solved for z_0 for $B = 0$, leads to:

$$z_0 = \frac{1}{2}\frac{\eta_{01}\varphi_1 h_1^2 - \eta_{02}\varphi_2 h_2^2}{\eta_{01}\varphi_1 h_1 + \eta_{02}\varphi_2 h_2} \tag{24}$$

parameters A, D, N_f, and M_f then become

$$\begin{cases} A = 6\eta_{01}\varphi_1 h_1 + 6\eta_{02}\varphi_2 h_2 \\ D = \frac{3}{2}\frac{4\left[\eta_{01}^2\varphi_1^2 h_1^4 + \eta_{02}^2\varphi_2^2 h_2^4\right] + 5\left[\eta_{01}\varphi_1\eta_{02}\varphi_2\left(h_1^3 h_2 + h_1 h_2^3\right)\right] + 2\eta_{01}\varphi_1\eta_{02}\varphi_2 h_1^2 h_2^2}{\eta_{01}\varphi_1 h_1 + \eta_{02}\varphi_2 h_2} \\ N_f = \left[6\eta_{01}\varphi_1 h_1\dot{\varepsilon}_{f1} + 6\eta_{02}\varphi_2 h_2\dot{\varepsilon}_{f2}\right] \\ M_f = \frac{3\eta_{01}\varphi_1 h_1\eta_{02}\varphi_2 h_2(h_1 + h_2)\left(\dot{\varepsilon}_{f1} - \dot{\varepsilon}_{f2}\right)}{\eta_{01}\varphi_1 h_1 + \eta_{02}\varphi_2 h_2} \end{cases} \tag{25}$$

In free sintering conditions, $N = 0$ and $M = 0$. Then parameters $\dot{\varepsilon}_0$ and $\dot{\kappa}$ are determined as:

$$\begin{cases} \dot{\varepsilon}_0 = \frac{N_f}{A} = \frac{\eta_{01}\varphi_1 h_1\dot{\varepsilon}_{f1} + \eta_{02}\varphi_2 h_2\dot{\varepsilon}_{f2}}{\eta_{01}\varphi_1 h_1 + \eta_{02}\varphi_2 h_2} \\ \dot{\kappa} = \frac{M_f}{D} - \kappa\sum_{i=1}^{n}(-1)^{1+n}\frac{\dot{h}_i}{h_i} = \frac{2\eta_{01}\varphi_1 h_1\eta_{02}\varphi_2 h_2(h_1 + h_2)\left(\dot{\varepsilon}_{f1} - \dot{\varepsilon}_{f2}\right)}{4\left[\eta_{01}^2\varphi_1^2 h_1^4 + \eta_{02}^2\varphi_2^2 h_2^4\right] + 5\left[\eta_{01}\varphi_1\eta_{02}\varphi_2\left(h_1^3 h_2 + h_1 h_2^3\right)\right] + 2\eta_{01}\varphi_1\eta_{02}\varphi_2 h_1^2 h_2^2} + \kappa\left(\frac{\dot{h}_2}{h_2} - \frac{\dot{h}_1}{h_1}\right) \end{cases} \tag{26}$$

The average strain rate in each of the layers equals that in the center of the layer as the strain rate distribution is linear. These will be denoted as $\bar{\dot{\varepsilon}}_1$ and $\bar{\dot{\varepsilon}}_2$:

$$\begin{cases} \bar{\dot{\varepsilon}}_1 = \dot{\varepsilon}_0 + \left\{\dot{\kappa} + \kappa\left[\frac{\dot{h}_2}{h_2} - \frac{\dot{h}_1}{h_1}\right]\right\}\left(z_0 - \frac{h_1}{2}\right) \\ \bar{\dot{\varepsilon}}_2 = \dot{\varepsilon}_0 + \left\{\dot{\kappa} + \kappa\left[\frac{\dot{h}_2}{h_2} - \frac{\dot{h}_1}{h_1}\right]\right\}\left(z_0 + \frac{h_2}{2}\right) \end{cases} \tag{27}$$

For thin layers, $\frac{1}{h_i} \gg \kappa$, therefore, one can neglect the term $\kappa\left[\frac{\dot{h}_2}{h_2} - \frac{\dot{h}_1}{h_1}\right]$ in Eq. (27). Hence, Eq. (27) can be rewritten as:

$$\begin{cases} \bar{\dot{\varepsilon}}_1 = \dot{\varepsilon}_0 + \dot{\kappa}\left(z_0 - \frac{h_1}{2}\right) \\ \bar{\dot{\varepsilon}}_2 = \dot{\varepsilon}_0 + \dot{\kappa}\left(z_0 + \frac{h_2}{2}\right) \end{cases} \tag{28}$$

where the curvature rate or the second equation in Eq. (26) is simplified as:

$$\dot{\kappa} = \frac{\dot{\varepsilon}_{f1} - \dot{\varepsilon}_{f2}}{2\frac{\eta_{01}\varphi_1 h_1^3 + \eta_{02}\varphi_2 h_2^3}{(h_1 + h_2)}\left[\frac{1}{\eta_{01}\varphi_1 h_1} + \frac{1}{\eta_{02}\varphi_2 h_2}\right] + \frac{h_1 + h_2}{2}} \tag{29}$$

Equation (29) is the viscous analogy of the known Timoshenko's equation[31] for the bending of bimetal strips. In Eq. (29), both free sintering strain rates $\dot{\varepsilon}_{f1}$ and $\dot{\varepsilon}_{f2}$ [see Eq. (5)] and the normalized viscous shear moduli φ_1 and φ_2 [see Eq. (3)] are functions of porosity evolving during sintering. Layer thicknesses h_1 and h_2 also change during the sintering process. Therefore, to find the kinetics of the bending curvature, Eq. (29) should be coupled with the evolution equations for both layer porosities and thicknesses.

Let us consider the procedure of the derivation of such evolution equations. Eq. (1) can be rewritten for the 1st and the 2nd layer as (for stress z-axis component):

$$-P_{\mathrm{Li}} = 2\eta_{0i}\left[\varphi_i\dot{\varepsilon}_{zi} + \left(\psi_i - \frac{1}{3}\varphi_i\right)\left(\dot{\varepsilon}_{zi} + 2\dot{\varepsilon}_{xi}\right)\right],\ i = 1, 2 \tag{30}$$

Based on Eqs. (5), (10), (26), (28), and (29), the average strain rates in each layer in the direction parallel to the layer interface are as follows:

$$\begin{cases} \bar{\dot{\varepsilon}}_{x1} = -\frac{\varphi_1 h_1\frac{P_{\mathrm{L}1}}{6\psi_1} + \varphi_2 h_2\frac{P_{\mathrm{L}2}}{6\psi_2}}{\eta_{01}\varphi_1 h_1 + \eta_{02}\varphi_2 h_2} + \frac{\frac{1}{12}\left(\frac{P_{\mathrm{L}2}}{\eta_{02}\psi_2} - \frac{P_{\mathrm{L}1}}{\eta_{01}\psi_1}\right)\frac{\eta_{02}\varphi_2 h_2(h_1 + h_2)}{\eta_{01}\varphi_1 h_1 + \eta_{02}\varphi_2 h_2}}{2\frac{\eta_{01}\varphi_1 h_1^3 + \eta_{02}\varphi_2 h_2^3}{(h_1 + h_2)}\left[\frac{1}{\eta_{01}\varphi_1 h_1} + \frac{1}{\eta_{02}\varphi_2 h_2}\right] + \frac{h_1 + h_2}{2}} \\ \bar{\dot{\varepsilon}}_{x2} = -\frac{\varphi_1 h_1\frac{P_{\mathrm{L}1}}{6\psi_1} + \varphi_2 h_2\frac{P_{\mathrm{L}2}}{6\psi_2}}{\eta_{01}\varphi_1 h_1 + \eta_{02}\varphi_2 h_2} + \frac{\frac{1}{12}\left(\frac{P_{\mathrm{L}1}}{\eta_{01}\psi_1} - \frac{P_{\mathrm{L}2}}{\eta_{02}\psi_2}\right)\frac{\eta_{01}\varphi_1 h_1(h_1 + h_2)}{\eta_{01}\varphi_1 h_1 + \eta_{02}\varphi_2 h_2}}{2\frac{\eta_{01}\varphi_1 h_1^3 + \eta_{02}\varphi_2 h_2^3}{(h_1 + h_2)}\left[\frac{1}{\eta_{01}\varphi_1 h_1} + \frac{1}{\eta_{02}\varphi_2 h_2}\right] + \frac{h_1 + h_2}{2}} \end{cases} \tag{31}$$

based on Eqs (30) and (31), the evolution of the layer thicknesses and the respective strain rate components are related as:

$$\dot{\varepsilon}_{zi} = \frac{\dot{h}_i}{h_i} = -\frac{\frac{P_{\mathrm{Li}}}{2\eta_{0i}} + 2\left(\psi_i - \frac{1}{3}\varphi_i\right)\bar{\dot{\varepsilon}}_{xi}}{\psi_i + \frac{2}{3}\varphi_i},\ i = 1, 2 \tag{32}$$

Equation (6) for each layer can be approximated by:

$$\frac{\dot{\theta}_i}{1 - \theta_i} = \dot{e}_i = \dot{\varepsilon}_{zi} + 2\bar{\dot{\varepsilon}}_{xi} = \frac{-\frac{P_{\mathrm{Li}}}{2\eta_{0i}} + 2\varphi_i\bar{\dot{\varepsilon}}_{xi}}{\psi_i + \frac{2}{3}\varphi_i},\ i = 1, 2 \tag{33}$$

Expressions (31)–(33) define a set of ordinary differential equations with respect to the four functions of time: h_1, h_2, θ_1, and θ_2. Equation (29) can be coupled with the above-mentioned equations to determine the evolution of the bending curvature.

The kinetic equations allow normalization, which enables the generalization of the obtained solution. The dimensionless form of the equations makes the solution applicable to various materials systems (similar to "master sintering curve" analyses).

Introducing the normalized form of the geometrical parameters (index "0" refers to the initial parameter value) and also utilizing dimensionless parameters (ξ, and λ):

$$\begin{aligned} &\bar{h}_1 = \frac{h_1}{h_{01}};\ \bar{h}_2 = \frac{h_2}{h_{02}};\ \bar{\kappa} = \frac{\kappa}{1/(h_{01} + h_{02})}; \\ &\chi = \frac{h_{02}}{h_{01}};\ \xi = \frac{\eta_{02}}{\eta_{01}};\ \lambda = \frac{P_{\mathrm{L}02}/\eta_{02}}{P_{\mathrm{L}01}/\eta_{01}} \end{aligned} \tag{34}$$

and taking into account the modified dimensionless specific time of sintering [see Eq. (9)], Eqs. (29) and (31)–(33) can be rearranged in the normalized form:

$$\begin{cases} \frac{d\bar{h}_1}{d\tau_s} = -\bar{h}_1 \frac{\frac{\bar{P}_{L1}}{2}+2\left(\psi_1-\frac{1}{3}\varphi_1\right)\bar{\dot{\varepsilon}}_{x1}}{\psi_1+\frac{2}{3}\varphi_1}; \quad \frac{d\bar{h}_2}{d\tau_s} = -\bar{h}_2 \frac{\lambda\frac{\bar{P}_{L2}}{2}+2\left(\psi_2-\frac{1}{3}\varphi_2\right)\bar{\dot{\varepsilon}}_{x2}}{\psi_2+\frac{2}{3}\varphi_2} \\ \frac{d\theta_1}{d\tau_s} = (1-\theta_1)\frac{-\frac{\bar{P}_{L1}}{2}+2\varphi_1\bar{\dot{\varepsilon}}_{x1}}{\psi_1+\frac{2}{3}\varphi_1}; \quad \frac{d\theta_2}{d\tau_s} = (1-\theta_2)\frac{-\lambda\frac{\bar{P}_{L2}}{2}+2\varphi_2\bar{\dot{\varepsilon}}_{x2}}{\psi_2+\frac{2}{3}\varphi_2} \\ \frac{d\bar{\kappa}}{d\tau_s} = \frac{\frac{1}{6}\left[\frac{\lambda\bar{P}_{L2}}{\psi_2}-\frac{\bar{P}_{L1}}{\psi_1}\right](1+\chi)}{2\frac{\varphi_1\bar{h}_1^3+\xi\chi^3\varphi_2\bar{h}_2^3}{\bar{h}_1+\chi\bar{h}_2}\left[\frac{1}{\varphi_1\bar{h}_1}+\frac{1}{\xi\chi\varphi_2\bar{h}_2}\right]+\frac{\bar{h}_1+\chi\bar{h}_2}{2}} \end{cases} \tag{35}$$

where

$$\begin{cases} \bar{\bar{\dot{\varepsilon}}}_{x1} = -\frac{\varphi_1\bar{h}_1\frac{\bar{P}_{L1}}{6\psi_1}+\lambda\xi\chi\varphi_2\bar{h}_2\frac{\bar{P}_{L2}}{6\psi_2}}{\varphi_1\bar{h}_1+\xi\chi\varphi_2\bar{h}_2} + \frac{\frac{1}{12}\left(\frac{\lambda\bar{P}_{L2}}{\psi_2}-\frac{\bar{P}_{L1}}{\psi_1}\right)\frac{\chi\xi\varphi_2\bar{h}_2(\bar{h}_1+\chi\bar{h}_2)}{\varphi_1\bar{h}_1+\xi\chi\varphi_2\bar{h}_2}}{2\frac{\varphi_1\bar{h}_1^3+\xi\chi^3\varphi_2\bar{h}_2^3}{(\bar{h}_1+\chi\bar{h}_2)}\left[\frac{1}{\varphi_1\bar{h}_1}+\frac{1}{\xi\chi\varphi_2\bar{h}_2}\right]+\frac{\bar{h}_1+\chi\bar{h}_2}{2}} \\ \bar{\bar{\dot{\varepsilon}}}_{x2} = -\frac{\varphi_1\bar{h}_1\frac{\bar{P}_{L1}}{6\psi_1}+\lambda\xi\chi\varphi_2\bar{h}_2\frac{\bar{P}_{L2}}{6\psi_2}}{\varphi_1\bar{h}_1+\xi\chi\varphi_2\bar{h}_2} + \frac{\frac{1}{12}\left(\frac{\bar{P}_{L1}}{\psi_1}-\frac{\lambda\bar{P}_{L2}}{\psi_2}\right)\frac{\varphi_1\bar{h}_1(\bar{h}_1+\chi\bar{h}_2)}{\varphi_1\bar{h}_1+\xi\chi\varphi_2\bar{h}_2}}{2\frac{\varphi_1\bar{h}_1^3+\xi\chi^3\varphi_2\bar{h}_2^3}{(\bar{h}_1+\chi\bar{h}_2)}\left[\frac{1}{\varphi_1\bar{h}_1}+\frac{1}{\xi\chi\varphi_2\bar{h}_2}\right]+\frac{\bar{h}_1+\chi\bar{h}_2}{2}} \end{cases} \tag{36}$$

the normal stresses in the layers can be determined from Eqs. (5), (15), and (31):

$$\sigma_1 = 6\eta_{01}\varphi_1(\dot{\bar{\varepsilon}}_{x1} - \dot{\varepsilon}_{f1}); \sigma_2 = 6\eta_{02}\varphi_2(\dot{\bar{\varepsilon}}_{x2} - \dot{\varepsilon}_{f2}) \tag{37}$$

The normal stresses in the normalized form ($\bar{\sigma}_i = 2\sigma_i/(P_{L1}+P_{L2}), i = 1, 2$) are given by:

$$\begin{cases} \frac{\dot{h}_1}{h_1} = -\frac{P_{L1}}{6\eta_{01}}\frac{\eta_{01}\varphi_1\left[1+\frac{2\varphi_1}{3\psi_1}\right]h_1+\left[3\eta_{02}\varphi_2-2\eta_{01}\left(\psi_1-\frac{1}{3}\varphi_1\right)\frac{P_{L2}\varphi_2}{P_{L1}\psi_2}\right]h_2}{\left(\psi_1+\frac{2}{3}\varphi_1\right)(\eta_{01}\varphi_1h_1+\eta_{02}\varphi_2h_2)}; \dot{\theta}_1 = -(1-\theta_1)P_{L1}\varphi_1\frac{\left[2\frac{\varphi_1}{\psi_1}+3\right]h_1+\left[2\frac{\varphi_2P_{L2}}{\psi_2P_{L1}}+3\frac{\varphi_2\eta_{02}}{\varphi_1\eta_{01}}\right]h_2}{6\left(\psi_1+\frac{2}{3}\varphi_1\right)(\eta_{01}\varphi_1h_1+\eta_{02}\varphi_2h_2)} \\ \frac{\dot{h}_2}{h_2} = -\frac{P_{L2}}{6\eta_{02}}\frac{\eta_{02}\varphi_2\left[1-\frac{2\varphi_2}{3\psi_2}\right]h_2+\left[3\eta_{01}\varphi_1-2\eta_{02}\left(\psi_2-\frac{1}{3}\varphi_2\right)\frac{P_{L1}\varphi_1}{P_{L2}\psi_1}\right]h_1}{\left(\psi_2+\frac{2}{3}\varphi_2\right)(\eta_{01}\varphi_1h_1+\eta_{02}\varphi_2h_2)}; \dot{\theta}_2 = -(1-\theta_2)P_{L2}\varphi_2\frac{\left[2\frac{\varphi_2}{\psi_2}+3\right]h_2+\left[2\frac{\varphi_1P_{L1}}{\psi_1P_{L2}}+3\frac{\varphi_1\eta_{01}}{\varphi_2\eta_{02}}\right]h_1}{6\left(\psi_2+\frac{2}{3}\varphi_2\right)(\eta_{01}\varphi_1h_1+\eta_{02}\varphi_2h_2)} \end{cases} \tag{45}$$

$$\bar{\sigma}_1 = \varphi_1\left(\bar{\bar{\dot{\varepsilon}}}_{x1} - \frac{\bar{P}_{L1}}{6\psi_1}\right); \bar{\sigma}_2 = \varphi_2\left(\bar{\bar{\dot{\varepsilon}}}_{x2} - \lambda\frac{\bar{P}_{L2}}{6\psi_2}\right) \tag{38}$$

(2) Kinetics of Shrinkage and Distortion Based on the Assumption of Strain Rate Uniformity Within Individual Layers

Expressions (35)–(38) can be significantly simplified if one assumes that longitudinal strain rates are uniformly distributed along the thickness of each layer. This assumption can be accepted for thin layer structures. In such a case, the force equilibrium in a bilayered system is given by:

$$\sigma_1h_1 = -\sigma_2h_2 \tag{39}$$

from Eqs. (15) and (39):

$$\dot{\varepsilon}'_1\eta_{01}\varphi_1h_1 = -\dot{\varepsilon}'_2\eta_{02}\varphi_2h_2 \tag{40}$$

the strain rate compatibility is given by:

$$\dot{\varepsilon}_1 = \dot{\varepsilon}'_1 + \dot{\varepsilon}_{f1}; \dot{\varepsilon}_2 = \dot{\varepsilon}'_2 + \dot{\varepsilon}_{f2}; \dot{\varepsilon}_1 = \dot{\varepsilon}_2 \tag{41}$$

Hence,

$$\dot{\varepsilon}'_2 - \dot{\varepsilon}'_1 = \dot{\varepsilon}_{f1} - \dot{\varepsilon}_{f2} \tag{42}$$

from Eqs. (40) and (42) we obtain the expression for the constraint-related strain rate components within individual layers:

$$\dot{\varepsilon}'_1 = \frac{\left(\dot{\varepsilon}_{f2}-\dot{\varepsilon}_{f1}\right)\eta_{02}\varphi_2h_2}{\eta_{01}\varphi_1h_1+\eta_{02}\varphi_2h_2}; \dot{\varepsilon}'_2 = \frac{\left(\dot{\varepsilon}_{f1}-\dot{\varepsilon}_{f2}\right)\eta_{01}\varphi_1h_1}{\eta_{01}\varphi_1h_1+\eta_{02}\varphi_2h_2} \tag{43}$$

based on Eqs. (5), (41), and (43), the radial strain rates in each layer are as follows:

$$\dot{\varepsilon}_{x1} = \dot{\varepsilon}'_1 - \dot{\varepsilon}_{f1}; \dot{\varepsilon}_{x2} = \dot{\varepsilon}'_2 - \dot{\varepsilon}_{f2} \tag{44}$$

from Eqs. (32), (33), and (44), one can obtain:

Similarly to expressions (31)–(33), Eq. (45) defines a set of ordinary differential equations with respect to the four functions of time: h_1, h_2, θ_1, and θ_2.

Equation (45) can be rewritten in a normalized form:

$$\begin{cases} \frac{d\bar{h}_1}{d\tau_s} = -\bar{P}_{L1}\frac{\varphi_1\left[1+\frac{2\varphi_1}{3\psi_1}\right]\bar{h}_1+\xi\chi\left[3\varphi_2-2\lambda\left(\psi_1-\frac{1}{3}\varphi_1\right)\frac{\bar{P}_{L2}\varphi_2}{\bar{P}_{L1}\psi_2}\right]\bar{h}_2}{6\left(\psi_1+\frac{2}{3}\varphi_1\right)\left(\varphi_1\bar{h}_1+\xi\chi\varphi_2\bar{h}_2\right)}; \quad \frac{d\theta_1}{d\tau_s} = -(1-\theta_1)\bar{P}_{L1}\varphi_1\frac{\left[2\frac{\varphi_1}{\psi_1}+3\right]\bar{h}_1+\xi\chi\left[2\lambda\frac{\varphi_2\bar{P}_{L2}}{\psi_2\bar{P}_{L1}}+3\frac{\varphi_2}{\varphi_1}\right]\bar{h}_2}{6\left(\psi_1+\frac{2}{3}\varphi_1\right)\left(\varphi_1\bar{h}_1+\xi\chi\varphi_2\bar{h}_2\right)} \\ \frac{d\bar{h}_2}{d\tau_s} = -\bar{P}_{L2}\frac{\lambda\xi\chi\varphi_2\left[1+\frac{2\varphi_2}{3\psi_2}\right]\bar{h}_2+\left[3\lambda\varphi_1-2\left(\psi_2-\frac{1}{3}\varphi_2\right)\frac{\bar{P}_{L1}\varphi_1}{\bar{P}_{L2}\psi_1}\right]\bar{h}_1}{6\left(\psi_2+\frac{2}{3}\varphi_2\right)\left(\varphi_1\bar{h}_1+\xi\chi\varphi_2\bar{h}_2\right)}; \quad \frac{d\theta_2}{d\tau_s} = -(1-\theta_2)\bar{P}_{L2}\varphi_2\frac{\lambda\xi\chi\left[2\frac{\varphi_2}{\psi_2}+3\right]\bar{h}_2+\left[2\frac{\varphi_1\bar{P}_{L1}}{\psi_1\bar{P}_{L2}}+3\lambda\frac{\varphi_1}{\varphi_2}\right]\bar{h}_1}{6\left(\psi_2+\frac{2}{3}\varphi_2\right)\left(\varphi_1\bar{h}_1+\xi\chi\varphi_2\bar{h}_2\right)} \\ \frac{d\bar{\kappa}}{d\tau_s} = \frac{\frac{1}{6}\left[\frac{\lambda\bar{P}_{L2}}{\psi_2}-\frac{\bar{P}_{L1}}{\psi_1}\right](1+\chi)}{2\frac{\varphi_1\bar{h}_1^3+\xi\chi^3\varphi_2\bar{h}_2^3}{\bar{h}_1+\chi\bar{h}_2}\left[\frac{1}{\varphi_1\bar{h}_1}+\frac{1}{\xi\chi\varphi_2\bar{h}_2}\right]+\frac{\bar{h}_1+\chi\bar{h}_2}{2}} \end{cases} \tag{46}$$

The normal stresses in the normalized form can be determined from Eqs. (5), (15), and (43) considering the parameters in Eq. (34)

$$\begin{aligned} \bar{\sigma}_1 &= 2\frac{\varphi_1}{\psi_1}\frac{\varphi_2}{\psi_2}\frac{\xi\chi\left(\psi_2-\psi_1\lambda\frac{\bar{P}_{L2}}{\bar{P}_{L1}}\right)\bar{h}_2}{(1+\lambda\xi)\left[\varphi_1\bar{h}_1+\xi\chi\varphi_2\bar{h}_2\right]}; \\ \bar{\sigma}_2 &= 2\frac{\varphi_1}{\psi_1}\frac{\varphi_2}{\psi_2}\frac{\xi\left(\psi_1\lambda\frac{\bar{P}_{L2}}{\bar{P}_{L1}}-\psi_2\right)\bar{h}_1}{(1+\lambda\xi)\left[\varphi_1\bar{h}_1+\xi\chi\varphi_2\bar{h}_2\right]} \end{aligned} \tag{47}$$

Three-dimensionless parameters: χ, ξ, and λ defined in Eq. (34) have to be known for solving the set of expressions in Eqs. (35) or (46). Parameter χ (the initial thickness ratio) is available from the measurement of the initial bilayered

geometry. Parameter λ can be obtained through the direct comparison of the data on the free sintering dilatometry conducted with the material of each individual layer. Parameter ξ, (the ratio of shear viscosities of fully dense materials of two layers) would usually require an independent experiment on the sintering under a known external load. In Section IV, we describe a way to circumvent the necessity of the pressure-assisted sintering experiment. Using the described approach, one can obtain the ratio of shear viscosities of fully dense materials of two layers ξ, through a sintering experiment conducted on the multilayered system with a special geometrical layer arrangement.

IV. Sintering of Trilayered Symmetrical Laminates: Determination of the Ratio of Shear Viscosities of Fully Dense Layer Materials

In the case of a trilayer porous laminate sintering, an approach similar to the one employed for the analysis of bilayered composites is used. Eq. (15) is modified as:

$$\sigma_i = 6\dot{\varepsilon}'_i \eta_{0i} \varphi_i \text{ for } i = 1 \text{ to } 3 \tag{48}$$

An interesting particular case of a trilayered system is a symmetric laminate, which comprises two identical layers at both sides of another layer (Fig. 2). This system has been analyzed in terms of the cosintering residual stress buildup by Cai *et al.* [6,7] and by Ollagnier *et al.*[25] Due to its symmetry, this system should not experience any bending (under ideal uniformity conditions, neglecting edge effects, and possible delamination).

It will shrink both perpendicular and parallel to the layer thickness directions. As shown below, the analysis of the respective geometrical changes in this system subjected to sintering provides the assessment of a useful constitutive parameter – the ratio of the shear viscosities of the fully dense materials of the respective layers. This parameter value can then be utilized when modeling cosintering of asymmetric bi- and trilayered (as well as, in general, multilayered) porous systems.

The conditions of the force equilibrium and the compatibility of the layers' strain rates [see Eqs. (39)–(42)] are given by:

$$\begin{aligned} &\sigma_1 h_1 + \sigma_2 h_2 + \sigma_3 h_3 = 0 \\ &\dot{\varepsilon}_i = \dot{\varepsilon}'_i + \dot{\varepsilon}_{fi}; \text{ for } i = 1 \text{ to } 3 \\ &\dot{\varepsilon}_1 = \dot{\varepsilon}_2 = \dot{\varepsilon}_3 \end{aligned} \tag{49}$$

and:

$$\begin{cases} \dot{\varepsilon}'_1 \eta_{01} \varphi_1 h_1 + \dot{\varepsilon}'_2 \eta_{02} \varphi_2 h_2 + \dot{\varepsilon}'_3 \eta_{03} \varphi_3 h_3 = 0 \\ \dot{\varepsilon}'_2 - \dot{\varepsilon}'_1 = \dot{\varepsilon}_{f1} - \dot{\varepsilon}_{f2} \\ \dot{\varepsilon}'_3 - \dot{\varepsilon}'_2 = \dot{\varepsilon}_{f2} - \dot{\varepsilon}_{f3} \end{cases} \tag{50}$$

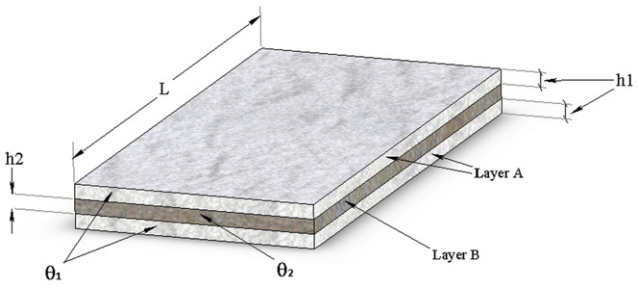

Fig. 2. Schematics of the symmetric trilayered porous composite.

Similarly Eqs. (43):

$$\begin{cases} \dot{\varepsilon}'_1 = \frac{\eta_{02}\varphi_2 h_2 (\dot{\varepsilon}_{f2} - \dot{\varepsilon}_{f1}) + \eta_{03}\varphi_3 h_3 (\dot{\varepsilon}_{f3} - \dot{\varepsilon}_{f1})}{\eta_{01}\varphi_1 h_1 + \eta_{02}\varphi_2 h_2 + \eta_{03}\varphi_3 h_3} \\ \dot{\varepsilon}'_2 = \frac{\eta_{03}\varphi_3 h_3 (\dot{\varepsilon}_{f3} - \dot{\varepsilon}_{f2}) + \eta_{01}\varphi_1 h_1 (\dot{\varepsilon}_{f1} - \dot{\varepsilon}_{f2})}{\eta_{01}\varphi_1 h_1 + \eta_{02}\varphi_2 h_2 + \eta_{03}\varphi_3 h_3} \\ \dot{\varepsilon}'_3 = \frac{\eta_{02}\varphi_2 h_2 (\dot{\varepsilon}_{f2} - \dot{\varepsilon}_{f3}) + \eta_{01}\varphi_1 h_1 (\dot{\varepsilon}_{f1} - \dot{\varepsilon}_{f3})}{\eta_{01}\varphi_1 h_1 + \eta_{02}\varphi_2 h_2 + \eta_{03}\varphi_3 h_3} \end{cases} \tag{51}$$

in the case of a symmetric trilaminate, the following relationships are valid:

$$\dot{\varepsilon}'_1 = \dot{\varepsilon}'_3;\ \eta_{01} = \eta_{03};\ \varphi_1 = \varphi_3;\ h_1 = h_3 \tag{52}$$

the substitution of Eq. (52) into Eq. (51) results in:

$$\dot{\varepsilon}'_1 = \dot{\varepsilon}'_3 = \frac{\eta_{02}\varphi_2 h_2 (\dot{\varepsilon}_{f2} - \dot{\varepsilon}_{f1})}{2\eta_{01}\varphi_1 h_1 + \eta_{02}\varphi_2 h_2}; \dot{\varepsilon}'_2 = \frac{2\eta_{01}\varphi_1 h_1 (\dot{\varepsilon}_{f1} - \dot{\varepsilon}_{f2})}{2\eta_{01}\varphi_1 h_1 + \eta_{02}\varphi_2 h_2} \tag{53}$$

the trilayered composite's length (in the direction parallel to the interface) will shrink according to:

$$\frac{\dot{l}}{l} = \dot{\varepsilon}_x = \dot{\varepsilon}'_1 + \dot{\varepsilon}_{f1} = \frac{\eta_{02}\varphi_2 h_2 (\dot{\varepsilon}_{f2} - \dot{\varepsilon}_{f1})}{2\eta_{01}\varphi_1 h_1 + \eta_{02}\varphi_2 h_2} + \dot{\varepsilon}_{f1} \tag{54}$$

taking into account Eq. (5):

$$\frac{\dot{l}}{l} = -\frac{\frac{\varphi_1}{\psi_1} P_{L1} h_1 + \frac{\varphi_2}{\psi_2} P_{L2} h_2}{6(2\eta_{01}\varphi_1 h_1 + \eta_{02}\varphi_2 h_2)} \tag{55}$$

The normalized form of Eq. (55) is ($\bar{l} = l/l_0$, where l_0 is the initial length of the composite laminate) as follows:

$$\frac{d\bar{l}}{d\tau_s} = -\frac{\frac{\varphi_1}{\psi_1}\bar{P}_{L1} + \lambda\xi\chi\frac{\varphi_2}{\psi_2}\bar{P}_{L2}\frac{\bar{h}_2}{\bar{h}_1}}{6\left(2\varphi_1 + \xi\chi\varphi_2\frac{\bar{h}_2}{\bar{h}_1}\right)}\bar{l} \tag{56}$$

The ratio ξ of the shear viscosities of the fully dense materials of the respective layers can be found from the following equation:

$$\xi = -\frac{2}{\chi}\frac{\varphi_1}{\varphi_2}\frac{\bar{h}_1}{\bar{h}_2}\frac{\left[\frac{\bar{P}_{L1}}{\psi_1}\bar{l} + 6\frac{d\bar{l}}{d\tau_s}\right]}{\left[6\frac{d\bar{l}}{d\tau_s} + \lambda\frac{\bar{P}_{L2}}{\psi_2}\bar{l}\right]} \tag{57}$$

It should be noted that the developed concept can be generalized for solving problems on sintering multilayered systems. For example, if we consider sintering of an asymmetric trilayered system (a–b–c), two ratios of the shear viscosities of the fully dense materials of respective layers can be found from the simultaneous dilatometry of the two symmetric trilayered systems (a–b–a and b–c–b) based on the respective layer combinations.

V. Sintering of Bilayered Porous Laminates: Calculation Results

The set of ordinary differential equations in (35) and (46) has been solved by using Matlab. The solutions in terms of the kinetics of both layer porosities, of normalized thicknesses, and of bending curvature are shown in Figs. 3 and 4 for different sets of input parameters. Figure 3 provides the results for the sintering of two layers composed of the same material (i.e., $\lambda = \xi = 1$) having different initial porosities ($\theta_{01} = 0.3$, $\theta_{02} = 0.5$). Both layer thicknesses are assumed equal in the beginning of sintering ($\chi = 1$). The solution of

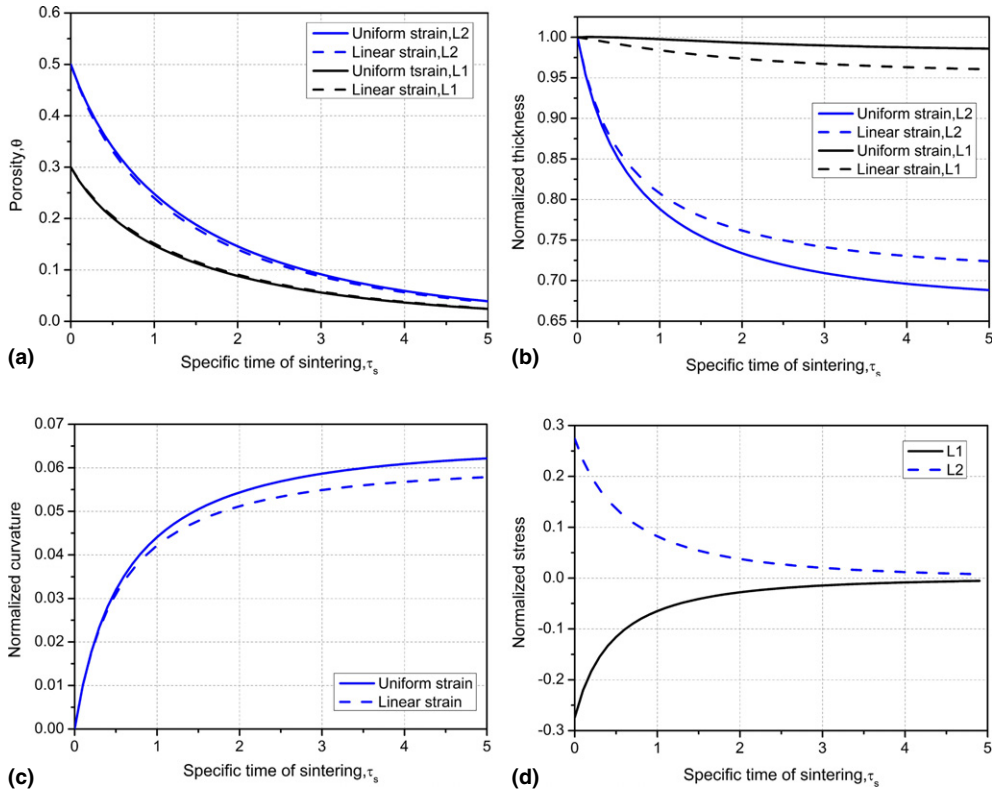

Fig. 3. Evolution of porosity (a), layer thickness (b), curvature (c), and normal stresses (d) in a bilayered composite of L1 and L2 (same layer material with different initial layer porosities) during cosintering: initial layer porosities $\theta_{01} = 0.3$, $\theta_{02} = 0.5$, $\lambda = 1$, $\xi = 1$, $\chi = 1$.

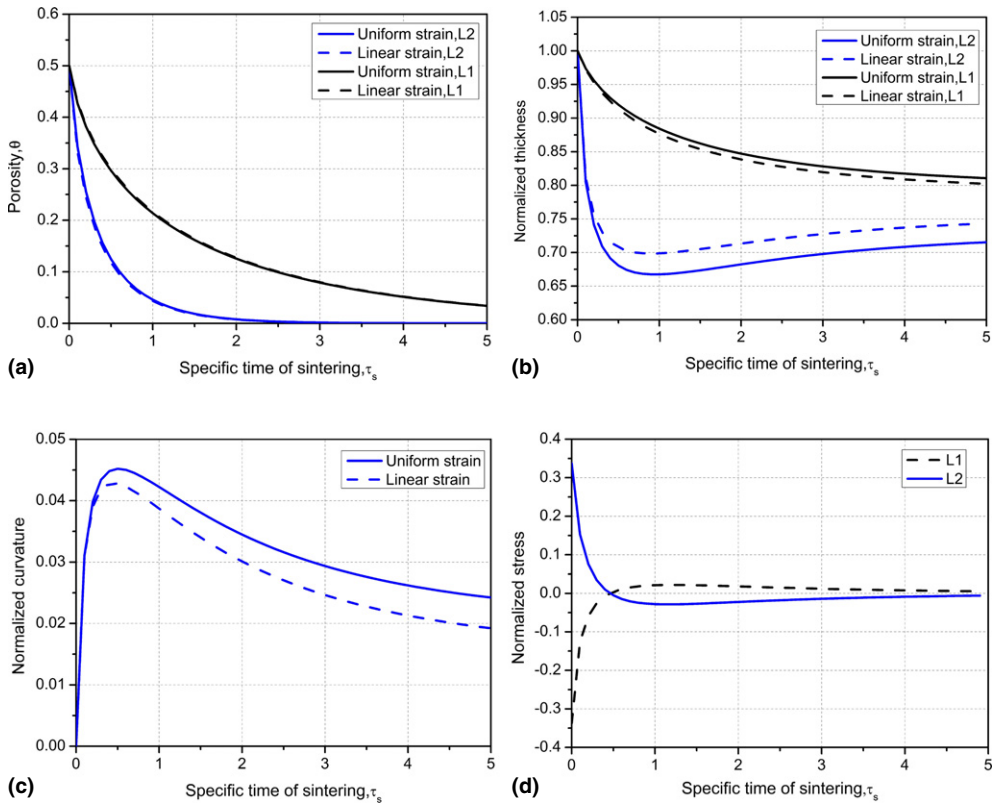

Fig. 4. Evolution of porosity (a), layer thickness (b), curvature (c), and normal stresses (d) in a bilayered composite of L1 and L2 (different layer material with the same initial layer porosities) during cosintering: initial layer porosities $\theta_{01} = 0.5$, $\theta_{02} = 0.5$, $\lambda = 4$, $\xi = 0.25$, $\chi = 1$.

the kinetic equations is also coupled with expressions (37) and (47) describing the evolution of normal stresses in both layers.

The calculation results indicate more rapid shrinkage of the second layer, which has higher initial porosity. Its thickness decreases during the process (for the duration of $\tau_s = 5$) by more than 30%, whereas the thickness of the first, initially more dense layer, decreases only slightly. The curvature increases monotonically throughout the entire cosintering process. The first slowly shrinking layer experiences

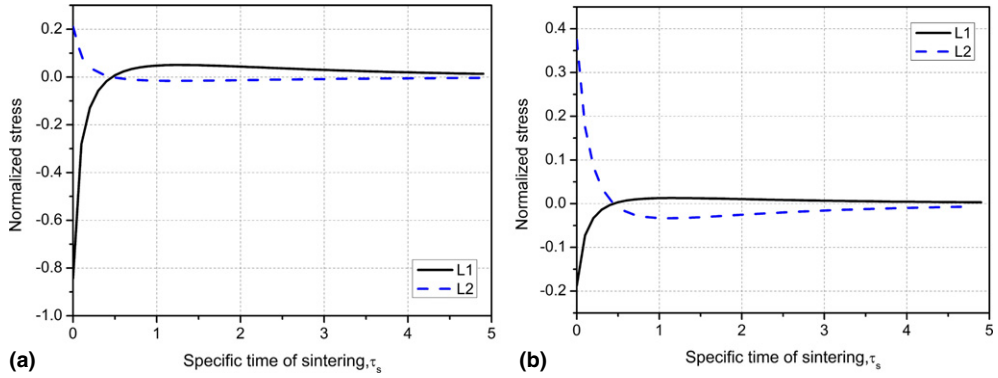

Fig. 5. Evolution of normalized stresses for two cases with different ratios of layer thicknesses (different layer material with the same initial layer porosities) during cosintering: initial layer porosities $\theta_{01} = 0.5$, $\theta_{02} = 0.5$, $\lambda = 4$, $\xi = 0.25$, $\chi = 1$, (a), $\chi = 4$ and (b), $\chi = 0.5$.

compressive stresses imposed on it by the faster shrinking second layer, which is under tensile stresses. The magnitude of stresses decreases during sintering – it is the highest in the beginning of the process. This fact indicates higher probability of in-sintering damage at the onset of cofiring when the stress level is the highest and the material strength is the lowest due to high porosity values in the beginning of sintering.

Figure 4 provides a sample solution for the cosintering of two different materials with the same initial porosity ($\theta_{01} = \theta_{02} = 0.5$). Free sintering of the material of the second layer is assumed to be four times faster than the free sintering of the material of the first layer (i.e., $\lambda = 4$). The difference in the free sintering rates is attributed to the difference in shear viscosities of the fully dense material substances, therefore, it is assumed that $\xi = 1/\lambda = 0.25$. The thicknesses are assumed equal in the beginning of sintering ($\chi = 1$).

In this case, the rate of shrinkage of the second layer is higher due to the higher sinterability of its material (four times higher than that of the first layer, $\lambda = 4$). Hence, the second layer reaches almost full density at about $\tau_s = 2$ when the first layer is still approximately 12% porous. At the point of time, when porosity of the second layer is less than 10%, the distortion direction changes, see Fig. 4(c), as indicated by the normalized curvature evolution. The much more porous (about 30% versus about 10%) first layer's shrinkage causes the relatively densified second layer to change the bending direction, which flattens out the overall composite to a certain degree. This geometrical transformation is accompanied also by the increase in the second layer thickness, which reaches its minimum at the same point of the bending direction reversal. The stress sign reversal occurs almost at the same point of time (slightly earlier), when initially subjected to tensile stress second layer starts experiencing a compressive load. This compressive load applied to the almost fully dense second layer results in the above-mentioned increase in its thickness due to the low compressibility of the material with low porosity level. That is, the in-plane shrinkage is compensated by a thickness increase (creep). Note that the average stress in the layer only gives partial information because (1) a layer can be globally under tension, but some part of it might nevertheless be under compression and (2) the average stress might be much lower than the maximum stress, which is important to predict fracture.

Note that in both types of material systems, the calculations are performed based on the linear as well as uniform strain distributions across the thickness of the layers as per the solutions in Sections III*(1)* and *(2)*, respectively.

Figure 5 demonstrates the optimization capability of the developed algorithm: it includes the stress evolution analysis for the comparative case of two bilayered composites of the same features with different ratio of initial layer thickness (χ).

The results in Fig. 5(a) indicate that if the thickness of the first layer, with lower sinterability, is smaller than the thickness of the second layer which has higher relative intensity of sintering by a factor of 4 ($\chi = 4$), then the maximum tensile stress in the second layer drops almost by a factor of 2 (see Fig. 4 for stresses with $\chi = 1$). The opposite effect is also shown in Fig. 5(b), in which case $\chi = 0.5$. This fact can serve as a basis for the technological recommendation on increasing the thickness of the second layer material to decrease the probability of possible in-sintering damage due to excessive tensile stress buildup.

Figure 6 includes another example of the usage of the developed model framework for controlling the cosintering outcomes. It shows the dependence of the final normalized curvature $\bar{\kappa} = \kappa/[1/(h_{01} + h_{02})]$ (at $\tau_s = 10$) on the initial layer thickness ratio χ. It is assumed that the initial layer porosities are $\theta_{01} = 0.3$, $\theta_{02} = 0.5$. Two representative cases are considered: layers composed of the same material ($\lambda = 1$, $\xi = 1$); and the layers composed of different materials and hence different sinterabilities ($\lambda = \frac{3}{2}, \xi = \frac{2}{3}$ – it is again assumed that the difference in the free sintering rates is due to the difference in shear viscosities of the fully dense material substances).

The results shown in Fig. 6 indicate that the final curvature can be controlled by manipulating the initial layer thickness ratio. By increasing the thickness of the second layer one can significantly reduce the residual curvature. In the limiting case, the curvature goes to zero, when the thickness of the first layer is negligible compared with the thickness of the second layer and vice versa. The calculation results indicate also that intrinsic material sinterability may be manipulated to counteract or enhance the sinterability due to the porosity level (by choosing an appropriate level of the initial

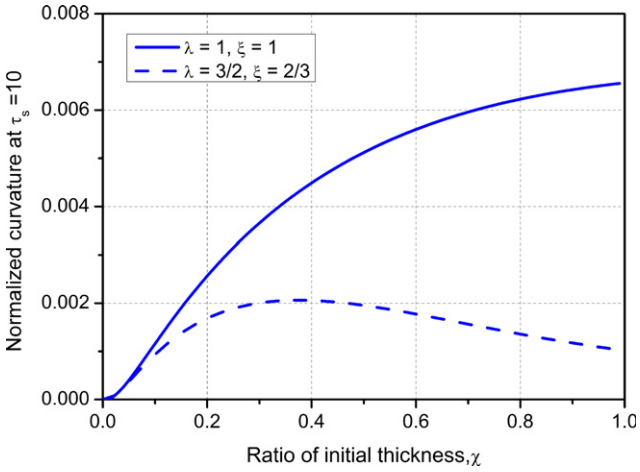

Fig. 6. The dependence of the final normalized curvature (at $\tau_s = 10$) of the sintered bilayered composite on the initial layer thickness ratio: it is assumed that the initial layer porosities are $\theta_{01} = 0.3$, $\theta_{02} = 0.5$.

porosity). The former principle (counteraction) can be naturally utilized for equalizing the shrinkage rates in both layers and thereby for the reduction in the final curvature. Interestingly, Fig. 6 demonstrates that the latter principle (enhancement) can be also employed for decreasing the final distortion level. Indeed, when switching from the same material system ($\lambda = 1$, $\xi = 1$) to the system composed of materials with different sinterabilities ($\lambda = \frac{3}{2}, \xi = \frac{2}{3}$), the final normalized curvature level drops on average by a factor of 3. This is the result of the rapid densification of the layer 2 followed by the consecutive reversal of the bending direction due to the continuing shrinkage of the layer 1 (similar to the effect reflected in Fig. 4).

It should be noted that the results of the calculations shown in Figs. 3–6 are based on the assumption that the parameters λ and ξ are constant, which corresponds to the conditions of isothermal sintering. In the case of sintering with varying temperature (e.g., iso-rate sintering), the specific time of sintering should be determined based on one of the layers and hence based on the evolving values of the parameters λ and ξ too.

VI. Conclusions

A model framework enabling engineering level solutions of the problems of sintering of bi and trilayered porous systems has been developed. Two types of solutions are suggested based on uniform and linear strain distributions across the thickness of each layer. The capabilities of the modeling framework are explained by two types of bilayer systems sintered in isothermal conditions. It is shown that the solutions from the uniform as well as linear strain distributions across the layers agree well. The elaborated solutions allow not only the predictions but also optimizations of the sintering outcomes by controlling the system initial geometry and structure characteristics as well as by adjusting the sintering regime.

Acknowledgments

The authors thank the Danish Council for Independent Research, Technology, and Production Sciences (FTP), which is part of the Danish Agency for Science, Technology, and Innovation (FI) (project #09-072888), for sponsoring the OPTIMAC research work. The research leading to these results has also received funding from the European Union's Seventh Framework Programme FP7/2007-2013 under grant agreement no. 228701 (NASA-OTM). The support of US National Science Foundation Division of Civil, Mechanical Systems, and Manufacturing Innovations (NSF grant no. CMMI 1234114) and Division of Materials Research (NSF grant no. DMR 0705914) is gratefully appreciated. The support of the Ministry of Science and Education of Russian Federation (grant Contract 11.G34.31.0051) is gratefully appreciated. The support by the US Department of Energy, Division of Materials Science and Engineering (DOE Award DE-SC0008581), is also gratefully appreciated.

References

[1]M. Chiang, J. Jean, and S. Ling, "The Effect of Anisotropic Shrinkage in Tape-Cast low-Temperature Cofired Ceramics on Camber Development of Bilayer Laminates," *J. Am. Ceram. Soc.*, **94**, 683–6 (2011).

[2]J. Chang, O. Guillon, J. Rödel, and S. Kang, "Characterization of Warpage Behaviour of Gd-Doped Ceria/NiO–Yttria Stabilized Zirconia bi-Layer Samples for Solid Oxide Fuel Cell Application," *J. Power Sources*, **185**, 759–64 (2008).

[3]G. Jung, C. Wei, A. Su, F. Weng, Y. C. Hsu,and S. Chan, Effect of Cosintering of Anode-Electrolyte Bilayer on the Fabrication of Anode-Supported Solid Oxide Fuel Cells, *J. Solid State Electrochem.*, **12**, 1605–10 (2008).

[4]Q. Liu, K. Khor, S. Chan, and X. Chen, "Anode-Supported Solid Oxide Fuel Cell With Yttria-Stabilized Zirconia/Gadolinia-Doped Ceria Bilayer Electrolyte Prepared by wet Ceramic co-Sintering Process," *J. Power Sources*, **162**, 1036–42 (2006).

[5]H. Li, C. Xia, X. Fang, X. He, X. Wei, and G. Meng, "Co-Sintering of SDC/NiO-SDC bi-Layers Prepared by Tape Casting," *Key Eng. Mater.*, **280–283**, 779–84 (2005).

[6]P. Cai, D. Green, and G. Messing, "Constrained Densification of Alumina/Zirconia Hybrid Laminates, I: Experimental Observations of Processing Defects," *J. Am. Ceram. Soc.*, **80**, 1929–39 (1997).

[7]P. Cai, D. Green, and G. Messing, "Constrained Densification of Alumina/Zirconia Hybrid Laminates, II: Viscoelastic Stress Computation," *J. Am. Ceram. Soc.*, **80**, 1940–8 (1997).

[8]D. Green, P. Cai, and G. Messing, "Residual Stresses in Alumina-Zirconia Laminates," *J. Eur. Ceram. Soc.*, **19**, 2511–7 (1999).

[9]R. Zuo, E. Aulbach, and J. Rödel, "Shrinkage-Free Sintering of low-Temperature Cofired Ceramics by Loading Dilatometry," *Acta Mater.*, **51**, 4563–74 (2003).

[10]R. Hsu and J. Jean, "Key Factors Controlling Camber Behavior During the Cofiring of bi-Layer Ceramic Dielectric Laminates," *J. Am. Ceram. Soc.*, **88**, 2429–34 (2005).

[11]D. Ravi and D. Green, "Sintering Stresses and Distortion Produced by Density Differences in bi-Layer Structures," *J. Eur. Ceram. Soc.*, **26**, 17–25 (2006).

[12]S. Schoenberg, D. Green, A. Segall, G. Messing, A. Grader, and P. Halleck, "Stresses and Distortion due to Green Density Gradients During Densification," *J. Am. Ceram. Soc.*, **89**, 3027–33 (2006).

[13]E. Olevsky, V. Tikare, and T. Garino, "Multi-Scale Modeling of Sintering – A Review," *J. Am. Ceram. Soc.*, **89**, 1914–22 (2006).

[14]J. Feng, M. Qiu, Y. Fan, and N. Xu, "The Effect of Membrane Thickness on the co-Sintering Process of bi-Layer ZrO2/Al2O3 Membrane," *J. Membr. Sci.*, **305**, 20–6 (2007).

[15]T. Cheng and R. Raj, "Flaw Generation During Constrained Sintering of Metal–Ceramic and Metal–Glass Multilayer Films," *J. Am. Ceram. Soc.*, **72**, 1649–55 (1989).

[16]G. Lu, R. Sutterlin, and T. Gupta, "Effect of Mismatched Sintering Kinetics on Camber in a low-Temperature Cofired Ceramic Package," *J. Am. Ceram. Soc.*, **76**, 1907–14 (1993).

[17]J. Jean and C. Chang, "Camber Development During co-Firing Ag-Based low Dielectric-Constant Ceramic Package," *J. Mater. Res.*, **12**, 2743–50 (1997).

[18]J. Jean and C. Chang, "Co-Firing Kinetics and Mechanisms of an Ag-Metallized Ceramic-Filled Glass Electronic Package," *J. Am. Ceram. Soc.*, **80**, 3084–92 (1997).

[19]C. Chang and J. Jean, "Effects of Silver-Paste Formulation on Camber Development During the Cofiring of a Silver-Based, low-Temperature-Cofired Ceramic Package," *J. Am. Ceram. Soc.*, **81**, 2805–14 (1998).

[20]J. Arterberry, E. Olevsky, and V. Tikare, "Co-Firing of Multilayer Ceramic Composites," *Adv. Powder. Metall. Part. Mater.*, 1-202, 12 pp (2001).

[21]E. Olevsky, A. Maximenko, J. Arterberry, and V. Tikare, "Sintering of Multilayer Powder Composites: Distortion and Damage Control," *Adv. Powder. Metall. Part. Mater.*, 5-156, 8 pp (2002).

[22]A. Maximenko and E. Olevsky, "Damage in Sintering of Powder Laminates," pp. 197–201 in *Proc. Intern. Conf. On Process Modeling in Powd. Met. And Partic. Mater.*, Edited by A. Lawley and J. E. Smugeresky. MPIF, Newport-Beach, 2002.

[23]J. Kanters, U. Eisele, and J. Rödel, "Cosintering Simulation and Experimentation: Case Study of Nanocrystalline Zirconia," *J. Am. Ceram. Soc.*, **84**, 2757–63 (2001).

[24]J. Ollagnier, O. Guillon, and J. Rödel, "Constrained Sintering of a Glass Ceramic Composite: I. Asymmetric Laminate," *J. Am. Ceram. Soc.*, **93**, 74–81 (2010).

[25]J. Ollagnier, D. Green, O. Guillon, and J. Rödel, "Constrained Sintering of a Glass Ceramic Composite: II. Symmetric Laminate," *J. Am. Ceram. Soc.*, **92**, 2900–6 (2009).

[26]T. Molla, H. Frandsen, R. Bjørk, D. Ni, E. Olevsky, and N. Pryds, "Modeling Kinetics of Distortion in Porous Bilayered Structures," *J. Eur. Ceram. Soc.*, **33**, 1297–305 (2013).

[27]R. Bordia and G. Scherer, "On Constrained Sintering.I. Constitutive Model for a Sintering Body," *Acta Metall.*, **36**, 2393–7 (1988).

[28]E. Olevsky and V. Skorohod, "Some Questions of Sintering Kinetics Under External Forces Influence in Technological and Structural Plasticity of Porous Materials," *IPMS UNAS*, 97–103 (1988).

[29]E. Olevsky, "Theory of Sintering: From Discrete to Continuum," *Mater. Sci. Eng., R*, **23**, 41–100 (1998).

[30]G. Stoney, "The Tension of Metallic Films Deposited by Electrolysis," *Proc. Roy. Soc. Lond. A*, **82**, 172–5 (1909).

[31]S. Timoshenko, "Analysis of Bi-Metal Thermostats," *J. Opt. Soc. Am. & Rev. Sci. Instrum.*, **11**, 233–55 (1925).

[32]V. Tikare, M. Braginsky, D. Bouvard, and A. Vagnon, "Numerical Simulation of Microstructural Evolution During Sintering at the Mesoscale in a 3D Powder Compact," *Comput. Mater. Sci.*, **48**, 317–25 (2010).

[33]R. Bjørk, V. Tikare, H. Frandsen, and N. Pryds, "The Sintering Behavior of Close-Packed Spheres," *Script. Mater*, **67**, 81–4 (2012).

[34]R. Bjørk, V. Tikare, H. Frandsen, and N. Pryds, "The Effect of Particle Size Distributions on the Microstructural Evolution During Sintering," *J. Am. Ceram. Soc.*, **96**, 103–10 (2013).

[35]D. Ni, E. Olevsky, V. Esposito, T. Molla, S. Foghmoes, R. Bjørk, H. Frandsen, E. Aleksandrova, and N. Pryds, "Sintering of Multilayered Porous Structures Part II: Experiment and Model Application," *J. Am. Ceram. Soc.*, in press, doi:10.1111/jace.12374. □

C. PAPER-III

D.W. Ni, E. Olevsky, V. Esposito, T.T. Molla, S.P. Foghmoes, R. Bjørk, H.L. Frandsen, E. Alexandrova and N. Pryds, "Sintering of multi-layered porous structures: Part II-Experiments and model applications," *J Am Ceram Soc*, **96** [8] 2666–2673 (2013)

journal

J. Am. Ceram. Soc., **96** [8] 2666–2673 (2013)
DOI: 10.1111/jace.12374

Sintering of Multilayered Porous Structures: Part II–Experiments and Model Applications

De Wei Ni,[‡,†] Eugene Olevsky,[§,¶] Vincenzo Esposito,[‡] Tesfaye T. Molla,[‡] Søren P. V. Foghmoes,[‡] Rasmus Bjørk,[‡] Henrik L. Frandsen,[‡] Elena Aleksandrova,[¶] and Nini Pryds[‡]

[‡]Department of Energy Conversion and Storage, Technical University of Denmark, Frederiksborgvej 399, P.O. Box 49, Roskilde DK-4000, Denmark

[§]Mechanical Engineering Department, San Diego State University, 5500 Campanile Dr., San Diego, California 92182-1323

[¶]Key Laboratory for Electromagnetic Field Assisted Processing of Novel Materials, Moscow Engineering Physics Institute, Moscow 115409, Russia

Experimental analyses of shrinkage and distortion kinetics during sintering of bilayered porous and dense gadolinium-doped ceria $Ce_{0.9}Gd_{0.1}O_{1.95-\delta}$ structures are carried out, and compared with the theoretical models developed in Part I of this work. A novel approach is developed for the determination of the shear viscosities ratio of the layer fully dense materials. This original technique enables the derivation of all the input parameters for the bilayer sintering modeling from one set of optical dilatometry measurements, including the conversion between real and specific times of sintering, the layers' relative sintering intensity, and the shear viscosities ratio of the layer fully dense materials. These optical dilatometry measurements are conducted simultaneously for each individual layer and for a symmetric trilayered porous structure based on the two layers utilized in the bilayered system. The obtained modeling predictions indicate satisfactory agreement with the results of sintering of a bilayered cerium–gadolinium oxide system in terms of distortion and shrinkage kinetics.

I. Introduction

ALIOVALENT-DOPED ceria is an important class of materials that offers high stability, tolerance against harsh environments, and high ionic and electronic conductivity at high temperatures. Particularly, trivalent-acceptor–doped ceria is used in several electrochemical applications because at high temperatures and under low oxygen activity, e.g., in fuel atmospheres, it is a mixed ionic and electronic conductor (MIEC), whereas in oxidative conditions at intermediate temperatures it is an almost pure and fast ionic conductor. Gadolinium 10% molar-doped ceria $Ce_{0.9}Gd_{0.1}O_{1.95-\delta}$ (CGO10) has attracted much interest as electrolyte material for intermediate-temperature solid oxide fuel cells (IT-SOFCs), as ceramic component in Ni-based ionic conductor-composite anodes in SOFC and as oxygen transport membranes (OTM) for high-temperatures applications in hydrocarbons conversion.[1–7] Particularly in the latter application, the partial oxidation with direct feed of pure oxygen from OTM is an efficient and clean process which results in the desired product ratio of H_2/CO suitable for Fischer–Tropsch synthesis.[7] For many of such technologies CGO is shaped as dense membrane components to separate different gases reacting in the electrochemical processes. High performances in real operative conditions are usually ensured by reducing the thickness of the membrane film to few microns. Thin films usually need to be supported mechanically by thicker layers in multilayer systems where a support layer is used. The main requirements for the support layer are to be chemically compatible, mechanically stable, porous to allow the diffusion of the gas species toward the membrane, and to have comparable coefficient of thermal expansion (CTE) with the membrane layer to avoid critical thermal stresses. The processing route for the multilayer systems' fabrication typically includes shaping of each layer as tapes by tape-casting procedure from designed slurries.[7] The tapes are then laminated or cocasted together in a multilayer system to be finally sintered simultaneously by a cofiring sintering procedure. The multilayer system after sintering in many cases should be flat to allow further processing steps such as the deposition of porous catalysts, electrodes, etc., as well as to ensure a proper stacking and sealing of the membrane components in the final device.

The selection of the materials for the porous support layer of CGO10 membrane is, however, not trivial because CGO10 has relatively low mechanical strength, and any thermal expansion difference in the support layer which would exceed 0.1%–0.3% can create tensile stresses in the membrane that may well be critical for its integrity.[8–11] Moreover, ceria-based materials often undergoes a large chemical expansion in chemically reducing conditions[6]; this can drastically limit the choice of materials compatible with CGO for the support and the choice of other layers. Therefore, designing and processing of multilayer systems should involve crucial steps to overcome such issues. An effective and reliable solution commonly adopted to control critical stresses between the layers is to use the same materials for both the dense membrane and the porous support. However, although the bilayered CGO10 with different density level does not present CTE or chemical expansion mismatches, different densification rates and total shrinkage of the layers during cofiring, due to the different porosity level, can still easily lead to shape distortions and stress buildup. The cofiring procedure is thus highly important in the ceramic multilayer technology and a full control of the sintering parameters is particularly essential to ensure the necessary flatness (or specific configuration) and quality of the final shape. In Part I of this work, a theoretical model analyzing the shrinkage and distortion kinetics during sintering of bilayered structures has been developed.[12] Here, it is applied to study the cofiring of bilayered porous support and dense membrane CGO10 structures and the modeling results are compared with the experimentally observed results.

R. Bordia—contributing editor

Manuscript No. 32473. Received December 14, 2012; approved April 10, 2013.
[†]Author to whom correspondence should be addressed. e-mail: dwei@dtu.dk and deweini2013@gmail.com

II. Sintering of Porous CGO Laminates: Experimentation

Powders with ultra–low surface area (ULSA) of CGO10 (Rhodia S.A., La Rochelle Cedex, France) were used for the development of the membrane and support layers. The specific surface areas of the starting powder were measured by the BET method to be 6.6 m^2/g (particle size d_{50}: ~0.2 μm). Some CGO10 powder was further heat-treated at 1100°C for 2 h and then milled. The specific surface area was reduced to ~5 m^2/g with homogenous particle size distribution (d_{50}: ~0.4 μm). For the preparation of the membrane and support layers, Co_3O_4 powder was used as sintering aid. This was added to the CGO10 dry powder in 2% molar content and mixed by mechanical milling. The resulting powder mixture was dispersed in a methylehylketone and ethanol (MEKET)-based suspension with polyvinylpyrrolidone (PVP) as dispersant and polyvinylbutyral (PVB) as binder.[7] The resulting slurry for the tape casting was homogenized by ball-milling for 72 h. For the preparation of the dense membrane, the precalcined powders were combined using the raw CGO10 powders with a ratio of 1:1. CGO10 slurry for the porous support structure was prepared in a similar way, but using only precalcined powders and graphite powder (V-UF1 99.9, Graphit Kropfmühl, Hauzenberg, Germany) as the pore former. Slurries for the preparation of dense membranes and porous supports were tape casted on Mylar® foil at constant speed (30 cm/min) in a controlled environment with a blade clearance around 300 μm for dense membranes and 1200 μm for porous support. Below, tape materials for dense membrane and porous support are named CGO_D and CGO_P, respectively. Final thickness of the CGO_D was approximately 150 μm and the support CGO_P was around 500 μm (green tapes after drying). Before sintering, a slow debinder cycle at 400°C was applied to avoid damage of the tapes, as will be discussed in detail in Section II (3). Further reduction in the thickness due to the debinding process led to estimated thickness of around 30 and 400 μm for CGO_D and CGO_P, respectively.

The microstructure of the membrane thin film and support CGO10 layers was investigated by field-emission scanning electron microscopy (FE-SEM; Supra, Carl Zeiss, Oberkochen, Germany). Freeware software ImageJ® was used for the image analysis of the porosity from the SEM images with the aim to have a comparison with the porosity calculated from the dilatometry data. The image analysis of the SEM data was carried out by using a binary mask with a suitable threshold value at grain-pore boundaries. However, for porosity in the nano-range, the contrast between the grains and the pores was provided with low resolution, causing a large uncertainty in the estimation of the porosity. Also, in general, the porosity determined from two-dimensional slices of a sample may be overestimated.[13] The SEM images were taken at random positions in the samples, and the samples are assumed to be uniform in terms of the microstructure.

(1) Material Systems

As shown in the companion study,[12] the analysis of the shrinkage kinetics in a symmetric trilayer system along with the dilatometry data on the free sintering of the individual-layer materials allows the determination of the complete set of constitutive parameters for the study of the shrinkage and distortion during sintering of the respective bilayered composite. Therefore, the conducted experimental efforts involved the tests necessary for obtaining the input parameters for modeling (sintering of the individual-layer materials and sintering of a symmetric trilayered laminate) as well as the test necessary for the model result validation (sintering of a bilayered laminate). All the above-mentioned tests could be conducted simultaneously under the same conditions provided by the optical dilatometry system described below.

Table I. Geometrical Parameters and Porosities Before Debinding and After Sintering for the Laminated Samples Obtained by the Optical Dilatometry Measurements†

Geometric parameter		Symmetric trilayered laminate	Asymmetric bilayered laminate
Initial size	h_{01} (CGO_D)	0.15 mm	0.15 mm
	h_{02} (CGO_P)	0.50 mm	0.50 mm
	l_0	27.4 mm	24.5 mm
	b_0	4.3 mm	5.1 mm
Final size	$h_{1,f}$ (CGO_D)	0.02 mm	0.02 mm
	$h_{2,f}$ (CGO_P)	0.28 mm	0.28 mm
	l_f	20.2 mm	19.3 mm
	b_f	2.9 mm	3.3 mm
	$\theta_{1,f}$ (CGO_D)	1.0 ± 0.4%	1.6 ± 0.3%
	$\theta_{2,f}$ (CGO_P)	27.7 ± 3.6%	27.3 ± 3.6%

†l, b, and h are the length, width, and thickness of the multilayer, respectively. The subscript 0 and f refer to the initial and final size, respectively. The subscript 1 and 2 refer to the layer CGO_D and CGO_P, respectively. The porosity (θ) was evaluated from SEM images.

The multilayered CGO10 samples used in the optical dilatometry and other sintering tests were assembled by the lamination of the CGO_D and CGO_P tapes together, whereas individual materials were prepared by tight rolling and pressing each tape separately. Individual CGO_D and CGO_P tapes were rolled and pressed to obtain "bulky" sample of the thin layers which could be measured using dilatometry. Final shapes of the samples were obtained by cutting the rolled tapes in cylindrical chips of about 3–5 mm in length and 2–3 mm in diameter. The asymmetric CGO_D–CGO_P bilayered sample was obtained by colamination of the CGO_D and CGO_P green tapes, both oriented along the tape-casting direction. A further lamination of the CGO_P tape on the CGO_D–CGO_P bilayer sample was carried out to assemble the symmetric CGO_P-CGO_D–CGO_P trilayered system. Final shape of the laminated samples was obtained by stamping and punching rectangular shapes out from the green material. Table I shows geometrical size and porosities of laminated samples before debinding (green after drying) and the final size after sintering. Debinding process of the sample was carried out directly during the optical dilatometry measurement. Actual sizes of the samples after debinding were not measured because of the shape distortions and the poor mechanical properties of the samples after the debinding process. Therefore, SEM observations and the measurement of the individual-layer thickness before sintering were performed on presintered samples at 875°C for 2 h. Here, both the bilayer and trilayer samples had an average thickness of about 26 and 400 μm for CGO_D and CGO_P, respectively (i.e., thickness of individual CGO_D and CGO_P layers after debinding before sintering). The microstructural evolution during the treatment at 875°C for 2 h is assumed not to have introduced significant changes to the microstructure.

(2) Experimental Setup for Processing and Sintering Video Monitoring

Dilatometric measurement was performed simultaneously on the different samples in an optical dilatometer (TOMMI, Fraunhofer ISC, Würzburg, Germany). This allows for the sample shape evolution during sintering to be followed *in situ*, by simply collecting the sequential images (i.e., a video sequence) of the samples' silhouettes projected by a source of visible light onto a high definition camera. After heat treatment, the asymmetric laminate shows large bending due to the different shrinkage of the CGO_D and CGO_P layers. At the same time, the symmetric trilayered laminate and the rolled tapes showed shape stability maintaining a similar flat shape during the densification. Rolled tape samples were oriented

along the length of the sample lying in the projection plane in the way to allow measuring the evolution of the samples' shrinkage in the direction of the length of the cylindrical samples. TOMMI's software included tools to measure the shrinkage of the thick rolled tape along different directions (width and height). The measurement of the shrinkage of the thin symmetric trilayered system was performed manually using the image frames taken at different temperatures.

(3) Processing Conditions and Results

The complete thermal cycle of the processing of the multilayered systems and rolled tapes, including debinding step and sintering, was performed directly in the optical dilatometer to avoid moving the samples with possible mechanical failure after the debinding step. The thermal cofiring cyclogram used in the optical dilatometry measurement and in the fabrication of samples used for the SEM investigation of microstructures includes debinding, sintering, and cooling cycles. The debinding cycle includes a slow heating ramp at 0.25°C/min step from r.t. to 400°C and an isothermal treatment step at 400°C for 4 h aimed to remove the organic component from the samples. Sintering cycle was performed by an iso-rate heating ramp step up to 1100°C at 0.834°C/min rate, followed by an isothermal treatment step at 1100°C for 4 h. The cooling of the samples was at 1.67°C/min.

(A) Free Sintering of Individual Layers: The optical dilatometry results were collected both as sequence of images of the samples' silhouettes (video) and as plots of the samples size and/or shape with time and temperature. Assuming the free sintering shrinkage isotropic, the relative density evolution is calculated based on the dilatometry data and on the measured final density of the sample, as estimated from SEM images, using the following equation:

$$\rho = \rho_f \frac{\left(1+\frac{(\Delta l)_f}{l_0}\right)^3}{\left(1+\frac{\Delta l}{l_0}\right)^3} \quad (1)$$

Figure 1(a) shows the densification process of CGO_D rolled tape measured by monitoring the shape evolution at TOMMI dilatometer as a function of time (red points) and temperature (black points) in the different steps of the sintering cycle, starting from 400°C. Data show a continuous densification of the CGO_D sample starting from a temperature of around 745°C with relative density (hereafter r.d.) values of around 56% as a result of the debinding process. Rapid increase in the density at 800°C–900°C (see point A at 875°C: r.d. 63%) is followed by an almost full densification at 1100°C already during the iso-rate heating (see also point B at 1100°C: r.d. 98%) and a completion of densification at the isothermal step at 1100°C (see point C at 1100°C: r.d. 100%). Low sintering temperatures for the CGO sample observed in Fig. 1(a) compared with conventional pure CGO in other works were attributed to both the homogenous dispersion of the CGO powder in the slurry [14] and to the use of cobalt oxide as the sintering aid.[15]

Figure 1(b) shows the densification process measured monitoring the shape evolution of the CGO_P rolled tape at TOMMI dilatometer as a function of time (red points) and temperature (black points) in the different steps of the sintering cycle. CGO_P sample shows a lower starting density (~24%) than CGO_D because of the large amount of the binder and the pore former used in the slurry. Similar to CGO_D, the densification of CGO_P was also activated at around 745°C but, due to the large amount of porosity, with a lower rate of the densification during the iso-rate step, which led to r.d. = 26% at 875°C [point A in Fig. 1(b)] and r.d. = 46% at 1100°C [point B, Fig. 1 (b)]. Isothermal sintering at 1100°C for 4 h left residual porosity in the layer of around 26% [r.d. = 74%, point C in Fig. 1(b)].

Relative density of CGO_D and CGO_P samples showed in Fig. 1 was calculated assuming that the shrinkage of the sample was isotropic and considering the geometrical features of the samples before and after the dilatometry. To support these calculations with a direct observation of the samples' microstructure, SEM observations were carried out on the postmeasured samples and on the samples treated following the same thermal cycle and interrupting the treatment at selected temperatures. Figure 2 shows SEM images of the CGO_P (a) and CGO_D (b) after dilatometry (bottom), with thermal cycle interrupted at 1100°C after 0.1 h and after a thermal treatment at 875°C for 2 h. As shown in Fig. 1, despite some further densification could occur at 875°C during the holding compared with the zero-time measurement in the dilatometry, 2 h holding was applied to ensure that the samples had necessary mechanical properties to allow for SEM preparation. SEM observation and image analysis confirmed the measurements at the optical dilatometer showing a full densification for CGO_D sample and r.d. = 72%~75% for the sample CGO_P postdilatometry. Estimation of porosity of the samples treated at 1100°C for 0.1 h by image analysis procedure confirmed the dilatometric results indicating an almost complete densification in CGO_D above 93% and a residual porosity of about 45% in CGO_P. The specimen can continue to densify during cooling, especially, if the experiment is interrupted at the highest sintering rate. That is why the porosity of CGO_P treated at 1100°C for 0.1 h is relatively lower compared with the dilatometry result [Fig. 1(b)]. Whereas this influence on CGO_D is negligible as it is almost fully densified after heat treatment at 1100°C for 0.1 h. As large amount of nano-metric porosity was still present in the samples at low temperatures [see also Fig. 2(a) and (b) top], image analysis failed to evaluate the relative density of the samples treated at 875°C. It is also found that

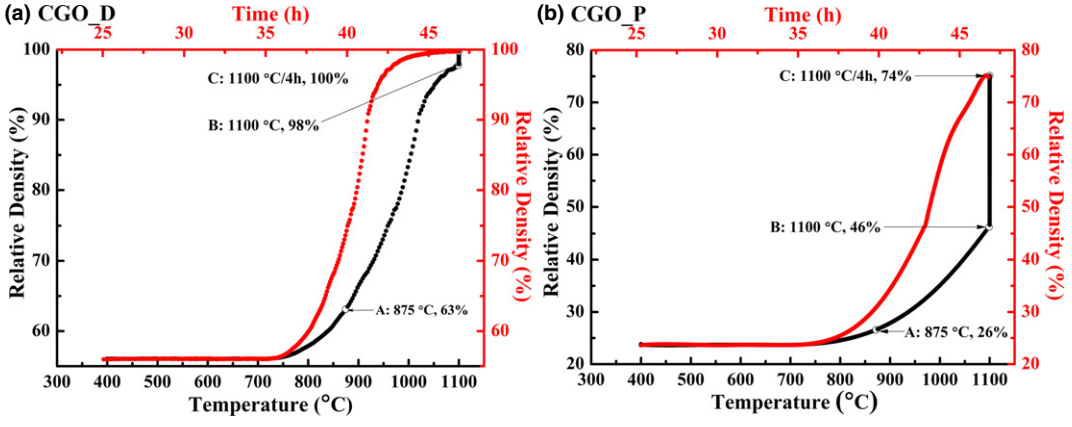

Fig. 1. Results of optical dilatometry for CGO_D (a) and CGO_P (b) free sintering.

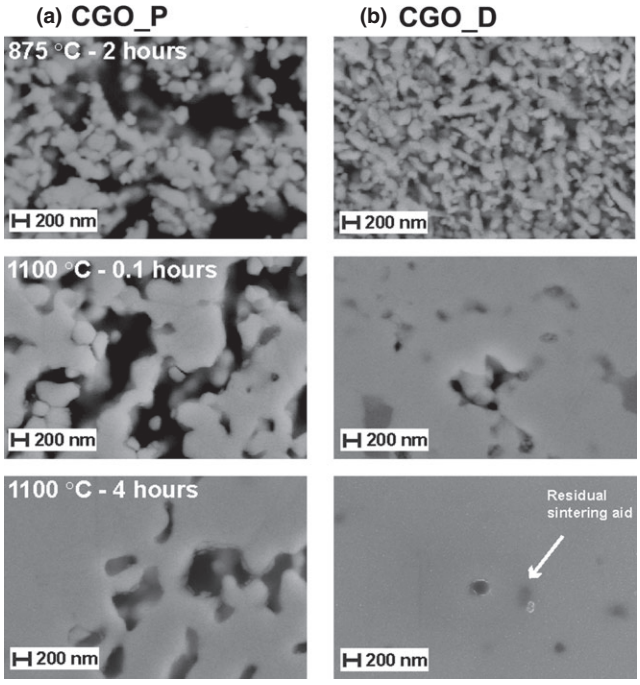

Fig. 2. Results of SEM characterization during sintering (interruptive) and postoptical dilatometry for (a) CGO_P rolled tape and (b) CGO_D rolled tape.

no anisotropic microstructure was observed in SEM images (Fig. 2). This validated that the assumption of isotropic shrinkage in relative density calculation is reasonable.

Some of the samples used in the study, especially for those samples treated at the higher temperatures, showed the presence of the cobalt oxide, which was used as the sintering aid, as an extraphase at grain boundaries or at triple points of the polished cross sections. An example of the cobalt oxide segregation is shown in Fig. 2(b) (arrows) where the presence of the extraphase was easily detected in the fully dense CGO_D matrix treated at 1100°C and in the postdilatometry structures.

(B) Sintering of Bilayered System: Figure 3 shows the shape evolution with time (red points) and temperature (black points) of the bilayered laminated system. The measured value was the maximum deflection R reached by the sample during debinding and sintering steps (see also pictures inserted in Fig. 3). The sample was placed with CGO_D layer at the top and CGO_P at the bottom in contact with the furnace. Conventionally for this work, *R* was taken positive with the sample bending downward and negative upward. Adopting such a convention it can be recognized that the sample bent in two different directions during the debinding process below 400°C. Shape distortion during debinding was expected and can usually be mitigated by smooth and slow heating treatments. Due to the debinding process, the sample resulted upward bent starting from 400°C up to 700°C. At higher temperatures during the iso-rate treatment, the cosintering of the layers occurred. At a first step, different shrinkage led to further contraction of the top layer (CGO_D) up to 980°C followed by a rapid inversion of the bending direction ascribed to a rapid shrinkage of the bottom layer (CGO_P) in the last part of the iso-rate treatment. At the last step of the process, the isothermal treatment at 1100°C for 4 h led to a slight and progressive reduction in *R* (red plot) due to a probable effect of creep, gravity, or further contraction of the CGO_P layer in the final stage of sintering.[16,17]

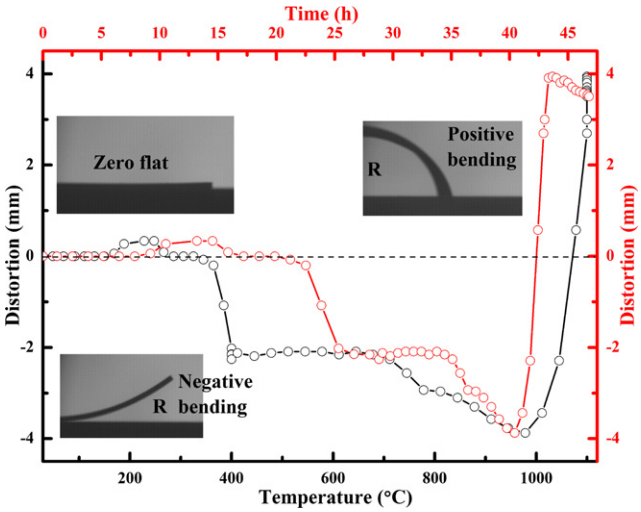

Fig. 3. Results of optical dilatometry for CGO_D–CGO_P bilayer system.

Figure 4 shows SEM observations on postdilatometry bilayered laminated specimen (bottom) and on the same sample treated following the thermal cycle and interrupted at 1100°C for 0.1 h and at 875°C after 2 h (top). The observation on the microstructures in Fig. 4 reveals the effect of the sintering heat treatment on the individual layers in the bilayered laminate. CGO_D resulted to be fully dense after the scheduled thermal treatment in accord with the postdilatometry (r.d. = 98.4 ± 0.3%) SEM analysis, although at 1100°C for 0.1 h it presented large fraction of nano-porosity uniformly spread in the cross section; CGO_P showed slightly higher porosity (2%–4%) compared with the free sintering of the individual CGO_P rolled tape (Fig. 2 bottom left). A comparison with the individual CGO_D sample in Fig. 2, treated under same conditions, points out a different degree of densification in the bilayered sample which was most probably due to the effect of stress (and strain) induced by the CGO_P support layer. To interpret such a behavior it is necessary to recognize the shape evolution of the bilayered sample showed in optical dilatometry in Fig. 3: the densification of the support layer is fully activated at temperatures above 980°C leading to a remarkable bending of the sample downward. Such a change in the sample shape will lead to an imposed stress on the CGO_D layer affecting its densifica-

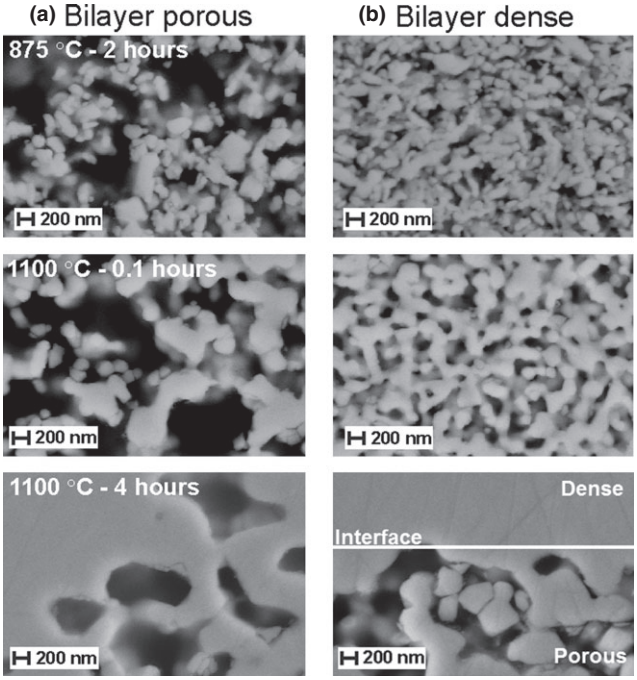

Fig. 4. Results of SEM characterization during sintering (interruptive) and postoptical dilatometry of the CGO_D–CGO_P bilayered system for (a) CGO_P and (b) CGO_D.

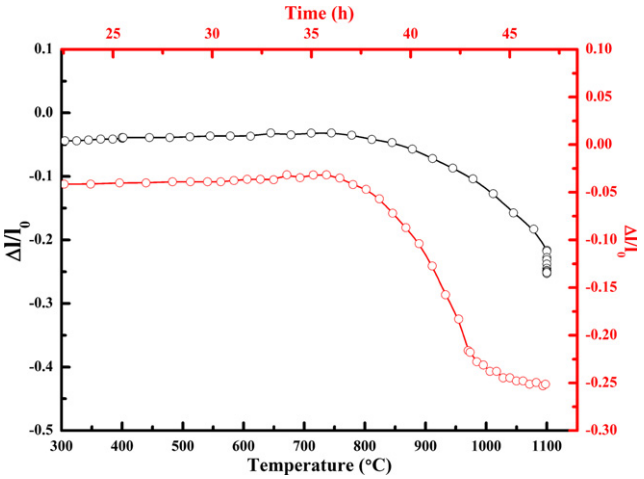

Fig. 5. Results of optical dilatometry for CGO_P–CGO_D–CGO_P trilayer system.

tion process. The top CGO_D layer, although ultimately subjected to shrinkage, was thus under a tensile stress induced by the shape distortion. These conditions led also to a slight increase in the layer thickness from around 26 μm at 875°C for 2 h to above 27 μm at 1100°C for 0.1 h, as expected for mass conservation.

(C) Sintering of Symmetric Trilayered System: Compared with sintering of a bilayered laminate, a different stress state was observed in the symmetric trilayered system. Figure 5 shows the relative length (l) shrinkage of the symmetric trilayered CGO_P–CGO_D–CGO_P laminate with time (red color) and temperature (black color) during the thermal cycle. Conversely, to the asymmetric sample, the trilayered laminate maintained a flat shape both during the debinding and along all the sintering steps. A slight relative shrinkage around 5% of the sample initial size was observed during the debinding step. Further shrinkage of around 15% (total 20%) was observed at temperatures above 850°C with a continuous contraction in the iso-rate step up to 1100°C. A further densification of about 5% (total 25%) was also resulted in the final isothermal step.

Figure 6 shows SEM analysis of the postdilatometry trilayered laminated specimen (bottom) and of the same sample treated following the thermal cycle interrupted at 1100°C for 0.1 h and at 875°C for 2 h. For both the CGO_P and CGO_D layers, the postdilatometry images in Fig. 6 show comparable microstructures to those obtained in the bilayered sample (Fig. 4) and to the individual tapes rolled samples (Fig. 2). All the CGO_D postdilatometry specimens (trilayered, bilayered, and individual tapes rolled samples) were fully dense. As shown in Table I, the amount of porosity in CGO_P in the trilayered laminated postdilatometry specimens (27.3 ± 3.6%) resulted in comparable values with those in the CGO_P in the bilayer postdilatometry specimens (27.7 ± 3.6%), but slightly higher than those for the individual CGO_P rolled-sample postdilatometry specimens (~26%). This fact indicates a certain influence of the stress developed in the multilayer on the final microstructures. As shown in Fig. 6, the CGO_D layer reached almost full densification after the interrupted treatment at 1100°C for 0.1 h (r.d. = 99.0 ± 0.4%, as shown in Table I). Such a result indicates that the stress/strain generated during the iso-rate treatment of the symmetric configuration is favorable to the densification of the CGO_D layer, which was opposite to the conditions observed and discussed above for the asymmetric bilayered sample [Fig. 4(b)]. Moreover, a general overview and comparison between the microstructures showed in Figs. 6(a) and (b) for the CGO_P and CGO_D at 875°C for 2 h with the other samples treated under the same conditions shown in Figs. 2 and 4 indicated that the layers have comparable features after debinding and that the effect of grain growth is negligible.

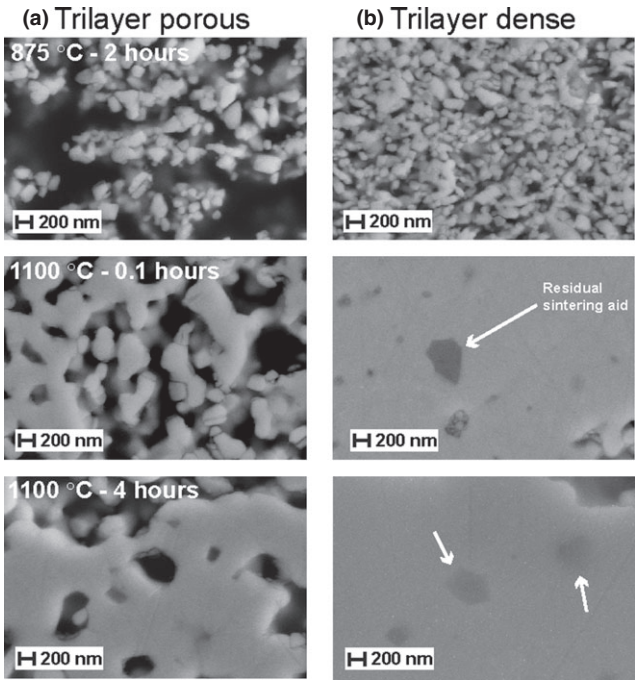

Fig. 6. Results of SEM characterization during sintering (interruptive) and postoptical dilatometry of the CGO_P–CGO_D–CGO_P trilayered system for (a) CGO_P and (b) CGO_D.

III. Assessment of Modeling and Experimental Data

(1) Determination of Input Parameters for Modeling

Based on the theoretical framework described in Part I of this work,[12] the modeling of sintering of a bilayered system requires nine input parameters. Those include four initial dimensions (layer initial length l_0, initial width b_0, and two initial layer thicknesses:h_{01} *and* h_{02}), two initial porosities θ_{01} and θ_{02}, and three sintering constitutive parameters: the conversion factor P_{L01}/η_{01} from the real time to specific time (τ_s) of sintering, the layers' relative sintering intensity λ, and the ratio ξ of the shear viscosities of the fully dense layer materials. The geometrical parameters and porosities are listed in Table I. In the modeling processes, the initial porosities θ_{01} and $\theta_{02}$of the bilayer are assumed to be similar to the trilayer sample.

The conversion between the real and specific time of sintering can be obtained based on expression (8): $\theta = \theta_0 \exp(-\frac{3}{8}\tau_s)$ obtained in the companion study.[12] Figure 7 shows the results of the free sintering conducted for two individual layers (CGO_D and CGO_P) in terms of the real time of sintering and the specific time of sintering as a function of temperature. The determined specific time of sintering is based on the dilatometry data for the CGO_P material. The curves shown in Fig. 7(a) represent the respective truncated portions of the curves provided by Fig. 1. The truncation, which provides the analysis starting point at about 745°C, has been conducted to distinguish the pure sintering densification stage of processing avoiding the debinding-related phenomena and omitting the initial sintering period when no essential shrinkage is present.

The layers' relative sintering intensity λ is based on eq. (34) in the companion study.[12] It can be determined from the expression:$\lambda = \frac{\theta_1}{\theta_2}\frac{d\theta_2}{d\theta_1}$. To find the derivative $\frac{d\theta_2}{d\theta_1}$ in the latter relationship, the layer porosities can be plotted with respect to each other (Fig. 8). The conducted regression provided the analytical relationship:$\theta_2 = (0.093 \pm 0.002)\ln(\theta_1) + (0.835 \pm 0.006)$, which in turn, resulted in the following assessment:$\lambda = \frac{0.093}{\theta_2}$. The fitted expression is purely chosen for the quality of the fit and is not based on any physical

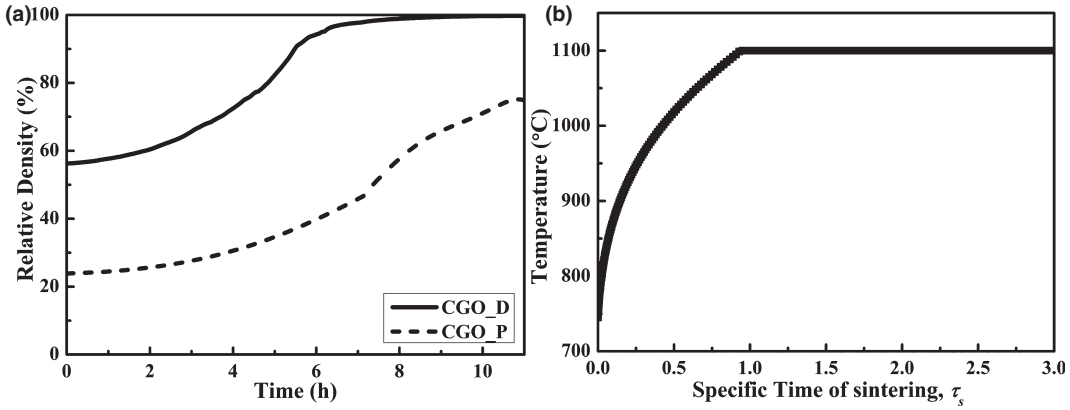

Fig. 7. (a) Results of optical dilatometry for free sintering of CGO_P and CGO_D tapes in terms of the real time of sintering; (b) sintering temperature regime in terms of the specific time of sintering.

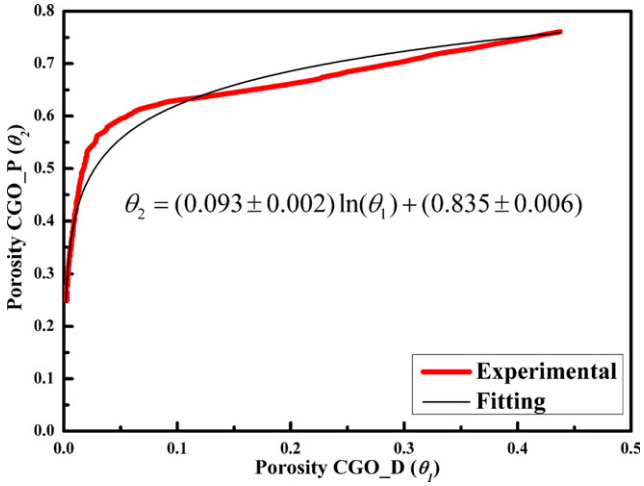

Fig. 8. Regression of the experimental data utilized in the derivation of the coefficient of the relative sintering intensity λ.

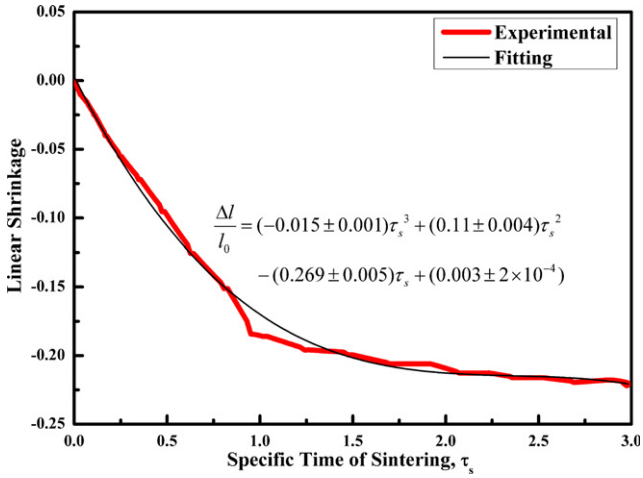

Fig. 9. Regression of the experimental data on the linear shrinkage in the symmetric trilayer CGO_P–CGO_D–CGO_P system.

model. The regression of the obtained data provides the expression for λ as a function of specific time of sintering: $\lambda = 0.1224\exp(0.375\tau_s)$.

The determination of the ratio ξ of the shear viscosities of the fully dense layer materials is based on eq. (57) of the companion study[12] derived for the case of the sintering of a symmetric trilayer system. To utilize the above-mentioned equation, the normalized linear shrinkage rate $d\bar{l}/d\tau_s$, the evolution of the ratio of the normalized thicknesses $\bar{h}_2/\bar{h}_1$, and the evolution of layer porosities $\theta_1$and θ_2 should be known. The linear shrinkage rate of the symmetric trilayer CGO_P–CGO_D–CGO_P system is provided by the optical dilatometry (Fig. 5) and plotted versus specific time of sintering in Fig. 9. The regression of the experimental data provides:

$$\frac{\Delta l}{l_0} = (-0.015 \pm 0.001)\tau_s^3 + (0.11 \pm 0.004)\tau_s^2 - (0.269 \pm 0.005)\tau_s + (0.003 \pm 2 \times 10^{-4})$$

Again, the fitted expression is purely chosen for the quality of the fit and is not based on any physical model. Thus, the normalized linear shrinkage rate can be described by the relationship:

$$\frac{d\bar{l}}{d\tau_s} = -0.0477\tau_s^2 + 0.2256\tau_s - 0.2698$$

The optical dilatometry data does not contain information on the kinetics of the porosity and layer thickness evolution. The conducted SEM characterization of the sintered specimens as well as the initial specimen geometry data provide the initial and final values of layer thicknesses, tape widths and porosities (Table I). It should be noted that the experimentally observed differences in the shrinkage rates along the tape width and length directions indicate an impact of sintering anisotropy phenomena, which are not taken into account in this work. Assuming linear kinetics of layer thicknesses ($\bar{h}_1$and$\bar{h}_2$) and the same shrinkage kinetics between the length and width evolution: $\bar{b} = \bar{l}$, one can determine the evolution of the layer porosities based on the mass conservation for each layer:

$$\theta_i = 1 - (1 - \theta_{i,f})\frac{\bar{l}_f\bar{b}_f\bar{h}_{i,f}}{\bar{l}_x\bar{b}_x\bar{h}_i}, i = 1, 2 \text{ and } \theta_{i,f}$$

is taken from Table I. The results of the respective estimation of the sintering kinetics of the trilayer dimensions and porosities are shown in Fig. 10. During sintering of the symmetric trilayer, the shrinkage of CGO_P was constrained by CGO_D in the length and width directions, whereas their shrinkage in the thickness direction was free. That makes the strain in the thickness direction of the CGO_P larger than the one observed in the longitudinal direction, as shown in Fig. 10(a). Figure 10(b) indicates the results of the assessment of the porosity evolution in the symmetric trilayer system and the evaluation of the shear viscosities ratio ξ of the fully dense layer materials. It is shown that the determined parameter ξ increases as sintering proceeds, but

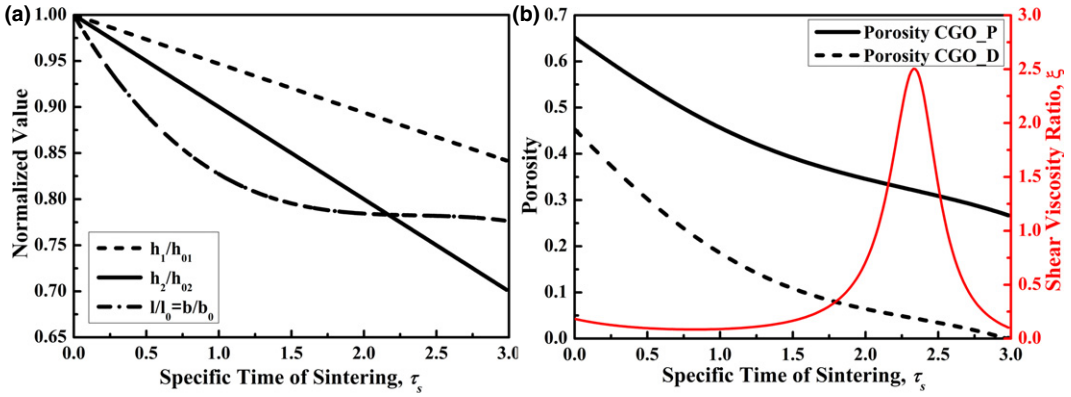

Fig. 10. (a) Experimental data-based assessment of the geometry evolution (length, width, and thickness) of the symmetric trilayered CGO_P–CGO_D–CGO_P system during optical dilatometry; (b) determination of the shear viscosities ratio ξ, of the fully dense materials of the respective layers based on the sintering results of the symmetric CGO_P–CGO_D–CGO_P trilayer system

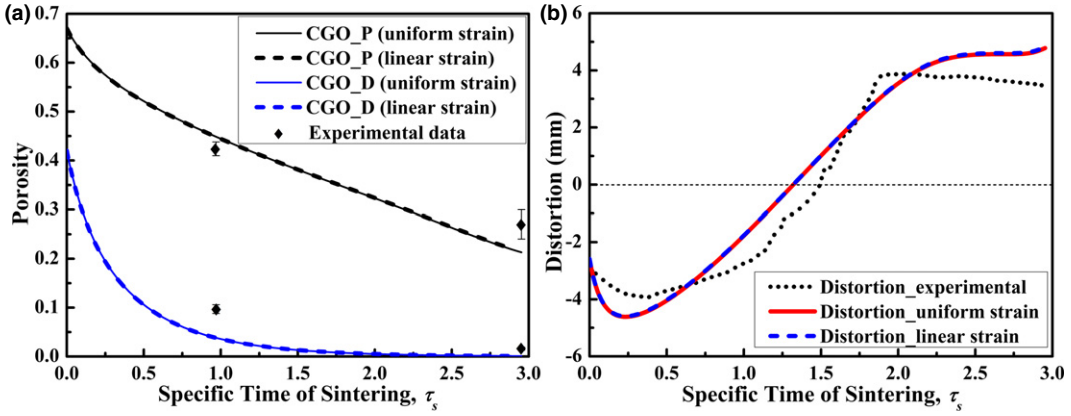

Fig. 11. Comparison of the experimental and modeling results in terms of porosity (a) and distortion (b) in the bilayered CGO_D–CGO_P (asymmetric) system. The modeling results based on both the linear and uniform strain distributions are presented together, which showed almost the same values in terms of evolution of porosity as well as the distortion.

decreases at the moment about $\tau_s = 2.4$. This can be explained by the fast grain growth of CGO_D in the final stage of sintering. Normally, grain growth of ceramics is linear and slow in the early stage of sintering, but it turns nonlinear and rapid at a certain densification point (normally when relative density is greater than 90%) during the final stage of sintering.[18]

Thus, two essential constitutive parameters, λ and ξ, required for the modeling of sintering of the bilayered CGO_D–CGO_P (asymmetric) porous system, are determined based on the optical dilatometry and on the SEM characterization of the sintered single layer and symmetric trilayered specimens.

(2) Comparison of Modeling and Experimental Results

The available optical dilatometry data on the sintering of the bilayered CGO_D–CGO_P (asymmetric) porous system provide the assessment of the kinetics of the distortion span R (see Fig. 3). The distortion parameter R is replotted as a function of the specific time of sintering in Fig. 11(b).

The modeling of sintering of the bilayered CGO_D–CGO_P (asymmetric) porous system has been conducted based on the solution of eqs. (35) and (46) in Part I of this work,[12] taking into account the expressions for parameters λ and ξ, derived in Section III. (1). In Fig. 11, the modeling results are compared with the experimental data in terms of distortion R (see Fig. 3), taking into consideration the following geometrical relationship:

$$R = \frac{\bar{h}_1 h_{01} + \bar{h}_2 h_{02}}{\bar{\kappa}} \left(1 - \cos\left(\frac{\bar{l}_0 \bar{\kappa}}{2\left[\bar{h}_1 h_{01} + \bar{h}_2 h_{02}\right]}\right)\right) \tag{2}$$

where $\bar{\kappa}$ is the normalized curvature, which is defined as eq. (34) in Part I of this work[12]:

$$\bar{\kappa} = \frac{\kappa}{1/(h_{01} + h_{02})} \tag{3}$$

The modeling results shown in Fig. 11(a) agree well with the experimental data in terms of the porosity evolution for both layers. An image analysis carried out for the SEM images shown in Fig. 4 indicates the final volume fractions of pores equal to 27.3% and 1.6% for CGO_P and CGO_D layers (as the dots shown in Fig. 11(a), also shown in Table I), respectively. These values agree very well with the results of porosity evolution shown in Fig. 11(a). Simultaneously, it can be found that the modeling results shown in Fig. 11 from the linear and uniform strain distributions give almost similar results in terms of evolution of porosity as well as the distortion.

The results of modeling indicate rather good qualitative agreement with the experimental data on shape distortion. The quantitative discrepancies between the theoretical and experimental shape distortion and porosities-related results can be attributed to various factors. Those include the

simplification assumed in the model developed in the companion study,[12] such as omitting possible anisotropy of viscosity and of the sintering stress. Possible structure spatial heterogeneity as well as nonuniformity of temperature distribution could have an impact on the experimental outcomes too. In addition, gravity of thin layers tends to flatten the camber, therefore acting against the formation of shape distortion.[19,20] This effect is not considered in this work. Frandsen *et al.*[16,17] considered the possible gravity effect during cofiring of bilayered CGO structures and it was indicated that the gravity had a significant effect on the shape distortion development especially at the final stage of sintering.

One important assumption influencing the agreement between the theoretical and experimental data is the assumption of linear kinetics of layer thicknesses during sintering of the symmetric trilayer CGO_P–CGO_D–CGO_P system. A possible refinement of this assumption can be achieved through calculating the normalized thickness evolutions ($\bar{h}_1$ and $\bar{h}_2$) using expressions (51)–(53) of Part I of this work[12] instead of the linear shrinkage assumption followed here. The obtained thickness kinetics can be then further substituted in eq. (57) of Part I to determine the new value of coefficient ξ, which can be again substituted in the equation set (51)–(53) of Part 1 of this work,[12] and so on, until this iterative process reaches a satisfactory level of conversion. As one of the major objectives of the conducted analysis is the formulation of engineering-level solutions avoiding comprehensive computer codes, the described iteration approach is left outside the scope of the conducted work.

The modeling results shown in Fig. 11(b) point toward the change in the sign of the bilayered system's distortion (from concave to convex shape), which is fully confirmed by the experimental data on the distortion given in Fig. 11(b). The reason for this change in the distortion sign can be explained based on the regularities of the shrinkage kinetics. In the beginning of the sintering process, the CGO_D layer sinters faster due to the sintering aid and smaller initial grain size. This causes the larger contraction of the CGO_D layer compared with the CGO_P layer, with the respective bending/distortion occurring in the bilayered system. At the moment corresponding to about 0.5 value of the specific time of sintering (at about 1000°C), the CGO_D is significantly densified, and the intensity of the shrinkage of the CGO_P exceeds the intensity of the shrinkage of the CGO_D layer. At this moment, the direction of bending changes, the systems "flattens out", and at the moment about $\tau_s = 1.5$ the sign of the system curvature reverses. Despite some quantitative discrepancies, this phenomenon is described qualitatively well by the developed model.

The obtained results indicate that despite a number of simplifying assumptions, the developed theoretical framework is capable of qualitatively reliable predictions of distortion and shrinkage kinetics in bilayered porous systems.

IV. Conclusions

The theoretical model analyzing shrinkage and distortion kinetics during sintering of bilayered structures developed in Part I of this work was applied to the cofiring of the bilayered porous and dense gadolinium-doped ceria system. The novel approach making possible the determination of all the bilayered system sintering modeling input parameters from a single dilatometry run conducted simultaneously for the individual single layers and for a symmetric trilayered system composed of the layers utilized in the bilayered system is put forward. The solutions obtained based on the developed modeling technique agree well with the results of the conducted experiments in terms of the distortion and shrinkage kinetics.

Acknowledgments

The authors thank the Danish Council for Independent Research Technology and Production Sciences (FTP), which is part of The Danish Agency for Science, Technology, and Innovation (FI) (Project #09-072888), for sponsoring the OPTIMAC research work. The research leading to these results has also received funding from the European Union's Seventh Framework Programme FP7/2007-2013 under grant agreement No. 228701 (NASA-OTM). The support of US National Science Foundation Division of Civil, Mechanical Systems and Manufacturing Innovations (NSF Grant No. CMMI 1234114), and Division of Materials Research (NSF Grant No. DMR 0705914) is gratefully appreciated. The support of the Ministry of Science and Education of Russian Federation (Grant Contract 11.G34.31.0051) is also gratefully appreciated. The support by the US Department of Energy, Division of Materials Science and Engineering (DOE Award DE-SC0008581), is gratefully appreciated.

References

[1]C. Kleinlogel and L. J. Gauckler, "Sintering and Properties of Nanosized Ceria Solid Solutions," *Solid State Ionics*, **135** [14] 567–73 (2000).
[2]S. J. Skinner and J. A. Kilner, "Oxygen Ion Conductors," *Mater. Today*, **6**, 30–7 (2003).
[3]B. C. H. Steele, "Oxygen-Transport and Exchange in Oxide Ceramics," *J. Power Sources*, **49**, 1–14 (1994).
[4]R. T. Leah, N. P. Brandon, and P. Aguiar, "Modelling of Cells, Stacks and Systems Based Around Metal-Supported Planar IT-SOFC Cells with CGO Electrolytes Operating at 500–600°C," *J. Power Sources*, **145**, 336–52 (2005).
[5]B. C. H. Steele, I. Kelly, and H. Middelton, "Oxidation of Methane in Solid State Electrochemical Reactors," *Solid State Ionics*, **28**, 1547–52 (1998).
[6]M. Mogensen, N. M. Sammes, and G. A. Tompsett, "Physical, Chemical and Electro- Chemical Properties of Pure and Doped Ceria," *Solid State Ionics*, **129**, 63–94 (2000).
[7]A. Kaiser, S. Foghmoes, C. Chatzichristodoulou, M. Søgaard, J. A. Glasscock, H. L. Frandsen, and P. V. Hendriksen, "Evaluation of Thin Film Ceria Membranes for Syngas Membrane Reactors-Preparation, Characterization and Testing," *J. Membr. Sci.*, **378**, 51–60 (2011).
[8]P. V. Hendriksen, P. H. Larsen, M. Mogensen, F. W. Poulsen, and K. Wiik, "Prospects and Problems of Dense Oxygen Permeable Membranes," *Catal. Today*, **56**, 283–95 (2000).
[9]P. V. Hendriksen, J. R. Høgsberg, A. M. Kjeldsen, B. F. Sørensen, and H. G. Pedersen, "Failure Modes of Thin Supported Membranes"; pp. 347–60 in *Advanced in Solid Oxide Fuel Cells II, Ceramic Engineering and Science Proceedings*, 27,Cocoa Beach, Edited by A. Wereszczak. Wiley, Hoboken, 2007
[10]I. Lubomirsky, "Stress Adaptation in Ceramic Thin Films," *Phys. Chem. Chem. Phys.*, **9**, 3701–10 (2007).
[11]A. Kossoy, A. I. Frenkel, Q. Wang, E. Wachtel, and I. Lubomirsky, "Local Structure, Strain-Induced Distortion in $Ce_{0.8}Gd_{0.2}O_{1.9-\delta}$," *Adv. Mater.*, **22**, 1659–62 (2010).
[12]E. Olevsky, T. T. Molla, H. L. Frandsen, V. Esposito, D. W. Ni, R. Bjørk, A. Ilyina, and N. Pryds, "Sintering of Multilayered Porous Structures: Part I - Constitutive Models," *J. Am. Ceram. Soc.*, (2012) doi: 10.1111/jace.12375. (in press).
[13]E. Moreau, B. Velde, and F. Terribile, "Comparison of 2D and 3D Images of Fractures in a Vertisol," *Geoderma*, **92**, 55–72 (1999).
[14]J. Glasscock, V. Esposito, S. Foghmoes, T. Stegk, D. Matuschek, M. Ley, and S. Ramousse, "The Effect of Forming Stresses on the Sintering of Ultra-Fine $Ce_{0.9}Gd_{0.1}O_{2-\delta}$," *J. Eur. Ceram. Soc.*, **33**, 1289–96 (2011). accepted
[15]J. D. Nicholas and L. C. De Jonghe, "Prediction and Evaluation of Sintering Aids for Cerium Gadolinium Oxide," *Solid State Ionics*, **178**, 1187–94 (2007).
[16]H. L. Frandsen, E. Olevsky, T. T. Molla, V. Esposito, R. Bjørk, and N. Pryds, "Modeling Sintering of Multilayers Under Influence of Gravity," *J. Am. Ceram. Soc.*, **96**, 80–9 (2013).
[17]T. T. Molla, H. L. Frandsen, R. Bjørk, D. W. Ni, E. Olevsky, and N. Pryds, "Modeling Kinetic of Distortion in Porous bi-Layered Structures," *J. Eur. Ceram. Soc.*, **33**, 1297–305 (2013).
[18]Z. He, H. Yuan, J. A. Glasscock, C. Chatzichristodoulou, J. W. Phair, A. Kaiser, and S. Ramousse, "Densification and Grain Growth During Early-Stage Sintering of $Ce_{0.9}Gd_{0.1}O_{1.95-\delta}$ in a Reducing Atmosphere," *Acta Mater.*, **58**, 3860–6 (2010).
[19]M. Cologna and V. M. Sglavo, "Vertical Sintering to Measure the Uniaxial Viscosity of Thin Ceramic Layers," *Acta Mater.*, **58**, 5558–64 (2010).
[20]J. Ollagnier, O. Guillon, and J. Rödel, "Constrained Sintering of a Glass Ceramic Composite: I. Asymmetric Laminate," *J. Am. Ceram. Soc.*, **93** [1] 74–81 (2010). □

D. PAPER-IV

T.T. Molla, D.W. Ni, R. Bulatova, R. Bjørk, C. Bahl, N. Pryds and H.L. Frandsen, "Finite element modeling of camber evolutions during sintering of bi-layer structures," *J Am Ceram Soc*, *in press* (2014)

J. Am. Ceram. Soc., 1–8 (2014)
DOI: 10.1111/jace.13025

journal

Finite Element Modeling of Camber Evolution During Sintering of Bilayer Structures

Tesfaye Tadesse Molla,† De Wei Ni, Regina Bulatova, Rasmus Bjørk, Christian Bahl, Nini Pryds, and Henrik Lund Frandsen

Department of Energy Conversion and Storage, Technical University of Denmark, Risø Campus, Frederiksborgvej 399, P.O. Box 49, Building 779, 4000 Roskilde, Denmark

The need for understanding the mechanisms and optimization of shape distortions during sintering of bilayers is necessary while producing structures with functionally graded architectures. A finite element model based on the continuum theory of sintering was developed to understand the camber developments during sintering of bilayers composed of $La_{0.85}Sr_{0.15}MnO_3$ and $Ce_{0.9}Gd_{0.1}O_{1.95}$ tapes. Free shrinkage kinetics of both tapes were used to estimate the parameters necessary for the finite element models. Systematic investigations of the factors affecting the kinetics of distortions such as gravity and friction as well as the initial geometric parameters of the bilayers were made using optical dilatometry experiments and the model. The developed models were able to capture the observed behaviors of the bilayers' distortions during sintering. Finally, we present the importance of understanding and hence making use of the effect of gravity and friction to minimize the shape distortions during sintering of bilayers.

I. Introduction

Ceramic structures with functionally graded multilayer architectures are generally considered as promising materials for various applications related to efficient energy technologies. Some of the application areas include solid oxide fuel cells, piezoelectric actuators, gas membranes etc.[1–4] Manufacturing of multilayered structures often includes co-sintering of laminated tapes prepared from different sets of powders. One of the problems often observed during sintering of bi-layer systems is distortion of the samples which often poses as a problem in the final assembly of the different components. For example, in the case of solid oxide fuel cells it is important to cofire the different layers with little or no shape distortion of the planar geometry to succeed with the intended assembly of the solid oxide fuel cell stacks.[4,5]

Distortion during sintering of bilayers occurs mainly due to mismatch in the shrinkage behaviors of the layers. The other factor affecting distortion in bilayers is the evolution of relative viscosity between the layers during the sintering cycle.[6,7] In an effort to reduce the distortions during sintering of bilayers, it is sometimes necessary to modify the intrinsic material behaviors of each tape. For example, though it requires cumbersome experimental works, tailoring the densification kinetics of each layer so as to minimize the mismatch in shrinkage strains could significantly reduce stress developments during cofiring. In addition to modifying the intrinsic material behaviors of the tapes, few authors have also suggested other techniques like applying external loads resisting the deformation[8] and optimization of the sintering temperature profile.[9]

However, camber evolution is also affected by geometrical parameters such as the ratio of layers' thickness and length of the sample.[6,10] Furthermore, additional factors like own weight of the sample (gravity) and friction (between the edges of the bilayer and the surface of the sample support while the bi-layer deforms) have often significant effect on the overall distortion of the sample.[3,5,11,12]

With regards to the effect of geometrical parameters, methodical studies describing the effect of the thickness ratio of layers on the camber evolution have been previously reported.[8,10] Olevsky *et al.* also discussed how the initial porosity of each layer making the bi-layer could also be used to optimize the camber evolution during cofiring.[10] On the other hand, Mücke *et al.* showed the effect of gravity on the evolution of camber by sintering bilayers in the horizontal and vertical orientations.[5]

For the basic understanding of the influence of materials intrinsic properties on the evolution of camber during sintering of bilayers, the continuum theory of sintering together with the use of beam theory have been applied and its use is widely reported.[2,13,14] In general, to model the sintering behavior of multilayers, the continuum theory of sintering with the assumption of linear response of the shrinkage rate to the applied load can be used.[2,3,13–16] Often free sintering of tapes is assumed to be isotropic but anisotropies due to nonuniform initial density distributions can also be introduced into the continuum model.[17]

Despite these works, there are still needs to create better understanding on how stress and distortions develop with respect to geometrical parameters and factors like gravity and also friction during cofiring in order to have better and refined process optimizations. This can be achieved by the use of numerical techniques, such as the finite element method.

The use of finite element method to describe stresses during the sintering process has so far focused mainly on the powder compaction process.[18–21] Numerical implementation of the continuum theory of sintering to describe shape distortions of cylindrical porous specimen under free sintering in the presence of gravitational forces is reported by Olevsky *et al.*[22] Schoenberg *et al.* modeled stresses during cofiring of bilayers consisting of layers with different initial densities.[23] In their study, Schoenberg *et al.* used temperature-dependent artificial coefficient of expansion (CTE) as an input to the finite element model to simulate the volumetric shrinkage strain in each layer. A good agreement between the stress predicted from the finite element model and analytical models is shown.[23] However, it is difficult to use the technique proposed by Schoenberg *et al.* to model stresses and distortions during isothermal sintering cycle as the artificial CTE is a function of the changing temperature in their iso-rate sintering experiment. Similarly, analysis of stresses during sintering of multilayered structures using the continuum the-

D. J. Green—contributing editor

Manuscript No. 34533. Received February 12, 2014; approved April 28, 2014.
†Author to whom correspondence should be addressed. e-mail: ttmo@dtu.dk

ory is reported by Brown *et al.*[24] Brown *et al.* was able to show the distortions during sintering of trilayered solar cells using experimental measurements of the free shrinkage of each layers to estimate the input parameters for the 3D finite element model.

In this study we have developed a finite element model in the commercial software, ABAQUS™, based on the continuum theory of sintering in order to be able to predict the curvature evolution during sintering of bilayered structures. To verify the model, different sintering experiments of bilayers composed of $La_{0.85}Sr_{0.15}MnO_3$ (LSM) and $Ce_{0.9}Gd_{0.1}O_{1.95}$ (CGO) tapes have been conducted. In addition, the influence of the geometric parameters of the bilayer, gravity, and friction on the evolutions of curvature have been studied both experimentally and numerically. For such purpose, systematic variation of the initial length of the samples and thickness ratio between the layers making the bilayer is made. Sintering experiments of similar bilayers with different orientations is also made to study the effect of gravity and friction on the evolution of curvature.

II. Experimental Procedures

$Ce_{0.9}Gd_{0.1}O_{1.95}$ (CGO, specific surface area: 5.2 m^2/g, Rhodia S.A., La Défense, France) and $La_{0.85}Sr_{0.15}MnO_3$ (LSM, d_{50}: 0.6 μm; specific surface area: 23.24 m^2/g, Haldor Topsoe A/S, Copenhagen, Denmark) were used as starting powders for the development of CGO and LSM tape cast layers by standard processing. Details of the tape casting processing can be found in Ni *et al.*[25,26] After drying, both the CGO and LSM green tapes had a uniform thickness of 220 and 110 μm respectively.

In this work, the conducted experiments involve measurements necessary for obtaining material input parameters for modeling (free shrinkage kinetics of the individual layers) as well as experiments necessary for validation of the model (sintering of bilayered laminates).

Individual CGO and LSM green tapes were rolled and pressed to obtain 'bulky' sample of the thin layers for dilatometry measurements. Final shapes of the samples were obtained by cutting the rolled tapes in cylindrical shapes of 3–5 mm in length and 2–3 mm in diameter.

The asymmetric CGO/LSM bilayered samples were assembled by colamination of the CGO and LSM green tapes both oriented along the tape-casting direction. Five different CGO/LSM bilayered samples with different thickness ratio and length were prepared by laminating different numbers of CGO and LSM green tapes. Final shapes of the laminated samples were obtained by stamping and punching rectangular shapes from the green material. Table I summarizes the initial size of five different CGO/LSM bilayered samples used in this work.

Measurements of shrinkage and curvature evolutions on all the samples were performed under the same heating profile in an optical dilatometer (TOMMI, Fraunhofer Institut Silicatforschung ISC, Neunerplatz 2, D-97082 Würzburg, Germany). This allows for the sample shape evolution during sintering to be followed *in situ* and noncontact, by simply collecting the sequential images (i.e., a video sequence) of the samples silhouettes projected by a source of visible light onto a high definition camera.

Table I. Initial Sizes of the Bilayered CGO/LSM Samples

Samples	Length l_0(mm)	Width b_0(mm)	Thickness ratio X(CGO:LSM)	Thickness of CGO h_{01}(μm)	Thickness of LSM h_{02}(μm)
1	25	5	2:1	220	110
2	25		6:1	660	
3	25		4:1	440	
4	15		4:1	440	
5	40		4:1	440	

The rolled tape samples were oriented in a way to allow measurement of the evolution of shrinkage of the samples in the length direction of the cylindrical samples. During the dilatometric measurements of bilayered samples, the CGO was placed on the bottom side of the asymmetric laminates. The bilayer samples were placed on a plane support (Alumina repton plates). The complete thermal cycle of the processing, including the de-binding step and sintering, was performed directly in the optical dilatometer to avoid moving the samples with possible mechanical failure after the de-binding step. The de-binding cycle includes a slow heating ramp at 0.33°C/min from room temperature to 400°C and an isothermal step at 400°C for 4 h aimed at removing the organic component from the samples. The sintering cycle was performed by an iso-rate heating ramp step up to 1250°C at a heating rate of 1°C/min, followed by an isothermal step at 1250°C for 4 h. The shrinkage (free sintering) and curvature evolution (bilayered CGO/LSM samples) were monitored *in situ* continuously during the heating and cooling cycles. Microstructures of cross-section were characterized using scanning electron microscopy (SEM, Supra, Carl Zeiss, Germany).

Figure 1 shows the dilatometric image from TOMMI depicting the sample geometry at the onset of the sintering cycle (i.e., after de-binding) for one of the bilayers built with an initial thickness ratio, X (CGO:LSM) = 4 and initial length of l_0 = 40 mm. Due to differential de-binding, significant deformations of the bilayer samples were observed after de-binding (600°C) or at the onset of the sintering cycle.

III. Model Development

The linear-viscous form of the continuum theory of sintering (SOVS) is used to define the inelastic (sintering related) strain rate in the porous body. According to SOVS, the total strain rate, $\dot{\boldsymbol{\varepsilon}}^{s}$, during sintering of a body is given by the sum of creep, $\dot{\boldsymbol{\varepsilon}}^{cr}$, and free sintering, $\dot{\boldsymbol{\varepsilon}}^{f}$,strain rates as:[14]

$$\dot{\boldsymbol{\varepsilon}}^{s} = \dot{\boldsymbol{\varepsilon}}^{cr} + \dot{\boldsymbol{\varepsilon}}^{f}$$

$$\dot{\boldsymbol{\varepsilon}}^{s} = \frac{\boldsymbol{\sigma}'}{2\eta_0\varphi} + \frac{\sigma_m - \sigma_s}{3(2\eta_0\psi)} I \tag{1}$$

where $\boldsymbol{\sigma}'$, σ_m, and σ_s are the deviatoric stress tensor, mean and sintering stresses, respectively. The mean stress is equivalent to the hydrostatic pressure, $\sigma_m = \frac{1}{3} tr(\boldsymbol{\sigma})$. During the implementation of SOVS, normalized parameters, φ and ψ, are used to relate the effective shear and bulk viscosities of the porous body to the viscosity of the fully dense body depending on the instantaneous amount of porosity, see Eq. (2).[14]

$$\varphi = (1-\theta)^2 \text{and } \psi = \frac{2}{3}\frac{(1-\theta)^3}{\theta} \tag{2}$$

In view of the continuum theory of sintering, the driving force for sintering or sintering stress is directly proportional

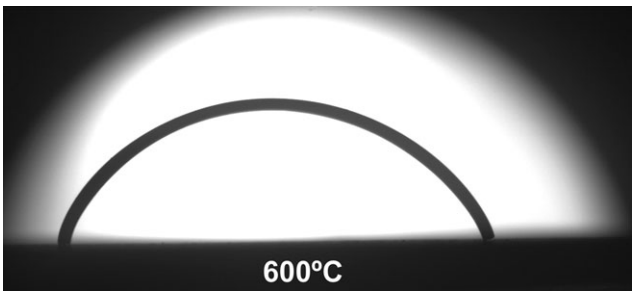

Fig. 1. Geometry of the sample at the onset of the sintering for bilayer with an initial length of 40 mm.

to the surface energy per unit area, α, of the porous surface and is given by:

$$\sigma_s = \frac{3}{2}\frac{\alpha}{G}(1-\theta)^2 \tag{3}$$

where θ and G are the instantaneous amount of porosity and grain size respectively. The viscosity of the fully dense body, η_0, varies with temperature,T, and is given by an Arrhenius form expression with an Arrhenius constant, A, and the effective or apparent activation energy for densification, E_a.[27] Here R is the universal gas constant.

$$\eta_0 = AT\exp(\frac{E_a}{RT}) \tag{4}$$

Sometimes the viscous parameters of the porous body are measured and reported in terms of the uniaxial viscosity, η_u, and viscous Poisson's ratio,ν_v, as:[10]

$$\eta_u = \frac{18\eta_0\psi\varphi}{6\psi+\varphi} \text{ and } \nu_v = \frac{3\psi-\varphi}{6\psi+\varphi} \tag{5}$$

The grain growth during the sintering process is a strong function of time, t, and the initial grain size, G_0, as given by:[28]

$$G^n = G_0^n + k_0\exp(\frac{-E_g}{RT})t \tag{6}$$

where k_0 and E_g are the grain growth pre-exponential factor and the activation energy for grain growth respectively. Here n is the grain growth exponent depending on the densification mechanism (e.g., $n = 3$ for volume diffusion).[28] In this work, the possible anisotropies in the pore-grain structure are not considered and hence the shrinkage rate in the free standing tape is assumed to be isotropic, which is formulated using Eqs. (2)–(4), see Eq. (7). For a detailed description of the continuum theory of sintering, please refer to Ref. [15].

$$\dot{\varepsilon}^f = -\frac{\sigma_s}{6\eta_0\psi} = -\frac{3}{8}\frac{\alpha}{AGT}\exp(\frac{-E_a}{RT})(\frac{\theta}{1-\theta}) \tag{7}$$

For the numerical implementation, the elastic part of the material response is assumed to be isotropic and characterized by Hooke's law as:

$$\dot{\boldsymbol{\sigma}} = \boldsymbol{C}\dot{\boldsymbol{\varepsilon}}^{el} \tag{8}$$

Here C is the elastic stiffness matrix and, $\dot{\varepsilon}^{el}$, is the elastic strain rate. The total strain rate, $\dot{\varepsilon}$, in the porous body can be given by:

$$\dot{\boldsymbol{\varepsilon}} = \dot{\boldsymbol{\varepsilon}}^{el} + \dot{\boldsymbol{\varepsilon}}^{s} \tag{9}$$

Combining Eqs. (1), (8), and (9), it is possible to get the constitutive relationship for the incremental stress during sintering as:

$$\dot{\boldsymbol{\sigma}} = \boldsymbol{C}\dot{\boldsymbol{\varepsilon}}^{el} = \boldsymbol{C}(\dot{\boldsymbol{\varepsilon}} - \dot{\boldsymbol{\varepsilon}}^{cr} - \dot{\varepsilon}^{f}\boldsymbol{I}) \tag{10}$$

The above model was used to simulate the sintering of bilayer systems made up of tapes with different initial density. This was made possible by implementing the linear-viscous form of the continuum theory of sintering (SOVS) in ABAQUS™ with the help of a user subroutine. The creep user subroutine provided by ABAQUS™ defines the total incremental inelastic strain, $d\boldsymbol{\varepsilon}$, as the sum of creep, $d\boldsymbol{\varepsilon}^{cr}$, and swelling, $d\boldsymbol{\varepsilon}^{sw}$, strains[40] which are obtained integrating Eq. (1) with time.

The evolving relative density or porosity in the structure can be updated using the principle of mass conservation. The inelastic volumetric strain is used to calculate the relative density as shown in Eq. (11) by using the initial relative density of the porous body, ρ_0.

$$\varepsilon^v = \varepsilon^{cr}\boldsymbol{I} + \varepsilon^{sw}$$

$$\rho_i = \rho_0\exp(-\varepsilon^v) \tag{11}$$

ABAQUS™ provides users with the ability to define solution-dependent state variables (SDVs) in the user subroutines. In this work, two SDVs have been employed to update the relative porosity and grain size in each layer. For example, the porosity in each tape is stored in one of the SDVs, such that it can be passed every time the subroutine is called, thereby updating the current value. At the end of the simulation, they can be used to analyze the model's behavior in time. The grain sizes and porosities in each layer are updated on every time step using the equations described above, see Eqs. (6) & (11).

Geometrically linear as well as nonlinear analysis can be performed using ABAQUS™ based on the strain measures defined as[41]:

$$\varepsilon = \begin{cases} \frac{L-L_0}{L_0}; & \text{Linear} \\ \ln\frac{L}{L_0}; & \text{Non-linear} \end{cases} \tag{12}$$

The effect of the evolving porosity on the mechanical properties of the tape i.e., on the elastic modulus, E, and Poisson's ratio,ν during densification is estimated by a composite sphere model suggested by Ramakrishnan and Arunachalam.[29] Here E_0 and ν_0 are the Young's modulus and Poison's ratio of the fully dense body.

$$E = E_0\frac{(1-\theta)^2}{(1+b_E\theta)} \text{ where } b_E = 2-3\nu_0$$

$$\nu = 0.25\frac{4\nu_0+3\theta-7\nu_0\theta}{1+2\theta-3\nu_0\theta} \tag{13}$$

Two dimensional plain strain formulations were used together with symmetry boundary conditions on half of the bilayer geometry. Quadratic elements with an average size of 50 μm have been chosen for meshing with visco analysis steps.

The distortion at the onset of the sintering, see Fig. 1, is taken into account as the initial geometric configuration of the bilayer model as shown in Fig. 2. The sintering temperature ramp is defined as a boundary condition on the entire geometry of the model. Figure 2 also shows examples of the directions of the gravity, F_g, and friction, F_f, forces acting on the bilayer bending towards the LSM layer. Note that the friction force is generated between edge and support of the sample in the furnace. The effect of gravity on the evolution of the distortions is considered by applying a body force obtained by using the theoretical density of each tape.

IV. Results and Discussions

(1) Obtaining Material Parameters

The parameters defining the viscosity of both CGO and LSM tapes, A and E_a, were estimated by fitting the free shrinkage strain model in Eq. (7) to experimental measure-

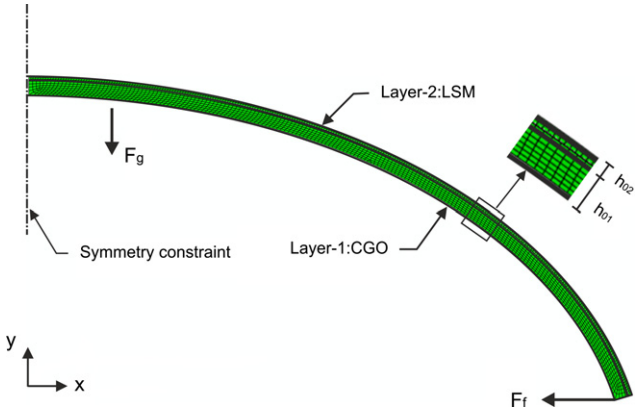

Fig. 2. The initial geometric configuration of the bilayer sample with an initial length of $l_0 = 40$ mm and initial thickness ratio of $X = \frac{h_{01}}{h_{02}} = 4$ with the finite element meshes.

ments of free sintering. The approach used here has been explained in detail in previous work by Molla *et al.*[12] and Reiterer *et al.*[27]

Based on the optimization procedure, Fig. 3(a) shows the comparison between the free shrinkage strains in each tape during the entire sintering cycle. About 11% and 26% of shrinkage was observed in CGO and LSM tapes respectively. The free shrinkage strain model is also shown to agree well with the experimental observations of shrinkage strains.

The evolution of the viscosity as a function of temperature is the other important parameter for modeling the distortions in the bilayer system. Figure 3(b) shows the fully dense viscosities of both CGO and LSM tapes during the iso-rate sintering cycle, which is calculated as per Eq. (4). The effect of porosity on the viscosity of the porous body is included based on the evolution of porosity during the sintering of the bilayer. The fully dense body viscosity results are consistent with previous observations of same materials reported in.[12]

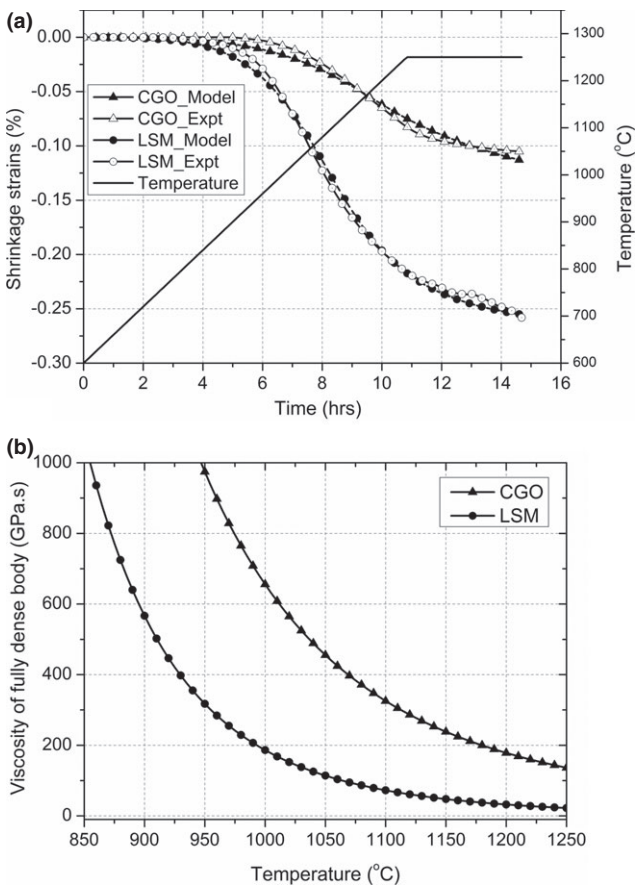

Fig. 3. (a) Comparison of model and experiments for free shrinkage strains and (b) The evolution of fully dense body viscosity as a function of temperature.

All the other parameters required to model densifications and distortions during the cofiring of CGO and LSM tapes are obtained from experimental measurements and are summarized in Table II. Note here that the impact of the grain growth on the viscosity of the fully dense tapes is not considered explicitly as shown by Eq. (4). But those effects can be included in the Arrhenius constant, A and the effective or apparent activation energy, E_a, as these, are made to be free parameters, while fitting the shrinkage strain model to the experimental measurements. This approach is explained in detail in previous works by Molla *et al.* [12] as well as Reiterer *et al.*[27]

The change in the elastic properties of both tapes as a function of the evolving porosity during the sintering process was considered using Eq. (13). Fan *et al.* and Atkinson *et al.* studied the elastic properties of CGO10 as a function of porosity where the fully dense CGO is reported to have a Young's modulus, $E_0 = 200$GPa at 800°C.[31,32] Similarly Giraud *et al.* studied the elastic properties of LSM tapes with different porosities in which he reported the Young's modulus of dense LSM at room temperature to be, $E_0 = 110$GPa and shown to change little with temperature between 350°C and 950°C.[33] In fact, the variation of the Young's modulus with temperature is not critically important as the elastic response from the porous bodies during sintering is very small. In this study, the Poisson's ratio for the dense bodies, ν_0, of both tapes is assumed to be 0.328.[32]

(2) Effect of Gravity and Geometric Nonlinearity

Figure 4 (left) shows the dilatometric images for the evolution of curvature at different temperatures for one of the bilayers built with an initial thickness ratio, X(CGO:LSM) = 4 and initial length $l_o = 40$ mm. The corresponding results from the finite element model are also shown in Fig. 4 (right). The model is shown to agree well with the experimental observations in terms of shape evolutions during the sintering cycle. Example of the 2D contour plot showing principal stresses in the xx direction (S11) at 1180°C is also shown where the CGO layer is under compressive stress due to the fast shrinking LSM layer.

Table II. The Parameters used in the Modeling for LSM and CGO Layers

Parameter	LSM	CGO	Source
Initial porosity, θ_0 (%)	0.58	0.38	Measurement
Initial grain size, G_0 (μm)	0.45	0.13	Measurement
Final grain size, G (μm)	1.34	0.2	Measurement
Surface energy, α (J/m^2)	2.5	1	[11,42]
Activation energy for grain growth, E_g (kJ/mol.K)	420	480	[25,30]
Grain growth coefficient, k_0	1.11 e^{-8}	4.39 e^{-9}	Fitting
Arrhenius constant, A (GPa.s/K)	121	1202	Fitting
Apparent activation energy, E_a (kJ/mol.K)	148	138	Fitting

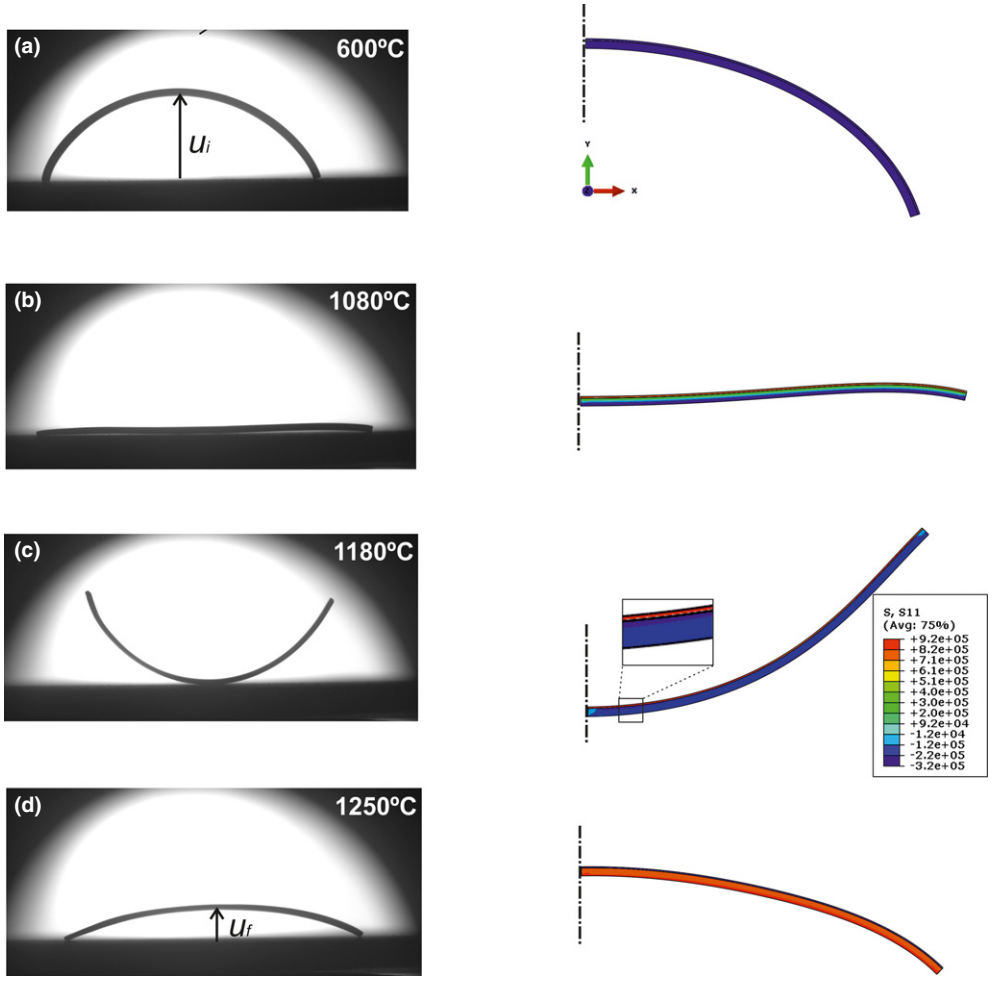

Fig. 4. Experimental (left) and finite element model results (right) showing the evolution of distortion during the sintering cycle.

To study the effect of gravity and geometric nonlinearity, the evolution of curvature during cofiring of CGO and LSM tapes is analyzed with different models. Two models based on linear-viscous theory as reported by Cai *et al.*,[6] which does not consider gravity, and Frandsen *et al.*,[11] which considers gravity, are compared with two finite element models based on geometrically linear and nonlinear analysis.

Comparison of model predictions for curvature including the experimental measurements in a bilayer with an initial length of $l_o = 40$ mm and thickness ratio $X = \frac{h_{01}}{h_{02}} = 4$ is shown in Fig. 5. Note that in this work, curvature development towards the bottom layer i.e., the CGO layer is taken as positive and vice versa.

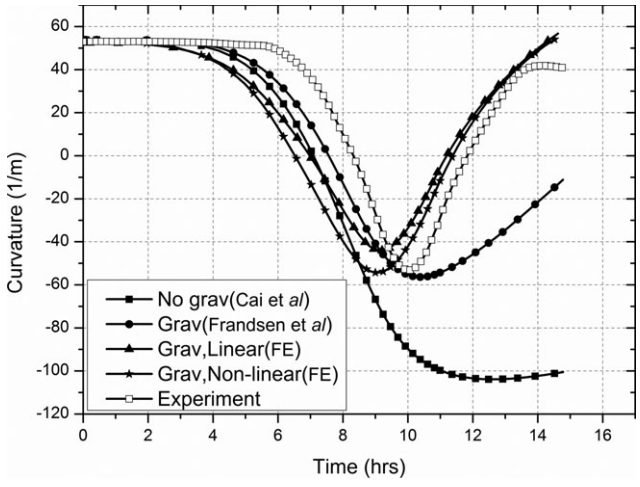

Fig. 5. Comparison of different model predictions for curvature evolution over time with the experimental measurements.

The experimental results show almost no curvature development for the first 5.5 h, which is due to the small shrinkage rate difference between the two layers. After this period of time the LSM (top) layer shrinks faster than the CGO layer. This is followed by development of stress in the bilayer sample and hence led to camber of the sample. After $t \approx 10$ h, the curvature changes in the bilayer sample starts to slowdown because of the combined effects of slower shrinkage activity in the LSM layer, gravity, and stress relaxation in the constraining CGO layer.

All the models considered predict a similar trend in camber growth for the first 9 h of the sintering. The model by Cai *et al.* predicts a further growth in curvature in the later stages of the sintering, while the other model by Frandsen *et al.* show reductions in the curvature after $t \approx 10$ h. The finite element models also show reductions in the curvature as observed in the experiment. Similarly almost all the models predict an early start in curvature evolution, when compared to the experiment, which may be caused by stress relaxations in the bilayer during the experiment. From the comparisons shown in Fig. 5, it is clear to see the significant effects of gravity on the evolution of curvature and it is obvious that including gravity capture the real physics of the camber development. It is also shown that the results from the linear-viscous model, which accounts for gravity (the model by Frandsen *et al.*) differs from the finite element models. This could be due to the absence of elasticity and/or the simplifications made by Frandsen *et al.* in the analytical

implementations of the effect of gravity in to the linear-viscous model.[11]

During the experiments, a significant amount of distortion after de-binding in the bilayer samples was observed. It is therefore important to model stresses and shape distortions because of differential de-binding of the layers during sintering of bilayer. In the finite element model, considering the initial deformed geometry of the sample at the onset of the sintering process is also important to properly include the effect of gravity. For example, in the beginning, the gravity force actually supports the evolution of curvature until the sample become flat (before bending to the LSM layer). The finite element model based on geometrically nonlinear analysis is also shown to predict the magnitude of the curvature better than the model based on geometrically linear analysis. Some discrepancy between the most advanced nonlinear model and the experiment are still present, though. Table III shows the convergence behavior of the FE model as a function of the total number of elements for bilayer sample with an initial length $l_0 = 15$ mm and thickness ratio $X = 4$.

(3) Effect of Initial Length and Thickness Ratio

Different finite element models based on geometrically nonlinear analysis have been developed to simulate the curvature evolutions for samples with different initial length and thickness ratio. As explained above, the respective initial deformations at the onset the sintering for all the samples are considered while building the bi-layer models.

Figure 6 shows the curvature measurements of three different bilayers of CGO/LSM tapes with the same initial thickness ratio of $X = \frac{h_{01}}{h_{02}} = 4$ but different initial length $l_o = 15$, 25, and 40 mm. For the sake of comparison, the initial curvature of all the samples is adjusted to zero. If there was no effect of gravity on the development of the distortions, all the three bilayer systems should have shown the same evolutions of curvatures. This is because the internal stresses balance over the thickness of the layers which makes the curvature to be affected only by the thicknesses in addition to the material properties.[9–11] However, it is observed that the curvature varies depending on the length of the samples where less curvature is shown as the length of the sample increases because of gravity.

Table III. Mesh Convergence Behavior of the Finite Element Model (for Bilayer Sample with an Initial Length of 15 mm and Thickness Ratio of 4)

Total number of elements	Maximum curvature (1 m^{-1})
200	93.62
250	100.21
390	112.43
940	136.84
1275	139.22
1850	140.01
2861	140.12

Figure 6 also shows the model predictions for curvatures of bilayers simulated for the three different samples described above. The variation of curvature with the length of the samples is also verified by the finite element models. The influence of gravity is pronounced when the length of the bilayer increases due to longer arm span of the distorted sample, which increases the effect of gravitational weight opposing the development of the distortion.

Similarly, three separate experiments and simulations have been made for bilayer geometries consisting of the same initial length $l_o = 25$ mm but different thickness ratios of $X = \frac{h_{01}}{h_{02}} = 2, 4,$ and 6. The simulations were used to study the effect of the initial thickness ratio of the layers on the curvature evolution, Fig. 7.

It is observed that for a bilayer having a thickness ratio of $X = 2$, the distortion is very large and it reduces with increasing thickness ratio. The trend shown in the experiments has also been verified by the finite element models built with different thickness ratios as shown also in Fig. 7. For the sake of comparison, the initial curvatures of all the samples have been adjusted to zero.

Although the model accounts for most of the known effects including geometric nonlinearity, some discrepancies between the model predictions and experimental measurements in all the bilayers are observed, see Figs. 6 and 7. These might be due to stress relaxation that results from some observed microcrack growth close to the interface of the bilayer after de-binding and/or during the sintering cycle. Microcracks close to the interface between the CGO and LSM layer and also around the surface of the CGO layer has been observed by SEM images taken from the bilayer samples at the end of the sintering cycle, see Fig. 8.

Development of microcracks especially in the constraining layer can reduce the stress development in the bilayer resulting in small curvature development. A similar observation is reported by Ollagnier *et al.*[3] The effect of micro-cracks is more pronounced when there is a very large stress as in the case of bilayer with initial thickness ratio $X = 2$, as seen on

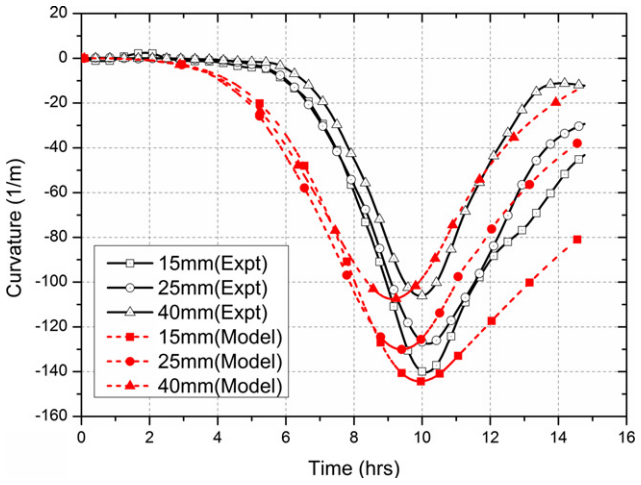

Fig. 6. Comparison of curvature evolutions for three bilayers with different initial lengths (solid lines) together with the corresponding model predictions (dashed lines).

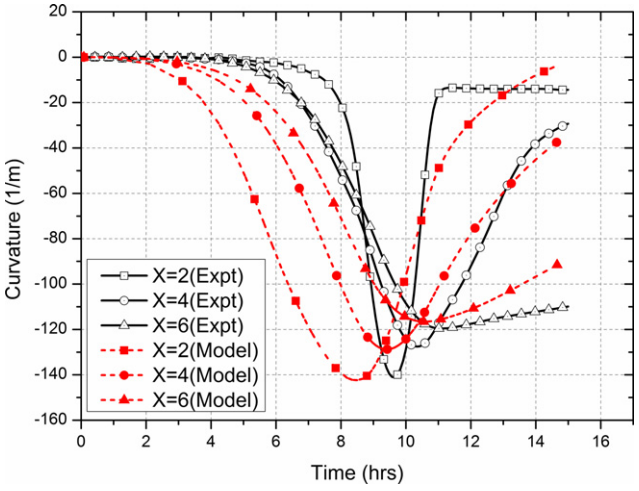

Fig. 7. Comparison of curvature evolutions for three bilayers with different initial thickness ratios (solid lines) together with the corresponding model predictions (dashed lines).

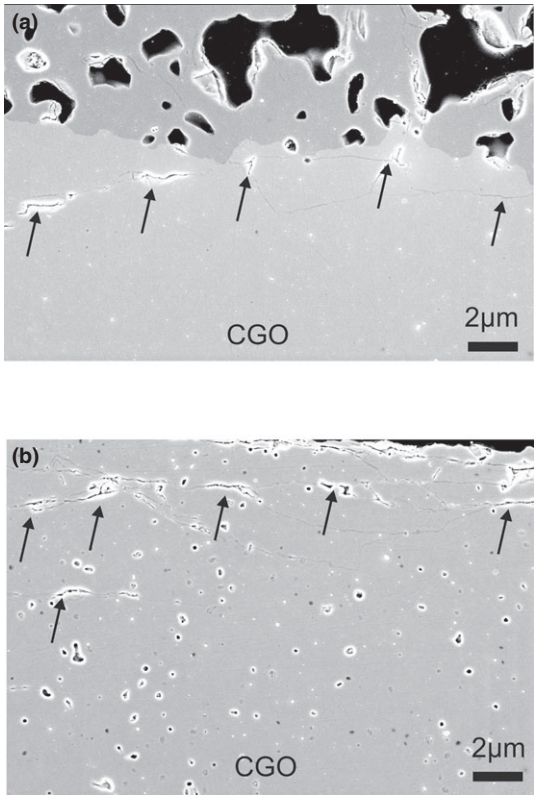

Fig. 8. Microcracks observed in the bilayers at the end of the sintering cycle (a) micro-cracks at the interface of the layers and (b) micro-cracks at the surface of the CGO layer.

Fig. 7 showing larger discrepancy between the model and experiments compared to the others. Other effects such as anisotropies in the pore-grain structure, which has not been considered in this work, could also explain the discrepancies between the models and experiments. Continuum theory of sintering, in its current state, is not able to account for these losses of continuity. The continuum theory of sintering could be combined with damage models [34] or meso-scale models[35–37] in order to describe the development of these micro-cracks and the consequent reduction of stresses. It is beyond the scope of this work to pursue such enrichments of the continuum theory of sintering.

In addition to the micro-cracks in the bilayer samples, the simplified constitutive models used in this study, for example, to describe sintering stress and creep properties could be the other factors for the discrepancy between the model and the experiments. For instance, the limitations of linear-viscous models, originally developed for bodies that sinter by viscous flow, are discussed by Garino *et al.*[38] Furthermore, the effective sintering viscosity could be described by more rigorous models which can account for additional parameters, e.g., grain size, as described by Argüello *et al.*[39] with more experimental works. Summary of the different models for sintering viscosity can also be found in Ref. [14].

As an example of how the change in the final curvature as a function of the initial thickness ratio of the layers after 8 h of sintering has also been shown in Fig. 9. The change in curvature is drastic for the range in the thickness ratio of $0 < X < 2$. By increasing the thickness of the slowly shrinking layer, in this case the CGO layer, it is possible to significantly reduce the curvature at the end of the sintering cycle.

(4) Effect of Friction

Finally the effect of friction between the edges of the sample and the surface of the sintering furnace has also been investigated. Two bilayers with the same initial length and thickness

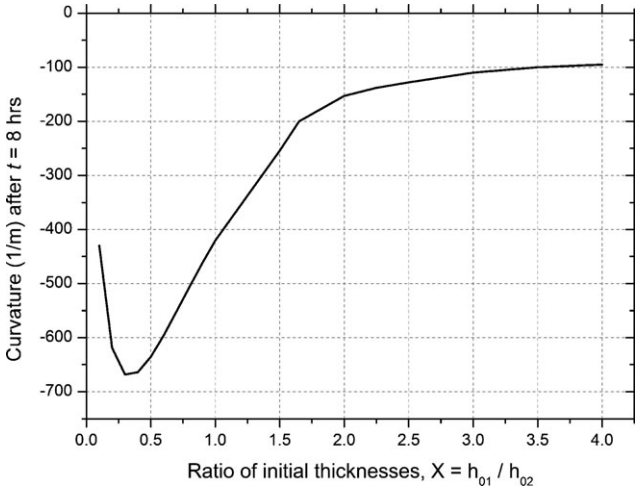

Fig. 9. Variation of final curvatures after sintering for 8 h as a function of initial thickness ratio.

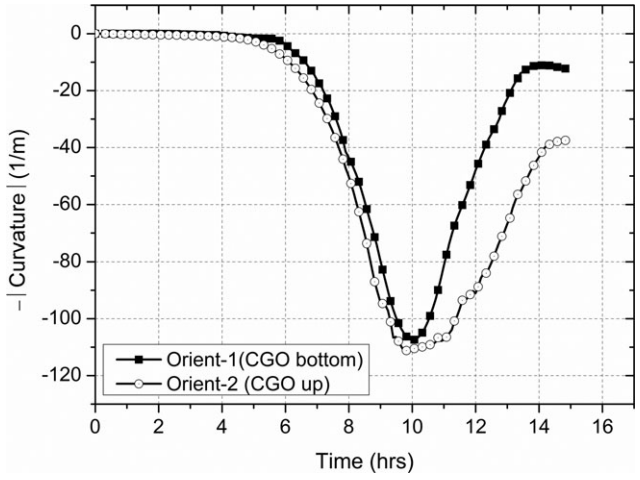

Fig. 10. Curvature evolution of the same bilayer samples in different orientations showing the effect of friction.

ratio of CGO and LSM tapes were cofired in different orientations. In the first orientation, the bilayer sample is cofired, where it is placed in such a way that the CGO layer is on the bottom side. The opposite is made in the second orientation i.e., the bilayer sample is placed in a way that the CGO layer is on the top side of the bilayer. Figure 10 shows the curvature evolutions measured during the sintering cycle. In the second orientation where the curvature is growing towards the LSM tape, in contact with the support surface, it is shown that the distortion is retarded compared to the first orientation. This is clearly due to the friction between the sample edges and the surface of the sample support hindering the kinetics of distortion. Furthermore the bumpy kinetics of distortion (curvature plot) in the second orientation clearly indicates the effect of friction. Note here that the curvature of the bilayer in the first orientation is opposite to the second one. The curvatures are plotted with opposite signs and normalized to zero at the start of the sintering for the sake of comparison.

V. Conclusions

A finite element model based on the continuum theory of sintering were developed to justify the distortions during sintering experiments of bilayers composed of LSM and CGO tapes. Free shrinkage kinetics of both tapes were used to estimate the input parameters necessary for finite element

models. Systematic studies on the effect of factors like gravity and friction together with the initial geometries on the kinetics of distortions of bilayers during sintering is presented. The finite element model simulations were able to capture the observed behaviors of distortions during different sets of experiments involving different bilayers. Some discrepancies are still observed, and it was speculated that these were due to stress relaxation near the interfaces of the bilayers due to micro-crack growth. Understanding the effect of factors like gravity and friction during sintering of bilayered porous structures could be helpful to reduce the shape distortion problems usually observed during cofiring.

Acknowledgment

The authors would like to acknowledge the support of the Danish Council for Independent Research Technology and Production Sciences (FTP) which is part of The Danish Agency for Science, Technology and Innovation (FI) (Project # 09-072888).

References

[1]J. Chang, O. Guillon, J. Rödel, and S. Kang, "Characterization of Warpage Behavior of Gd-Doped Ceria/Nio-Yttria Stabilized Zirconia bi-Layer Smaples for Solid Oxide Fuel Cell Applications," *J. Power Sources*, **185**, 759–67 (2008).

[2]J. Kanters, U. Eisele, and J. Rödel, "Cosintering Simulation and Experimentation: Case Study of Nanocrystalline Zirconia", *J. Am. Ceram. Soc.*, **84**, 2757–63 (2001).

[3]J. Ollagnier, O. Guillon, and J. Rödel, "Constrained Sintering of a Glass Ceramic Composite: I. Asymmetric Laminates", *J. Am. Ceram. Soc.*, **93**, 74–81 (2010).

[4]M. Cologna, V. Sglavo, and M. Bertoldi, "Sintering and Deformation of Solid Oxide Fuel Cells Produced by Sequential Tape Casting", *Int. J. Ceram. Technol.*, **7**[6] 803–13 (2010).

[5]R. Mücke, N. Menzler, H. Buchkremer, and D. Stöver, "Cofiring of Thin Zirconia Films During SOFC Manufacturing", *J. Am. Ceram. Soc.*, **92** [1] S95–102 (2009).

[6]P. Cai, D. Green, and G. Messing, "Constrained Densification of Alumina/Zirconia Hybrid Laminates, I: Experimental Observations of Processing Defects", *J. Am. Ceram. Soc.*, **80** [8] 1929–39 (1997).

[7]P. Cai, D. Green, and G. Messing, "Constrained Densification of Alumina/Zirconia Hybrid Laminates, II: Viscoelastic Stress Computation", *J. Am. Ceram. Soc.*, **80** [8] 1940–8 (1997).

[8]S. Lee, G. Messing, and D. Green, "Warpage Evolution of Screen Printed Multilayer Ceramics During co-Firing", *Key Eng. Mater.*, **264-268**, 321–8 (2004).

[9]A. Kaiser, A. Prasad, S. Foghmoes, S. Ramousse, N. Bonanos, and V. Esposito, "Sintering Process Optimization for Multi-Layer CGO Membranes by in Situ Techniques", *J. Eur. Ceram. Soc.*, **33**, 549–55 (2013).

[10]E. Olevsky, T. Molla, H. Frandsen, R. Bjørk, V. Esposito, D. Ni, A. Ilyina, and N. Pryds, "Sintering of Multilayered Porous Structures: Part I-Constitutive Models", *J. Am. Ceram. Soc.*, **96**[8], 2657–65 (2013).

[11]H. Frandsen, E. Olevsky, T. Molla, V. Esposito, R. Bjørk, and N. Pryds, "Modeling Sintering of Multilayers Under Influence of Gravity," *J. Am. Ceram. Soc.*, **96** [1] 80–9 (2013).

[12]T. Molla, H. Frandsen, R. Bjørk, D. Ni, E. Olevsky, and N. Pryds, "Modeling Kinetics of Distortion in Porous bi-Layered Structures," *J. Eur. Ceram. Soc.*, **33** [7] 1297–305 (2013).

[13]R. Bordia and G. Scherer, "On Constrained Sintering –I: Constitutive Model for Sintering Body," *Acta Mater.*, **36** [9] 2393-7 (1988).

[14]R. Bordia and G. Scherer, "On Constrained Sintering –II: Comparison of Constitutive Models," *Acta Mater.*, **36** [9] 2399–409 (1988).

[15]E. Olevsky, "Theory of Sintering: From Discrete to Continuum, "*Mater. Sci. Eng. R.: Reports*, **23**, 41–100 (1998).

[16]D. Green, O. Guillon, and J. Rödel, "Constrained Sintering: A Delicate Balance of Scales," *J. Eur. Ceram. Soc.*, **28**, 1451–66 (2008).

[17]S. Kiani, J. Pan, J. Yeomans, M. Barriere, and P. Blanchart, "Finite Element Analysis of Sintering Deformation Using Densification Data Instead of a Constitutive law," *J. Eur. Ceram. Soc.*, **27**, 2377–83 (2007).

[18]M. Gasik and B. Zhang, "A Constitutive Model and FE Simulation for Sintering Process of Powder Compacts," *Comp. Mater. Sci.*, **18**, 93–101 (2000).

[19]H. Zipse, "Finite Element Simulation of die Pressing and Sintering of Ceramic Components," *J. Eur. Ceram. Soc.*, **17**[14] 1707–13 (1997).

[20]M. Jeong, J. Yoo, S. Rhim, S. Lee, and S. Oh, "A Unified Model for Compaction and Sintering Behavior of Powder Processing," *Finite Elem. Anal. Des.*, 2012; **53**, 56–62.

[21]T. Kraft and H. Riedel, "Numerical Simulation of Solid State Sintering; Model and Application," *J. Eur. Ceram. Soc.*, **24**, 345–61 (2004).

[22]E. Olevsky, R. German, and A. Upadhyaya, "Effect of Gravity on Dimensional Change During Sintering-II: Shape Distortion," *Acta Mater.*, **48**, 1167–80 (2000).

[23]S. Schoenberg, D. Green, A. Segall, G. Messing, A. Grader, and P. Halleck, "Stress and Distortion due to Green Density Gradients During Densification," *J. Am. Ceram. Soc.*, **89** [10] 3027–33 (2006).

[24]G. Brown, R. Levine, A. Shaikh, and E. Olevsky, "Three Dimensional Solar Cell Finite Element Sintering Simulation," *J. Am. Ceram. Soc.*, **92** [7] 1450–5 (2009).

[25]D. Ni, C. Schmidt, F. Teocoli, A. Kaiser, K. Andersen, S. Ramousse, and V. Esposito, "Densification and Grain Growth During Sintering of Porous $Ce_{0.9}Gd_{0.1}O_{1.95}$ Tape Cast Layers: A Comprehensive Study on Heuristic Methods," *J. Eur. Ceram. Soc.*, **33**, 2529–37 (2013).

[26]D. Ni, V. Esposito, C. Schmidt, T. Molla, K. Andersen, A. Kaiser, S. Ramousse, and N. Pryds, "Camber Evolution and Stress Development of Porous Ceramic Bilayers During co-Firing," *J. Am. Ceram. Soc.*, **96**, 972–8 (2013).

[27]M. Reiterer, K. Ewsuk, and J. Arguello, "An Arrhenius-Type Viscosity Function to Model Sintering Using the Skorohod–Olevsky Viscous Sintering Model Within a Finite-Element Code," *J. Am. Ceram. Soc.*, **89**, 1930–5 (2006).

[28]F. Raether and P. Horn, "Investigation of Sintering Mechanisms of Alumina Using Kinetic Field and Master Sintering Diagrams," *J. Eur. Ceram. Soc.*, **29**, 2225–34 (2009).

[29]N. Ramakrishnan and V. Arunachalam, "Effective Elastic-Moduli of Porous Solids," *J. Mater. Sci.*, **25** [9] 3930–7 (1990).

[30]B. McCarthy, L. Pederson, R. Williford, and X. Zhou, "Low-Temperature Densification of Lanthanum Strontium Manganite ($La_{1-x}Sr_xMnO3$), x = 0.0-0.2," *J. Am. Ceram. Soc.*, **92** [8] 1672–8 (2009).

[31]X. Fan, E. Casen, Q. Yang, and J. Nicholas, "Room Temperature Elastic Properties of Gadolinia- Doped Ceria as a Function of Porosity," *Ceram. Int.*, **39**, 6877–86 (2013).

[32]A. Atkinson and A. Selcuk, "Mechnaical Behavior of Ceramc Oxygen ion-Conducting Membranes," *Solid State Ionics*, **134**, 59–66 (2000).

[33]S. Giraud and J. Canel, "Young's Modulus of Some SOFC Materials as a Function of Temperature," *J. Eur. Ceram. Soc.*, **28**, 77–83 (2008).

[34]G. Bruno, A. Efremov, A. Levandovskiy, I. Pozdnyakova, D. Hughes, and B. Clausen, "Thermal and Mechanical Response of Industrial Porous Ceramics," *Mater. Sci. Forum*, **652**, 191–6 (2010).

[35]T. Molla, R. Bjørk, E. Olevsky, N. Pryds, and H. Frandsen, "Multi-Scale Modeling of Shape Distortions During Sintering of bi-Laers," *J. Comp. Mat. Sci.*, **88**, 28–36 (2014).

[36]C. Martin and R. Bordia, "The Effect of a Substrate on the Sintering of Constrained Films," *Acta Mater.*, **57**, 549–58 (2009).

[37]T. Rasp, C. Jamin, A. Wonisch, T. Kraft, and O. Guillon, "Shape Distortion and Delamination During Constrained Sintering of Ceramic Stripes: Discrete Element Simulations and Experiments," *J. Am. Ceram. Soc.*, **95**[2] 586–92 (2012).

[38]T. Garino and H. Bowen, "Kinetics of Constrained-Film Sintering," *J. Am. Ceram. Soc.*, **73**[2] 251–7 (1990).

[39]J. Argüello, M. Reiterer, and K. Ewsuk, "Verification, Performance, Validation and Modifications to the SOVS Continuum Constitutive Model in a Nonlinear Large Deformation Finite Element Code," *J. Am. Ceram. Soc.*, **92** [7] 1442–9 (2009).

[40]Abaqus 6.11 User Subroutine Reference Manual, Providence RI, ©Dassault Systemes, 2011.

[41]Abaqus 6.11 Analysis User's Manual, Providence RI, ©Dassault Systemes, 2011.

[42]R. M. *Sintering of Ceramics*. 1st ed. CRC Press, Taylor & Francis Group, Boca Raton, Florida, 2008. □

E. PAPER-V

T.T. Molla, D.K. Ramachandran, D.W. Ni, V. Esposito, F. Teocoli, E. Olevsky, R. Bjørk, N. Pryds, A. Kaiser and H.L. Frandsen, "Constrained sintering of bi-layered tubular structures," *J Am Ceram Soc*, *under review* (2014)

Journal of the American Ceramic Society

Constrained Sintering of Bi-layered Tubular Structures

Journal:	*Journal of the American Ceramic Society*
Manuscript ID:	JACERS-34825
Manuscript Type:	Article
Date Submitted by the Author:	08-Apr-2014
Complete List of Authors:	Molla, Tesfaye; Technical University of Denmark , Department of Energy Storage and Conversion Kothanda Ramachandran, Dhavanesan; Technical University of Denmark, Energy Conversion and Storage Ni, De-Wei; Technical University of Denmark, Department of Energy Conversion and Storage ; Teocoli, Francesca; Technical University of Denmark, Department of Energy Conversion and Storage Olevsky, Eugene; San Diego State University, Mechanical Engineering Bjørk, Rasmus; Technical University of Denmark, Energy conversion and storage Pryds, Nini; Technical University of Denmark, Energy conversion and storage Kaiser, Andreas; Technical University of Denmark, Department of Energy Conversion and Storage Frandsen, Henrik; Technical University of Denmark, Department of Energy Conversion and Storage
Keywords:	sinter/sintering, multilayers, modeling/model, stress, processing

Constrained Sintering of Bi-layered Tubular Structures

Tesfaye Tadesse Molla[1], Dhavanesan Kothanda Ramachandran, De Wei Ni, Francesca Teocoli, Eugene Olevsky, Rasmus Bjørk, Nini Pryds, Andreas Kaiser, Henrik Lund Frandsen

Technical University of Denmark, Department of Energy Conversion and Storage, Risø Campus

Frederiksborgvej 399, P.O. Box 49, Building 779, 4000 Roskilde, Denmark

Abstract

Constrained sintering of tubular bi-layered structures is being used in the development of various technologies. Due to mismatch in the densification rate between the layers in the tubular geometry, stresses develop and sometimes create various processing defects. An analytical model is developed to describe the densification and stress developments during constrained sintering of tubular bi-layered samples. The direct correspondence between linear elastic and linear viscous theories is used as a basis for the model development. The developed analytical model is first verified by finite element simulation for the constrained sintering of tubular bi-layer system. Furthermore, the analytical model is validated using densification results from sintering of bi-layered tubular supported ceramic oxygen membrane based on porous MgO and $Ce_{0.9}Gd_{0.1}O_{1.95-d}$ layers. Model input parameters, such as the shrinkage kinetics and viscous parameters are obtained experimentally using optical dilatometry and thermo-mechanical analysis. Results from the analytical model are found to agree well with finite element simulations as well as measurements from sintering experiment.

Keywords: Constrained sintering, Tubular bi-layer, Oxygen membrane, Sintering, Stress

[1] Corresponding author:- Address: Frederiksborgvej 399, P.O. Box 49, Building 778, 4000 Roskilde, Denmark, Tele: +45 2074 5931, Fax: +45 4677 5858, e-mail: ttmo@dtu.dk

1. Introduction

Functionally graded tubular multi-layered ceramic structures are being used in the development of tubular type of solid oxide fuel cells and gas separation technologies [1 - 5]. A tubular multi-layer structure with thin film oxygen transport membrane layer on a porous support offers improved performance due to reduced thickness of the separation layer. Mechanical and dimensional stability together with the opportunity to use cost effective shaping processes for mass production such as extrusion and dip coating is some of the other reasons to use tubular multi-layers [1 - 3]. Nevertheless, an important and critical step in the manufacturing of such tubular multi-layers is the simultaneous sintering of the different layers (co-sintering), which is required to densify the green structure and give it higher strength [4]. Processing defects like cracks, delaminations and coating peel-offs are some of the problems associated with sintering of tubular multi-layer samples. Such defects are believed to occur mainly due to the transient stress development inside the structure in response to the differential shrinkage in the constituent layers. In order to produce defect free tubular multi-layered structures, it is important to control and optimize the transient stress generation during the entire sintering process. Thus, it is necessary to develop a model to understand development of stresses and densification mechanisms.

The problem of transient stresses during sintering of *planar* multi-layer structures including camber development in asymmetric multi-layers has been addressed in numerous publications [6 -20]. Generally to model densification and stress generations during co-firing of planar multi-layered samples, the continuum theory of sintering has been used [6, 7]. The porous structure has then assumed to have a linear viscous behavior, where the viscous strain rate is directly proportional to the applied load [6]. The total deformation in the sintering body is thus equal to the sum of the viscous strain rate and internal shrinkage rate, which is driven by a hydrostatic potential often referred to as the sintering stress [21].

Timoshenko and Goodier provided an analytical elastic solution for stresses in a single layered tube exposed to a gradient in internal strain (e.g. thermal or chemical) [22]. In addition, Lamé derived the stress field in a tube exposed to an external pressure [23]. Recently Kwok et *al*. generalized those analytical expressions in [22] and [23] for elastic materials to describe stress developments in bi-layered tubular supported oxygen membranes under internal and external pressures [24]. For bi-layer structures, Kwok et *al*. assumed the pressure in Lamé's model as the interaction pressure between the two monolithic tubular layers, which may arise due to mismatch in the internal strains of the layers. In this work, Kwok et *al*. tried to analyze elastic stress developments due to gradient and mismatch in the chemical and/or thermal strains during operations of bi-layered tubular structures, for example, in oxygen separation applications [24].

Based on the analogy between linear elasticity and linear viscous models, the methodology used by Kwok et *al*. to analyze elastic stresses could be extended for linear viscous materials and a time dependent analysis. This is made by invoking the analogy between internal strains (thermal or chemical) in the elastic materials and free shrinkage rates in the viscous materials. The mechanical viscous properties are then defined for a given temperature and microstructure during the sintering cycle. During sintering of porous bi-layered tubular body, mismatch in the densification rate between the two layers can also develop stresses. If the sintering bodies in the tubular bi-layer system are modeled by linear viscous materials, the mismatch in the internal shrinkage rate between the two layers should be directly proportional to the development of stress. By doing so, it is possible to model the development of stresses and densification in each layer during sintering of bi-layered tubular structures.

Therefore, an analytical model describing stress developments and densification during constrained sintering of bi-layered tubular structures has been developed in this work. In order to verify the analytical model, finite element simulations for constrained sintering of bi-layered tubular sample is

performed. The analytical model is also validated using constrained sintering experiment of tubular bi-layered oxygen membrane based on porous magnesium oxide (MgO) and $Ce_{0.9}Gd_{0.1}O_{1.95-d}$ (CGO) layers. Model input parameters such as the shrinkage kinetics and viscous parameters of the individual layers of the tubes are obtained experimentally using optical dilatometry and a thermo-mechanical analysis (TMA) respectively.

2. Experimental

Raw powders

Three types of powders were used for the preparation of asymmetric tubular membrane structures: 1) MgO powder (Product # 12R-0801, Inframat Advanced Materials, USA) and 2) a graphite powder (V-UF1 99.9, Graphit Kropfmühl AG, Germany) as a pore former, both for the porous support; and 3) CGO (GDC10-TC, Fuel Cell Materials, USA) for the dense membrane layer. The raw ceramic powders (MgO, CGO) were pre-calcined at 1000 °C with a heating rate of 100 °C/hr for 10 hrs to reduce the surface area of the powder and hence reduce the sintering activity. The specific surface areas of the calcined MgO and CGO powders were measured by the BET method to be 10.8 m^2/g and 4.3 m^2/g with a particle size of (d50: ~1.53 µm) and (d50: ~2.14 µm) respectively.

Layer preparation

MgO feedstocks for thermoplastic extrusion were prepared from MgO powder, graphite, a thermoplastic binder (Elvax 250, Du Pont; USA), paraffin wax (Sigma-Aldrich, USA) as a plasticizer, and stearic acid (Sigma-Aldrich, USA) as a dispersant. The MgO feedstocks were extruded into tubes (14 mm outer diameter and 1 mm wall thickness) using a Brabender extruder 19/20DN to prepare the porous membrane support layer.

For the dense membrane layer, first the pre-calcined CGO powder was dispersed in an ethanol based suspension with polyvinylpyrrolidone (PVP) as dispersant and polyvinylbutyral (PVB) as binder. The

resulting slurry for the dip coating was homogenized by ball milling for 72 hrs. The slurry for the preparation of the dense membrane was dip coated on the extruded MgO tubes at a constant speed of 2.5 mm/s in a controlled atmosphere. The green densities of the extruded and dip coated layers were measured on the basis of mass and volume measurements. The relative density of the sample was calculated from the ratio between the measured density and the theoretical density of the powder.

Sintering procedures

The heat treatment procedure for the tubular asymmetric bi-layered sample was performed by applying an iso-rate ramp of 0.25 ^{o}C/min for the de-binding cycle from room temperature to 650 °C and 0.5 °C/min for the sintering cycle. Further bi-layers were heated with the same heating profile to different temperatures of 250 °C, 450 °C, 650 °C, 850 °C, 1000 °C, 1100 °C and 1300 °C, followed by cooling down to room temperature. The bi-layers were checked for defects after each respective temperature cycle and simultaneously the necessary data were collected for comparison with model. Figure 1 shows a schematic cross section and a photo of the MgO tube with a dip coated CGO layer after heat treatment to 650 °C.

Figure 1: about here

The shrinkage in each layer was calculated from the sample thickness after each thermal treatment. The sample thickness was measured using scanning electron microscopy, SEM (TM300, Hitachi, Japan). After de-binding, a fractured surface of the cross section was analyzed for the microstructure characterization and thickness measurement. The samples sintered above 850 ^{o}C were imbedded in a polymer and afterwards polished. The polished cross sections were then used for measuring the shrinkage of MgO and CGO layer. The average values of thickness were determined from four measurements. Similarly, the porosities in each layer were calculated using the SEM Images from the fractured surfaces of the

sample. Table 1 shows the different dimensions and porosity values of the layers measured at the initial and final (1300 ^{o}C) stage of the sintering cycle.

Table 1 about here

By using the raw materials of both MgO and CGO described above, free standing tapes of each layer were prepared to measure the free shrinkage kinetics and viscosity. The heat treatment profile used for bi-layered tubular supported membrane is also applied while measuring the shrinkage and viscosity of each tape. For free sintering of individual layers, optical dilatometry (TOMMI, Fraunhofer ISC, Würzburg, Germany) results were collected for each sample size with time and temperature. Assuming isotropic shrinkage, the densification strains are calculated from the linear shrinkage data. Details of the methodologies used in the sample's processing and optical dilatometry can be found in Ni et *al*. [25].

The viscosities of MgO and CGO during sintering were determined using cyclic loading dilatometry with the help of thermo-mechanical analyzer (TMA 402 F1 Hyperion, Netzsch, Germany). The details of the methodology used are explained in [26]. For thermo-mechanical analysis, two layers with a final thickness of 1 mm for each material were shaped and cut into 20 mm x 5 mm bars. Specimens were calcined at 700 °C for 2 hrs with a heating rate of 0.25 °C/min, to obtain samples that were stiff enough to be placed in a three-point bending configuration. During the measurement, the samples were heated in air from room temperature at a heating rate of 0.5 °C/min applying a superimposed 8-min cyclic squared profile. The maximum load was 8 mN. The load was applied by a trapezoidal push rod at the center of the beam with 5 mm width and span of 1 cm. The deflection changes were measured with an accuracy of ± 0.125 nm.

3. **Model development**

Consider the cross section of porous bi-layered tubular structure made of support and membrane as shown in Figure 2. The tubular structure has the internal and external radii of r_i and r_o and an interfacial

radius of r_f in between the support and membrane. According to Bordia et al. a constitutive equation based on linear viscous behaviors is quite appropriate to use for porous bodies during sintering [6, 7]. In this theory, the viscous strain rate of isotropically deforming body is directly proportional to the stress components. There is also a direct correspondence between linear elasticity and linear viscous theories, where the viscous mechanical properties of the porous body can be defined either by bulk and shear viscosities or by uni-axial viscosity and viscous Poisson's ratio [6]. Therefore in this work, the analogy between linear elasticity and linear viscous theories, the elastic-visco elastic correspondence principle [27], has been used to describe the densification and stress developments during sintering of the porous bi-layered tubular structures.

Figure 2: about here

The length of the tube is assumed to be very large compared to the thickness of each layers, and hence plane strain analysis can be applied. Stresses develop only in the principal directions i.e. tangential, rr, radial, $\theta\theta$, and axial, zz, axis, as all the shear stresses vanish because of axisymmetry.

During sintering, stress in the support as well as membrane can develop because of:

1. The gradient of the internal free shrinkage rate, $\dot{\varepsilon}^f$, in each layer and
2. The interfacial pressure, P_f, that develop due to the mismatch in the shrinkage rates between the two layers.

Employing the correspondence between linear elasticity and linear viscous materials, the expressions in [24] can be adapted to linear viscous materials. In the case of a sintering tubular body, the internal strain, ε, can be replaced by the internal shrinkage rate, $\dot{\varepsilon}^f$. Table 2 summarizes how the equations for linear elastic model have been transformed into linear viscous materials.

Table 2 about here

In the expressions given in Table 2, the subscript *s* and *m* indicates the support and membrane, where as the superscript, ε, indicates stresses due to the internal strain in the elastic case or free strain rate, $\dot{\varepsilon}^f$, in the linear viscous case. As it is shown in Table 2, the stress expressions for linear viscous materials are found by replacing the Young's modulus and Poisson's ratio, E and ν, in the elastic model by uni-axial viscosity and viscous Poisson's ratio, η and ν'. Note that the expressions provided here represent stress/force balance of a viscous media at the specific geometry or radius, r, and not the time derivative of the elastic solution.

The stresses, σ, in the radial and tangential directions due to the interfacial pressure, P_f, that develops because of the mismatch in the shrinkage rate between the two layers, can be calculated based on expressions provided by Lame [23] as:

$$\sigma^P_{rr,s} = \frac{P_f r_f^2}{r_f^2 - r_i^2} - \frac{P_f r_f^2 r_i^2}{(r_f^2 - r_i^2) r^2} \quad (1)$$

$$\sigma^P_{\theta\theta,s} = \frac{P_f r_f^2}{r_f^2 - r_i^2} + \frac{P_f r_f^2 r_i^2}{(r_f^2 - r_i^2) r^2} \quad (2)$$

$$\sigma^P_{rr,m} = \frac{-P_f r_f^2}{r_0^2 - r_f^2} - \frac{-P_f r_0^2 r_f^2}{(r_0^2 - r_f^2) r^2} \quad (3)$$

$$\sigma^P_{\theta\theta,m} = \frac{-P_f r_f^2}{r_0^2 - r_f^2} + \frac{-P_f r_0^2 r_f^2}{(r_0^2 - r_f^2) r^2} \quad (4)$$

Here the superscript, P, indicates that stresses are from the interfacial pressure, whereas the subscripts *s* and *m* are again for the support and membrane. To calculate the stress components in Eqs (1) - (4), first the interfacial pressure has to be determined at each time during the sintering cycle based on the mismatch in the shrinkage rate, $\dot{\varepsilon}^f_{mis}$, between the two layers. To determine this, the continuity of

tangential strain rate, $\dot{\varepsilon}_{\theta\theta}$, at the interface between the support and membrane can be applied as suggested by Kwok et *al*. [24] This implies:

$$\dot{\varepsilon}_{\theta\theta,s} = \dot{\varepsilon}_{\theta\theta,m} \quad \text{at} \quad r = r_f \tag{5}$$

The boundary condition in Eq (5) gives the interfacial pressure, P_f, as:

$$P_f = \frac{1}{S_1}\dot{\varepsilon}^f_{mis} \tag{6}$$

where S_1 and $\dot{\varepsilon}^f_{mis}$ are given by:

$$S_1 = \frac{1-v'^2_m}{\eta_m}\frac{r_0^2+r_f^2}{r_0^2-r_f^2} + \frac{1-v'^2_s}{\eta_s}\frac{r_f^2+r_i^2}{r_f^2-r_i^2} + \frac{(1+v'_m)v'_m}{\eta_m} - \frac{(1+v'_s)v'_s}{\eta_s} \tag{7}$$

$$\dot{\varepsilon}^f_{mis} = \frac{2(1+v'_m)}{(r_0^2-r_f^2)}\int_{r_f}^{r_0} r\dot{\varepsilon}^f_m dr - \frac{2(1+v'_s)}{(r_f^2-r_i^2)}\int_{r_i}^{r_f} r\dot{\varepsilon}^f_s dr \tag{8}$$

For the details of the derivations, please refer to the work by Kwok et *al*. [24].

The total stress components, σ, in the radial and tangential directions can thus be given by Eqs (9) and (10) where the subscript, $j = s$ or m.

$$\sigma_{rr,j} = \sigma^P_{rr,j} + \sigma^{\varepsilon}_{rr,j} \tag{9}$$

$$\sigma_{\theta\theta,j} = \sigma^P_{\theta\theta,j} + \sigma^{\varepsilon}_{\theta\theta,j} \tag{10}$$

For derivation of the axial stress components, the axial strain rate components are assumed to be independent of the radius in the bi-layer structures and they can be written as [24]:

$$\sigma_{zz,s} = \eta_s(\dot{\varepsilon}_{zz} - \dot{\varepsilon}^f_s) + v'_s(\sigma_{rr,s} + \sigma_{\theta\theta,s}) \tag{11}$$

$$\sigma_{zz,m} = \eta_m(\dot{\varepsilon}_{zz} - \dot{\varepsilon}^f_m) + v'_m(\sigma_{rr,m} + \sigma_{\theta\theta,m}) \tag{12}$$

Here $\dot{\varepsilon}_{zz}$ is the axial strain rate in the bi-layer, which can be calculated from the force balance in the axial direction, see Eq (13). Substituting Eqs (11) and (12) into Eq (13), the axial strain rate can be found as:

$$\int_{r_i}^{r_f} 2\pi r\sigma_{zz,s}dr + \int_{r_f}^{r_0} 2\pi r\sigma_{zz,m}dr = 0 \tag{13}$$

$$\dot{\varepsilon}_{zz} = \frac{1}{S_2}\left[2(v'_m - v'_s)P_f r_f^2 + 2\eta_m \int_{r_f}^{r_0} r\dot{\varepsilon}_m^f dr + 2\eta_s \int_{r_i}^{r_f} r\dot{\varepsilon}_s^f dr\right] \tag{14}$$

Here the factor S_2 is given by:

$$S_2 = \eta_m(r_0^2 - r_f^2) + \eta_s(r_f^2 - r_i^2) \tag{15}$$

The equations up until now are adapted from the general elastic solution in [24] to linear viscous materials in order to calculate the stress levels at a given time during the sintering cycle. The stresses at each time step are then used to calculate the constraint related strain rates so as to update the porosity, radii and thickness of each layer.

Obtaining the porosity evolution

By dividing each layer through *n* equal points and by using numerical integrations, it is possible to find all the stresses components at each point in time and hence calculate the corresponding viscous strain rates over the thickness, $\dot{\varepsilon}^v$, in each layer as:

$$\dot{\varepsilon}^v_{rr,j} = \frac{1}{\eta_j}\left[\sigma_{rr,j} - v'_s(\sigma_{\theta\theta,j} + \sigma_{zz,j})\right] \tag{16}$$

$$\dot{\varepsilon}^v_{\theta\theta,j} = \frac{1}{\eta_j}\left[\sigma_{rr,j} - v'_s(\sigma_{rr,j} + \sigma_{zz,j})\right] \tag{17}$$

Here again the subscript, j, can be of either for the substrate, *s*, or membrane, *m*.

The total strain rate in the radial, rr, tangential, $\theta\theta$, and axial, zz, axis and the corresponding volumetric strain rate, $\dot{e}$, in either the support or membrane can be updated as:

$$\dot{\varepsilon}_{rr,j} = \dot{\varepsilon}_j^f + \dot{\varepsilon}_{rr,j}^v \tag{18}$$

$$\dot{\varepsilon}_{\theta\theta,j} = \dot{\varepsilon}_j^f + \dot{\varepsilon}_{\theta\theta,j}^v \tag{19}$$

$$\dot{\varepsilon}_{zz,j} = \dot{\varepsilon}_{zz} \tag{20}$$

$$\dot{e}_j = \dot{\varepsilon}_{rr,j} + \dot{\varepsilon}_{\theta\theta,j} + \dot{\varepsilon}_{zz,j} \tag{21}$$

Therefore the porosity in each layer can be updated based on the conservation of mass that relates the volumetric strain rate, $\dot{e}$, to the porosity, θ_p, as [21]:

$$\dot{\theta}_{p,j} = \dot{e}_j(1-\theta_{p,j}) \tag{22}$$

The uni-axial viscosity is obtained experimentally, see Section 2. But the viscous Poisson's ratio, ν', is updated based on the instantaneous porosity of each layer at each time step using [18,21]:

$$\nu' = \frac{3\psi - \varphi}{6\psi + \varphi} \quad \text{where} \quad \psi = \frac{2}{3}\frac{(1-\theta_p)^3}{\theta_p} \quad \text{and} \quad \varphi=(1\text{-}\theta_p)^2 \tag{23}$$

Obtaining the thickness evolution

The total tangential strain rate, $\dot{\varepsilon}_{\theta\theta}$, can be described using the expression given in Eq (24) [22]. Here, V_r, the radial deformational velocity field and $\partial V_t/\partial\theta$ is the change in the tangential velocity field with an angle θ, which vanishes for an axisymmetric body in cylindrical $r-\theta-z$ coordinate system.

$$\dot{\varepsilon}_{\theta\theta} = \frac{V_r}{r} + \frac{1}{r}\frac{\partial V_t}{\partial\theta} \tag{24}$$

By using the tangential strain rates from Eq (19), the deformational velocity field, V_r, is calculated from Eq (24) across the thickness of the layer. The corresponding thicknesses of the layers are updated based on the updated internal, interfacial and external radii. Note that during the sintering cycle, the above equations are solved in a time dependent manner where the shrinkage rate, mechanical properties and the geometrical parameters are updated for each time step.

Finite element model

To verify the analytical model described above, a two dimensional finite element model for the constrained sintering of bi-layered tubular structure has been developed using ABAQUS™. With the help of creep user subroutine the total inelastic strains and porosity evolutions during sintering has been defined based on the Skorohod Olevsky viscous sintering model (SOVS) [21]. Details about the implementation of the SOVS theory into ABAQUS™ with the help of creep user subroutines to model sintering of multi-layers are reported in Molla et *al*. [28].

Only one quarter of the cross sectional domain is modeled because of symmetry of the geometry, loading and boundary conditions. The domain was discretized using eight noded plane strain elements (commonly referred to as CPE8 in the ABAQUS element library) with an element size of 50 and 13 µm for the support and membrane respectively. Symmetry boundary conditions are imposed on the truncated ends of the finite element model.

4. Results and discussion

The analytical model for constrained sintering of bi-layered tubular structure explained in Section 3 is implemented using a Matlab program. The development of stresses and densification in each layer together with geometrical parameters (the different radii in the bi-layer system and thicknesses) are calculated. The stress calculations from the analytical model are verified with the help of the finite element model developed to simulate the constrained sintering of bi-layered tubular sample. Furthermore, the shrinkage results from the analytical model are compared with SEM measurements made during the sintering experiment of tubular samples. From the dilatometry data, densification starts first in CGO layer and hence the bi-layer model simulations are performed beginning from the temperature wherein the CGO membrane starts to densify.

Figure 3 shows results for the uni-axial viscosity of both MgO and CGO as function of temperature obtained using the data collected from the TMA analysis. The uni-axial viscosities of both tapes show an exponential drop at lower sintering temperatures and remain more or less constant as the temperature increases. The trend in the viscosity variation for the sintering temperatures is similar with the observations reported for most porous ceramic oxides during densification [8, 19, 26].

Figure 3 about here

0.1. Development of stresses

The tangential stress (often called hoop stress) evolution at the external surfaces of each layer i.e at $r = r_f$ in the case of the MgO support and at $r = r_o$ in the case of CGO membrane is calculated from the analytical model. Figure 4 shows comparison of results from the analytical and finite element simulations. As it is shown the hoop stresses from the analytical model agree very well with predictions from numerical simulations. The hoop stresses are shown to be maximum at the beginning of the sintering process, wherein the membrane and support are exposed to tensile and compressive stresses respectively.

Figure 4 about here

During the sintering cycle, the hoop stresses evolve and finally the membrane and support will be in compression and tension respectively. The hoop stress in the membrane is quite large compared to stresses in the support, which are usually the main causes for hindering the densification in the CGO membrane. This means that the hoop stress is also the main cause for defects like cracks and peel-offs.

Similarly the analytical model predictions for the evolutions of radial stresses in both layers have been compared with the respective stress values from the numerical simulations as shown in Figure 5. Here also, the MgO support is initially exposed to compressive radial stress and evolves to tensile stress in time. Generally the magnitude of radial stresses in both layers is very small compared to the hoop stress

throughout the sintering cycle. Such observations again show that, most of the processing defects occur due to the hoop stresses at the beginning of the sintering cycle as the magnitudes of radial stresses are almost insignificant in both layers.

Figure 5 about here

In addition to stress evolutions in time, the variation of the hoop stress across the radius of each layer for a given time has been invetigated using both the analytical as well as numerical simulations. Figure 6(a) and (b) shows the hoop stress variation across the radius of the support and membrane around the early stage of the sintering ($t \approx 4$ hrs). Again a good agreement of the stress calculations from the analytical and numerical models are obitained as shown in Figure 6. The maximum deviation between the analytical and finite element models, in this case is close 1.24%. Note here that, the variations of the stresses are plotted as a function of radius from the inner, r_i, to interfacial, r_f, in case of the support and from the interfacial, r_f, to outer, r_o, in case of the membrane at the given time.

Figure 6 about here

The analytical model and the finite element simulations are in good agreement for all stresses during constrained sintering of tubular bi-layered structure. The strains and displacements also compare well in the two models. Therefore the analytical model provides a very good alternative to a circumstantial finite element analysis (FEA). In the following, the evolutions of shrinkage, porosity and shape of the bi-layered sample from experiment are compared with results from the analytical model.

0.2. Shrinkage

Figure 7 shows the analytical model prediction for the linear shrinkage across the thickness of each layer in comparison with free shrinkage data and the measurements taken during the sintering of tubular bi-layer. Comparison of shrinkage in the constrained CGO membrane with the free CGO tape shows that the CGO membrane is exposed to tensile stresses, which hinder the densification during sintering of the

tubular bi-layer. The constrained shrinkage in the MgO support is almost unaffected by the level of stresses generated in it. Results from the model agree well with the shrinkage measurements from SEM images of the samples at four different temperatures. It is evident that the linear shrinkage in the CGO membrane dominates the sintering cycle, which exposes it to tensile stress from the MgO support for most of the time.

Figure 7 about here

0.3. Porosity evolution

The porosity evolutions in each layer during constrained sintering of the bi-layer tubular sample were measured using SEM images at four different temperatures. Figure 8 shows the example of SEM images of MgO support and CGO membrane at 1100 ^{o}C. From the analytical model, Eq (22) is used to update the porosity in time. Figure 9 shows the comparison between results from the analytical model and measurement values with the standard deviation from the measurement. The standard deviations are deduced from the variations in the thickness observed from SEM images of the layers. Predictions from the analytical model agree well with the measured values in both the support as well as membrane. Porosity evolution in the case of constrained bi-layered tubular structures is size dependent as the total stress varies with the radius of the sample during constrained sintering of tubular samples.

Figure 8 about here

Figure 9 about here

0.4. Evolution of shape

In addition to densifications, the geometrical parameters of the tubular samples were also calculated using the analytical model. Figure 10(a) shows the evolutions of the internal, r_i, interfacial, r_f, and external, r_0, radii of the bi-layer sample during the entire sintering cycle. Experimental values, deduced from measurements of the interface diameter and thickness of the MgO support at four temperatures,

are also in good agreement with the model. The model predictions for the thickness evolution of each layer have also been shown in Figure 10(b).

Figure 10 about here

Processing defects such as axial cracks and peel-offs of the coating or membrane often occur due to the transient hoop stress, which is maximum at the beginning of the sintering process as shown in Figure 4. This is similar with processing flaw generations during constrained sintering of planar multi-layers [29]. The densification and stress analysis during constrained sintering of tubular bi-layer structures would help to optimize stresses, for example, as a function of thickness of the support or membrane. Figure 11 shows example of variation of the maximum hoop stress as function of ratio of thickness (i.e. radial thickness of the CGO membrane to the MgO support). For the sample analyzed in this study, increasing the thickness ratio between the two layers would not only decrease the hoop stress in the membrane but also increases the compressive hoop stress on the support. The increase of compressive hoop stress on the support can have an effect on the final size of the sample. Sometimes the dimensions are of course set by the application of the tubular structure, and the possibility for tuning these parameters might not be available.

Figure 11 about here

5. Conclusion

A closed form analytical model based on the analogy between linear elastic and linear viscous theories has been developed to describe densification and stress development during sintering of tubular bi-layered samples. Stresses during constrained sintering of tubular bi-layered structures develop not only due to mismatch in the shrinkage rate of the layers but also because of the radial gradients in the internal shrinkage rate of each layer. The developed analytical model is first verified by finite element simulation for the constrained sintering of tubular bi-layer system. Furthermore, the analytical model is

validated using densification results from sintering of bi-layered tubular supported ceramic oxygen membranes based on porous MgO and $Ce_{0.9}Gd_{0.1}O_{1.95-d}$ layers. Results from the analytical model agree well with finite element simulations as well as measurements from the experiment.

In general, the radial stresses in the bi-layered tubular structures are very small throughout the sintering cycle as compared to the hoop stresses. Processing defects like axial cracks and coating peel-offs mainly occur due to the hoop stress which is maximum at the beginning of the sintering cycle. The model provided in this study could be used to minimize the transient stress generations during constrained sintering of tubular bi-layered structures.

Acknowledgment

The authors would like to acknowledge the support of the Danish Council for Independent Research Technology and Production Sciences (FTP) which is part of The Danish Agency for Science, Technology and Innovation (FI) (Project # 09-072888). The support of US National Science Foundation Division of Civil, Mechanical Systems, and Manufacturing Innovations (NSF grant no. CMMI 1234114) is also gratefully appreciated.

Reference

1. J. Powell, S. Assabumrungrat and S. Blackburn, 'Design of ceramic paste formulations for co-extrusion', Powder Technology, 2013; 245: 21–27.
2. R. Bredesen, K. Jordal, and O.Bolland, 'High-temperature membranes in power generation with CO_2 capture', Chem Eng Process, 2004; 43: 1129–1158.
3. C. Zhang, Z. Xu, X. Chang, Z. Zhang and W. Jin, 'Preparation and characterization of mixed-conducting thin tubular membrane', J Membr Sci, 2007; 299: 261–267.
4. Z. Liu, G. Zhang, X. Dong, W. Jiang, W. Jin, and N. Xu, 'Fabrication of asymmetric tubular mixed-conducting dense membranes by a combined spin-spraying and co-sintering process', J Membr Sci, 2012; 415–416 :313–319.
5. M. Salehi, E. Pfaff , R. Junior, C. Bergmann, S. Diethelm, C. Neururer, T. Graule , B. Grobéty, and F. Clemens, '$Ba_{0.5}Sr_{0.5}Co_{0.8}Fe_{0.2}O_{3-\delta}$ (BSCF) feedstock development and optimization for thermoplastic forming of thin planar and tubular oxygen separation membranes', J Membr Sci, 2013; 443: 237–245.
6. R. Bordia and G. Scherer, 'On Constrained Sintering-I, Constitutive Model For A Sintering Body', Acta Metall, 1988; 36 [9]: 2393-2397.
7. R. Bordia and G. Scherer, 'On Constrained Sintering-II, Comparison of constitutive models', Acta Metall, 1988; 36 [9]: 2399-2409.
8. P. Cai, D. Green and G. Messing, 'Constrained densification of alumina/zirconia hybrid laminates: 1. Experimental observations of processing defects', J Am Ceram Soc, 1997; 80 [8]:1929-1939.
9. P. Cai, D. Green and G. Messing, 'Constrained densification of alumina/zirconia hybrid laminates: 2. Viscoelastic stress computation', J Am Ceram Soc, 1997; 80 [8]:1940-1948.
10. J. Kanters, U. Eisele and J. Rodel, 'Co-sintering simulation and experimentation: Case study of nanocrystalline zirconia', J Am Ceram Soc, 2001; 84 [12]: 2757-2763.

11. J. Ollagnier, D. Green, O. Guillon and J. Roedel, 'Constrained Sintering of a Glass Ceramic Composite: II. Symmetric Laminate', J Am Ceram Soc, 2009, 92 [12]: 2900-2906.
12. J. Ollagnier, O. Guillon and J. Roedel, 'Constrained Sintering of a Glass Ceramic Composite: I. Asymmetric Laminate', J Am Ceram Soc, 2010, 93 [1]: 74-81.
13. J. Chang, O. Guillon, J. Roedel and S. Kang, 'Characterization of warpage behaviour of Gd-doped ceria/NiO-yttria stabilized zirconia bi-layer samples for solid oxide fuel cell application', J Power Sources, 2008; 185 [2]: 759-764.
14. G. Lu, R. Sutterlin and T. Guppta, 'Effect of Mismatched Sintering Kinetics on Camber in a Low-Temperature Cofired Ceramic Package', J Am Ceram Soc,1993; 76 [8]: 1907-1914.
15. R. Muecke, N. Menzler, H. Buchkremer and D. Stoever, 'Cofiring of Thin Zirconia Films During SOFC Manufacturing,' J Am Ceram Soc, 2009; 92 [1]: S95-S102.
16. J. Kim, R. Rudkin, X. Wang and A. Atkinson, 'Constrained sintering kinetics of 3YSZ films', J Eur Ceram Soc, 2011; 31 [13]: 2231-2239.
17. E. Olevsky, T. Molla, H. Frandsen, R. Bjork, V. Esposito, D. Ni, A. Ilyina and N. Pryds, 'Sintering of Multilayered Porous Structures: Part I-Constitutive Models', J Am Ceram Soc, 2013, 1-9.
18. H. Frandsen, E. Olevsky, T. Molla, V. Esposito, R. Bjork and N. Pryds, 'Modeling Sintering of Multi-layers Under Influence of Gravity', J Am Ceram Soc, 2013; 96 [1]: 80-89.
19. T. Molla, H. Frandsen, R. Bjørk, D. Ni, E. Olevsky and N. Pryds, 'Modeling kinetics of distortion in porous bi-layered structures', J Eur Ceram Soc, 2013; 33 [7]: 1297-1305.
20. D. Ni, V. Esposito, C. Schmidt, T. Molla, K Andersen, A. Kaiser, S. Ramousse, N. Pryds, 'Camber evolution and stress development of porous ceramic bilayers during co-firing', J Am Ceram Soc, 2013; 96: 972-8.
21. E. Olevsky, 'Theory of sintering: from discrete to continuum', Mater Sc & Eng R-Reports, 1998; 23 [2]: 41-100.

22. S. Timoshenko and J. Goodier, 'Theory of elasticity', McGraw-Hill Book Company, 1951.

23. G. Lamé, 'Leçons sur la théorie mathématique de l'élasticité des corps solides', Bachelier, 1852.

24. K. Kwok, H. Frandsen, M. Søgaard and P. Hendriksen, 'Stress analysis and fail-safe design of bi-layered tubular supported ceramic membranes', J Memb Sci,2014; 453: 253-262.

25. D. Ni, C. Schmidt, F. Teocoli, A. Kaiser, K. Andersen, S. Ramousse, and V. Esposito, 'Densification and grain growth during sintering of porous $Ce_{0.9}Gd_{0.1}O_{1.95}$ tape cast layers: A comprehensive study on heuristic methods', J Eur Ceram Soc, 2013; 33: 2529-37.

26. F. Teocoli and V. Esposito, 'Viscoelastic properties of doped-ceria under reduced oxygen partial pressure', Script Mater, 2014; 75: 82-85.

27. S. Mukherjee and G. Paulino, 'The elastic-viscoelastic correspondence principle for functionally graded materials', J of Appl Mech-Transactions of the Asme, 2003;70 [3]: 359-363.

28. T. Molla, D. Ni, R. Bulatova, R. Bjørk, C. Bahl, N. Pryds and H. Frandsen, 'Finite element modeling of shape distortions during sintering of bi-layers', J Am Ceram Soc, 2014 (submitted).

29. R. Bordia and A. Jagota, 'Cracks growth and damage in constrained sintering', J Am Ceram Soc, 1993; 76[10]:2475-85.

Figure captions

Figure 1: Schematics of the cross section (left) and photo of a tubular asymmetric MgO support/CGO membrane bi-layer (right) after heat treatment to 650 °C.

Figure 2: Schematic representation of the porous bi-layered tubular structure.

Figure 3: Uni-axial viscosity of MgO and CGO tapes as a function of temperature.

Figure 4: The evolution of hoop stress in the support and membrane during the sintering cycle.

Figure 5: The evolution of radial stress in the support and membrane during the sintering cycle.

Figure 6: Hoop stress variation across the radius (a) MgO support (b) CGO membrane.

Figure 7: Comparison of linear shrinkage in free and constrained sintering together with experimental measurements for constrained sintering.

Figure 8: SEM characterization of the bi-layered tubular sample after sintering to 1100°C (a) MgO support and (b) CGO membrane.

Figure 9: Comparison of the evolution of porosity from model and experiment during constrained sintering of tubular bi-layer sample.

Figure 10: Evolution of geometrical parameters during the sintering cycle: (a) the different radii in the bi-layer (b) thickness.

Figure 11: Variation of hoop stress with ratio of thickness of the layers (CGO-membrane to MgO-support) at the beginning of the sintering cycle.

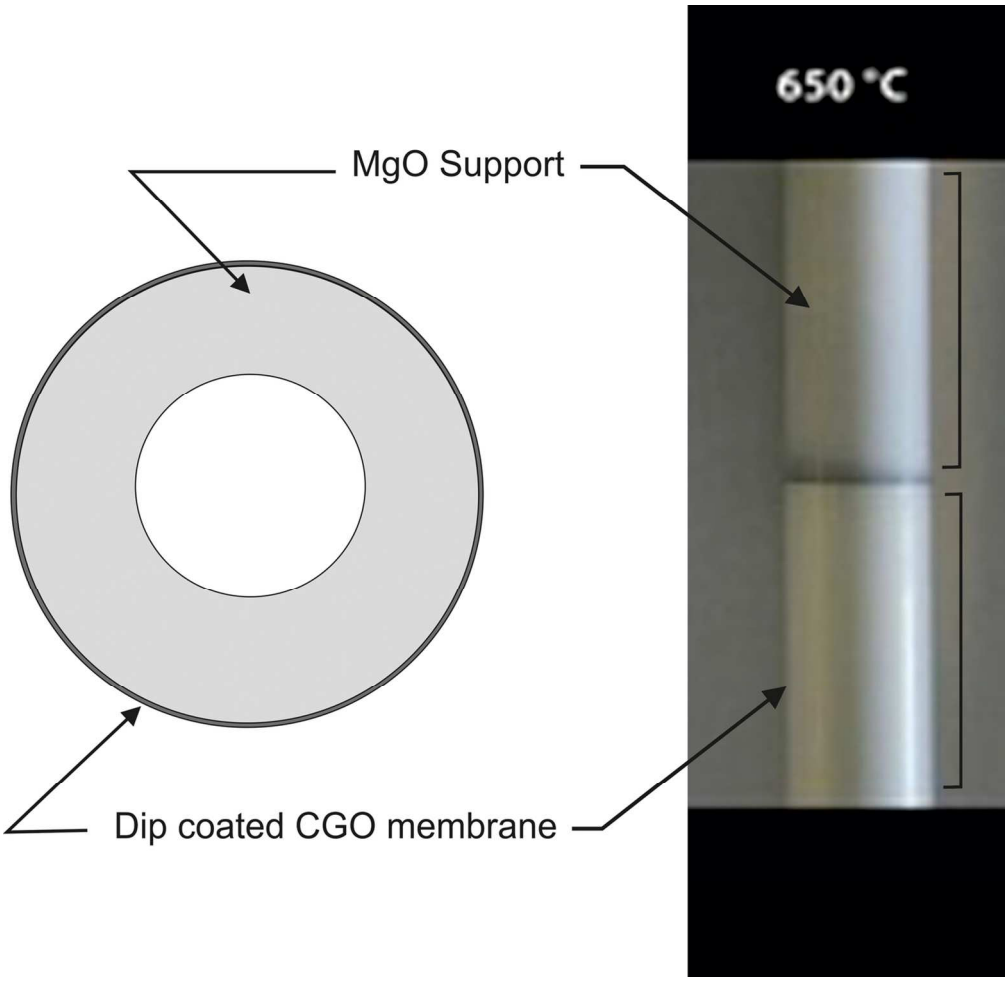

Figure 1: Schematics of the cross section (left) and picture of the asymmetric bi-layer tubular sample (right) consisting of dip coated CGO-membrane and MgO-support at 650 °C.
126x122mm (300 x 300 DPI)

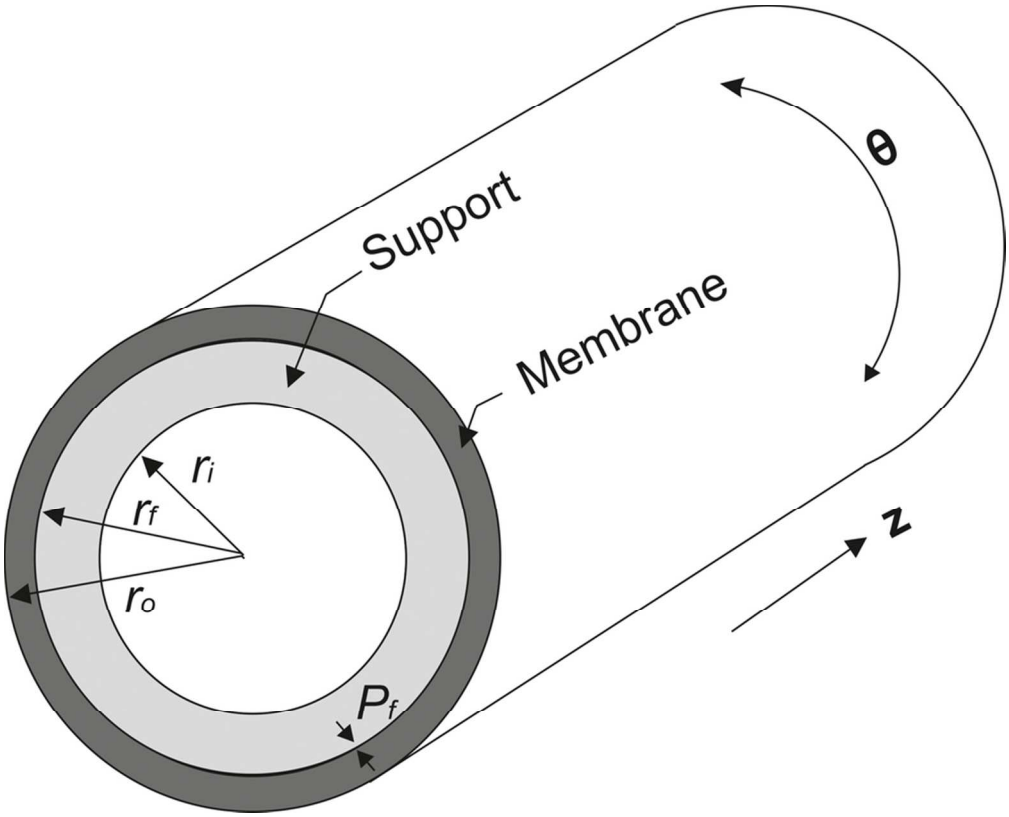

Figure 2: Schematic cross section of porous bi-layered tubular structure.
83x67mm (300 x 300 DPI)

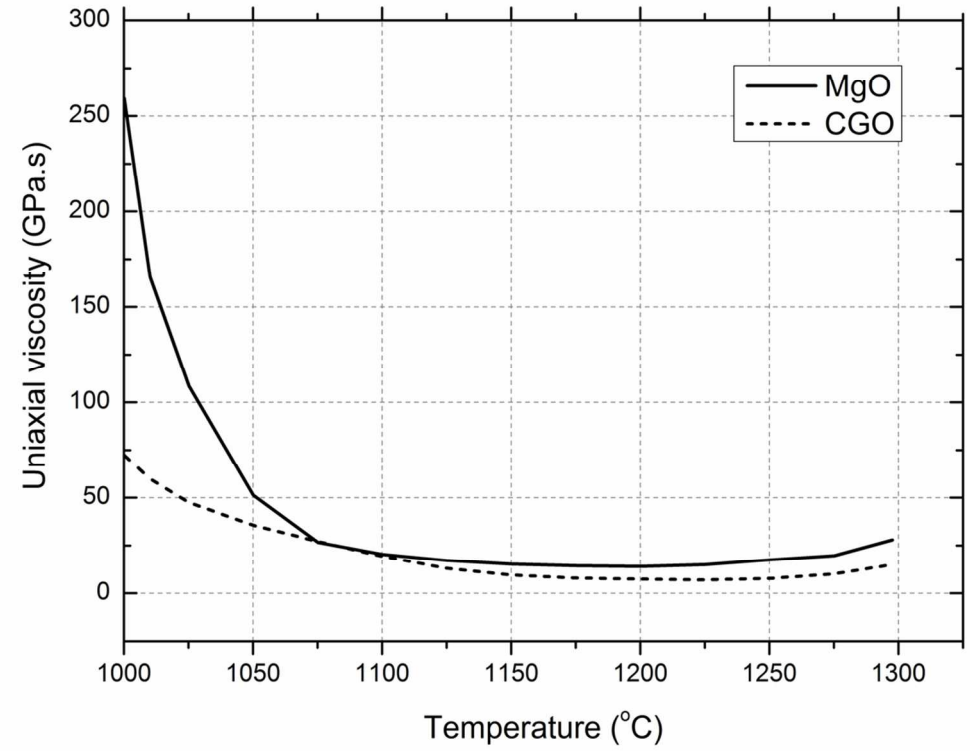

Figure 3: Uni-axial viscosity of MgO and CGO tapes as a function of temperature.
99x76mm (300 x 300 DPI)

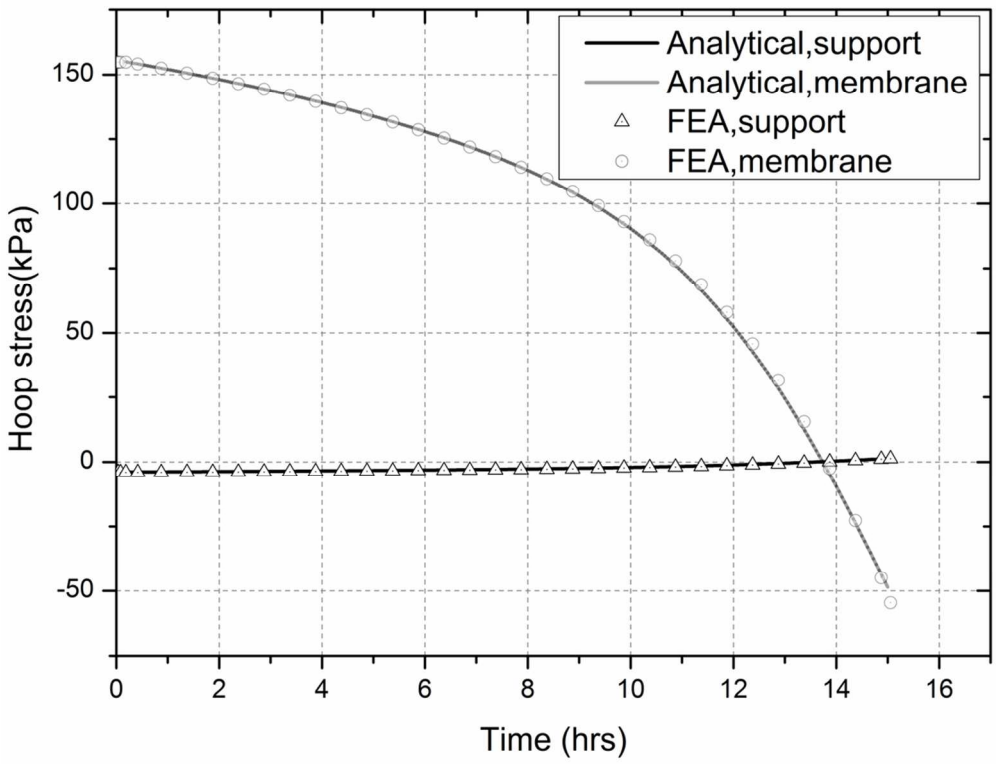

Figure 4: The evolution of hoop stress in the support and membrane during the sintering cycle.
99x76mm (300 x 300 DPI)

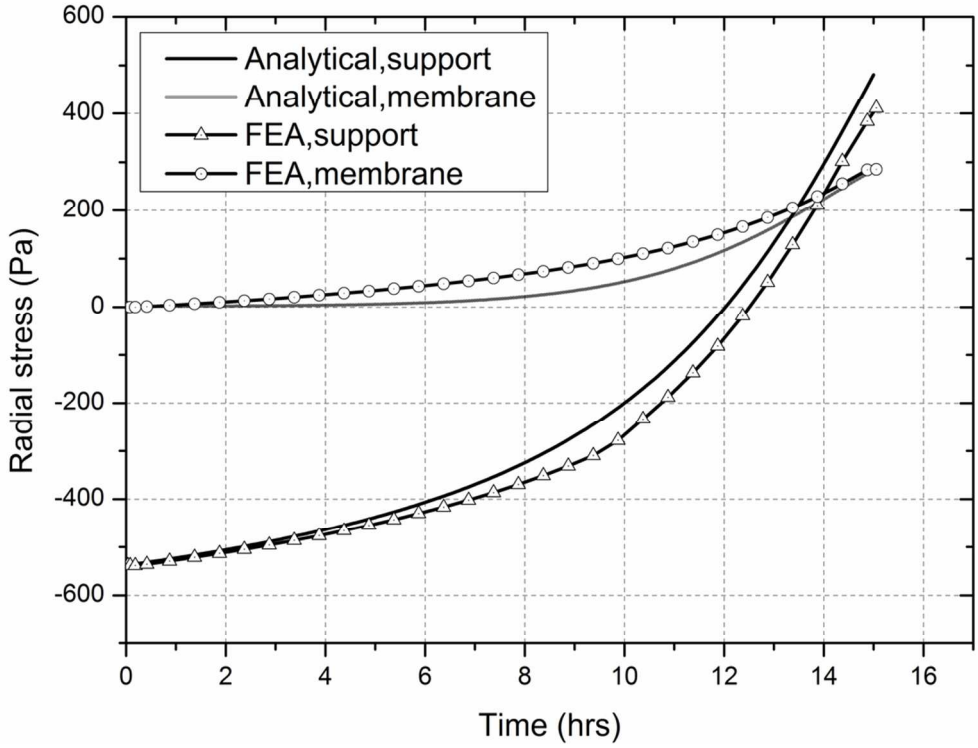

Figure 5: The evolution of radial stress in the support and membrane during the sintering cycle.
97x73mm (300 x 300 DPI)

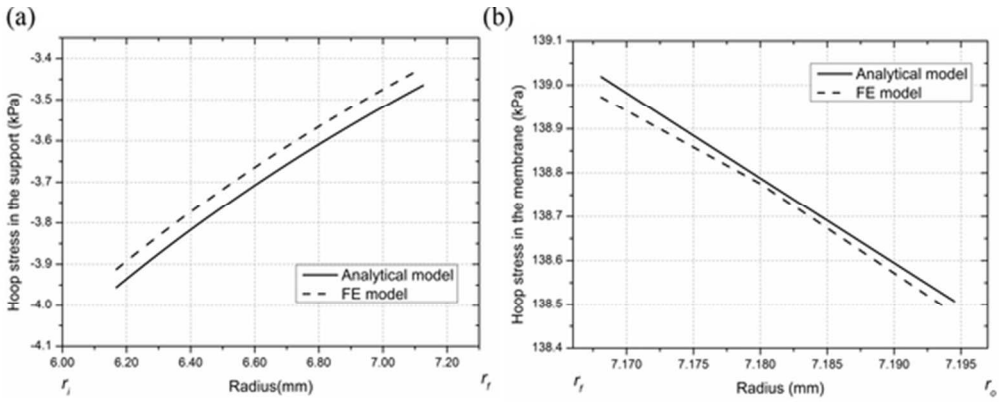

Figure 6: Hoop stress variation across the radius (a) MgO support (b) CGO membrane.
51x20mm (300 x 300 DPI)

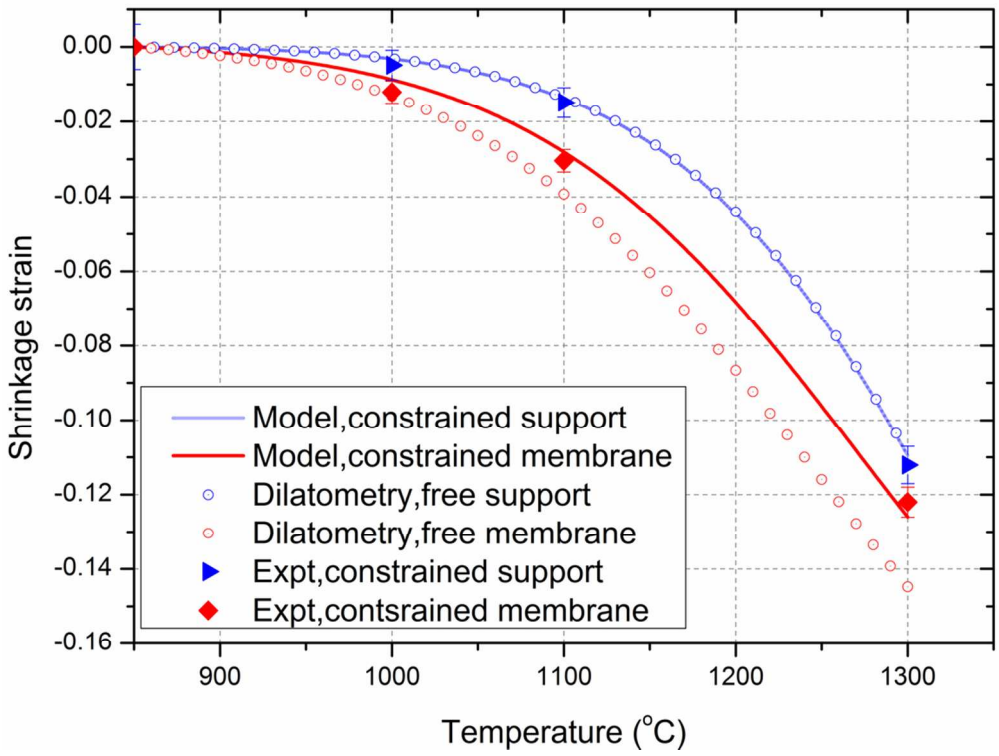

Figure 7: Comparison of linear shrinkage in free and constrained sintering together with experimental measurements for constrained sintering.
97x73mm (300 x 300 DPI)

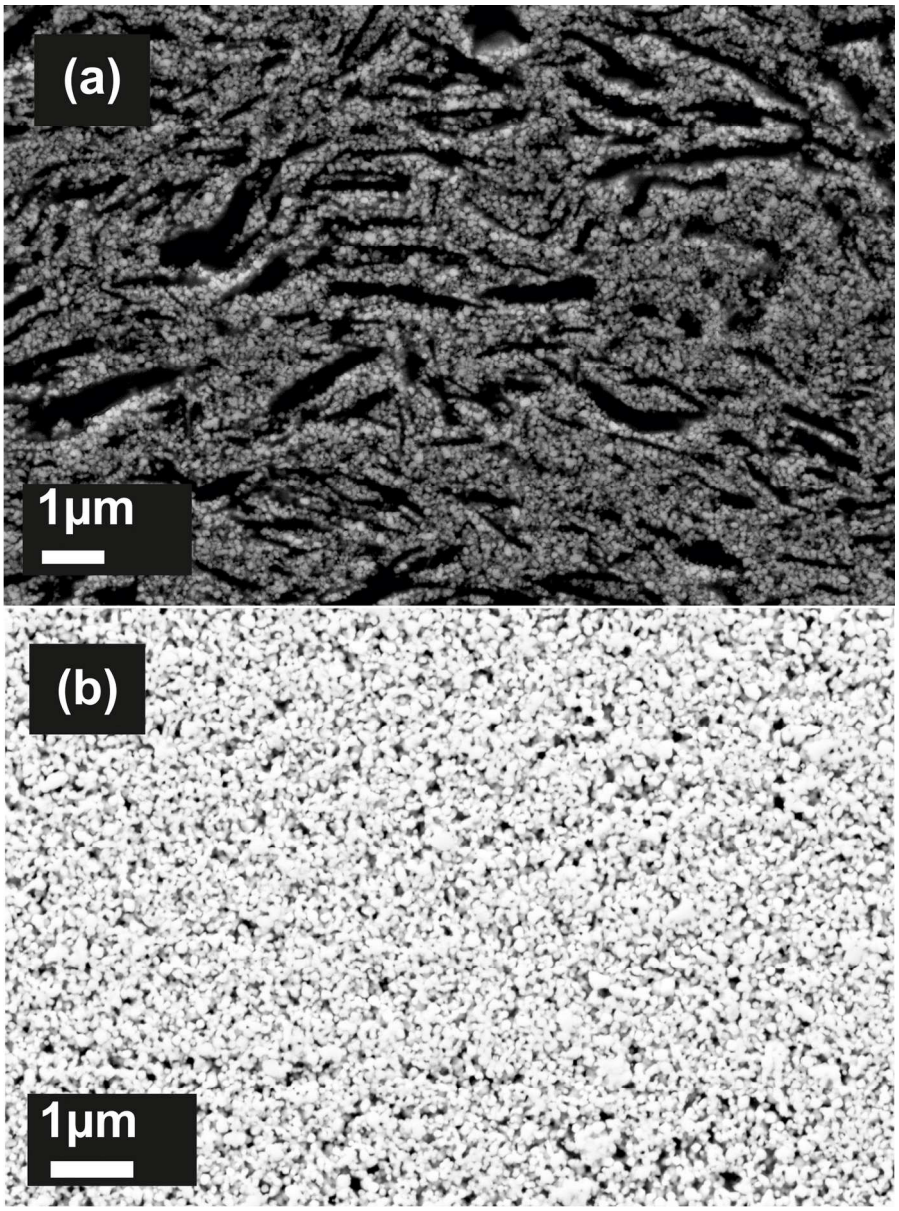

Figure 8: SEM characterization of the bi-layered tubular sample after sintering to 1100°C (a) MgO support and (b) CGO membrane.
138x186mm (300 x 300 DPI)

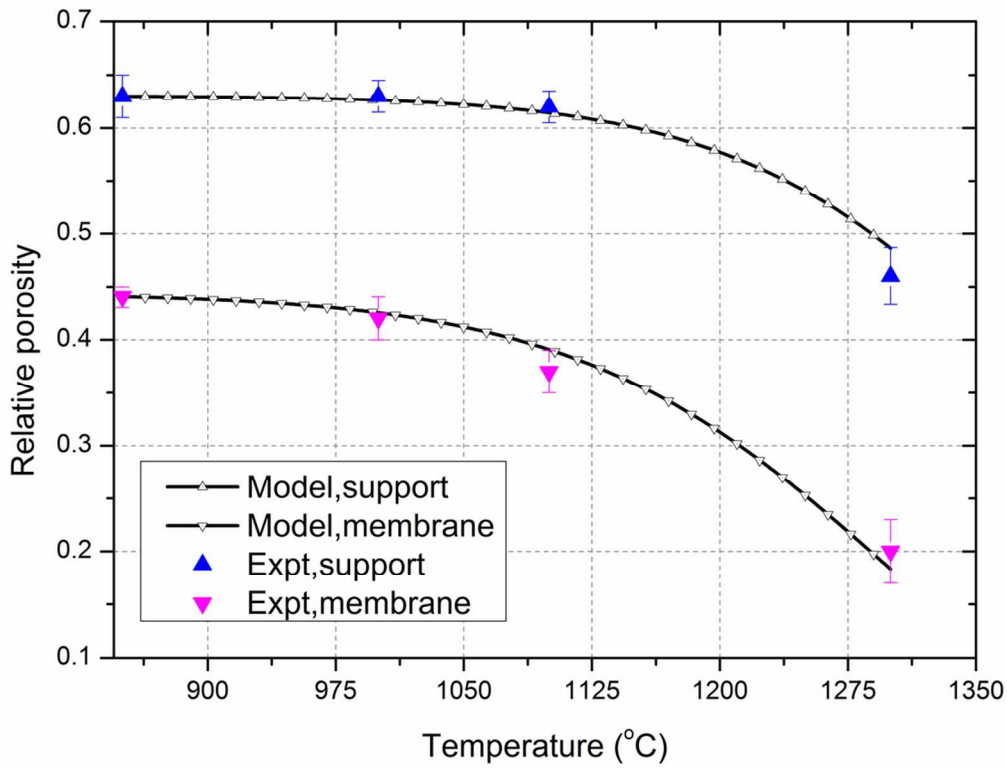

Figure 9: Comparison of the evolution of porosity from model and experiment during constrained sintering of tubular bi-layer sample.
98x75mm (300 x 300 DPI)

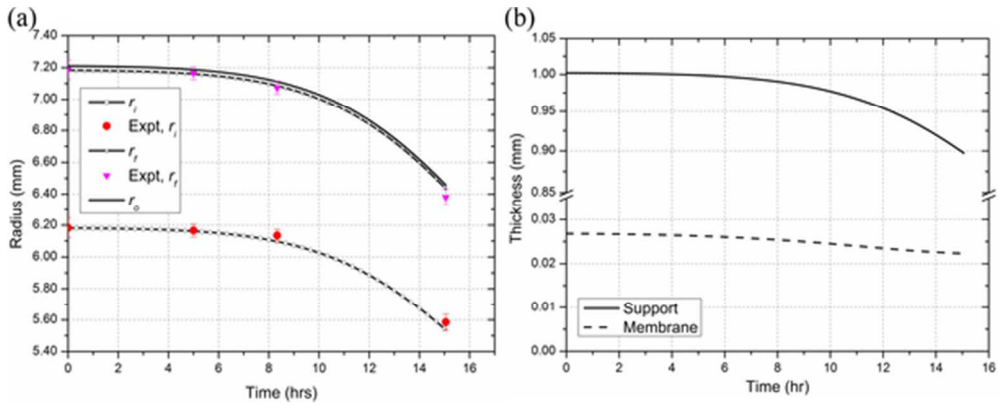

Figure 10: Evolution of geometrical parameters during the sintering cycle: (a) the different radii in the bi-layer (b) thickness.
51x20mm (300 x 300 DPI)

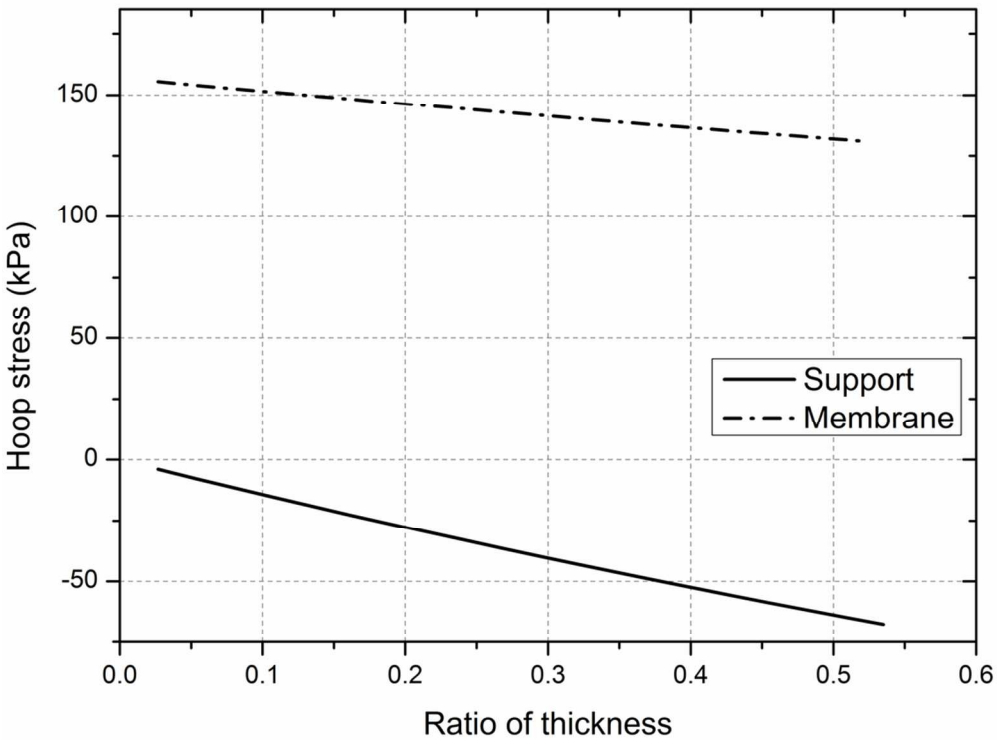

Figure 11: Variation of hoop stress with ratio of thickness of the layers (CGO-membrane to MgO-support) at the beginning of the sintering cycle.
96x71mm (300 x 300 DPI)

Tables

Table 1: Parameters of MgO and CGO layers before and after sintering of the tubular bi-layer at 1300°C

	Initial	Final
External diameter of CGO (mm)	14.42±0.10	12.61±0.61
Thickness of CGO (μm)	26.80±0.30	23.55±0.91
Thickness of MgO (μm)	1002±6.10	886.76±4.52
Relative porosity of CGO	0.44±0.01	0.20±0.03
Relative porosity of MgO	0.63±0.02	0.46±0.03

Table 2: The analogy between linear elasticity and linear viscous materials for stress at a given radius, *r*.

Linear elastic	Linear viscous
$\sigma^{\varepsilon}_{rr,s}=\frac{E_s}{1-\nu_s}\left[\frac{r^2-r_i^2}{(r_f^2-r_i^2)r^2}\int_{r_i}^{r_f} r\varepsilon_s dr-\frac{1}{r^2}\int_{r_i}^{r} r\varepsilon_s dr\right]$	$\sigma^{\varepsilon}_{rr,s}=\frac{\eta_s}{1-\nu'_s}\left[\frac{r^2-r_i^2}{(r_f^2-r_i^2)r^2}\int_{r_i}^{r_f} r\dot{\varepsilon}^f_s dr-\frac{1}{r^2}\int_{r_i}^{r} r\dot{\varepsilon}^f_s dr\right]$
$\sigma^{\varepsilon}_{\theta\theta,s}=\frac{E_s}{1-\nu_s}\left[\frac{r^2+r_i^2}{(r_f^2-r_i^2)r^2}\int_{r_i}^{r_f} r\varepsilon_s dr+\frac{1}{r^2}\int_{r_i}^{r} r\varepsilon_s dr-\varepsilon_s\right]$	$\sigma^{\varepsilon}_{\theta\theta,s}=\frac{\eta_s}{1-\nu'_s}\left[\frac{r^2+r_i^2}{(r_f^2-r_i^2)r^2}\int_{r_i}^{r_f} r\dot{\varepsilon}^f_s dr+\frac{1}{r^2}\int_{r_i}^{r} r\dot{\varepsilon}^f_s dr-\dot{\varepsilon}^f_s\right]$
$\sigma^{\varepsilon}_{rr,m}=\frac{E_m}{1-\nu_m}\left[\frac{r^2-r_f^2}{(r_0^2-r_f^2)r^2}\int_{r_f}^{r_0} r\varepsilon_m dr-\frac{1}{r^2}\int_{r_f}^{r} r\varepsilon_m dr\right]$	$\sigma^{\varepsilon}_{rr,m}=\frac{\eta_m}{1-\nu'_m}\left[\frac{r^2-r_f^2}{(r_0^2-r_f^2)r^2}\int_{r_f}^{r_0} r\dot{\varepsilon}^f_m dr-\frac{1}{r^2}\int_{r_f}^{r} r\dot{\varepsilon}^f_m dr\right]$
$\sigma^{\varepsilon}_{\theta\theta,m}=\frac{E_m}{1-\nu_m}\left[\frac{r^2+r_f^2}{(r_0^2-r_f^2)r^2}\int_{r_f}^{r_0} r\varepsilon_m dr+\frac{1}{r^2}\int_{r_f}^{r} r\varepsilon_m dr-\varepsilon_m\right]$	$\sigma^{\varepsilon}_{\theta\theta,m}=\frac{\eta_m}{1-\nu'_m}\left[\frac{r^2+r_f^2}{(r_0^2-r_f^2)r^2}\int_{r_f}^{r_0} r\dot{\varepsilon}^f_m dr+\frac{1}{r^2}\int_{r_f}^{r} r\dot{\varepsilon}^f_m dr-\dot{\varepsilon}^f_m\right]$

F. PAPER-VI

T.T. Molla, R. Bjørk, E. Olevsky, N. Pryds and H.L. Frandsen, “Multi-scale modeling of shape distortions during sintering of bi-layers,” *J Comp Mat Sci*, **88** 28–36 (2014)

Computational Materials Science 88 (2014) 28–36

Contents lists available at ScienceDirect

Computational Materials Science

journal homepage: www.elsevier.com/locate/commatsci

Multi-scale modeling of shape distortions during sintering of bi-layers

Tesfaye Tadesse Molla [a,*], Rasmus Bjørk [a], Eugene Olevsky [b], Nini Pryds [a], Henrik Lund Frandsen [a]

[a] Technical University of Denmark, Department of Energy Conversion and Storage, Risø Campus Frederiksborgvej 399, P.O. Box 49, Building 779, 4000 Roskilde, Denmark
[b] San Diego State University, Mechanical Engineering Department, 5500 Campanile Dr., San Diego, CA 92182-1323, USA

ARTICLE INFO

Article history:
Received 31 August 2013
Received in revised form 14 January 2014
Accepted 25 February 2014

Keywords:
Multi-scale modeling
Kinetic Monte Carlo
Bi-layer sintering
Distortion

ABSTRACT

Models for deformational behaviors of porous bodies during sintering often rely on limited number of internal variables as they are formulated based on simplified or ideal microstructures. Considering realistic microstructures can improve the predictive capabilities of the already established theories like the continuum theory of sintering. A new multi-scale numerical approach for modeling of shape distortions during sintering of macroscopically inhomogeneous structures combined with a microstructure model is developed. The microstructures of the porous body are described by unit cells based on kinetic Monte Carlo (*kMC*) model of sintering. During the sintering process the shrinkage rate is calculated from the *kMC* model. With the help of computational homogenization, the effective viscosity of the powder compact is also estimated from a boundary value problem defined on the microstructures of unit cells simulated by the *kMC* model. Examples of simulation of sintering of bi-layers based on different material systems are presented to illustrate the multi-scale model. The approach can be considered as an extension to the continuum theory of sintering combined with the meso-scale kinetic Monte Carlo model.

1. Introduction

Shape instabilities during sintering of functionally graded porous multi-layers is one of the problems often observed in the development of various technologies like the solid oxide fuel cells (SOFC), gas purification membranes, etc. [1–8]. Frequently, this problem is related to the differential shrinkage that arises from the macroscopic inhomogenities in the porous body [9–12]. The effect of the sample own weight has recently been shown to be another factor generating stress and distortions during sintering of multi-layer systems [4,6,7]. Generally there is a growing interest towards explicit understanding of the effect of inherent material properties on the extent of shape distortion during sintering of multi-layered porous structures [13]. Significant achievements in modeling of densifications and shape distortions in multi-layer systems have been made using the continuum theory of sintering [2,11,13,14]. The continuum theory of sintering predicts the macroscopic displacement rate in the porous bodies assuming that the powder particles behave in an incompressible linear viscous way [14]. The driving force for sintering (sintering stress) is treated as an additional hydrostatic pressure that arises due to the minimization of surface energy in the entire volume of the sintering specimen. Therefore, to implement the continuum theory of sintering, it is necessary to experimentally measure the sintering behavior i.e. sintering stress or shrinkage rate and the effective viscosity of the porous body. Usually separate set of experiments is used to study those two properties which are then implemented in a model of multi-layer systems [5,10,15,16].

In general, the magnitude of shrinkage rate and the effective viscosity are functions of the internal parameters of the porous structure [14]. These internal parameters are for example the amount and size of pores, grain size of particles, average neck radius, pore diameter to grain size ratio, powder packing, dihedral angle, etc. [17]. Traditionally porosity and grain sizes are considered as the internal parameters defining the evolution of sintering stress and viscosity in the continuum theory of sintering [11,18,19]. This practice however needs to be extended further to account for other internal parameters and hence refine the predicting capabilities of the models. The challenge here is not only the lack of explicit knowledge about which internal parameters are necessary for accurate modeling of the material behaviors, but also that these parameters are very cumbersome to obtain by direct experimental investigations.

The natural extension of the continuum model is to directly consider the internal geometric features of the porous structure to estimate the shrinkage as well as the viscous behaviors. This can be done through a so called multi-scale modeling procedures [17,20,21]. If a representative unit cell of the microstructures evolution is defined during the sintering cycle, it is possible to extract

* Corresponding author. Tel.: +45 2074 5931; fax: +45 4677 5858.
E-mail address: ttmo@dtu.dk (T.T. Molla).

http://dx.doi.org/10.1016/j.commatsci.2014.02.041
0927-0256/

the viscous behaviors of the porous body using techniques in multi-scale modeling. The first challenge here is to be able to predict the proper microstructural geometry of the powder compact and to model its evolution in time. Kuzmov et al. have considered simplified unit cells with circular and elliptical pores and they have also demonstrated the impact of shape of pores on the densification as well as distortion of bi-layered structures [21]. Kuzmov et al., however, assumed the sintering stress to be a curvature dependent traction applied on the surface of the pore, which still limits the effect of other internal parameters on the shrinkage rate of the porous body [21].

Recently there have been a number of reports showing the capabilities of a numerical model based on a kinetic Monte Caro (*kMC*) method [22,23]. The *kMC* model is able to simulate both densification and microstructural evolution during sintering of a powder compact at the meso-scale level. This model is based on solid state sintering having the ability to simulate the different underlying phenomenon during sintering of a powder compact including grain growth, pore migration and vacancy annihilation. It has demonstrated its robust capabilities in predicting the microstructural evolution during sintering of porous bodies [22]. The model has been compared with the sintering of copper spheres as observed using X-ray tomography [22], as well as been used to study the sintering of close packed spheres and powders with a particle size distribution [23,24].

In an attempt to obtain more accurate expressions for sintering stress and bulk viscosity, Olevsky et al. used the 2D microstructures of porous body simulated by the *kMC* model [25]. Olevsky et al. were able to determine the interfacial-free energy for a series of microstructures in time so as to calculate the sintering stress. The sintering stress and normalized bulk viscosity obtained from the *kMC* model is also compared with the result found using the model suggested by Skorohod [41] where a good agreement is shown in the case of normalized bulk viscosity [25].

In this work, a unit cell based on the *kMC* model is established for multi-scale modeling of sintering. This approach is advantageous as the *kMC* model can be extended to provide the important parameters to the continuum model i.e. the densification/shrinkage and viscous behaviors of the powder compact, without having to conduct large amount of experiments. Furthermore the microstructural simulation based on the *kMC* model has the potential to incorporate any of the internal parameters for the given powder compact without limitations.

Therefore the objective of this study is to create a unified model, which couple the local kinetic Monte Carlo (*kMC*) model with a global finite element model in order to predict the shape distortions, e.g. during sintering of bi-layered porous structures. The *kMC* model provides the microstructure evolution as a function of time and temperatures for the representative volume elements (*RVEs*), which are then used to extract the shrinkage as well as viscous parameters of the powder compact that often require tedious experimental work.

2. Multi-scale modeling

The multi-scale modeling approach used in this study consists of two models; one at meso- and another at macro-scale. The meso-scale model is the previously discussed *kMC* model for solid state sintering, where as the macro-scale model is based on finite element method. The meso-scale model is considered to be the *RVE* of the macro-scale geometry, where the *RVEs* are assumed to be distributed throughout the finite element nodal points of the macrostructure.

Two main mechanisms are considered in the deformation of the microstructure, i.e. (1) sintering contraction through diffusion mechanisms (2) viscous deformation of the microstructure from stresses. (1) Is the shrinkage rate in the powder compact $\dot{\varepsilon}^s_{kk}$, which is simulated by the *kMC* model. Hereby introduction of concepts like sintering stress is avoided. In the current work the influence of stress on the annihilation processes and pore migration in the *kMC* are disregarded. This approach is valid for systems where the microstructural evolution is not strongly affected by the stresses throughout the system. While the change in microstructural evolution of course depends on the magnitude of the internal or external stresses, it has been shown that while pores orient depending on the external stress, properties such as the mean grain size can differ little between constrained and freely sintered samples [26,27]. The onset of microstructural anisotropy also depends on the sintering mechanisms; Alumina, sintering by solid state sintering, develops anisotropy during the final stage of sintering [28], while glass, sintering by viscous flow, is anisotropic during sintering but becomes isotropic at the end of the process [29]. Furthermore, the influence of the stress also varies within the sample, allowing parts of a constrained sample to behave as though it was freely sintering [30]. (2) The viscous deformation of the microstructure is handled by a microstructural finite element model with which a homogenization procedure is performed.

The extractions of the viscous properties of the powder compact D_{ijkl}, are based on a special set of boundary value problems (*BVPs*) established on the *RVEs*. The theory of computational homogenization is implemented on each *RVE*, which in this case is based on the microstructure obtained from the *kMC* model in time. The boundary conditions applied on the *RVE* are updated in each time step using the viscous strain rate from the macro-scale model. Fig. 1 shows a schematic flow diagram of the multi-scale modeling procedure used in this study.

Below are the details for the different parts of the multi-scale model.

2.1. Unit cell model or RVE

The kinetic Monte Carlo defines individual grains and pores on a two or three dimensional square/cubical grid, where a single grid cell is referred to as a voxel in both two and three dimensions. The model simulates grain growth, pore migration and vacancy formation and annihilation through diffusion processes. The driving force for sintering in the model is the capillarity (reduction of interfacial free energy), which is defined by the neighbor interaction energy between voxels. Only a brief description of the model is given here as it has been described in detail in previous works [22,31].

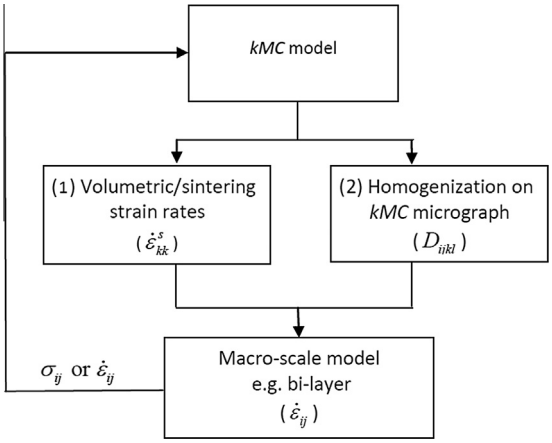

Fig. 1. Schematics of organization in the multi-scale modeling.

The energy at a given site, i, is proportional to the sum of unlike neighbors to that site, i.e.

$$E_i = \frac{1}{2}\sum_{j=1}^{8\,or\,26} J(1-\delta(q_i,q_j)) \tag{1}$$

where J is the neighbor interaction energy, q_i and q_j are the state of the sites i and j respectively, and δ is the Kronecker delta function. A value of $J = 1$ is chosen, as this constitutes the simplest case possible. Grains are identified by different values of q, while all pore sites all have the same state, $q = 0$. The number of neighboring sites considered is 8 for a two dimensional simulation and 26 for a three dimensional one.

Sintering is modeled by interchanging two neighboring sites, altering the state of a single grain site or collapsing an isolated pore site, called a vacancy, by moving it to the surface of the sample. If any of these "moves" lowers the total energy of the system, as calculated in the equation above, then the move is accepted, whereas if the energy is increased the move may be accepted with probability P based on the standard Metropolis algorithm, defined as:

$$P = \begin{cases} \exp\left(\frac{-\Delta E}{k_B T}\right) & \text{for } \Delta E > 0 \\ 1 & \text{for } \Delta E \leqslant 0 \end{cases} \tag{2}$$

Here T is the temperature and k_B is Boltzmann's constant and the different types of events can have different temperatures. The attempt frequency of each type of event can also be varied, allowing different magnitudes of pore surface diffusion, grain boundary diffusion and grain boundary mobility. The attempt frequency is the probability that a given type of move is attempted.

In this study, a two dimensional *kMC* model is used. The shrinkage strain rate of the powder compact is calculated from the densification data at each time step during the simulation of the *kMC* model. Simultaneously the simulated microstructure as shown in Fig. 2 is used as the *RVE* for computational homogenization. Only an internal part of the simulated volume shown in the rectangle is used, in order to remove surface effects.

The microstructure predicted by the *kMC* model is considered to be a typical structural unit of the macroscopic composite. It is thus assumed that any macroscopic piece of the material has the internal structure corresponding to the *RVE*. The typical microstructure of the *RVE* in time is meshed using quadrilateral elements, see Fig. 3. The finite element mesh built on the *RVE* micrograph is consequently used to set up the boundary value problem (*BVP*) for homogenization of the effective viscosity of the powder compact. The computational homogenization over the volume of the *RVE* is based on a linear viscous material model. The details about setting up the boundary value problem and the corresponding homogenization procedures are explained in Section 2.2. For the sake of simplicity only 2D model in plain strain formulation is considered in this study.

In the case of inhomogeneous specimen, e.g. a bi-layer system with different initial porosity, different sets of *RVEs* can be considered depending on the macrostructural domain. Note that the different *RVEs* deform in a different way depending on the macrostructural domain they belong to.

2.2. Homogenization for effective viscous parameters

Computational homogenization theories are used to estimate the effective viscosities of the microstructure using finite element methods. The effective properties of the macroscopic body can be found by the solution of a boundary value problem formulated on a single unit cell or *RVE* with a proper boundary condition [20,21,32–35]. This is based on the assumption that any material

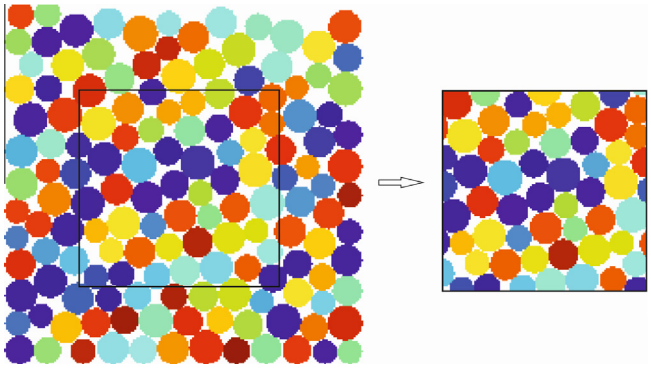

Fig. 2. Example of the representative volume element (RVE) micrograph (400×400 pixels) with each grain having different color.

point $X_p \in \bar{V}$ in the continuum scale can be associated to the local *RVE* whose domain is V with a boundary ∂V. Fig. 4 shows the schematics of the continuum macrostructure and the *kMC* based *RVE*. Note that the characteristic length of the *RVE* is much smaller than the continuum model.

In order to estimate the effective viscosity of the heterogeneous body, the sub-scale modeling approach described by Nguyen et al. [32] is used with the theory of direct correspondence between linear elastic and linear viscous problems [36]. Table 1 below shows the analogies between the linear elastic and linear viscous models. For details of the sub-scale modeling in the case of linear elasticity, please refer the work by Nguyen et al. [32].

The extraction of the viscous parameters from the boundary value problems described above is based on the Hill-Mandel principle of consistency of energy dissipation rate between the meso and macro-scale models [32,34]. For the meso-scale model to be energetically consistent, the rate of deformation energy at the macroscopic level should be equal to the volume average of the meso-scale stress energy dissipation.

$$\begin{aligned} &\bar{\sigma}_{ij}\dot{\bar{\varepsilon}}_{ij} = \frac{1}{V}\int_V \sigma_{ij}\dot{e}_{ij}\,dV \\ &U = \frac{V}{2}\bar{\sigma}_{ij}\dot{\bar{\varepsilon}}_{ij} \end{aligned} \tag{3}$$

For a material that can be analyzed by a linear viscous behaviors, the general constitutive relation between the macro-scale stress and strain rate tensors and hence the stress energy dissipation is:

$$\bar{\sigma}_{ij} = D_{ijkl}\dot{\bar{\varepsilon}}_{kl} \Rightarrow U = \frac{V}{2}\dot{\bar{\varepsilon}}_{ij}D_{ijkl}\dot{\bar{\varepsilon}}_{kl} \tag{4}$$

By solving the boundary value problem on the *RVE* using the periodic boundary conditions described above, it is possible to calculate the stress work (the energy dissipation rate due to deformation, U). Therefore the effective viscosity tensors, D_{ijkl}, of the macrostructure can be obtained by applying a suitable macro-strain rate tensors, $\dot{\bar{\varepsilon}}_{ij}$, depending on the viscous tensor required. To find all componenents of D_{ijkl}, independent load cases in different directions are considered on each *RVE*. For the macro-scale model with 2D plain strain formulation, the entire viscosity tensors can be obtained using separate uniaxial strain conditions and one pure shear deformation. For example, for pure uni-axial strain rate applied in the x-direction $\dot{\bar{\varepsilon}}_{11} = 1$, the rate of stress energy dissipation computed on the *RVE* is given by Eq. (5) from which the tensor, D_{1111}, is calculated.

$$U = \frac{V}{2}D_{1111}\left(\dot{\bar{\varepsilon}}_{11}\right)^2 = \frac{V}{2}D_{1111} \tag{5}$$

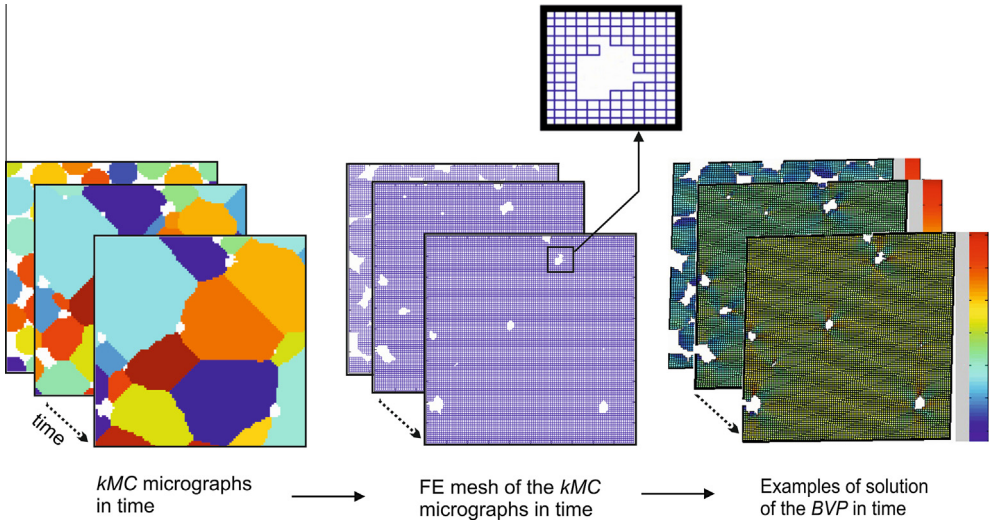

Fig. 3. Schematics of the procedure used to model the effective viscosity of the porous body using boundary value problems (BVP).

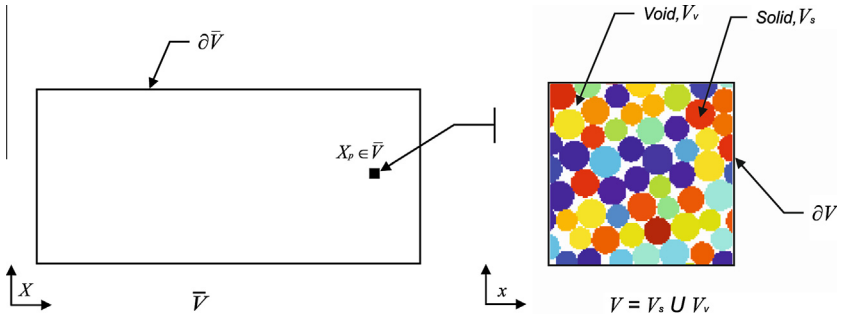

Fig. 4. Schematics of the continuum macrostructure (left) and the representative volume element (RVE) model (right).

Table 1
Field variables and related governing equations for linear elastic model as described in [32] and linear viscous model in this work,

	Linear elastic	Linear viscous	Remarks
Microscopic field variables	Displacement ($\tilde{u}_i$) Strain (e_{ij}) Stress (σ_{ij})	Velocity ($\tilde{v}_i$) Strain rates ($\dot{e}_{ij}$) Stress (σ_{ij})	
Governing equations	$\frac{\partial \sigma_{ij}}{\partial x_j} = 0 \quad \forall x \in V$ $e_{ij} = \frac{1}{2}\left(\frac{\partial \tilde{u}_i}{\partial x_j} + \frac{\partial \tilde{u}_j}{\partial x_i}\right)$	$\frac{\partial \sigma_{ij}}{\partial x_j} = 0 \quad \forall x \in V$ $\dot{e}_{ij} = \frac{1}{2}\left(\frac{\partial \tilde{v}_i}{\partial x_j} + \frac{\partial \tilde{v}_j}{\partial x_i}\right)$	No body force
Boundary conditions	Mean and fluctuation fields on the boundary of the *RVE* $u_i = \bar{u}_i + \tilde{u}_i$ $\tilde{u}(x^+) = \tilde{u}(x^-) \quad \forall x^+ \in \partial V^+$ and matching $\forall x^- \in \partial V^-$	Mean and fluctuation fields on the boundary of the *RVE* $v_i = \bar{v}_i + \tilde{v}_i$ $\tilde{v}(x^+) = \tilde{v}(x^-) \quad \forall x^+ \in \partial V^+$ and matching $\forall x^- \in \partial V^-$	Periodic boundary condition
Initial conditions	$\sigma_{ij} = e_{ij} = \tilde{u}_i = 0$	$\sigma_{ij} = \dot{e}_{ij} = \tilde{v}_i = 0$	
Averaging theory	$\bar{\sigma}_{ij} = \frac{1}{V}\int_V \sigma_{ij} dV$ $\bar{\varepsilon}_{ij} = \frac{1}{V}\int_V e_{ij} dV$	$\bar{\sigma}_{ij} = \frac{1}{V}\int_V \sigma_{ij} dV$ $\dot{\bar{\varepsilon}}_{ij} = \frac{1}{V}\int_V \dot{e}_{ij} dV$	

2.3. Macro-scale model

The finite element method is used to solve the continuum model in the macrostructural model using the shrinkage strain rate $\dot{\varepsilon}^s_{kk}$, and the effective viscosity tensor D_{ijkl}, of the porous body. The finite element equations are formulated based on the direct correspondence between linear elastic and linear viscous problems [36]. The constitutive relationship for linear viscous problems can be written as:

$$\sigma_{ij} = D_{ijkl}\dot{\varepsilon}^c_{kl} \tag{6}$$

where $\dot{\varepsilon}^c_{kl}$ and σ_{ij} are the viscous/creep strain rate and viscous stress respectively. The total strain rate in the sintering body is given by:

$$\dot{\varepsilon}_{kl} = \dot{\varepsilon}^c_{kl} + \dot{\varepsilon}^s_{kl} \tag{7}$$

The sintering related strain rate (densification strain rate) is calculated from the *kMC* based *RVE* model and can be expressed in terms of the relative density ρ, of the powder compact as:

$$\dot{\varepsilon}^s_{kk} = -\frac{\dot{\rho}}{\rho} \tag{8}$$

Considering Eqs. (6) and (7), it is possible to write the constitutive relation for the sintering body as:

$$\sigma_{ij} = D_{ijkl}(\dot{\varepsilon}_{kl} - \dot{\varepsilon}^s_{kl}) \tag{9}$$

The finite element formulations used for the 2D linear viscous analysis is similar to the one used for linear elasticity where the strain is replaced by strain rate defined with the help of the nodal velocity fields. Once the velocity fields are calculated, the displacements of the nodal points are then calculated by integrating the velocity field through the sintering time. The details of the finite element formulations are described in Appendix A.

3. Model application: bi-layer porous structure

The multi-scale modeling procedures described above are implemented using Matlab code. In this section, two types of porous bi-layered structures are considered to illustrate the capabilities of the approach. These are:

I. Bi-layer composed of layers of same materials (similar sinterabilities) but with different initial porosities.
II. Bi-layer composed of layers of different materials (different sinterabilities) but having equal initial porosities.

Bi-layer systems of the first and second type shall be referred to as bi-layer A and bi-layer B, respectively. Fig. 5 shows example of the schematics of the continuum bi-layer structure with the respective *RVEs* of each layer having different porosities. Note that the sinterability of the layer is related to the material's intrinsic driving force for sintering [13].

The initial microstructures were generated by simulation of the pouring of spherical particles with a uniform size distribution with radii between 15 and 20 pixels into a cubic container 400×400 voxels. The powder with lower initial density also contained a number of spherical pore former particles that were removed before sintering. The numerical code used to simulate pouring and packing is the Large-scale Atomic/Molecular Massively Parallel Simulator (LAMMPS) code, available as open source from Sandia National Laboratories. Each powder particle is a single grain.

The sintering behavior of the powders was simulated assuming isothermal heating. All simulations are run for the same length of time, which scales linearly with physical time [22]. The simulation parameters used for this study are temperatures for grain growth, pore migration and for vacancy formation of $k_BT = 0$, 0.7 and 1.5, respectively. The attempt frequencies were chosen in the ratio 1:1:5 for grain growth pore migration and vacancy formation, respectively. The values for the temperatures and attempt frequencies were chosen such that the modeled samples displayed a realistic sintering behavior for a powder compact.

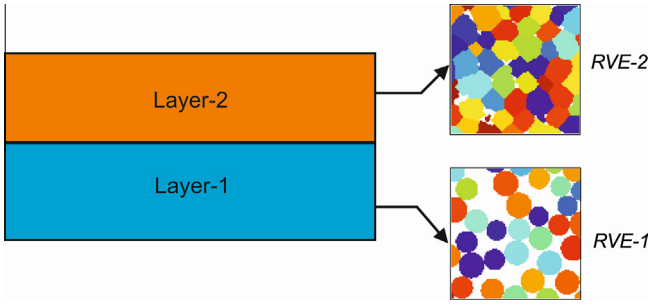

Fig. 5. Schematics showing the continuum bi-layer structure having layers of same material with different initial porosities and the respective representative volume elements (RVEs).

Since both layers of bi-layer A are of same materials, the shear viscosity of the fully dense bodies are assumed to be equal i.e. $\eta_1 = \eta_2 = 40$ GPa s. In the case of bi-layer B, the fully dense body of Layer-2 is assumed to have higher shear viscosity than Layer-1 i.e. $\eta_1 = 40$ GPa s and $\eta_2 = 55$ GPa. In both cases the viscous Poisson's ratio of the fully dense bodies are assumed to be $\nu = 0.48$ [7]. The viscous behaviors of the fully dense bodies are considered to be constant which corresponds to the isothermal sintering where there is no effect of temperature change. In bi-layer A, the initial relative densities of the first and second layers are 0.64 and 0.83 respectively where as in bi-layer B both layers have equal initial relative densities of 0.85.

For the analysis of the macro-scale model, 2D plain strain formulation is used with an initial length of the sample $l_0 = 20$ mm. Both layer's thicknesses are also assumed to be equal at the beginning of the sintering. While simulating the macro-scale bi-layer model, symmetric condition is used by taking half of the entire length of the sample. To account for the randomness in the *kMC* model, the extraction of shrinkage strain rate as well as the effective viscosity of each layer is made based on the average values taken from simulation of nine unit cells or *RVEs* with the same initial microstructures.

The relationship between Monte Carlo and physical time should be evaluated by fitting experimental measurements of densification and the Monte Carlo model prediction for a given powder compact as explained in Mori et al. [37]. Often the physical time of sintering is related to the Monte Carlo simulation time in a linear manner [22]. In this work, a common constant, C with a unit of physical time is used to convert the *kMC* time steps to physical time step τ as shown in Eq. (22).

$$\tau = Ct_{kMC} \tag{10}$$

In this study, it is also assumed that the evolution of the microstructure in each layer is unaffected by the amount of stress in the bi-layer system. This assumption is valid when the shear stress in the bi-layer is not significantly higher than the sintering stress, similar to the observations reported in Ref. [6]. The multi-scale model solutions in terms of kinetics of shrinkage rates in each layer and bending curvature are discussed here under.

The shrinkage strain rate of each layer in both bi-layer A and B are shown in Fig. 6 with the standard deviation from the nine *kMC* simulations of unit cells with the same initial microstructures. In case of bi-layer A, the results indicate more rapid shrinkage in the Layer-1, which has higher initial porosity. In bi-layer B, the shrinkage in Layer-1 is also observed to increase rapidly because of its faster sinterability and/or lower viscosity of the fully dense body. The evolutions of the microstructures of each of the layers in bi-layer A and B at three sample time steps are also shown in Fig. 7. At the initial time step, it is visible to see the difference in the amounts of voids between Layer-1 and Layer-2 in bi-layer A compared to the seemingly similar microstructures between Layer-1 and Layer-2 in bi-layer B. In bi-layer B, it is also clear to notice the rapid densification and the associated grain growth in Layer-1 compared to Layer-2. The different colors on the *kMC* micrographs represent different grains within the powder compact. Fig. 8 shows the average normalized grain growth in each of the layers from the nine *kMC* simulations. The normalized grain growth in the both layers of bi-layer B is higher than those in bi-layer A. This could indicate the effect of sinterability of the materials on the grain growth compared to the initial density.

The homogenized shear viscosities for each of the layers have been modeled based on the procedures outlined in Section 2.2. Note that several authors proposed different models based on

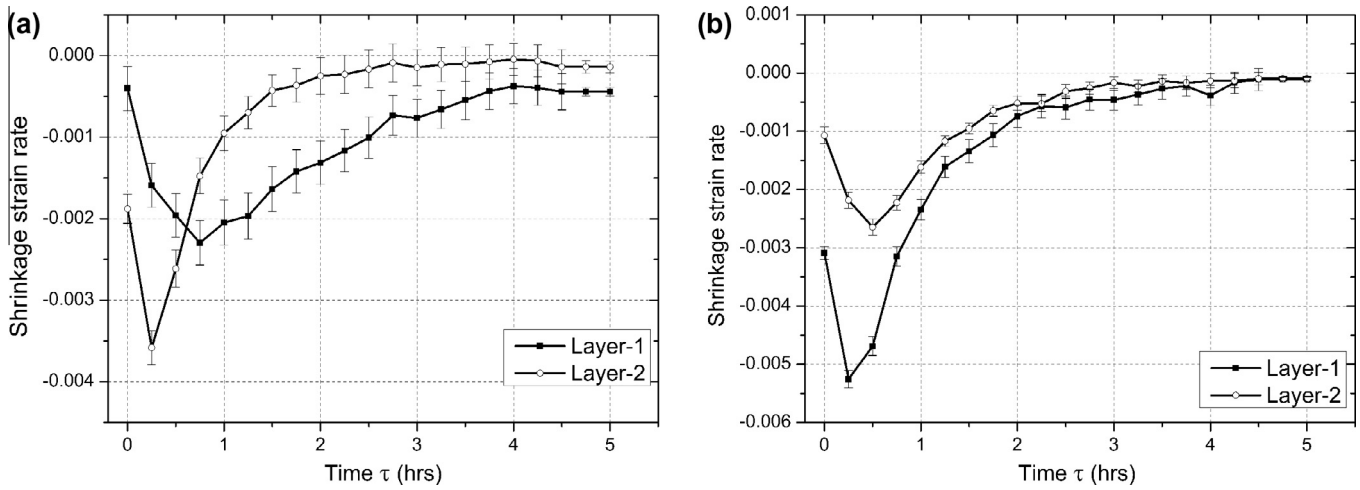

Fig. 6. Sintering strain rates obtained from the kinetic Monte Carlo (kMC) models: (a) bi-layer A and (b) bi-layer B.

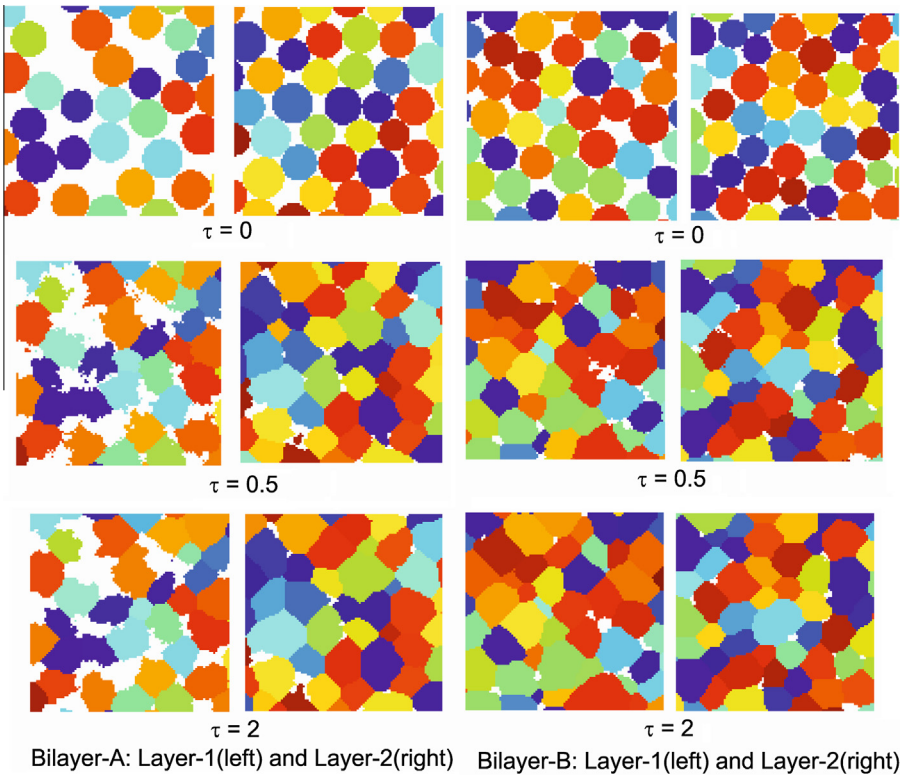

Fig. 7. Microstructural evolutions of each layer in bi-layer A and bi-layer B.

simplified assumptions of the microstructures to describe the shear viscosity as a function of density. Comparison of some of these models is summarized by Bordea and Scherer [38] which show deviations from one model to the other. In this work, the results for the evolution of the homogenized shear viscosity is compared with the model suggested by Skorohod and Olevsky i.e. the Skorohod–Olevsky Viscous Sintering model (SOVS) [14,41], the experimental model determined by Rahaman et al. for shear viscosity of porous CdO [39] and the composite sphere model (CSM) of Ramakrishnan and Arunachalam for shear modulus [40]. Fig. 9 shows the normalized shear viscosities of the Layer-1 (in bi-layer B) as a function of relative density. The shear viscosity extracted from the *RVEs* is shown to be lower than those predicted by the SOVS and CSM theories at lower densities but agrees well with the one suggested by Rahaman et al. The 2D plain strain formulation used while solving the *BVPs* over the unit cell models could affect the accuracy of the results of homogenized viscosities. But at higher densities, all the models show good agreements converging to unity at fully dense state.

The average effective shear viscosities of each layer in bi-layer A and B as estimated from the nine unit cell models are shown in Fig. 10. In bi-layer A, Layer-2 which has higher initial density is shown to have higher effective shear viscosity throughout the time considered. In case of bi-layer B, Layer-2 which has higher dense body viscosity, is found to have higher effective shear viscosity than Layer-1. The lower rate of densification in Layer-2 as shown in Fig. 6(b) is also found to be consistent with the higher effective shear viscosity.

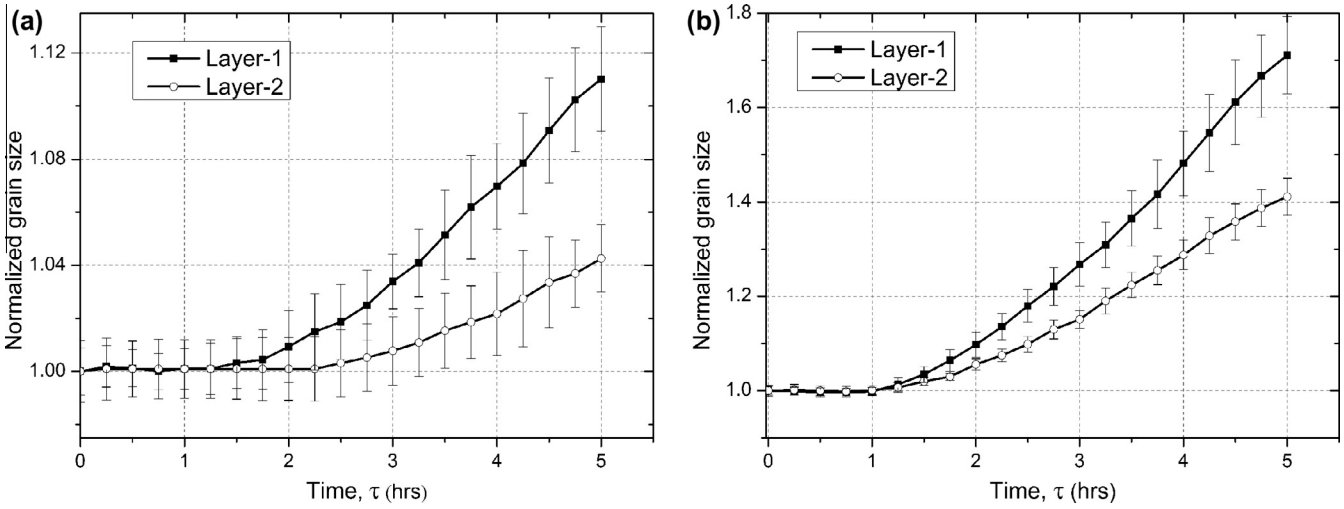

Fig. 8. Grain growth as obtained from the kinetic Monte Carlo (kMC) models: (a) bi-layer A and (b) bi-layer B.

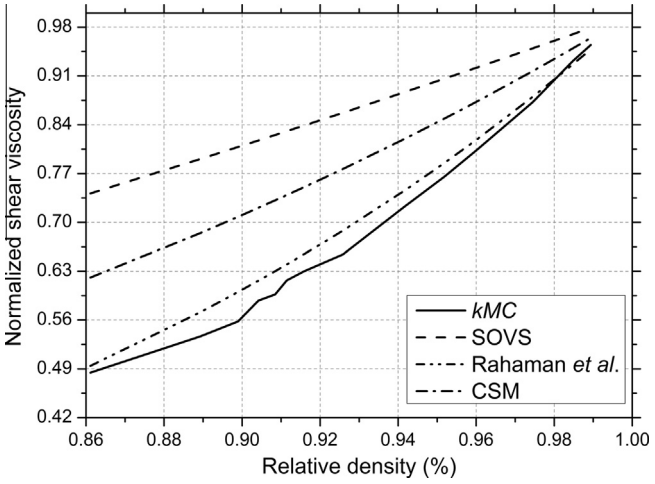

Fig. 9. Normalized shear viscosities.

The contour plot showing the stresses in the *x*-axis in case of bi-layer B is also shown in Fig. 11(a) with a distortion towards Layer-1. The slowly shrinking layer experiences tensile stress imposed on it by the faster shrinking layer which is under compressive stress. Finally the camber evolution in time is also shown in Fig. 11(b) where bi-layer A shows shape reversal in the early stage of the sintering in contrast to a monotonic increase shown in bi-layer B. For the same range of time, the magnitude of distortion in bi-layer A which has layers with different initial porosities is larger than bi-layer B consisting layers of same initial porosities with different sinterabilities.

The approach adopted here could help to explicitly understand the influences of the intrinsic internal parameters on the kinetics of shrinkage and viscous behaviors of powder compacts. Appropriate modeling of those parameters will in turn help to model shape distortions or stresses often observed during sintering of macroscopically inhomogeneous structures. To increase the accuracy of the model, it is also possible to consider distinct unit cells or *RVEs* at each integration point of the elements in the macro-scale model. It is also possible to extend the method described in this work into 3D as the *kMC* model is also able to predict the three dimensional microstructural evolutions of the powder compact during sintering. As the densification proceeds, the number of elements in the representative volume element (*RVE*) increases with the sintering

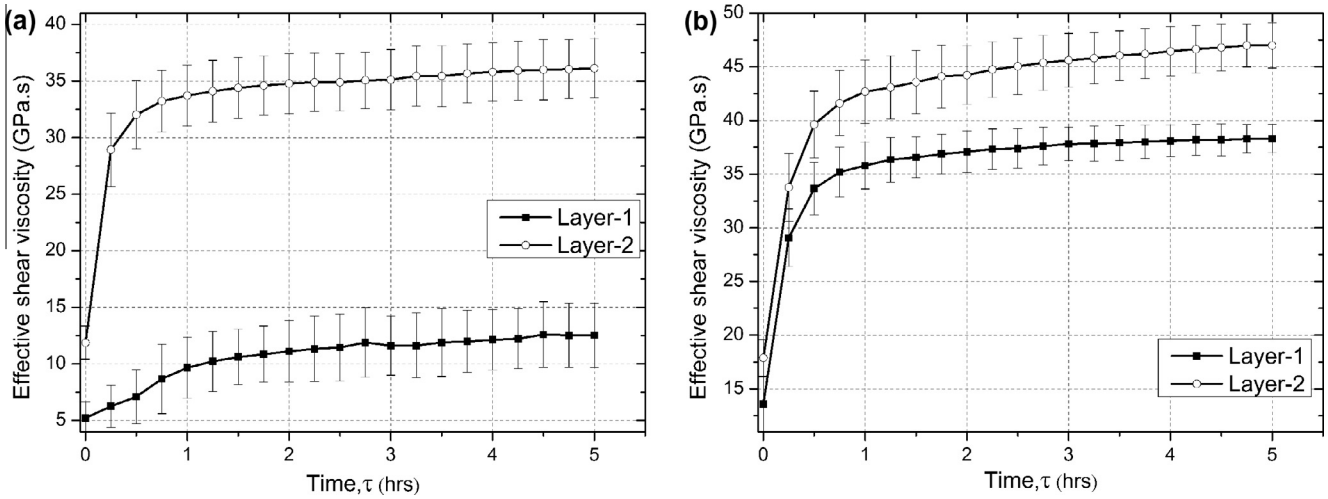

Fig. 10. The effective shear viscosities of each layer in (a) bi-layer A and (b) bi-layer B.

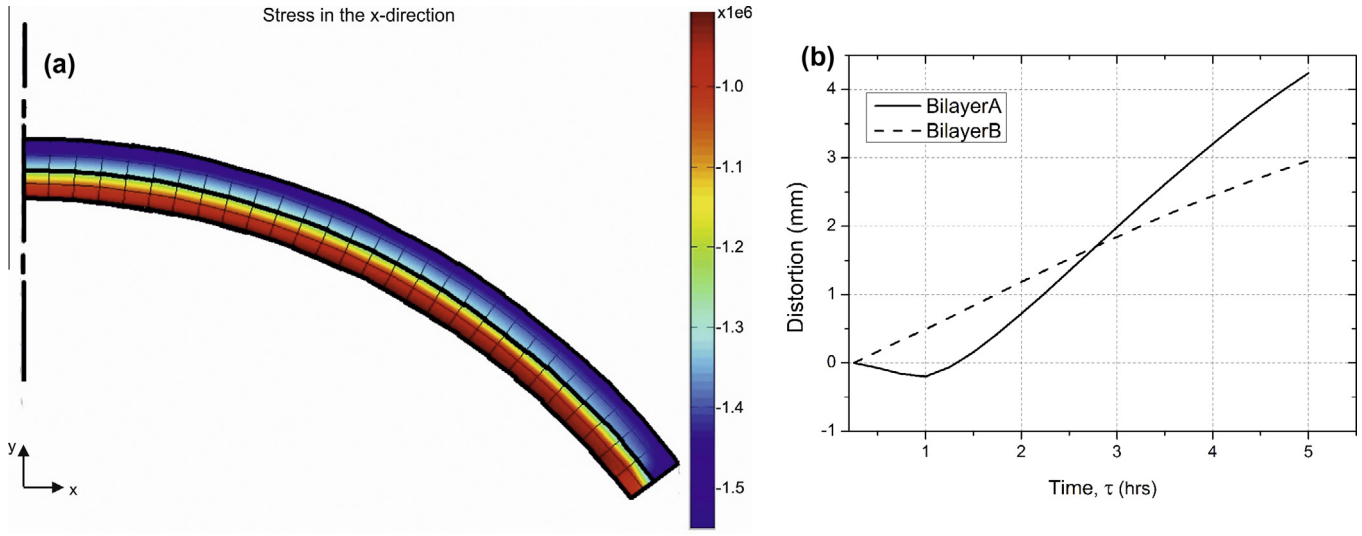

Fig. 11. Distortion in the bi-layer system: (a) contour plot of stress and (b) distortions in bi-layer A and B.

time which in turn increases the computational time to homogenize each *RVEs*. In this study, for an average of 5000 elements in the *RVE* and 112 elements in the macro-scale model, the computational time required to simulate 25 data points in time is approximately 30 min. Experimental validation of the model can also be made by characterizing features of the initial powder compacts of samples so as to get a proper data for the *kMC* model.

4. Conclusions

A new multi-scale modeling procedures using unit cells simulated by the kinetic Monte Carlo method is developed to be able to model shape distortion during sintering of bi-layer systems. The *kMC* model is able to predict the shrinkage rate as well as the microstructure of the powder compact, which is then used to homogenize the effective viscosities. The approach presented here has no limitation on the number of internal parameters considered for modeling the densification as well as viscous behaviors of powder compacts. Comparison of the normalized shear viscosities calculated using the approach developed is found to be in good agreement with other theories from the literature. Using the new procedures, it was possible to model curvature evolution of bi-layers consisting layers of the same and different materials. The expected behavior of the distortion of the bi-layer is observed. The developed multi-scale algorithm can be considered as an extension to the continuum theory of sintering in which the kinetic Monte Carlo model is included.

Acknowledgments

The authors would like to acknowledge the support of the Danish Council for Independent Research Technology and Production Sciences (FTP) which is part of The Danish Agency for Science, Technology and Innovation (FI) (Project # 09-072888). The support of US National Science Foundation Division of Civil, Mechanical Systems, and Manufacturing Innovations (NSF Grant No. CMMI 1234114) is gratefully appreciated. The support of Dr. Veena Tikare from Sandia National Laboratories, USA is also appreciated.

Appendix A. Finite element formulations for 2D linear viscous analysis

The strong form or the equilibrium equation for 2D linear viscous analysis is similar to the equilibrium equation for linear elasticity with the stress in elasticity replaced by viscous stress σ_{ij} as described in Eq. (A2). The viscous/creep strain rate is defined by the velocity field $\boldsymbol{v}^c$ as shown in Eq. (A3). The internal load due to gravity ($\boldsymbol{b}$) is also considered in the equilibrium equation with boundary traction ($\boldsymbol{t}$):

$$\left.\begin{array}{l}\frac{\partial\sigma_x}{\partial X}+\frac{\partial\sigma_{xy}}{\partial X}+b_x=t_x\\ \frac{\partial\sigma_y}{\partial Y}+\frac{\partial\sigma_{xy}}{\partial X}+b_y=t_y\end{array}\right\}\Longleftrightarrow\nabla^T\boldsymbol{\sigma}+\boldsymbol{b}=\boldsymbol{t}\tag{A1}$$

where

$$\nabla^T=\begin{bmatrix}\frac{\partial}{\partial X}&0&\frac{\partial}{\partial Y}\\0&\frac{\partial}{\partial Y}&\frac{\partial}{\partial X}\end{bmatrix};\quad\boldsymbol{\sigma}=\begin{Bmatrix}\sigma_x\\\sigma_y\\\sigma_{xy}\end{Bmatrix};\quad\boldsymbol{b}=\begin{Bmatrix}b_x\\b_y\end{Bmatrix};\quad\boldsymbol{t}=\begin{Bmatrix}t_x\\t_y\end{Bmatrix}\tag{A2}$$

$$\boldsymbol{\sigma}=\boldsymbol{D}(\dot{\boldsymbol{\varepsilon}}-\dot{\boldsymbol{\varepsilon}}^s)\text{ for }\dot{\boldsymbol{\varepsilon}}=\nabla\mathbf{v}^c\quad\text{where }\boldsymbol{v}^c=\begin{Bmatrix}v_x^c\\v_y^c\end{Bmatrix}\text{ and }\nabla\boldsymbol{v}^c=\begin{Bmatrix}\frac{\partial v_x^c}{\partial X}\\\frac{\partial v_y^c}{\partial Y}\\\frac{\partial v_x^c}{\partial X}+\frac{\partial v_y^c}{\partial Y}\end{Bmatrix}\tag{A3}$$

The corresponding weak form of the equilibrium equation is derived from Eq. (A1) with the help of an arbitrary weight function $\boldsymbol{W}(\boldsymbol{X},\boldsymbol{Y})$ [42] and is given as:

$$\int_A(\nabla\boldsymbol{W})^T\boldsymbol{\sigma}\,dA=\int_A\boldsymbol{W}^T\boldsymbol{b}\,dA+\oint_L\boldsymbol{W}^T\boldsymbol{t}\,dL\tag{A4}$$

Note that in 2D analysis, the area A can be loaded with stress $\boldsymbol{\sigma}$ and body force $\boldsymbol{b}$. In addition the boundary can be loaded with traction L_t and/or given a prescribed displacement L_u. The finite element formulation for linear viscous analysis is therefore derived in the following:

Introducing the constitutive equation i.e. Eq. (9) to the weak form or Eq. (A4):

$$\int_A(\nabla\boldsymbol{W})^T\boldsymbol{D}(\dot{\boldsymbol{\varepsilon}}-\dot{\boldsymbol{\varepsilon}}^s)\,dA=\int_A\boldsymbol{W}^T\boldsymbol{b}\,dA+\oint_L\boldsymbol{W}^T\boldsymbol{t}\,dL\tag{A5}$$

The total strain rate is expressed in terms of the gradient of the velocity field as $\dot{\boldsymbol{\varepsilon}}=\nabla\boldsymbol{v}^c$ and hence Eq. (A5) can be written as:

$$\int_A(\nabla\boldsymbol{W})^T\boldsymbol{D}\nabla\boldsymbol{v}^c\,dA-\int_A(\nabla\boldsymbol{W})^T\boldsymbol{D}\dot{\boldsymbol{\varepsilon}}^s\,dA=\int_A\boldsymbol{W}^T\boldsymbol{b}\,dA+\oint_L\boldsymbol{W}^T\boldsymbol{t}\,dL\tag{A6}$$

The same shape function, $\boldsymbol{N}$ is used to define the velocity field $\boldsymbol{v}^c$, and the weight function $\boldsymbol{W}$, i.e. $\boldsymbol{v}^c = \boldsymbol{N}\boldsymbol{v}$; $\boldsymbol{W} = \boldsymbol{N}\boldsymbol{w}$ where $\boldsymbol{v}$ and $\boldsymbol{w}$ are nodal values of the velocity field and the arbitrary weight function respectively. After introducing the gradient of the shape function $\boldsymbol{B} = \nabla \boldsymbol{N}$, it is possible to re-write Eq. (A6) as:

$$\int_A \boldsymbol{B}^T \boldsymbol{D}\boldsymbol{B}\, dA \cdot \boldsymbol{v} - \int_A \boldsymbol{B}^T \boldsymbol{D}\, dA \cdot \dot{\boldsymbol{\varepsilon}}^s = \int_A \boldsymbol{N}^T \boldsymbol{b}\, dA + \oint_L \boldsymbol{N}^T \boldsymbol{t}\, dL \tag{A7}$$

The term in the left side of Eq. (A7) is formulated as:

$$\left[\int_A \boldsymbol{B}^T \boldsymbol{D}\boldsymbol{B}\, dA\right][\boldsymbol{v}] - \left[\int_A \boldsymbol{B}^T \boldsymbol{D}\, dA\right][\dot{\boldsymbol{\varepsilon}}^s] = \boldsymbol{K}[\boldsymbol{v}] - \boldsymbol{K}_f[\dot{\boldsymbol{\varepsilon}}^s] \tag{A8}$$

where

$$\boldsymbol{K} = \int_A \boldsymbol{B}^T \boldsymbol{D}\boldsymbol{B}\, dA \quad \text{and} \quad \boldsymbol{K}_f = \int_A \boldsymbol{B}^T \boldsymbol{D}\, dA \tag{A9}$$

Here $\dot{\boldsymbol{\varepsilon}}^s$ is the free sintering strain rate, which is to be found from the *kMC* based *RVE* model and $\boldsymbol{v}$ is the nodal velocity field associated with the total strain rate to be calculated.

Terms in the right side of Eq. (A7) represent body and traction loads. The load due to internal body forces, e.g. due to gravity is represented as $\boldsymbol{F}_b$ and is also given by:

$$\boldsymbol{F}_b = \int_A \boldsymbol{N}^T \boldsymbol{b}\, dA \tag{A10}$$

The boundary traction and/or prescribed displacement field vectors are denote by $\mathbf{F_t}$ and is given as:

$$\boldsymbol{F}_t = \oint_L \boldsymbol{N}^T \boldsymbol{t}\, dL \tag{A11}$$

Therefore the overall finite element linear formulation can be written using Eqs. (A8)–(A11) as:

$$\begin{aligned} &\boldsymbol{k}\boldsymbol{V} - \boldsymbol{K}_f \dot{\boldsymbol{\varepsilon}}^s = \boldsymbol{F}_t + \boldsymbol{F}_b \\ &\boldsymbol{k}\boldsymbol{V} - \boldsymbol{K}_f \dot{\boldsymbol{\varepsilon}}^s = \boldsymbol{F}_{tb} \\ &\boldsymbol{k}\boldsymbol{V} = \boldsymbol{F}_{tb} + \boldsymbol{K}_f \dot{\boldsymbol{\varepsilon}}^s \\ &\boldsymbol{k}\boldsymbol{V} = \boldsymbol{F} \end{aligned} \tag{A12}$$

References

[1] P. Cai, D. Green, G. Messing, J. Am. Ceram. Soc. 80 (8) (1997) 1929–1939.
[2] D. Green, O. Guillon, I. Roedel, J. Eur. Ceram. Soc. 29 (3) (2009) (537-537).
[3] J. Ollagnier, O. Guillon, J. Roedel, J. Am. Ceram. Soc. 93 (1) (2010) 74–81.
[4] R. Muecke, N. Menzler, H. Buchkremer, D. Stoever, J. Am. Ceram. Soc. 92 (1) (2009) S95–S102.
[5] J. Chang, O. Guillon, J. Roedel, S. Kang, J. Power Sources 185 (2) (2008) 759–764.
[6] H. Frandsen, E. Olevsky, T. Molla, V. Esposito, R. Bjork, N. Pryds, J. Am. Ceram. Soc. 96 (1) (2013) 80–89.
[7] T. Molla, H. Frandsen, R. Bjork, D. Ni, E. Olevsky, N. Pryds, J. Eur. Ceram. Soc. 33 (7) (2013) 1297–1305.
[8] G. Lu, R. Sutterlin, T. Guppta, J. Am. Ceram. Soc. 76 (8) (1993) 1907–1914.
[9] H. Moon, D. Kang, H. Park, S. Hyun, Int. J. Hydrogen Energy 36 (17) (2011) 10991–10997.
[10] P. Cai, D. Green, G. Messing, J. Am. Ceram. Soc. 80 (8) (1997) 1940–1948.
[11] J. Kanters, U. Eisele, J. Rodel, J. Am. Ceram. Soc. 84 (12) (2001) 2757–2763.
[12] J. Kim, R. Rudkin, X. Wang, A. Atkinson, J. Eur. Ceram. Soc. 31 (13) (2011) 2231–2239.
[13] E. Olevsky, T. Molla, H. Frandsen, R. Bjork, V. Esposito, D. Ni, A. Ilyina, N. Pryds, J. Am. Ceram. Soc. (2013) 1–9.
[14] E. Olevsky, Mater. Sci. Eng. R-Reports 23 (2) (1998) 41–100.
[15] J. Chang, J. Jean, Y. Hung, J. Am. Ceram. Soc. 92 (9) (2009) 1946–1950.
[16] T. Garino, H. Bowen, J. Am. Ceram. Soc. 73 (2) (1990) 251–257.
[17] A. Maximenko, A. Kuzmov, E. Grigoryev, E. Olevsky, J. Am. Ceram. Soc. 95 (8) (2012) 2383–2388.
[18] M. Reiterer, K. Ewsuk, J. Am. Ceram. Soc. 92 (7) (2009) 1419–1427.
[19] M. Reiterer, K. Ewsuk, J. Arguello, J. Am. Ceram. Soc. 89 (6) (2006) 1930–1935.
[20] J. Pan, R. Huang, High-Perform. Ceram. V, Pts 1 and 2 368–372 (2008) 1668–1672.
[21] A. Kuzmov, E. Olevsky, A. Maximenko, Modell. Simul. Mater. Sci. Eng. 16 (3) (2008) 035002–035012.
[22] V. Tikare, M. Braginsky, D. Bouvard, A. Vagnon, Comput. Mater. Sci. 48 (2) (2010) 317–325.
[23] R. Bjørk, V. Tikare, H. Frandsen, N. Pryds, J. Am. Ceram. Soc. 96 (2013) 103–110.
[24] R. Bjørk, V. Tikare, H. Frandsen, N. Pryds, Scripta Mater. 67 (2012) 81–84.
[25] E. Olevsky, V. Tikare, T. Garino, J. Am. Ceram. Soc. 89 (6) (2006) 1914–1922.
[26] O. Guillon, L. Weiler, J. Rödel, J. Am. Ceram. Soc. 90 (5) (2007) 1394–1400.
[27] J. Lu, H. Hng, X. Song, J. Am. Ceram. Soc. 94 (5) (2011) 1528–1535.
[28] O. Guillon, I. Nettleship, J. Am. Ceram. Soc. 93 (3) (2010) 627–629.
[29] D. Bernard, O. Guillon, N. Combaret, E. Plougonven, Acta Mater. 59 (2011) 6228–6238.
[30] T. Rasp, C. Jamin, A. Wonisch, T. Kraft, O. Guillon, J. Am. Ceram. Soc. 95 (2) (2012) 586–592.
[31] C. Cardona, V. Tikare, S. Plimpton, Int. J. Comput. Mater. Sci. Surf. Eng. 4 (1) (2011) 37–54.
[32] V. Nguyen, E. Bechet, C. Geuzaine, L. Noels, Comput. Mater. Sci. 55 (2012) 390–406.
[33] J. Pinho-da-Cruz, J. Oliveira, F. Teixeira-Dias, Comput. Mater. Sci. 45 (4) (2009) 1073–1080.
[34] J. Michel, H. Moulinec, P. Suquet, Comput. Meth. Appl. Mech. Eng. 172 (1-4) (1999) 109–143.
[35] D. Griffiths, J. Paiboon, J. Huang, G. Fenton, Int. J. Solids Struct. 49 (14) (2012) 2006–2014.
[36] S. Mukherjee, G. Paulino, J. Appl. Mech–Trans. ASME 70 (3) (2003) 359–363.
[37] K. Mori, H. Matsubara, N. Noguchi, Int. J. Mech. Sci. 46 (2004) 841–854.
[38] G. Scherer, C. Brinker, E. Roth, J. Non Cryst. Solids 72 (2-3) (1985) 369–389.
[39] M. Rahaman, L. De Jonghe, R. Brook, J. Am. Ceram. Soc. 69 (1) (1986) 53–58.
[40] N. Ramakrishnan, V. Arunachalam, J. Mater. Sci. 25 (9) (1990) 3930–3937.
[41] V. Skorohod, Rheological Basis of the Theory of Sintering, Naukova Dumka, Kiev, 1972.
[42] D. Robert, S. David, E. Micael, Concepts and Applications of Finite Element Analysis, third ed., John Wiley and Sons Inc, Canada, 1989.